

NON-LINEAR RESPONSE OF REINFORCED CONCRETE
COUPLING SLAB WITH DROP PANEL IN EARTHQUAKE-
RESISTING SHEAR WALL STRUCTURES

by

ALBERT KEE WAH LIM

Department of Civil Engineering and Applied Mechanics

McGill University

Montréal, Canada

July 1989

A thesis submitted to the Faculty of Graduate Studies
and Research in partial fulfillment of the requirements
for the degree of Master of Engineering

© Albert K.W. Lim 1989

**Response of Slab With Drop Panel
in Coupled Slab-Shear Wall Structures**

ABSTRACT

This thesis reports the response of the coupling member in a selected coupled slab-shear wall system with a drop panel. Four $\frac{1}{3}$ scale reinforced concrete models were tested under reversed cyclic loading with progressively increasing imposed displacements. These specimens were identical in all respects except for variations in the stirrup spacings and concentrated transverse reinforcement near the wall toe. The crack patterns, force-displacement characteristics, reinforcement and concrete strains, and displacement profiles are presented.

The results obtained were compared with the work by other researchers on plain coupling slabs and coupling slabs with shallow beams. An improved response of the coupling slab with drop panel was observed, compared with the other slab coupling systems. The results also compared well with the theoretical strength predictions using the yield line theory and with the punching shear strength calculated using an empirical equation derived based on the observed failure mechanisms. Evaluation of the effective widths and the slab stiffnesses reveals the highly unconservative nature of the available elastic analysis methods. Recommendations for design of coupling slab members in coupled slab-shear wall structures are presented.

RESUME

Cette thèse présente le comportement de dalles jointe à des murs de cisaillement avec panneaux. Quatre modèles à l'échelle $\frac{1}{3}$ fait de béton armé furent testés sous l'effet de charge cyclique avec déformations imposées et amplitudes croissantes. Ces spécimens étaient identiques sauf pour l'espacement des étriers et la quantité d'armature transversale à la base du mur. Les relations force-déplacement, les déformations du béton et de l'armature, les profils de déplacement, ainsi que la distribution des fissures ont été présentés.

Les résultats obtenus furent comparés aux études antérieures faites sur les dalles jointe à des murs de cisaillement avec poutres peu profondes. Une réponse favorable des dalles avec panneaux fut observée comparativement aux autres types de dalles jointes. Les résultats se comparent bien aux prédictions théoriques du "yield line theory", ainsi que le calcul de la résistance au cisaillement utilisant des équations empiriques dérivées des résultats expérimentaux. L'évaluation de la largeur réelle et de la rigidité de la dalle démontre la sous-estimation des modèles élastiques disponibles. Des recommandations sur le design de dalles jointe à des murs de cisaillement sont présentées.

ACKNOWLEDGEMENT

The author would like to express his gratitude to Dr. M.S. Mirza, Professor, Department of Civil Engineering and Applied Mechanics, McGill University, who acted as the research advisor for this research program. The invaluable advice, guidance and encouragement contributed by Dr. Mirza has made the successful completion of this thesis possible.

Thanks are also extended to Dr. William D. Cook for his contribution to making typesetting the thesis so much easier and fun. The excellent computing facilities in the Department of Civil Engineering and Applied Mechanics, McGill University, set up by Dr. Cook enabled the accurate generation of a large number of graphs and drawings presented in this thesis.

The assistance of Mr. Douglas Robertson and Mr. Nicolino Palumbo in testing two specimens (Specimens D3 and D4) is appreciated.

The superb French translation of the abstract by Mr. Claude Pillete is also very much appreciated.

The partial funding provided by the National Research Council of Canada is gratefully acknowledged. The author is immensely indebted to the Graduate Faculty of McGill University for the generous award, the Dalbir Bindra Fellowship, without which this research would not be possible.

The technical assistance of the laboratory technicians Mr. Brian Cockayne, Mr. Ron Sheppard and Mr. Marek Przykorski, and the typing skills of Ms. Linda Tom are very much appreciated.

Thanks are also extended to the author's colleagues in Room 498, McDonald Engineering Building, McGill University for their encouragement and humor throughout the author's residency at McGill University.

Finally, the author wishes to express special thanks to Ms. Anne Marie Mar for

her encouragement and partial assistance in the research program, her patience with the author and, particularly, her loving support.

TABLE OF CONTENTS

ABSTRACT	i
RESUME	ii
ACKNOWLEDGEMENT	iii
TABLE OF CONTENTS	v
LIST OF FIGURES	viii
LIST OF TABLES	xiii
LIST OF SYMBOLS	xiv
1 INTRODUCTION	1
1.1 General Problems in Coupled Shear Wall Structures	1
1.2 Review of Previous Work	6
1.3 Scope of the Research Program	23
2 THE PROTOTYPE STRUCTURE AND THE MODELING PROCESS	25
2.1 The Prototype	25
2.2 Design of the Prototype Slab	26
2.2.1 Transverse Reinforcement for Gravity Load	26
2.2.2 Longitudinal Reinforcement for Seismic Action	26
2.3 The Modeling Process	27
2.3.1 Choice of Geometric Scale	27
2.3.2 Material Similitude	28
2.3.3 Load and Deformation Similitude	32
3 THE MODEL STRUCTURE AND THE TEST SET-UP	37
3.1 Configuration of the Model	37
3.1.1 The Model Geometry and Assembly	37
3.1.2 Limitations	40
3.2 Material Properties	41
3.2.1 Concrete	41
3.2.2 Steel	43
3.3 Design of the Model Structure	45
3.3.1 Wall Reinforcement	50
3.3.2 Transverse Slab Reinforcement	51
3.3.3 Longitudinal Slab Reinforcement	56
3.3.4 Central Cage Stirrups	57

TABLE OF CONTENTS (Continued)

3.4	Instrumentation	58
	3.4.1 Dial Gauges and LVDT's	58
	3.4.2 Load Cells and Load Jacks	60
	3.4.3 Strain Gauges	60
	3.4.4 Demec Gauges	61
3.5	Loading System	64
3.6	Testing Procedure	67
	3.6.1 Loading Program Parameters	67
	3.6.2 Laboratory Loading History	68
	3.6.3 Loading Sequence	70
3.7	Problems Encountered	71
4	EXPERIMENTAL RESULTS	73
4.1	Crack Propagation and Modes of Failure	73
4.2	Force-Displacement Results	91
4.3	Slab Deflection Profile	101
4.4	Longitudinal Seismic Reinforcement and Concrete Strains	106
4.5	Concrete and Steel Strains - Transverse Direction	109
4.6	Strains in Vertical Stirrup Legs	119
5	DISCUSSION OF RESULTS	124
5.1	Crack Propagation	124
5.2	Ultimate Strength	126
5.3	Degradation of Strength and Stiffness	127
5.4	Steel Strains	131
5.5	Effective Slab Width	133
6	SUMMARY AND COMPARISON WITH PREVIOUS WORK	137
6.1	Comparison with Previous Work by Malyszko ¹⁵ and Khan ¹⁶	137
	6.1.1 Introduction	137
	6.1.2 Strength and Stiffness Degradation	139
	6.1.3 Ultimate Strengths	142
6.2	Effective Slab Width	144
6.3	Summary	150
	6.3.1 Ultimate Strengths	150

TABLE OF CONTENTS (Continued)

6.3.2	Crack Propagation	151
6.3.3	Stirrup Performance	151
6.3.4	Stiffness	153
6.3.5	Longitudinal Strains	153
6.3.6	Displacement Profiles	154
6.3.7	Punching Shear Strength	154
7	RECOMMENDATIONS AND CONCLUSIONS	156
7.1	Design Recommendations	156
7.2	Conclusions	158
7.3	Recommendations for Future Research	160
	REFERENCES	164

LIST OF FIGURES

1.1	Types of Earthquake-Resisting Shearwalls	2
1.2	Contribution of Internal Coupling to the Resistance of Overturning Moments in Coupled Shear Walls. (Ref. 3)	5
1.3a	Value of Slab Stiffness Number k and $\frac{V_c}{V}$ as a Function of $\frac{L}{X}$ for $\frac{C}{X} = 0$ (Ref. 7)	7
1.3b	Value of Slab Stiffness Number k and $\frac{V_c}{V}$ as a Function of $\frac{L}{X}$ for $\frac{C}{X} = \frac{1}{7}$ (Ref. 7)	8
1.3c	Value of Slab Stiffness Number k and $\frac{V_c}{V}$ as a Function of $\frac{L}{X}$ for $\frac{C}{X} = \frac{1}{16}$ (Ref. 7)	9
1.4	Critical Section for Shear Suggested by Chang (Ref. 8)	11
1.5	Reinforcing Layout Suggested by Chang (Ref. 8)	12
1.6	$\frac{1}{10}$ -Scale Models Tested by Mirza and Jaeger (Ref. 9)	13
1.7	Representation of Moment Transfer Between Wall and Slab by Discrete Forces (Ref. 29)	15
1.8	15 Storey Prototype Structure Adopted by Taylor and Schematic View of a Typical Interior Bay Section (Ref. 14)	16
1.9	Typical Plan View of Prototype Structure by Taylor (Ref. 14)	17
1.10	Dimensions and Reinforcing Details of Taylor's Test Specimens (Ref. 14)	18
1.11	Cross-Section of Taylor's Specimens 1-4 (Ref. 14)	19
1.12	Schematic Illustration of Taylor's Test Model (Ref. 14)	21
2.1	Similitude Requirements	30
2.2	Relative Movements of Shearwalls Subjected to Lateral Loading	34
2.3	Modeling of Slab Deformation	35
2.4	Illustration of Forces Exerted on West Shearwall	36
3.1	Dimensions of the Model	38
3.2	Assembly of Precast Wall Segments	39
3.3	Grading of Aggregates Used in Specimens D3 and D4 concrete	42
3.4	Typical Concrete Stress-Strain Curve	44
3.5	Typical Stress-Strain Curve for D8.5 Reinforcing Steel	46
3.6	Typical Stress-Strain Curve for Heat Treated D7 Reinforcing Steel	47
3.7	Typical Stress-Strain Curve for D3 Reinforcing Steel	48
3.8	Typical Stress-Strain Curve for Heat Treated D3 Reinforcing Steel	49
3.9	Wall Reinforcement Detail	50
3.10	Slab Flexural Reinforcement Detail of Specimens D1 and D2	52
3.11	Slab Flexural Reinforcement Detail of Specimen D3	53

LIST OF FIGURES (Continued)

3.12 Slab Flexural Reinforcement Detail of Specimen D4	54
3.13 Cross-Section of Slab Reinforcement at Wall Toes of Specimens D1 and D2	55
3.14 Cross-Section of Slab Reinforcement at Wall Toes of Specimens D3 and D4	55
3.15 Dimensions of the Four-Legged Stirrups	57
3.16 Locations of Dial Gauges and LVDT's	59
3.17 Strain Gauge Locations of Specimen D1	61
3.18 Strain Gauge Locations of Specimens D2, D3 and D4	61
3.19 Demec Stud Locations on Top and Bottom Longitudinal Slab Reinforcement of Specimens D1 and D2	62
3.20 Demec Stud Locations on Concentrated Transverse Reinforcement of Specimen D3	63
3.21 Demec Stud Locations on Concentrated Transverse Reinforcement of Specimen D4	64
3.22 Test Set-up and Loading System	65
3.23 Loading History	69
4.1 Crack Pattern for Specimen D1 at Cycle 6, $\Delta = -4.02$ mm	75
4.2 Crack Pattern for Specimen D1 at Cycle 12, $\Delta = -4.91$ mm	75
4.3 Crack Pattern for Specimen D1 at Cycle 24, $\Delta = -8.61$ mm	76
4.4 Crack Pattern for Specimen D1 at Cycle 29, $\Delta = 9.58$ mm	76
4.5 Crack Pattern for Specimen D1 at the Onset of Punching Shear Failure	77
4.6 Crack Pattern on the Underside for Specimen D1 at Cycle 24, $\Delta = -8.61$ mm	77
4.7 Crack Pattern on the Underside for Specimen D1 at Cycle 29, $\Delta = 9.58$ mm	78
4.8 Close Up View on the Crack Patterns for Specimen D1 Near the Wall Toes at Cycle 29, $\Delta = 9.58$ mm	78
4.9 Crack Pattern for Specimen D1 Near the Wall Toes at Failure	79
4.10 Close Up View of the Underside for Specimen D1 Near the Wall Toe Region at Failure (South-East side)	79
4.11 Close Up View of the Underside for Specimen D1 Near the Wall Toe Region at Failure (South-West side)	80
4.12 Crack Pattern for Specimen D2 at Cycle 5, $\Delta = 1.67$ mm	81
4.13 Crack Pattern for Specimen D2 at Cycle 12, $\Delta = -5.09$ mm	81

LIST OF FIGURES (Continued)

4.14 Close Up View of Crack Pattern in Specimen D2 Near the Shear Wall Toes at Onset of Punching Shear Failure	82
4.15 Crack Pattern for Specimen D2 at Cycle 31, $\Delta = 14.73$ mm	82
4.16 Close Up View for Specimen D2 Near the Wall Toes at Failure ($\Delta = 18.07$ mm)	83
4.17 Plan View of the Crack Pattern for Specimen D2 at Failure	83
4.18 Close Up Top View for Specimen D2 Near the West Wall Toe After Failure	84
4.19 Crack Pattern on the Underside for Specimen D2 at Cycle 8, $\Delta = -1.62$ mm	84
4.20 Crack Pattern on the Underside for Specimen D2 at Cycle 18, $\Delta = -8.26$ mm	85
4.21 Close Up View of Drop Panel for Specimen D2 at Onset of Punching Shear Failure	85
4.22 Close Up View of Drop Panel for Specimen D2 at Cycle 37, $\Delta = 18.07$ mm	86
4.23 Close Up Bottom View for Specimen D2 Near the Wall Toe Regions After Failure	86
4.24 Crack Pattern for Specimen D3 at Cycle 1, $\Delta = 3.12$ mm	88
4.25 Crack Pattern for Specimen D3 at Cycle 5, $\Delta = 12.30$ mm	88
4.26 Crack Pattern on the Drop Panel for Specimen D3 at Cycle 14, $\Delta = -19.30$ mm	89
4.27 Close Up View for Specimen D3 Near the Wall Toes at Onset of Punching Shear Failure ($\Delta = 27.99$ mm)	89
4.28 Crack Pattern for Specimen D3 at Cycle 20, $\Delta = -26.85$ mm	90
4.29 Crack Pattern for Specimen D3 at Failure ($\Delta = -34.70$ mm)	90
4.30 Crack Pattern for Specimen D4 at Cycle 8, $\Delta = -7.98$ mm	92
4.31 Crack Pattern for Specimen D4 at Cycle 13, $\Delta = 13.25$ mm	92
4.32 Crack Pattern for Specimen D4 at Cycle 20, $\Delta = -19.05$ mm	93
4.33 Crack Pattern on the Underside for Specimen D4 at Cycle 4, $\Delta = -2.58$ mm	93
4.34 Crack Pattern on the Underside for Specimen D4 at Onset of Punching Shear Failure ($\Delta = -19.05$ mm)	94
4.35 Crack Pattern on the Underside for Specimen D4 at Cycle 26, $\Delta = -23.77$ mm	94
4.36 Punching and Crushing of Concrete Slab for Specimen D4 at Failure ($\Delta = -28.86$ mm)	95
4.37 Load-Deformation Characteristics for Specimen D1	96

LIST OF FIGURES (Continued)

4.38 Load-Deformation Characteristics for Specimen D2	97
4.39 Load-Deformation Characteristics for Specimen D3	98
4.40 Load-Deformation Characteristics for Specimen D4	99
4.41 Longitudinal Slab Displacement Profiles for Specimen D1	102
4.42 Longitudinal Slab Displacement Profiles for Specimen D2	103
4.43 Transverse Slab Displacement Profiles for Specimen D1	104
4.44 Transverse Slab Displacement Profiles for Specimen D2	105
4.45 Longitudinal Strains for Specimen D1	107
4.46 Longitudinal Strains for Specimen D2	108
4.47 Transverse Variation of the Concentrated Transverse Reinforcement Strain of Specimen D3	110
4.48 Transverse Variation of the Concrete Strain of Specimen D3 in the Transverse Direction	111
4.49 Longitudinal Variation of the Concentrated Transverse Reinforcement Strain of Specimen D3	112
4.50 Longitudinal Variation of the Concrete Strain of Specimen D3 in the Transverse Direction	113
4.51 Transverse Variation of the Concentrated Transverse Reinforcement Strain for Specimen D4	115
4.52 Transverse Variation of the Concrete Strain for Specimen D4 in the Transverse Direction	116
4.53 Longitudinal Variation of the Concentrated Transverse Reinforcement Strain for Specimen D4	117
4.54 Longitudinal Variation of the Concrete Strain for Specimen D4 in the Transverse Direction	118
4.55 Strains in Inner Vertical Stirrup Legs for Specimen D1	119
4.56 Strains in Inner Vertical Stirrup Legs for Specimen D2	120
4.57 Strains in Outer Vertical Stirrup Legs for Specimen D2	120
4.58 Strains in Inner Vertical Stirrup Legs for Specimen D3	121
4.59 Strains in Outer Vertical Stirrup Legs for Specimen D3	121
4.60 Strains in Inner Vertical Stirrup Legs for Specimen D4	122
4.61 Strains in Outer Vertical Stirrup Legs for Specimen D4	122
5.1 Schematic Diagrams of Crack Propagation	125
5.2 Deformed Shape of Coupling Slab at Failure (Specimen D2)	132
5.3 Fixed-Ended Beam Subjected to Relative Vertical Displacement, Δ	134

LIST OF FIGURES (Continued)

6.1	Details of Coupled Slab-Shear Wall Systems Investigated	138
6.2	Variation of Coupled Slab-Shear Wall System Stiffness with Relative Wall Displacement	140
6.3	Variation of Coupled Slab-Shear Wall System Strength with Relative Wall Displacement	143
6.4	Taylor's Unit 2 Force-Displacement Characteristics (ref 14)	146
6.5	Longitudinal and Transverse Reinforcement Detail	152
7.1	Critical Section for Punching Shear Around the Wall Toe	157
7.2	Possible Wall Configurations for Future Studies	163

LIST OF TABLES

2.1	Typical Model Scale Factors (Ref. 17)	27
2.2	Similitude Requirements, Static Elastic Modeling (Ref. 17)	29
2.3	Summary of Scale Factors for Reinforced Concrete Strength Models (Ref. 17)	31
2.4	Possible Distortions in Reinforced Concrete Models (Ref. 17)	32
2.5	Summary of Scale Factors and Scaled Model Values	32
3.1	Proportions of Aggregates Used in Specimens D3 and D4	43
3.2	Reinforcement Specifications	45
3.3	Reinforcing Steel Properties	45
3.4	“Displacement Ductility of 1” During the First Excursion to Inelastic Deformation	70
5.1	Experimental Ultimate Strength Results and Predictions	126
5.2	Relative Load-Deformation Relationships for Specimen D1	129
5.3	Relative Load-Deformation Relationships for Specimen D2	129
5.4	Relative Load-Deformation Relationships for Specimen D3	129
5.5	Relative Load-Deformation Relationships for Specimen D4	130
5.6	Stiffness Variation for Specimen D1	130
5.7	Stiffness Variation for Specimen D2	130
5.8	Stiffness Variation for Specimen D3	131
5.9	Stiffness Variation for Specimen D4	131
5.10	Effective Slab Width for Specimen D1	135
5.11	Effective Slab Width for Specimen D2	135
5.12	Effective Slab Width for Specimen D3	135
5.13	Effective Slab Width for Specimen D4	136
5.14	Stiffness Values of Lines L1 to L5 Used in Figures 4.37 through 4.40	136
6.1	Summary of Experimental Results of Phases 1, 2 and 3 Specimens	139
6.2	Equivalent Effective Widths of Model Structure Suggested by Various Investigators	147
6.3	Effective Widths of Phase 1 and Phase 3 Specimens Based on I_{cr} and I_{st}	148
6.4	Calculated Effective Widths of Phase 1 and Phase 3 Specimens Based on Experimental Results	148

LIST OF SYMBOLS

A_r	area of reinforcement
b	half bay width
b_{eff}	effective width of slab
c	width of corridor opening
C	projection of slab from outer edge of shear wall
d	effective depth of slab
D	flexural rigidity of plate = $Eh^3/[12(1 - \nu^2)]$
E	modulus of elasticity
E_c	modulus of elasticity of concrete
E_r	modulus of elasticity of reinforcement
f'_c	concrete strength at age of 28 days
h	thickness of slab
i_m	model quantity
i_p	prototype quantity
I	second moment of area
I_{cr}	second moment of cracked concrete cross-sectional area
I_g	second moment of gross concrete cross-sectional area
I_{st}	second moment of steel area alone
k	non-dimensional slab stiffness number
K	slab stiffness = V/Δ
l	center to center distance between walls of a coupled shear wall structure
L	clear span between shear walls; width of corridor opening
M	bending moment at ends of a fixed ended beam
M_o	overturning moment at base of shear wall structure
M_1	bending moment in first wall of a coupled shear wall structure
M_2	bending moment in second wall of a coupled shear wall structure
q	pressure
Q	concentrated load
S_i	scale factor for quantity $i = i_p/i_m$
S_E	scale factor for modulus of elasticity
S_l	scale factor for linear dimension
S_ϵ	scale factor for strain
S_σ	scale factor for stress
t	wall thickness

LIST OF SYMBOLS (Continued)

T	axial force in walls of a coupled shear wall structure
u	bond stress
V	net shear force in coupling beam of coupled shear wall structure
w	uniform line load
W	larger cross-sectional dimension of shear wall
X	distance between outer edges of in-plane shear walls
Y	width of slab in a typical bay
Y_e	effective width of slab
β	angular displacement
δ	displacement
Δ	relative vertical wall displacement
ε	strain
ε_c	concrete strain
ε_m	model strain
ε_p	prototype strain
ε_r	reinforcement strain
ε_y	steel yield strain
θ	rotation of shear wall and slab connection
μ	displacement ductility ratio
ν	poisson's ratio
ν_c	poisson's ratio for concrete
ρ	reinforcement ratio
ρ_c	mass density of concrete
ρ_{\min}	minimum allowable reinforcement ratio
σ	stress
σ_r	stress in reinforcement
σ_c	stress in concrete
v_n	nominal punching shear stress

CHAPTER 1

INTRODUCTION

1.1 General Problems in Coupled Shear Wall Structures

The past two decades have seen rapid increase in the popularity of shear walls in multistorey buildings to resist wind and earthquake forces. With increasing knowledge of the inelastic behaviour of shear walls and coupled shear wall systems under lateral loading, the erroneous notion that shear wall structures are inherently brittle, has been dispelled. Their inherent economy, natural stiffness and inelastic behaviour², along with the ductility of properly detailed shear walls³ has led to their wide acceptance in high-rise buildings. In fact, in recent years, shear walls have been used not just in high-rise buildings, but also in many low rise commercial buildings.

The simplest form of shear wall - a tall, single, solid cantilever as illustrated in Figure 1.1a - is an excellent classroom example but is otherwise rarely used in practice. Most often, cantilever walls are pierced throughout; commonly by a single row of openings as illustrated in Figures 1.1b and 1.1c. Such structural form is referred to as a coupled shear wall, where two shear walls are joined together by a series of coupling or "link" beams. The focus of this thesis is on thin coupling beams (Figure 1.1c) such as monolithic concrete floor slabs. The use of such elements is common particularly in high-rise apartment buildings.

A well designed structure is expected to resist light to moderate earthquakes with

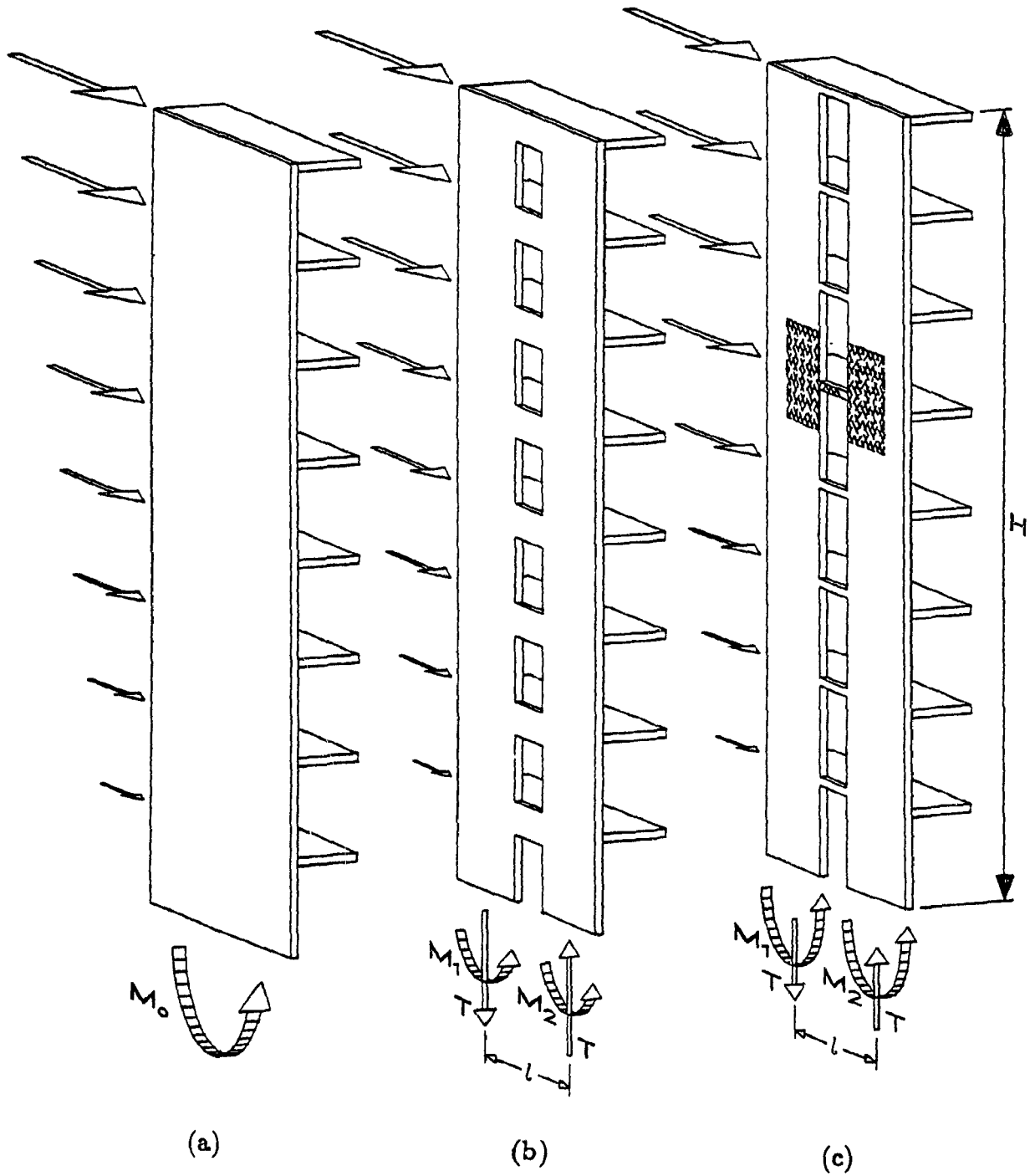


Figure 1.1 Types of Earthquake-Resisting Shearwalls
 (a) Cantilever Walls
 (b) Two Walls Coupled by Beams
 (c) Two Walls Coupled by Floor Slabs.

no damage or minor repairable damage. However, it would be uneconomical to provide for inertial forces caused by large earthquakes and the designer must rely upon the energy dissipation associated with the transient excursions of the system into the "postelastic" range⁴. The emphasis is on protection of essential elements such as the shear walls and columns, against early damage and on provision for the dissipation of energy through large deformations in elements such as the coupling beams and slabs, which can be repaired after the earthquake to restore the structure to serviceable conditions.²¹

The significant weakening of the structure resulting from piercing of cantilever shear walls with one row of openings has led engineers and researchers into finding ways of improving the effectiveness of the coupling member in participating in the earthquake-resisting actions³. In particular, for the extreme case of coupled shear walls where the coupling member is so shallow, such as two walls coupled by floor slabs only, as shown in Figure 1.1c, the ability of the slab to maintain sufficient strength and stiffness, providing adequate ductility and exhibiting stable hysteretic response is crucial. Provided that the hierarchy of failure mechanisms of the slabs is such that a majority of them will yield significantly before the development of plastic hinges at the base of the walls, a very significant part, if not all of the required energy dissipation can take place in the coupling system, thereby protecting the walls against "early damage"³.

One desirable feature in a shear wall structure subjected to earthquake forces is its hysteretic response - the ability of the structure to dissipate energy. For a single, plain, solid cantilever shear wall, such energy dissipation takes place when inelastic deformations caused by an overturning moment, M_o , (Figure 1.1a) occur due to a single plastic hinge in the bottom storeys of the wall. For a coupled shear wall, the overturning moment, M_o , is resisted at the base of the coupled shear walls by moments in each of the two walls, M_1 and M_2 , and by axial forces, T , forming a couple with a significant internal lever arm l as shown in Figures 1.1(b) and 1.1(c). The equilibrium

of the forces at the base of the coupled structure leads to the equation :

$$M_o = M_1 + M_2 + lT \quad (1-1)$$

The axial load, T , induced at any level in either of the walls is the sum of the shear forces induced in the coupling beams situated above that level. The ability of the coupling beams to dissipate part of the total energy of the coupled shear wall structure subjected to lateral load, as shown in Figures 1.1(b) and 1.1(c), depends on the contribution of these beams to the resistance of the overturning moment. The relative magnitudes of resistance to the overturning moment for the three structural systems shown in Figure 1.1 are shown in Figure 1.2. It is evident from Figure 1.2 that the stiff and suitably reinforced coupling beams (Figure 1.1(b)) will develop significant shear forces and consequently introduce large axial forces to the walls. These large axial forces form the large coupling action, lT , for the beam coupled shear wall structure, as shown in Figure 1.2, which become the major source of resistance and energy dissipation during large seismic displacements. For a coupled slab-shear wall structure (Figure 1.1(c)), relatively small axial forces in the walls can be induced due to the slab flexibility relative to the walls and small potential strengths. Consequently the dissipation of energy through internal couple formed by the induced axial forces in the walls will be low (Figure 1.2) and sometimes ignored by practicing engineers. The major source of resistance against overturning moment and energy dissipation required of such systems will be flexure at the base of the walls, as shown in Figure 1.1(c). However, during an inelastic cyclic response, the relative proportions of the terms $(M_1 + M_2)$ and lT of the total resistance may change depending on the nature of stiffness and strength degradation that may occur in various components during a seismic response of the structure.

The response of coupled shear wall systems subjected to the random vibratory motions caused by earthquakes or winds is further complicated by the effects of variable

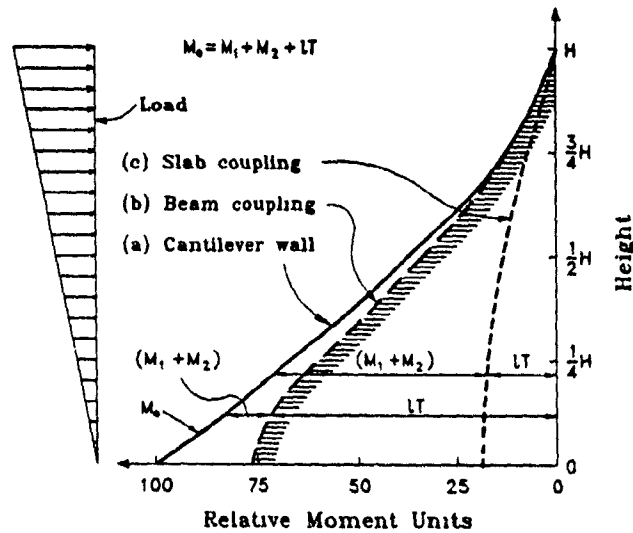


Figure 1.2 Contribution of Internal Coupling to the Resistance of Overturning Moments in Coupled Shear Walls. (Ref. 3).

reversed and repeated loading, rate of loading and degradation of strength and stiffness during large excursions.

In the design process, accurate assessments of the coupling system attributes – stiffness, yield moment and ductility – can be very important. Axial forces on the walls can be underestimated if the “actual” stiffness of the coupling member is greater than its “design” stiffness. However, when the reverse is true, the moment can be significantly underestimated⁵. It is therefore important for the designer to understand the behaviour of coupled shear wall system subjected to earthquake or wind loads. Considerable information on the elastic response and analysis of coupled slab-shear wall systems is available presently; however, the data on the post-cracking and post-yielding nonlinear response of such systems is relatively scarce. A brief historical review of the literature follows.

1.2 Review of Previous Work

Despite the fact that much research work – both theoretical and experimental – has been conducted on subjects related to shear wall structures, very little research has been undertaken on the behaviour of coupling slab members in coupled slab-shear wall structures. Hence, relatively little information related to this subject is available. In this section, a brief summary of the previous work in this area is presented chronologically.

In 1966, Barnard and Schwaighofer⁶ conducted three tests on $\frac{1}{64}$ th-scale epoxy models of 22-storey shear wall structures inter-connected with floor slabs⁷. In comparison with Rosman's theory, they found that their results compared well when the entire bay width was considered as the effective slab width.

Qadeer and Stafford Smith⁷ (1969) presented results for the bending stiffness of slabs connecting shear walls based on finite difference analyses of an idealized elastic plate. The results, presented graphically (Figures 1.3a—1.3c), enable evaluation of the nondimensional stiffness, or the effective width of a slab for different slab proportions, wall spacings, and slab and wall lengths. For a particular coupled slab-shear wall configuration, the ratio of the projection of the slab from the outer edge of the shear wall to the distance between the outer edges of the in-plane shear walls (C/X), the ratio of the clear span between the shear walls to the distance between the outer edges of the in-plane shear walls (L/X), and the ratio of the slab width to the distance between the outer edges of the in-plane shear walls (Y/X) can be determined. Based on these C/X , L/X , and Y/X values and using the charts presented in Figures 1.3a—1.3c, the non-dimensional stiffness number (k) and the ratio of the effective width of the slab to the slab width (Y_e/Y) can be obtained. The non-dimensional stiffness number k can be used to compute the flexural rigidity of the slab, EI , using the expression:

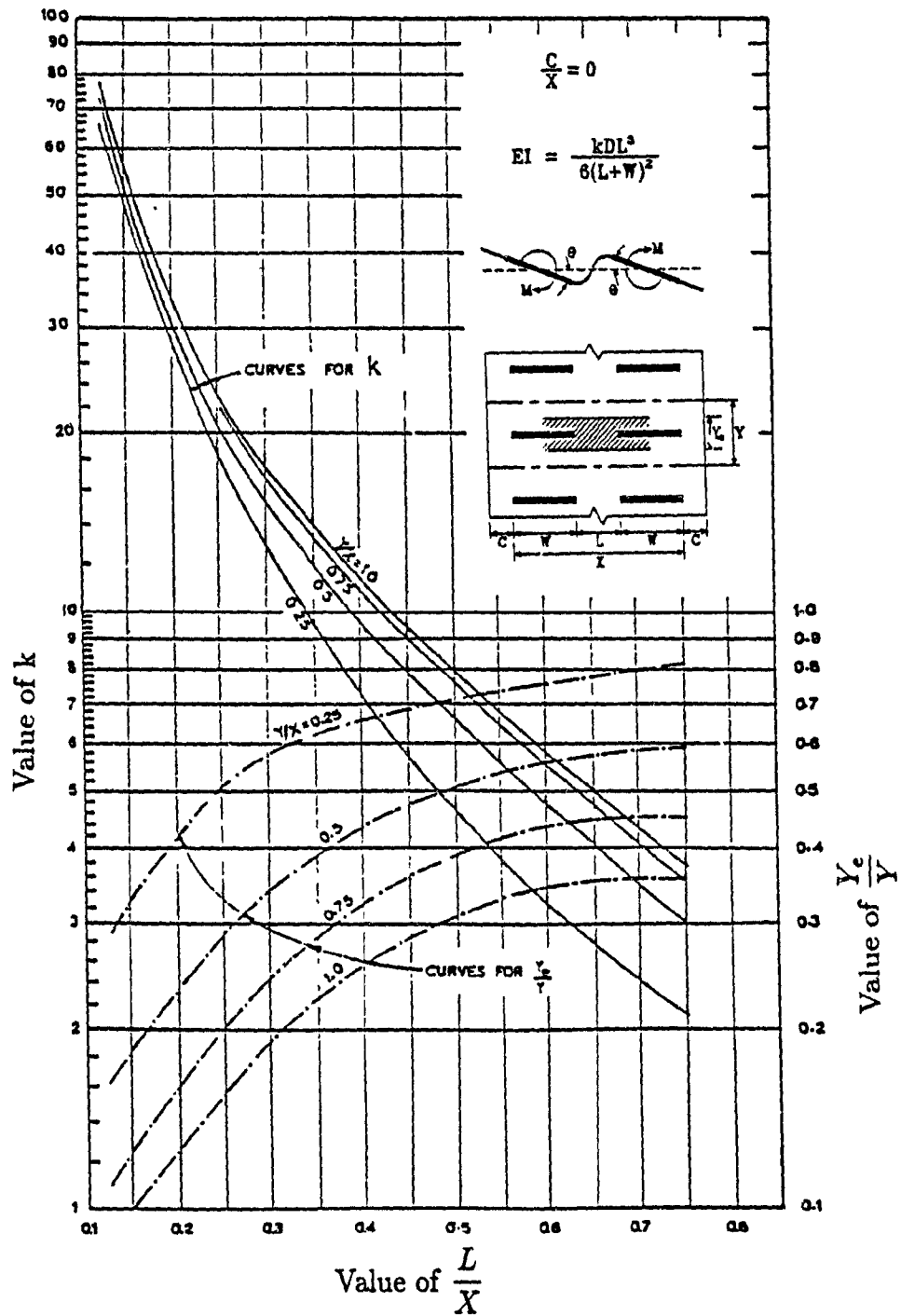


Figure 1.3a Value of Slab Stiffness Number k and $\frac{Y_c}{Y}$ as a Function of $\frac{L}{X}$ for $\frac{C}{X} = 0$ (Ref. 7).

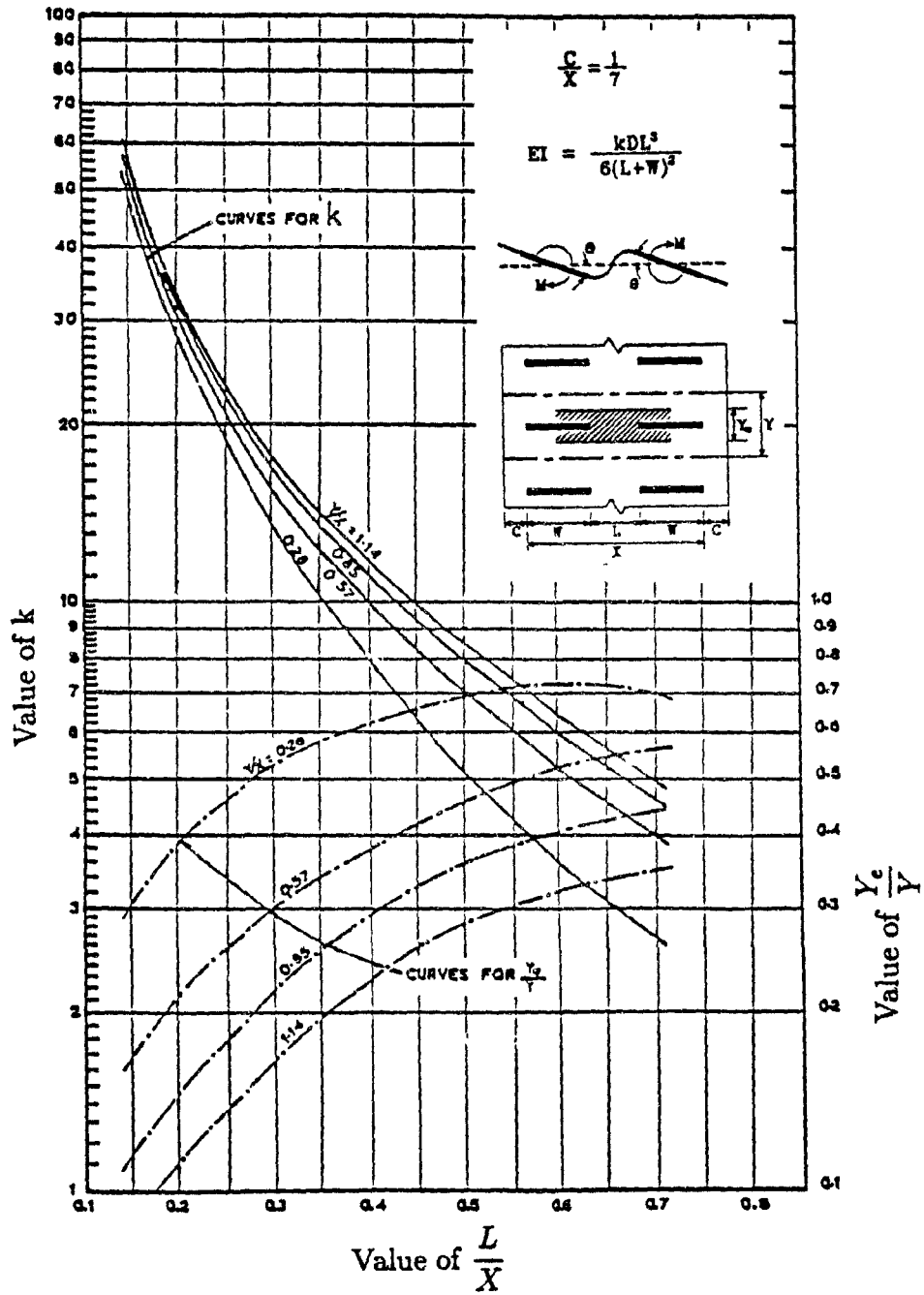


Figure 1.3b Value of Slab Stiffness Number k and $\frac{Y_c}{Y}$ as a Function of $\frac{L}{X}$ for $\frac{C}{X} = \frac{1}{7}$ (Ref. 7).

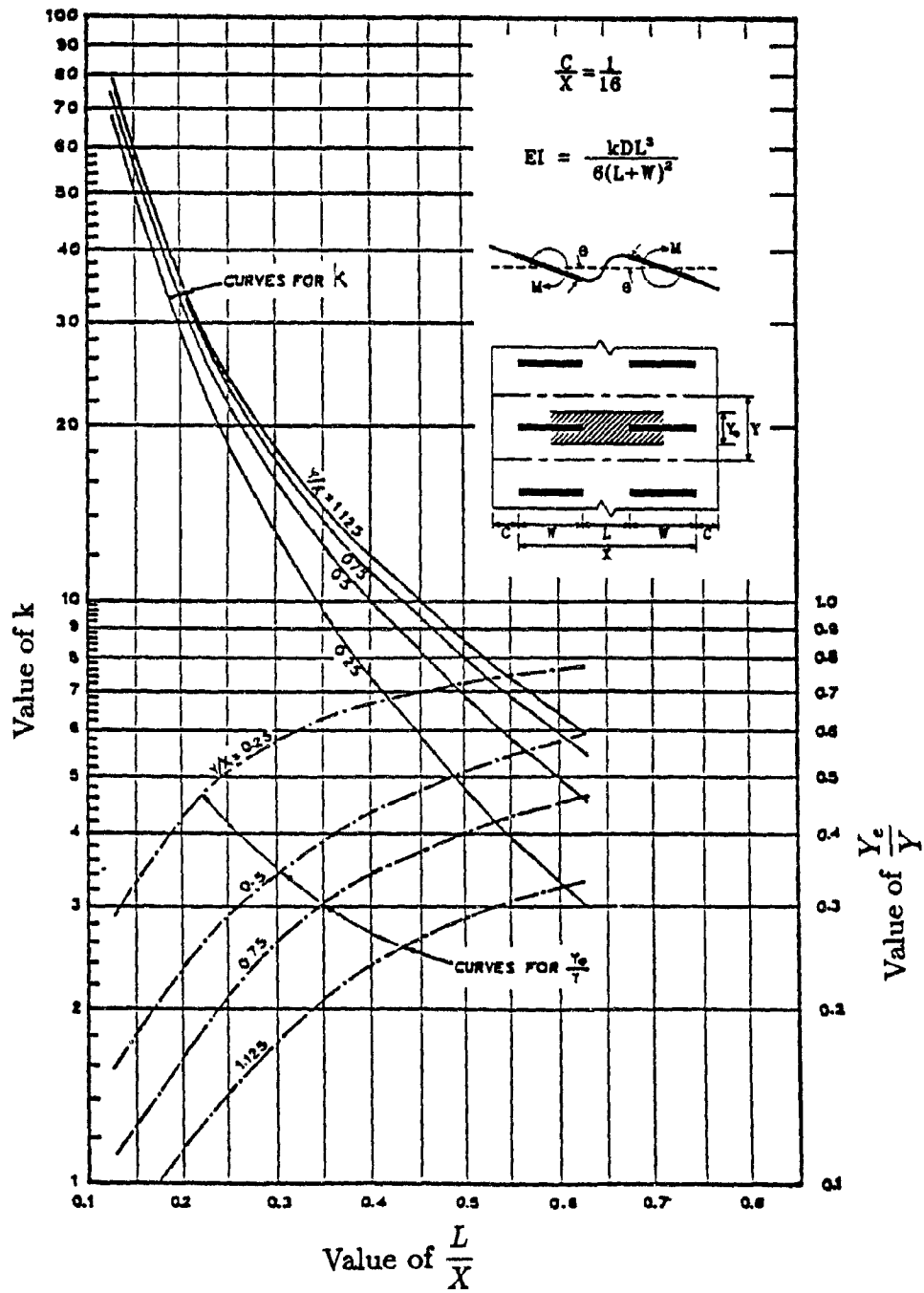


Figure 1.3c Value of Slab Stiffness Number k and $\frac{Y_c}{Y}$ as a Function of $\frac{L}{X}$ for $\frac{C}{X} = \frac{1}{16}$ (Ref. 7).

$$EI = \frac{kDL^3}{6(L+W)^2} \quad (1-2)$$

where k = non-dimensional stiffness number
 D = flexural rigidity of the slab
 $\quad = \frac{Eh^3}{12(1-\nu^2)}$
 L = clear span between the shear walls
 W = larger cross-sectional dimension of the shear wall
 h = thickness of the slab
 ν = poisson's ratio

while the ratio Y_e/Y can be used to compute the effective width of the slab, Y_e . Close comparison with the theoretical work was obtained from small scale model tests comprising two pin-based laterally loaded steel walls coupled with asbestos slab. They also demonstrated that a fixed "angle of dispersion" can not be adapted for the calculation of the slab stiffness.

During the same year, Chang⁸ carried out parametric studies using the finite difference method on the distribution of bending moments in the slabs of slab-shear wall structures for various bay, corridor and wall widths. He recommended that the critical section for shear should be confined to one-fourth of the corridor width from the toe of the wall at a distance equal to half the effective depth of the slab from the wall faces, as shown in Figure 1.4. He also recommended that the effective width of the slab be one corridor width on either side of the walls and that the concentrated transverse and longitudinal reinforcements should extend a distance of at least one corridor width beyond the shear wall toe. This reinforcing pattern is shown in Figure 1.5.

In 1971, Mirza and Jaeger⁹ reported on tests performed on eight $\frac{1}{10}$ -scale direct models of two-storey reinforced microconcrete coupled slab-shear wall structures. The specimens were subjected to monotonically increasing static loads until failure. In these small scale tests, the two two-storey walls were fixed at their bases and were

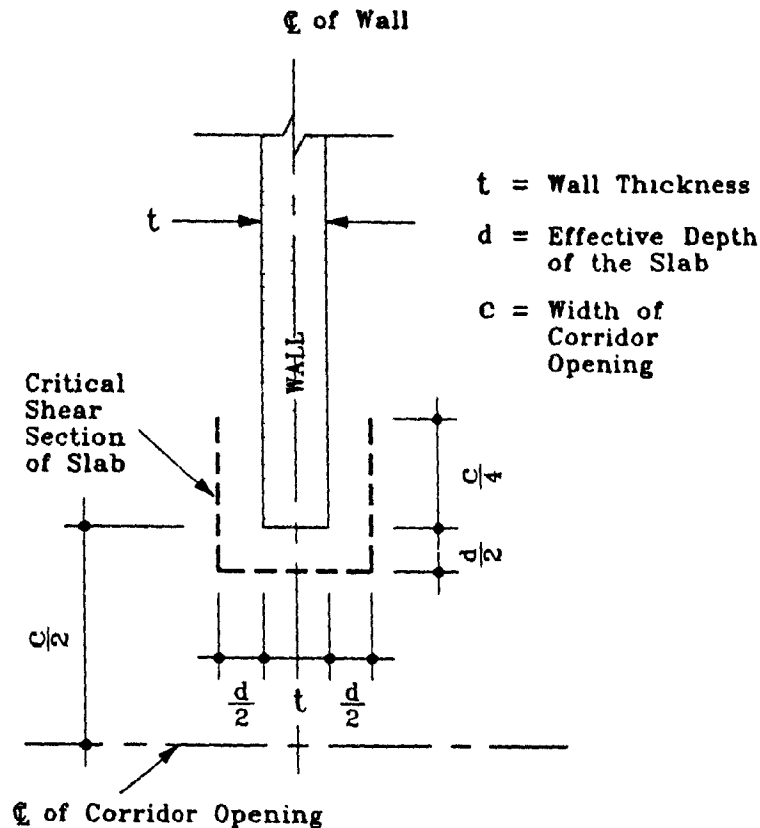


Figure 1.4 Critical Section for Shear Suggested by Chang (Ref. 8).

tested together with the two floor slabs (Figure 1.6). No special slab reinforcement was provided in the wall toe region, nor was there any tendency towards punching shear failure. The authors presented the recorded crack patterns photographically and plotted the force-displacement relationships. No strains were measured. It was noted that the behaviour of the coupled slab-shear wall structures changes gradually from cantilever action to frame action depending on the relative stiffness of the connecting slabs. The authors concluded that the delay or complete elimination of the "shear-compression" failure at the toe of the shear walls and a more ductile flexural failure is possible with proper reinforcing details.

In 1975, Coull and El Hag¹⁰ presented graphically the results of tests on a series of small scale models, similar to those of Qadeer and Stafford Smith⁷, indicating the

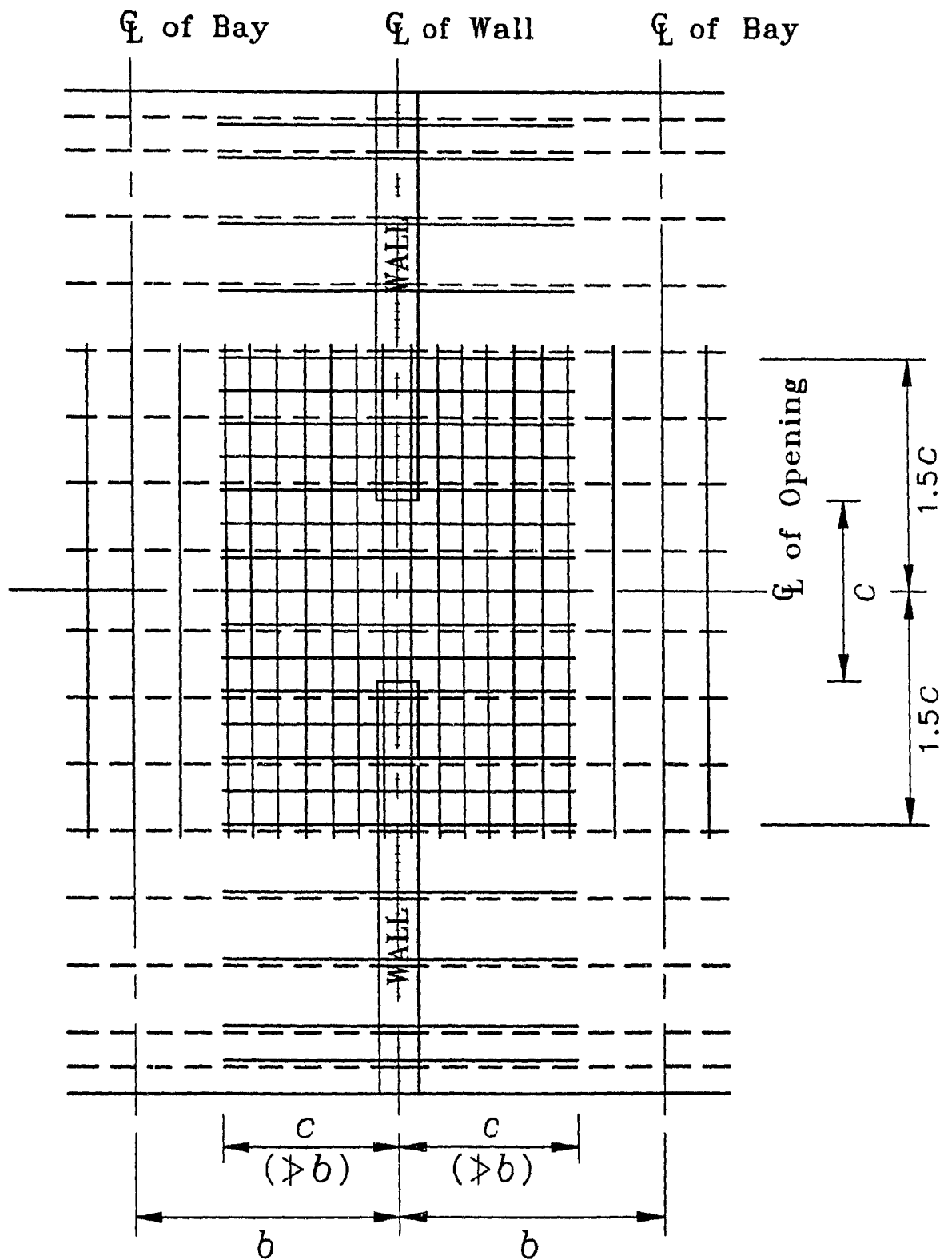
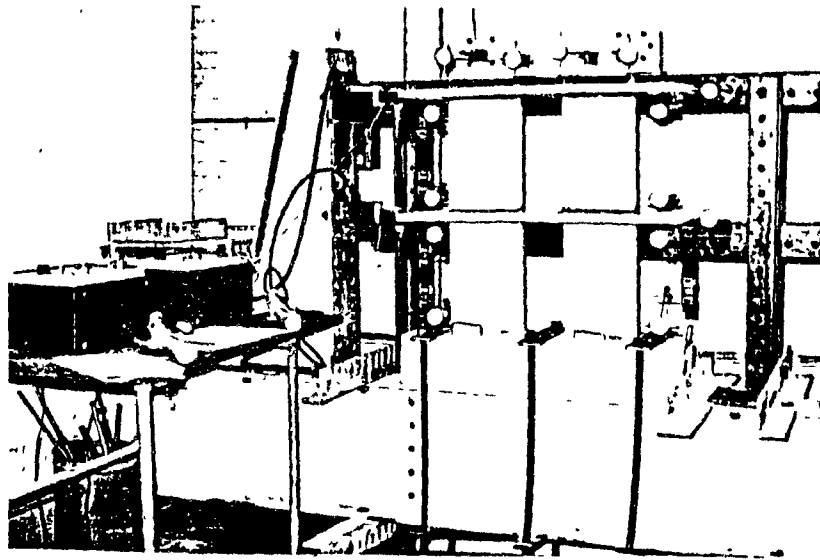
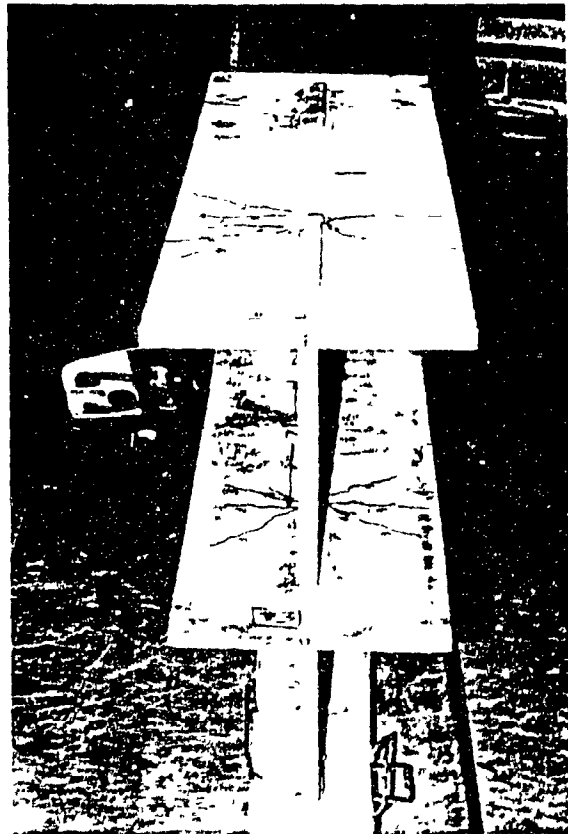


Figure 1.5 Reinforcing Layout Suggested by Chang (Ref. 8).



(a) Test Set-Up



(b) Typical Tension Cracks in Slabs at Slab Wall Junction (Series #2 Model #4)

Figure 1.6 $\frac{1}{10}$ -Scale Models Tested by Mirza and Jaeger (Ref. 9).

effective bending stiffness of floor slabs coupling shear walls. The coupled walls were fixed rigidly at their bases and the effect of varying the slab width was examined. The force-displacement relationships were used to determine the relative influence of the dimensions and shape of the walls (plane walls, flanged walls, and box cores), the wall spacing, and the slab dimensions on the effective width and stiffness of the connecting slab. Wall thickness, however, was not a parameter.

In 1976, the finite element method was employed by Black *et al.*¹¹ to improve the results of Qadeer and Stafford Smith⁷. This investigation included the effects of the wall thickness on the overall stiffness of the system. The results showed large stress concentration at the toe of the shear wall and the slab stiffnesses were generally 33% higher than those predicted by Qadeer and Stafford Smith's⁷ method.

Tso and Mahmoud²⁸ also reported on the finite element method for evaluating the effective slab width of the coupled slab-shear wall system. Various wall configurations was studied and the results were presented in the form of design charts similar to those presented by Qadeer and Stafford Smith⁷.

Wong and Coull²⁹ presented a series solution for evaluating the stiffness, effective width and stress distribution of the slab using the influence coefficient technique. The transfer of moment from the wall to the slab was idealized as a distributed reactive pressure which was replaced by a system of discretized loads and couples acting at a discrete set of nodes, as shown in Figure 1.7. The results of the numerical analysis performed by Wong³⁰ were tested for convergence and accuracy against those obtained by the finite element methods reported by Petersson³¹, Tso and Mahmoud²⁸ and Black *et al.*¹¹ and those obtained by the finite difference method reported by Qadeer and Stafford Smith⁷.

Schwaighofer and Collins¹² reported on an experimental study by Szalwinski¹³ on a $\frac{1}{3}$ -scale reinforced concrete coupled slab-shear wall model, subjected to monotonically increasing load. No special reinforcements were provided in the slab across the corridor

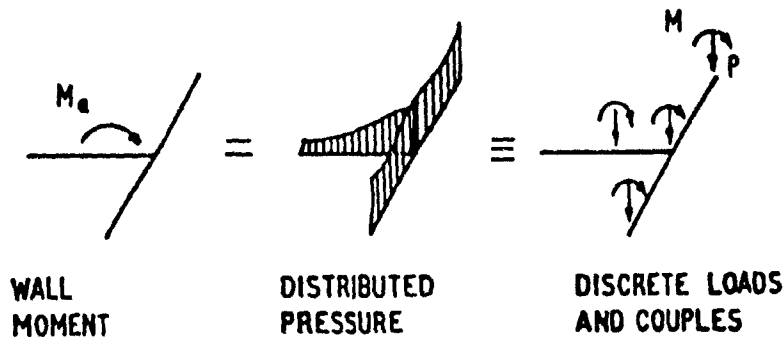


Figure 1.7 Representation of Moment Transfer Between Wall and Slab by Discrete Forces (Ref. 29).

opening. The report presented useful results including the force-displacement envelope, crack patterns and steel strains. In the absence of shear-reinforcement at the wall toe region, the punching-shear in this region resulted in the final failure of the slab. Several recommendations were made for calculating the stiffness of the cracked and uncracked coupling slab, the shear and flexural strength of the coupling slab and the lateral reinforcement layout in the coupling slab.

A more comprehensive study was reported by Taylor¹⁴ in 1977 and presented by Paulay and Taylor³ in 1981. A series of four experimental investigations were carried out to study the non-linear behaviour of coupled slab-shearwall structures under reversed cyclic loading in the post-elastic range. The four $\frac{1}{2}$ -scale models were derived from a 15-storey prototype structure (Figure 1.8) of typical plan (Figure 1.9) chosen for the study. The study involved various arrangements of longitudinal and transverse slab reinforcements, the use of embedded transverse structural steel beams, and the composite action of a longitudinal beam with the slab. Figures 1.10 and 1.11 show the dimensions and reinforcing details of the test units. Additional slab reinforcement was placed in the vicinity of the door opening, based on the suggestion by Qadeer and Stafford Smith⁷ for equivalent effective slab width, aimed at the utilization of the

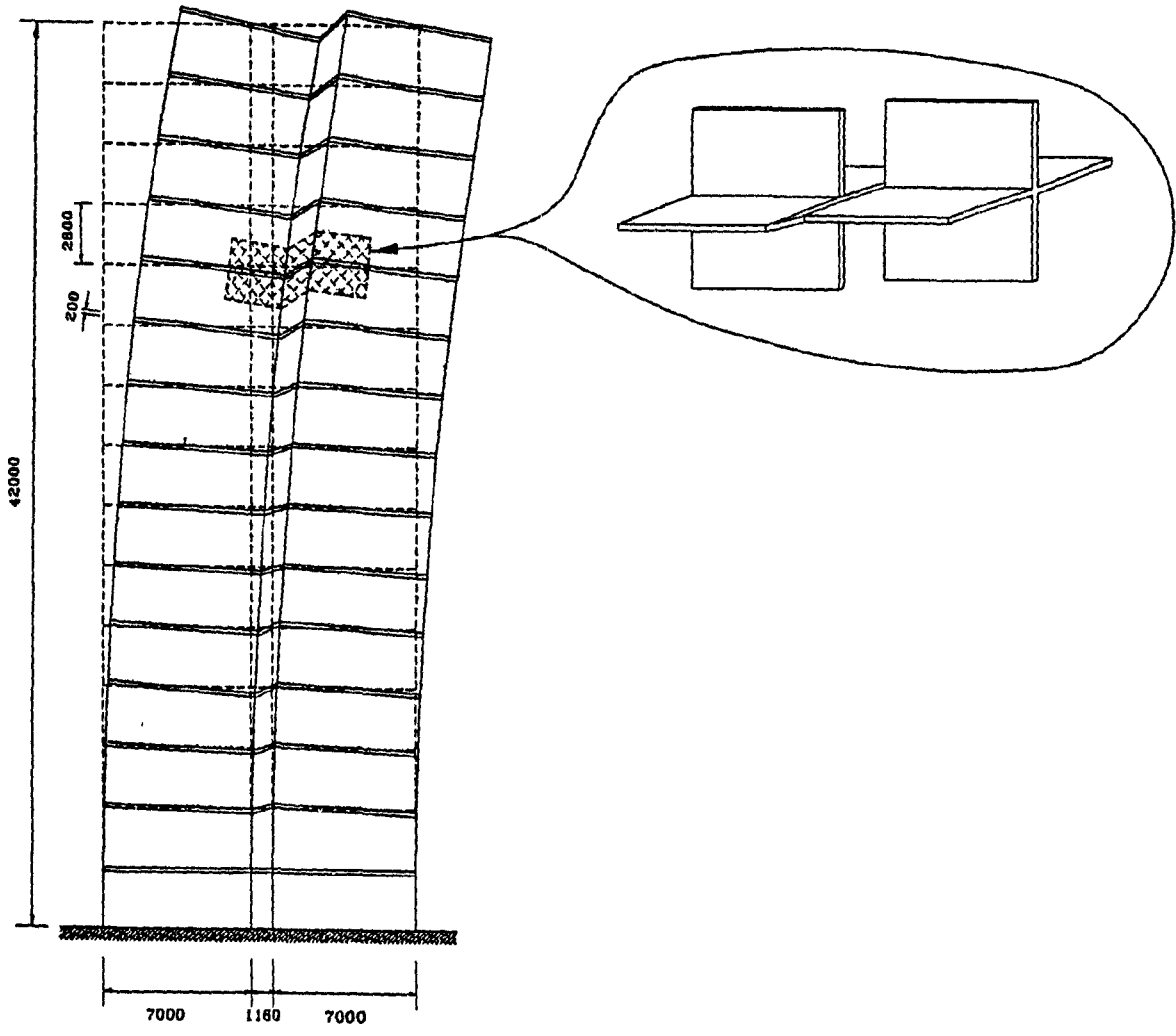


Figure 1.8 15 Storey Prototype Structure Adopted by Taylor and Schematic View of a Typical Interior Bay Section (Ref. 14).

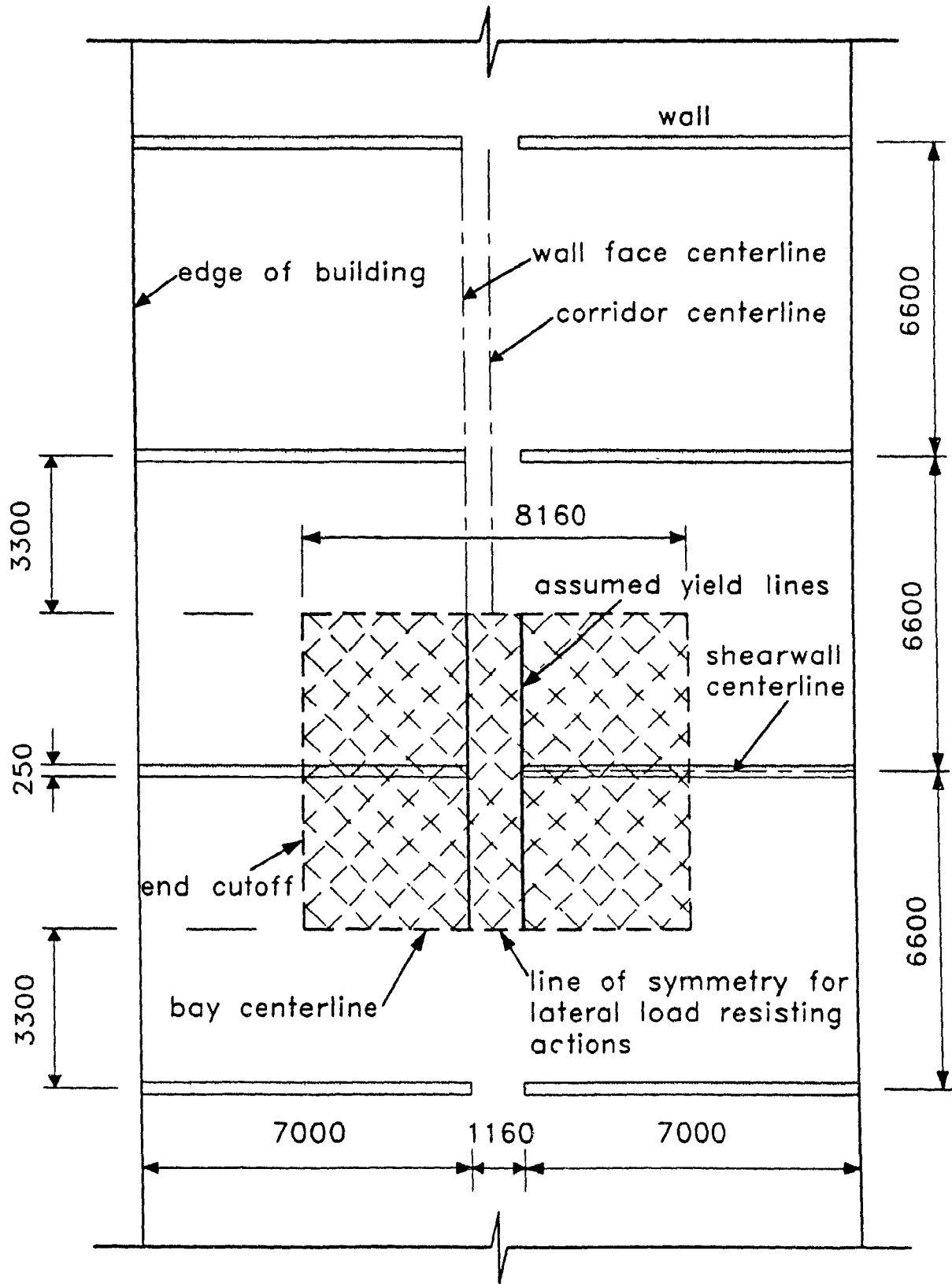


Figure 1.9 Typical Plan View of Prototype Structure by Taylor (Ref. 14).

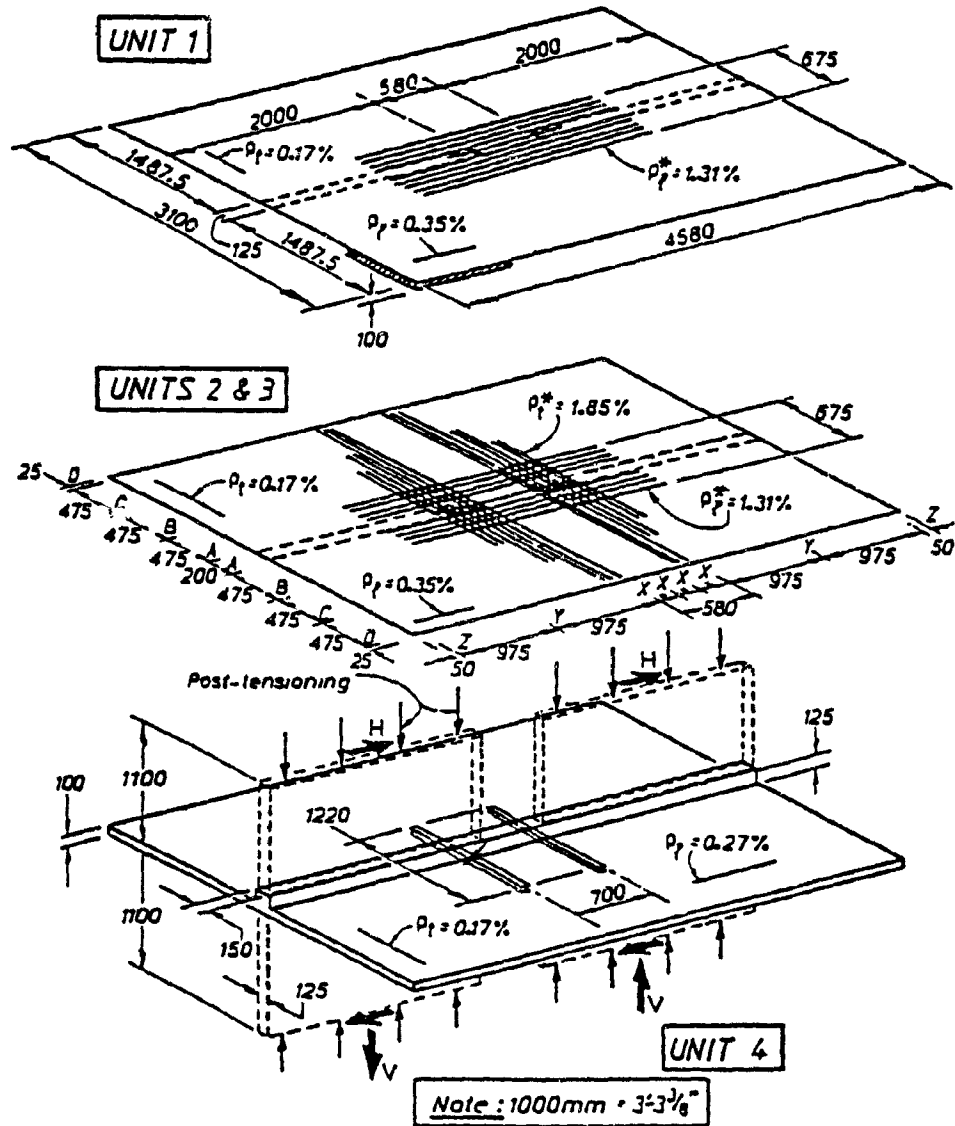
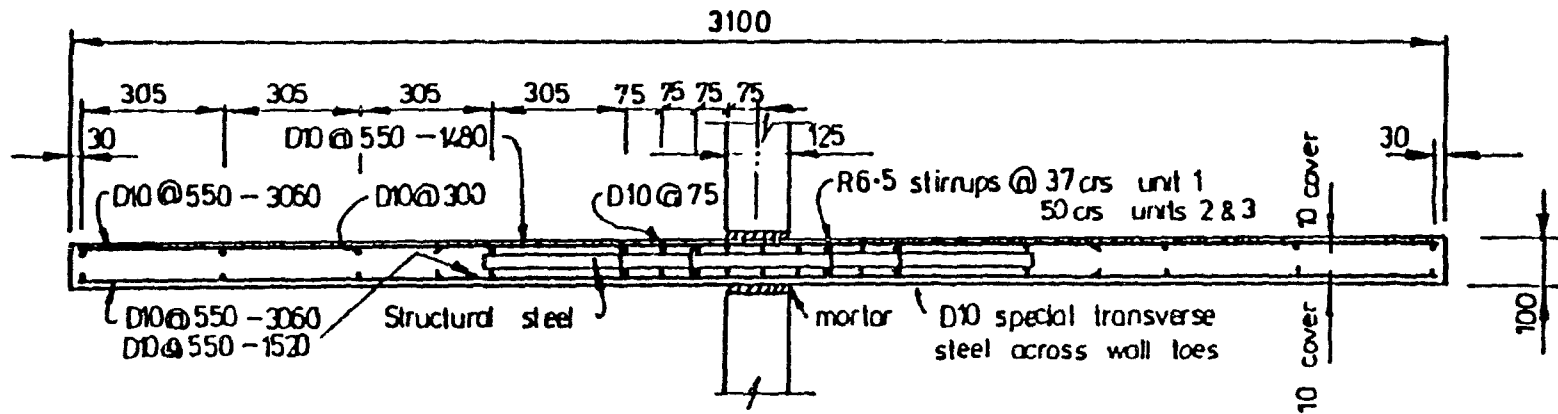
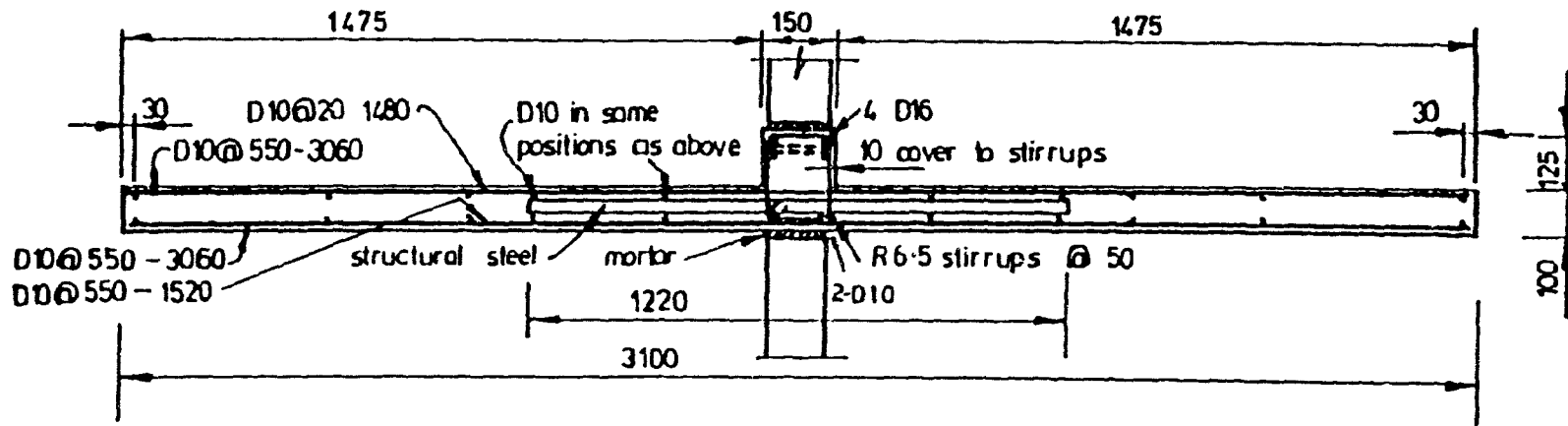


Figure 1.10 Dimensions and Reinforcing Details of Taylor's Test Specimens (Ref. 14).



(a) Cross-Sections at Wall Edge of Specimens 1-3



(b) Cross-Section at Wall Edge of Specimen 4

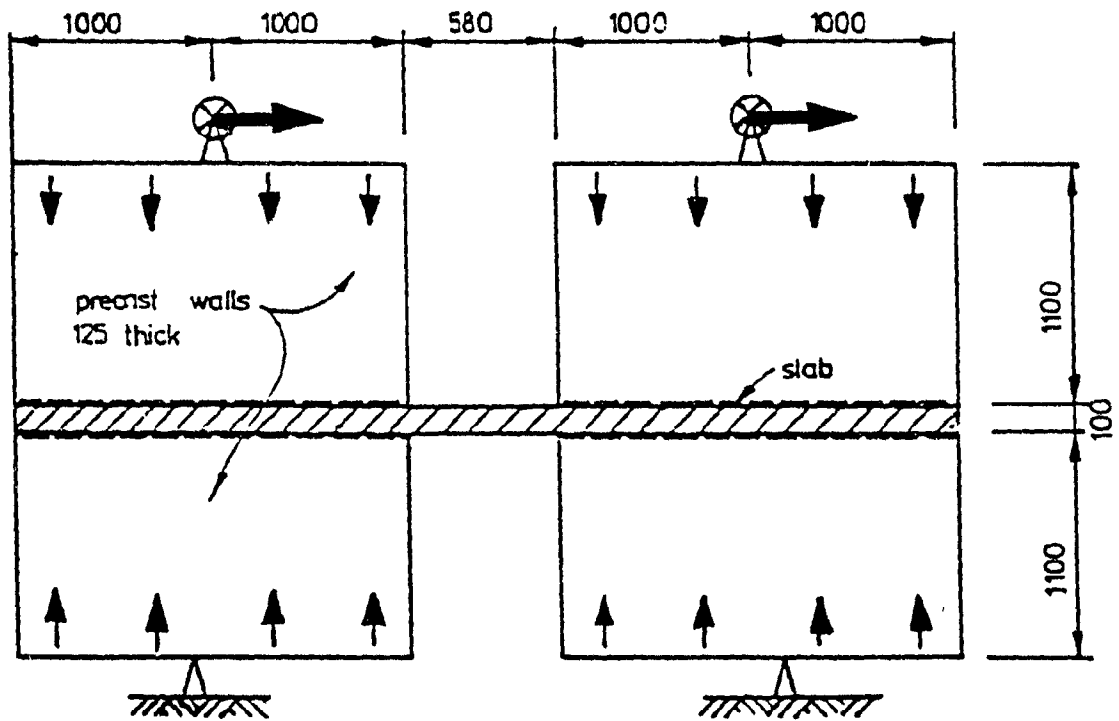
Figure 1.11 Cross-Section of Taylor's Specimens 1-4 (Ref. 14).

slab as an effective shear transfer element for service load resistance with the exception of Specimen 4. Specimens 1-3 were provided with progressively improved transverse reinforcement at the wall toe regions, while maintaining the same longitudinal reinforcement. Specimen 3 was identical to Specimen 2 excepting for an added embedded transverse structural steel beam at each wall toe region. The fourth specimen incorporated a shallow coupling beams cast monolithically with the slab and an embedded transverse structural steel beam at each wall toe region similar to those of Specimen 3 without any special transverse or longitudinal reinforcement.

Equal horizontal forces were applied at the top of each shear wall in each specimen, and the shear walls were free to rotate about the close tolerance pins shown in Figure 1.12. Ultimate failure occurred as a result of punching shear at the wall toe regions in the first three tests and as a horizontal sliding shear at the beam-slab junction in the test on Specimen 4.

Of particular importance was the performance of the stirrups in the central cage, where the results from the tests showed enhanced ductility of the slab by confining the excessively cracked concrete and by preventing premature buckling of the flexural reinforcement. Although Taylor¹⁴ intended to improve the transverse flexural strength by providing transverse reinforcement at the wall toes, no significant contribution to flexural strength in the transverse direction was observed. However, these transverse bars tended to act as shear friction reinforcement, which prevented total punching failure of the slab at the wall toes.

In 1986, Malyszko¹⁵ performed a series of three tests to study the behaviour of shear reinforcement in the central cage of the coupling slab. He selected a prototype structure similar to that used by Taylor¹⁴. Three $\frac{2}{3}$ -scale reinforced concrete models based on the design of the $\frac{1}{2}$ -scale models of the specimens tested by Taylor¹⁴ were constructed; each specimen differed only in the spacing of the shear reinforcement in the central cage. Specimen S1 was not provided with any stirrups while Specimens S2 and



KEY

-  jack forces
-  lateral support
-  close tolerance pin
-  prestress rod forces
-  mortar joint

Figure 1.12 Schematic Illustration of Taylor's Test Model (Ref. 14).

S3 was provided with four-legged closed stirrups at spacings of $\frac{1}{2}d$ and d respectively. The principal objective of Malyszko's¹⁵ study was to investigate the effectiveness of the shear reinforcement within the slab corridor width (the central cage) in improving the performance of the coupled slab-shear wall structure. He observed that the Specimen S2, with shear reinforcement spacing of $\frac{1}{2}d$, failed in a flexural mode while the other two specimens failed in vertical sliding shear at the toes of the shear walls. The results reconfirm Taylor's¹⁴ observation that the shear resistance of the slabs due to the inclusion of stirrups within the slab corridor width is at best marginal but the increase in ductility is substantial. These stirrups controlled the severity of the damage to the slab at high displacement ductilities and reduced the probability of occurrence of brittle failure or complete collapse. It was also observed that the stiffness degradation after the initial load cycle into the inelastic range was rapid and severe. The participation of the concentrated longitudinal seismic reinforcement in the corridor opening was found to be relatively higher than the longitudinal reinforcement closer to the bay centerline. However, at high displacement ductilities, the reverse was observed.

As a follow-up to Malyszko's¹⁵ work, Khan¹⁶, in 1987 perform 3 more tests using the same prototype and model structures that were used by Malyszko¹⁵. To verify Malyszko's¹⁵ results, Khan¹⁶ performed a similar test on his first specimen, Specimen S4, using a stirrup spacing of $\frac{3}{4}d$. In his second and third specimens, Specimens B1 and B2, Khan¹⁶ used a shallow longitudinal beam cast monolithically with the slab similar to that used in Taylor's¹⁴ Specimen 4. Two concealed transverse reinforced concrete beams, one under each shear wall toe, were provided in each of these specimens. Specimens B1 and B2 differed in the amount of reinforcement provided for the concealed transverse beams. The primary objectives of the investigation were to enhance the stiffness, energy absorption capacity and ductility of the coupling system and to investigate the function of the concealed transverse beams at the shear wall toe regions against punching shear failure. Punching shear failure was observed in the first

test showing the inadequacy of the stirrups at a spacing of $\frac{3}{4}d$ in preventing this failure mode. The effect of this punching shear at higher ductility ($\mu \geq 5$) reduces significantly the energy absorption capacity of the coupling member. In Specimens B1 and B2, the system failed by horizontal sliding shear in the shallow longitudinal beam. Because of the stiffer coupling system, both specimens showed higher strengths but lower energy absorption capacity with a severe stiffness degradation. It is also interesting to note that the test results indicated that the provision of the concealed beam does not significantly improve the stiffness and energy absorption capacity of the coupling system, however, it prevents the premature failure of the coupling system due to punching at the critical wall-toe region. It was also observed that the transverse concealed beam designed for 50% of the transverse vertical shear was adequate to control the punching shear failure. This result further supports the suggestion by Taylor¹⁴ that provision of a transverse beam under the shear wall-toe with a shear strength of 40% of the transverse vertical shear is adequate for punching shear control.

The experimental studies of Taylor¹⁴, Malyszko¹⁵ and Khan¹⁶ are referred throughout this thesis.

1.3 Scope of the Research Program

This experimental study is third of a series of studies performed to investigate the behaviour of the slab coupling members in coupled shear wall structures subjected to reversed cyclic loading in the non-linear range. The basic objective of the program is to develop some practical design recommendations and useful observations for the engineering profession in the area of design of slab coupling of shear walls.

The experimental program consisted of tests on four specimens which are derived from the same prototype and model structures that were used by Malyszko¹⁵. A drop panel with a width equal to the width of the central cage of the slab and a depth equal to half the slab thickness was provided along the full length of the wall and the corridor

in each specimen. The difference between the specimens was the spacing of the central cage shear reinforcement and the transverse secondary reinforcements near the wall toe regions.

The primary objectives of this investigation were:

- (i) To determine the effectiveness of the drop panel in improving the response of coupled slab-shear wall structures subjected to reversed cyclic loading.
- (ii) To determine the effectiveness of stirrups within the drop panel in improving the performance of coupled slab-shear wall structures.
- (iii) To study the effects of the various transverse secondary reinforcement arrangements under the wall toe regions in controlling punching shear failure.
- (iv) To compare the hysteretic response of the four specimens in relation to each other and with the previous work by Malyszko¹⁵ and Khan¹⁶ at McGill University.
- (v) To derive conclusions and design recommendations leading to a practical design approach for an improved response of slab coupling member in coupled slab-shear wall structures.

CHAPTER 2

THE PROTOTYPE STRUCTURE AND THE MODELING PROCESS

This chapter describes the prototype structure, the design of the prototype slab and the modeling process.

2.1 The Prototype

This study is a part of a continuing investigation of the behaviour of coupled slab-shear wall systems at McGill University. To enable direct correlation and comparison with the work by Malyszko¹⁵ and Khan¹⁶, similar experimental set-up and test procedure were used in this research program.

The prototype structure, originally selected by Taylor¹⁴ in 1977, is a typical 15-storey apartment building in New Zealand. These typical buildings have bay sizes of 6-7 m, widths of 15-20 m, floor heights of 2.8 m and building heights of 30-60 m. A typical floor plan of the 15-storey apartment building is shown in Figure 1.8. For the experimental study of the coupling across the corridor, only a part of the slab and the walls, as shown in Figure 1.8, and the cross-hatched area in Figure 1.9 were investigated. This part of the structure at a typical floor was isolated and reproduced at $\frac{1}{3}$ -scale in this investigation.

2.2 Design of the Prototype Slab

The design of the prototype slab was based on the use of mild steel and medium strength concrete. The reinforcement layout of the slab is such that seismic action is resisted by longitudinal reinforcing, and gravity load by transverse reinforcing. The gravity load was assumed to be carried as a one-way continuous slab over spans of 6600 mm, the spacing of the shear walls (Figure 1.9). The earthquake induced lateral loads in the direction of the shear walls were assumed to be resisted by the coupled slab-shear wall system.

2.2.1 Transverse Reinforcement for Gravity Load

The transverse reinforcement was designed for dead load and a prescribed live load of 1.1 kPa (40 lbs/ft²) for one-way action assuming that the slab is fixed at the wall-slab junction. To account for inelastic moment redistribution and to allow for uniformity in the placement of the transverse bars, the negative bending moment and the negative moment reinforcement were reduced by 20% and the positive bending moment and the positive moment reinforcement were increased by 14%. This reinforcement was placed in the first layer for negative moment reinforcement and in the second layer for the positive moment reinforcement.

2.2.2 Longitudinal Reinforcement for Seismic Action

The quantity of the longitudinal reinforcement was based on the lateral seismic load analysis of the 15-storey prototype building by Taylor¹⁴ and on the recommendation by Qadeer and Stafford Smith⁷. An effective slab width was computed based on the analysis of the slab stiffness in its elastic uncracked state. To allow for cracking, the slab stiffness was reduced by 50% for the lateral load analysis. The resulting seismic reinforcement was placed in a second layer below and above the top and bottom reinforcement for gravity loads, respectively.

Table 2.1 Typical Model Scale Factors (Ref. 17).

Type of Structure	Elastic Models	Strength Models
Shell roof	$\frac{1}{200}$ to $\frac{1}{50}$	$\frac{1}{30}$ to $\frac{1}{10}$
Highway bridge	$\frac{1}{25}$	$\frac{1}{20}$ to $\frac{1}{4}$
Reactor vessel	$\frac{1}{100}$ to $\frac{1}{50}$	$\frac{1}{20}$ to $\frac{1}{4}$
Slab structures	$\frac{1}{25}$	$\frac{1}{10}$ to $\frac{1}{4}$
Dams	$\frac{1}{400}$	$\frac{1}{75}$
Wind effects	$\frac{1}{300}$ to $\frac{1}{50}$	Not Applicable

2.3 The Modeling Process

To consider the behaviour of concrete structures beyond the elastic range up to and including the ultimate strength, it is necessary to use a "direct" model. Such a direct model is "geometrically similar to the prototype in all respects, and the loads are applied to it in the same manner as to the prototype"¹⁷. However, in order to predict the prototype behaviour, the "strength" model must be employed whereby the model is a direct model made of materials that have properties similar to the prototype materials.

2.3.1 Choice of Geometric Scale

Table 2.1 shows typical model scale factors for several classes of structures. Sabnis *et al.*¹⁷ state, "Any given model being built in a given laboratory has an optimum geometric scale factor". For a strength model of a coupled slab-shear wall structure, the appropriate range of scale factors is about $\frac{1}{10}$ to $\frac{1}{4}$. A scale factor of $\frac{1}{3}$ on the prototype model (or a scale factor of $\frac{2}{3}$ on Taylor's¹⁴ test models) was chosen for this study and that of Malyszko's¹⁵ studies in consideration of the following criteria:

- (i) The laboratory space available for such a comprehensive test, and the lifting capacity of the laboratory cranes (1820 kg, 4000 lbs) to manouvre the specimen during assembly.
- (ii) The range of load jacks (152 mm, 6 in).
- (iii) The range of displacement transducers (127 mm, 5 in).

- (iv) The mass density distortions in such a test; for a true model, the model mass density must be exactly three times that of the prototype.
- (v) Inelastic stresses and displacements occurring during the test.

Since the design of the $\frac{1}{3}$ -scale models was based on Taylor's¹⁴ $\frac{1}{2}$ -scale test specimen, the actual scaling factor, for comparative purposes between this study and Taylor's¹⁴ work is, $\frac{2}{3}$.

2.3.2 Material Similitude

"Any structural model must be designed, loaded and interpreted according to a set of similitude requirements that relate the model to the prototype structure"¹⁷. The requirements vary according to the degree of similarity planned between the model and the prototype boundary and initial conditions, geometry, and material properties. In modeling, departures from complete similarity are frequently experienced. Such deviations, whether accidental, deliberate or necessary are permitted as long as their influence can be determined.

The basic similitude requirements for the design of structural models are based upon the theory of modeling, which can be derived from dimensional analysis of the physical phenomena involved in the behaviour of the structure. The use of scale factors is typical of any structural modeling process. The scale factor, S_i , is defined as the multiplier required to convert the model quantity, " i_m ", to the corresponding prototype quantity, " i_p ", or

$$i_p = S_i i_m \quad (2-1)$$

Although geometric distortions must be minimized, "of greater importance to the structural engineer is the possibility of permitting distortion in the reproduction of the prototype stress-strain characteristics"¹⁷. The similitude requirements for static, elastic modeling are summarized in Table 2.2 where the independent scale factors chosen are those for the modulus of elasticity S_E and the length S_l and all of the remaining scale

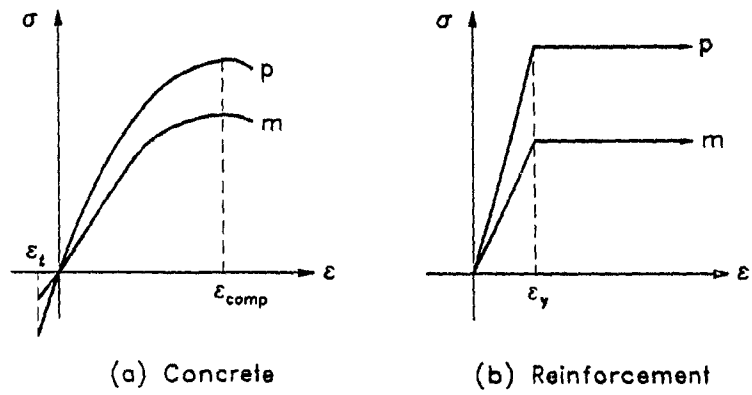
Table 2.2 Similitude Requirements, Static Elastic Modeling (Ref. 17).

Quantities	Dimensions	Scale Factor
Material Properties		
Stress	FL^{-2}	S_E
Modulus of Elasticity	FL^{-2}	S_E
Poisson's ratio	-	1
Mass density	FL^{-3}	$\frac{S_E}{S_l}$
Strain	-	1
Geometry		
Linear dimension	L	S_l
Linear displacement	L	S_l
Angular displacement	-	1
Area	L^2	S_l^2
Moment of inertia	L^4	S_l^4
Loading		
Concentrated load, Q	F	$S_E S_l^2$
Line load, w	FL^{-1}	$S_E S_l$
Pressure or uniformly distributed load, q	FL^{-2}	S_E
Moment, M or Torque, T	FL	$S_E S_l^3$
Shear force, V	F	$S_E S_l^2$

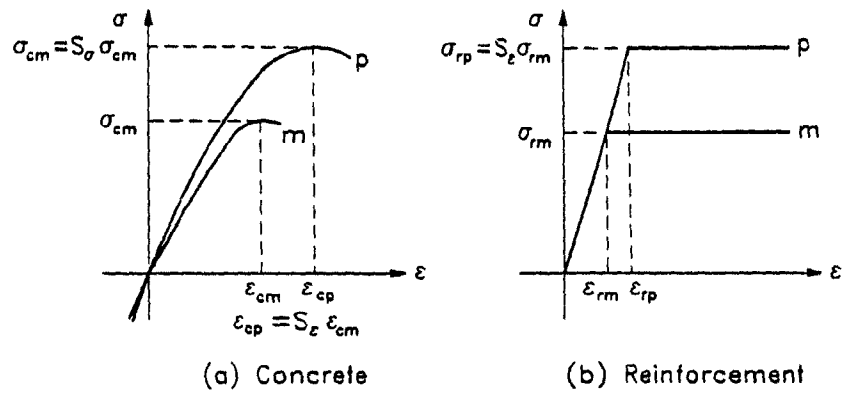
factors are either unity or functions of S_E or S_l . Such static, elastic modeling may be used as long as the model material remains elastic within the model loading range and the Poisson's ratio is the same as that of the prototype.

However, the above similitude requirements do not apply for a study of the failure mode, capacity, and inelastic behaviour of a reinforced concrete structure. Ideally, for such a study, the constitutive relationships and the failure criteria for the model concrete subjected to multiaxial stresses should be identical to those for the prototype concrete. Since this failure criterion is not well defined, this requirement may be relaxed. The resulting requirements shown in Figure 2.1(a) and Column 3 of Table 2.3 require that the stress-strain curves be geometrically similar in the model and the prototype concrete for both uniaxial tension and compression and that $\epsilon_m = \epsilon_p$ at failure under uniaxial tension and compression.

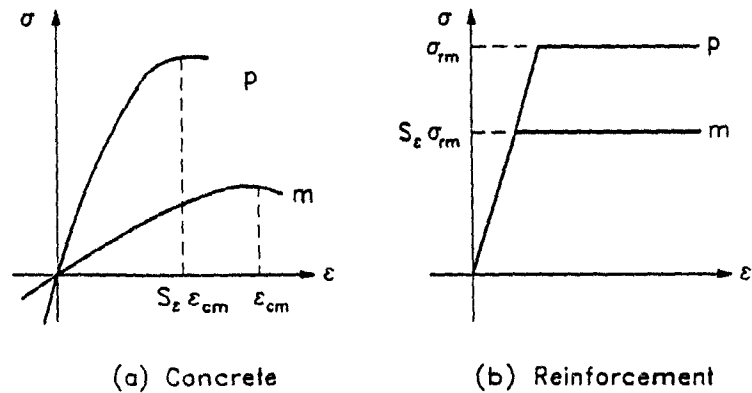
When the model materials do not respond as shown in Figure 2.1(a), various other distorted models must be considered as shown in Table 2.4 and Figures 2.1(b)



(a) Similitude Requirement for True Model



(b) Similitude Requirement for Case 1 Distorted Model



(c) Similitude Requirement for Case 3 Distorted Model

Figure 2.1 Similitude Requirements.

Table 2.3 Summary of Scale Factors for Reinforced Concrete Strength Models (Ref. 17).

Quantity (1)	Dimension (2)	True Model (3)	Practical True Model (4)	Distorted Model Case 1 (5)	Distorted Model Case 3 (6)
Material Properties					
Concrete stress, σ_c	FL^{-2}	S_σ	1	S_σ	S_σ
Concrete strain, ϵ_c	-	1	1	S_ϵ	S_ϵ
Modulus of concrete, E_c	FL^{-2}	S_σ	1	$\frac{S_\sigma}{S_\epsilon}$	$\frac{S_\sigma}{S_\epsilon}$
Poisson's ratio, ν_c	-	1	1	1	1
Mass density, ρ_c	FL^{-3}	$\frac{S_\sigma}{S_l}$	$\frac{1}{S_l}$	$\frac{S_\sigma}{S_l}$	$\frac{S_\sigma}{S_l}$
Reinforcing stress, σ_r	FL^{-2}	S_σ	1	S_σ	S_σ
Reinforcing strain, ϵ_r	-	1	1	S_ϵ	S_ϵ
Modulus of reinforcing, E_r	FL^{-2}	S_σ	1	1	1
Bond stress, u	FL^2	S_σ	1	S_σ	*
Geometry					
Linear dimension, l	L	S_l	S_l	S_l	S_l
Displacement, δ	L	S_l	S_l	$S_\epsilon S_l$	$S_\epsilon S_l$
Angular displacement, β	-	1	-	S_ϵ	S_ϵ
Area of reinforcement, A_r	L^2	S_l^2	S_l^2	S_l^2	$\frac{S_\sigma S_l^2}{S_\epsilon}$
Loading					
Concentrated load, Q	F	$S_\sigma S_l^2$	S_l^2	$S_\sigma S_l^2$	$S_\sigma S_l^2$
Line load, w	FL^{-1}	$S_\sigma S_l$	S_l	$S_\sigma S_l$	$S_\sigma S_l$
Pressure, q	FL^{-2}	S_σ	1	S_σ	S_σ
Moment, M	FL	$S_\sigma S_l^3$	S_l^3	$S_\sigma S_l^3$	$S_\sigma S_l^3$

* Function of choice of distorted reinforcing area

and 2.1(c). Cases 2 and 4 in Table 2.4 are not considered, since in these two cases, reinforcing material other than steel is required. According to Sabnis *et al.*¹⁷, "it is necessary to utilize a distorted model approach when the available concrete does not have $S_\sigma = S_E = 1$ ". The Case 3 scale factors were considered appropriate for this study because the model concrete strength (37 MPa) was significantly higher than the prototype concrete strength (25 MPa). Table 2.5 contains a summary of the Case 3 distorted model scale factors, the prototype material values and the corresponding scaled model material values (using the Case 3 distorted model scale factors), and the experimental model material values used for Specimens D1 and D2

Table 2.4 Possible Distortions in Reinforced Concrete Models (Ref. 17).

Case	Concrete			Reinforcement		
	S_ϵ	S_σ	S_E	S'_ϵ	S'_σ	S'_E
1	$\neq 1$	S_ϵ	1	S_ϵ	S_ϵ	1
2	$\neq 1$	1	$\frac{1}{S_\epsilon}$	S_ϵ	1	$\frac{1}{S_\epsilon}$
3	$\neq 1$	$\neq 1$	$\neq 1$	S_ϵ	S_ϵ	1
4	$\neq 1$	$\neq 1$	$\neq 1$	S_ϵ	S_σ	$\neq S_E$

Table 2.5 Summary of Scale Factors and Scaled Model Values.

Quantity (1)	Distorted Model Case 3 (2)	Prototype Values (3)	Distorted Model Values (4)	Specimen D1 Experimental Values (5)	Specimen D2 Experimental Values (6)
Concrete stress	1.7	25 MPa	15 MPa	37 MPa	35 MPa
Concrete strain	2.0	.003 [†]	.0015	.0011	.0045
Modulus of concrete	0.85	27500 MPa [†]	32350 MPa [†]	24000 MPa	30000 MPa
Reinforcing stress	1.7	345 MPa	205 MPa	275 MPa	275 MPa
Reinforcing strain	2.0	.002 [†]	.001	.00125	.00125
Modulus of reinforcing	1.0	200000 [†]	200000	220000	270000
Linear dimension	1.5				
Displacement	3.0				
Area of reinforcing	1.9	78 mm ² †	41 mm ²	45 mm ²	45 mm ²
Concentrated load	3.8				

[†] Assumed values

[‡] Based on information from Figures 1.9 and 1.10

Other factors influencing similitude are bond and mass density. Mirza¹⁸ has shown that as long as the selection of modeling materials, construction and testing is done prudently, bonding is well modeled. It is assumed for this series of tests that these criteria have been met. The mass density scale factor in this study is $S_\sigma/S_l = 1.7/1.5 = 1.13$. Such a distortion is considered negligible with respect to the nature and the relative magnitude of the loading exerted on the specimens.

2.3.3 Load and Deformation Similitude

Figure 2.2 shows a schematic view of the nature of the load and deformation for a typical coupled slab-shear wall structure. Taylor¹⁴ had directly modeled the displacement, rotation and lateral loading of the system in his specimens, as shown in

Figure 1.12. The deformations of the prototype can be simulated by applying relative vertical displacements of the two shear walls, as shown in Figure 2.3.

This simulation also avoids the possibility of introducing unequal horizontal jack forces required in Taylor's¹⁴ specimens to maintain equal imposed wall rotations. In this study, the relative vertical displacement method is employed.

For the purpose of comparison with Taylor's¹⁴ results, the differences in the methods of load application and specimen displacements must therefore be considered. To convert Taylor's¹⁴ wall rotations, θ , to the relative vertical wall displacements, Δ , (see Figure 2.3) each 1 radian of rotation is equivalent to a relative displacement of 2680 mm. Similarly, each 1 kN horizontal jack load (H) applied at each shear wall in Taylor's¹⁴ test is equivalent to 1.78 kN net vertical force (V) in this study. Figure 2.4 illustrates the forces in the model structure under imposed vertical translation of one wall relative to the other.

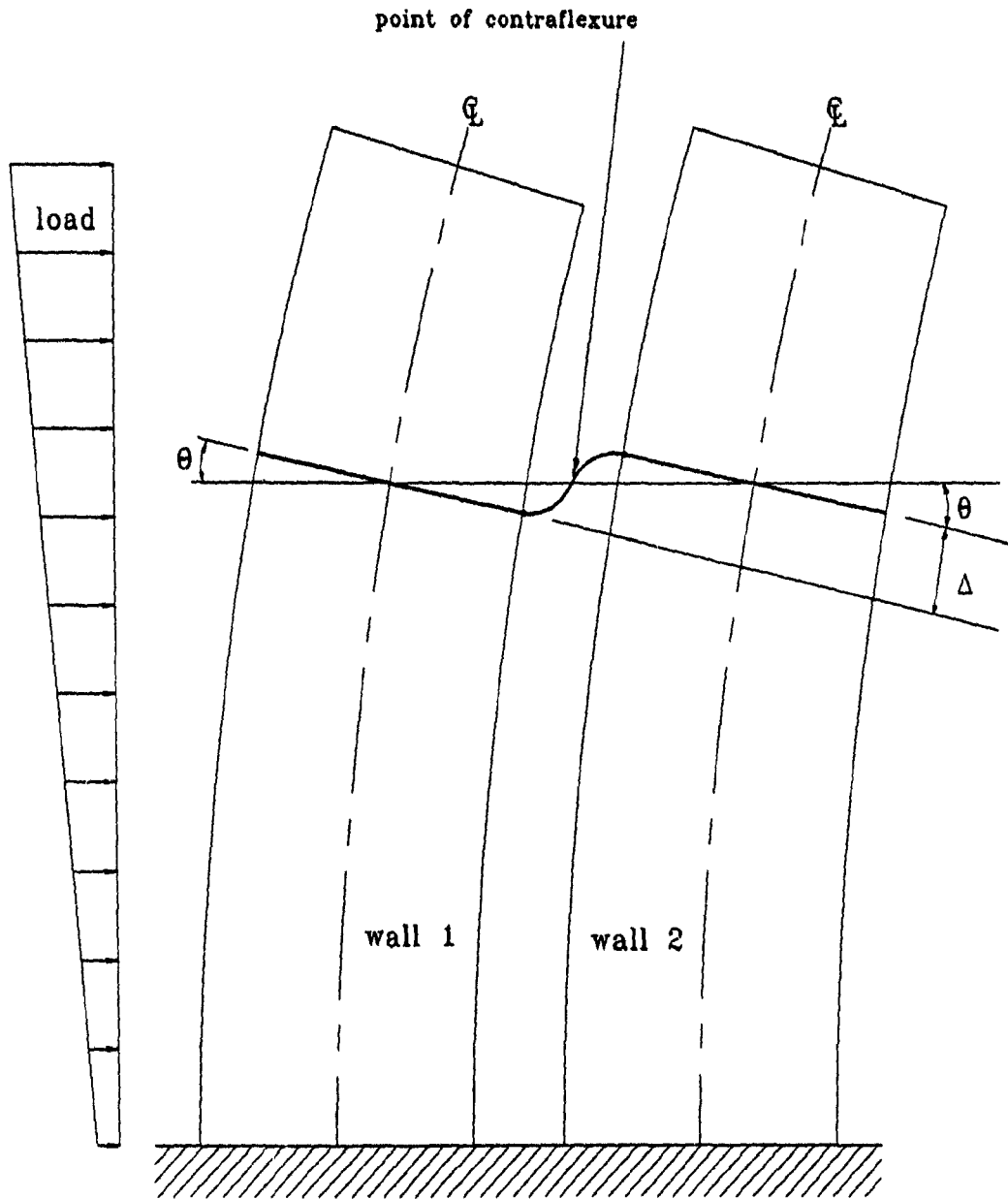
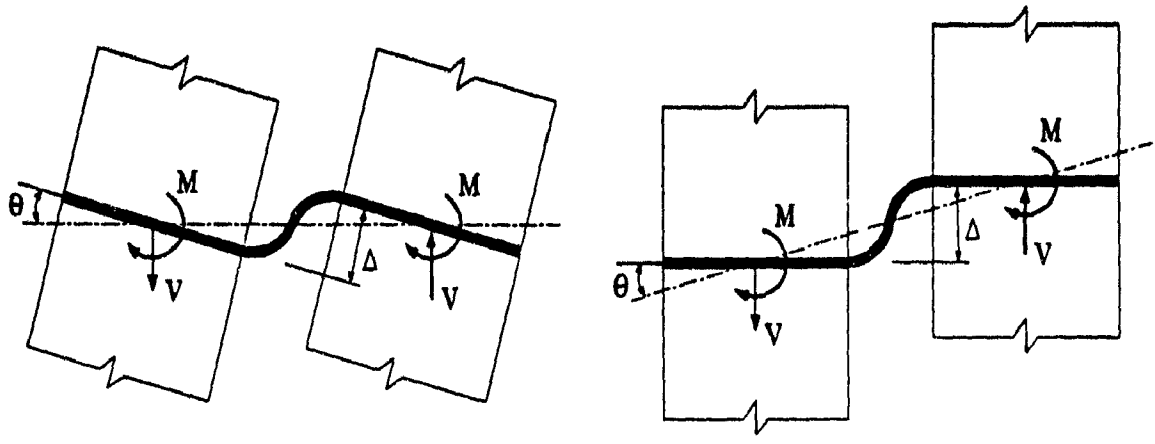


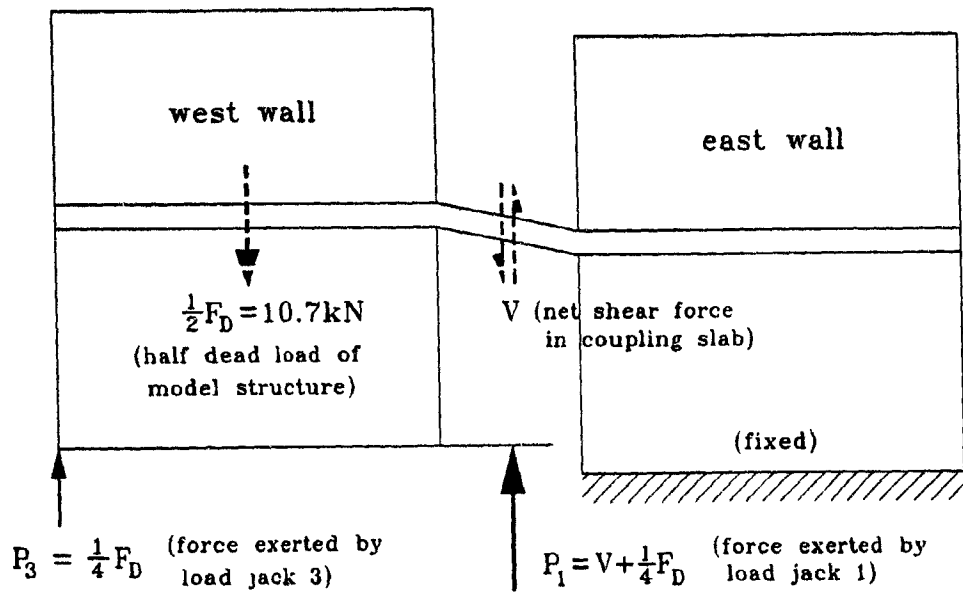
Figure 2.2 Relative Movements of Shearwalls Subjected to Lateral Loading.



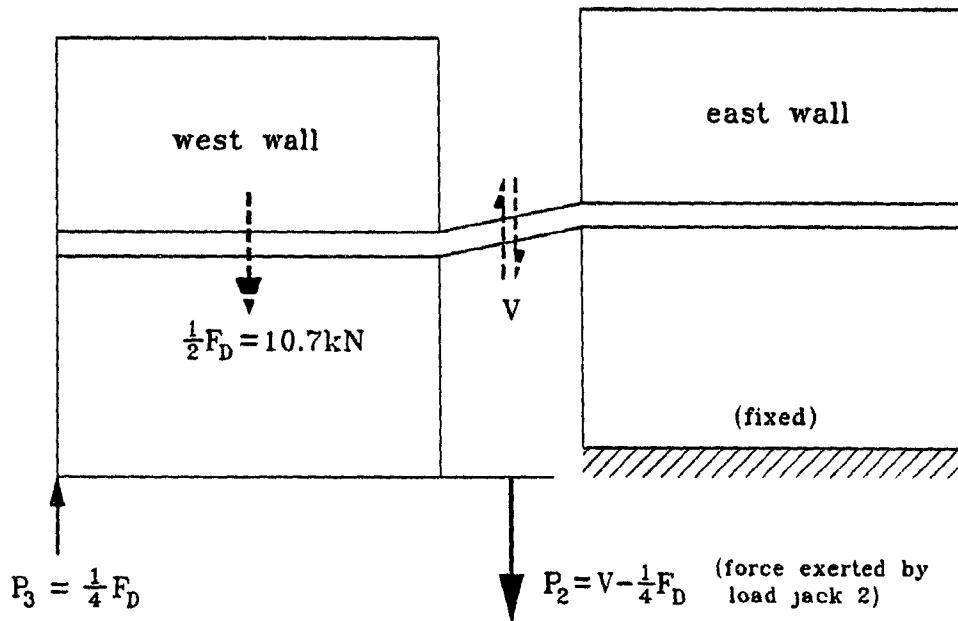
(a) Wall Rotations

(b) Vertical Wall Displacements

Figure 2.3 Modeling of Slab Deformation.



(a) Upward Loading



(b) Downward Loading

Figure 2.4 Illustration of Forces Exerted on West Shearwall.

CHAPTER 3

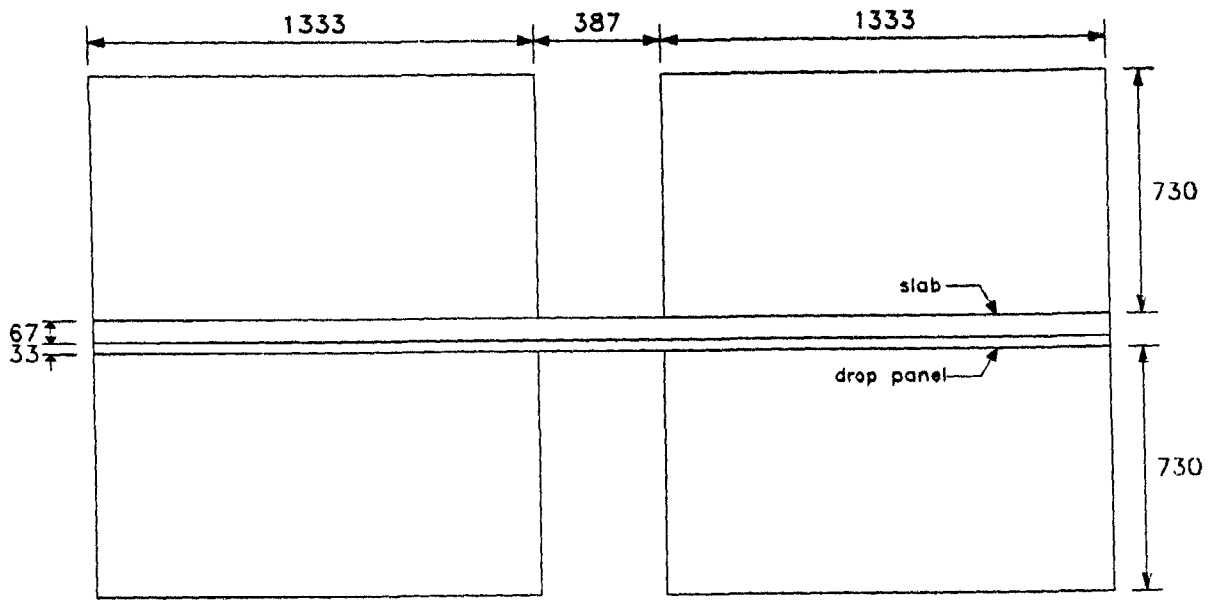
THE MODEL STRUCTURE AND THE TEST SET-UP

The prototype configuration and design and the selected model scale factors were presented in the previous chapter. These scale factors were employed in this chapter which describes the configuration, design, material properties, instrumentation, loading system and loading history of the model specimens.

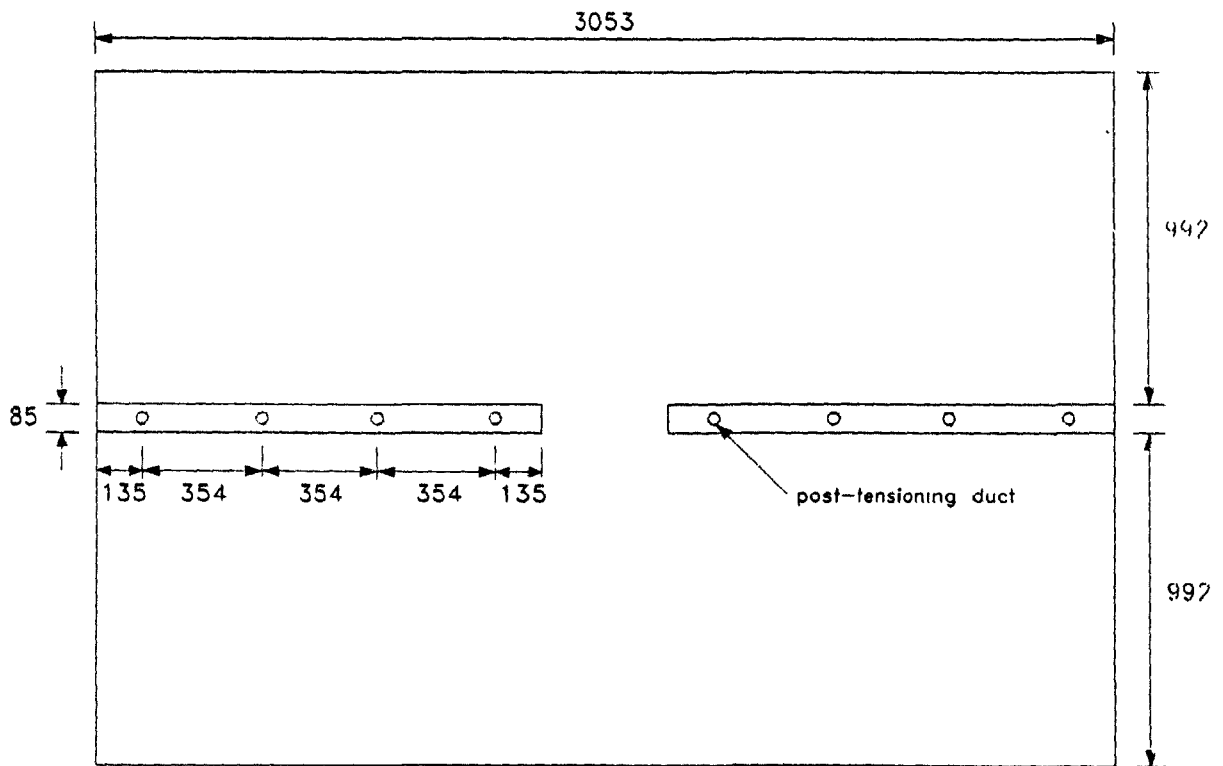
3.1 Configuration of the Model

3.1.1 The Model Geometry and Assembly

Four model slabs were constructed and tested in this series. Each model comprised five separate elements: a 3053×2065 mm slab and four separate 730×1332 mm wall segments. Each specimen was provided with a drop panel, 450 mm wide by 33 mm deep, which extended the entire length of the slab. The width of the drop panel was chosen based on the recommendations of Qadeer and Stafford Smith⁷. The $\frac{1}{3}$ -scale reinforced concrete model is shown in Figure 3.1. The model walls were precast and reused for all four tests in a manner similar to that used by Taylor¹⁴, Malyszko¹⁵ and Khan¹⁶. For each test, the specimen was assembled as shown in Figure 3.2. The walls and the slab were snugly clamped together by tightening the nuts on either end of each 19 mm diameter threaded rod passing through the ducts in the walls and through small



(a) Elevation



(b) Plan

Figure 3.1 Dimensions of the Model.

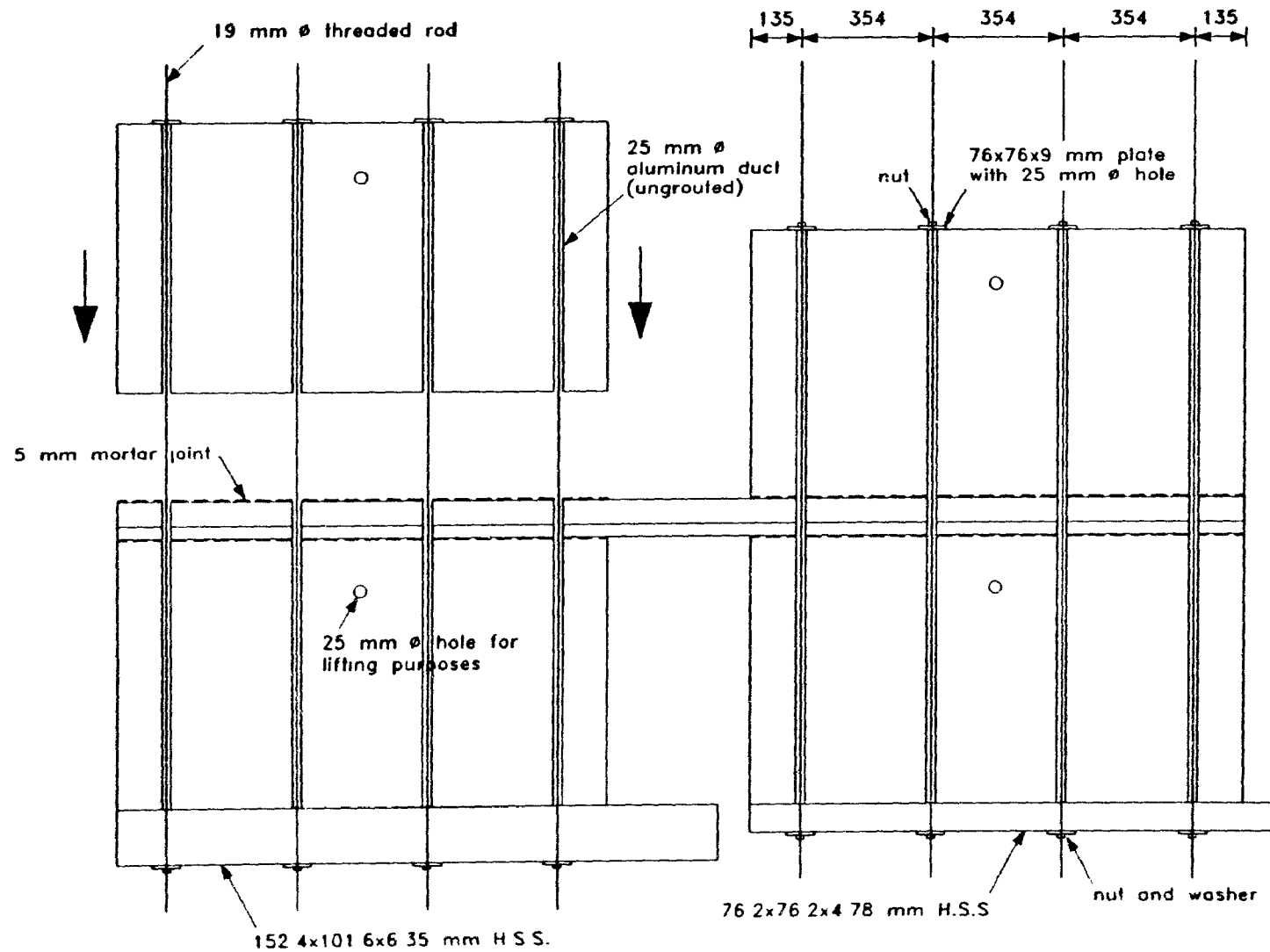


Figure 3.2 Assembly of Precast Wall Segments.

pre-formed holes in the slab. Each rod was then post-tensioned by rotating the nut one full turn after the "snug" position to ensure a tight fit between each wall and the slab.

Overall, this method of assembly led to significant economy and greatly facilitated the construction and handling of each test specimen.

3.1.2 Limitations

As mentioned in Section 2.3.1, the model used in this study is a $\frac{2}{3}$ -scale reinforced concrete model of Taylor's¹⁴ specimen. As such, certain assumptions put forth by Taylor¹⁴ will apply here:

- (i) "The use of precast wall segments, which were moderately stressed during the tests, instead of cast-in-place construction is unlikely to affect slab performance significantly."
- (ii) "Failure to accurately model dead and live load actions has only minor effects on the failure mechanisms and the ultimate moments due to lateral loading. The use of a longitudinal line of symmetry is therefore reasonable in the model."
- (iii) "The model is of sufficient length so that the free end boundary conditions of the model slab are of minimal importance."
- (iv) "Insignificant separation forces in the slab are generated as a consequence of small differences in yield moments at wall faces."
- (v) In designing the slab, moment redistribution caused a reduction of 20% in the negative moments at the support.
- (vi) For the lateral load analysis, the cracked slab stiffness value was assumed to be 50% of the uncracked stiffness based on recommendations by Qadeer and Smith⁷.

However, unlike Taylor's¹⁴ tests where the jack loads were applied horizontally (see Figure 1.12), the load was applied vertically in this study. The following additional assumptions were made for this study.

- (vii) The deformation pattern of the model slab as a result of vertical loading is representative of the prototype slab deformation.
- (viii) The bending moment and shear force distributions within the slab are similar in all respects to that of the prototype taking into consideration the similitude requirements set forth in Section 2.3.3 of this report and as a result of assumption (vii) above.

3.2 Material Properties

3.2.1 Concrete

The concrete used in Specimens D1 and D2 was provided by a local ready-mix supplier while the concrete used in Specimens D3 and D4 was mixed at the McGill University's Jamieson Structures Laboratory. Type 30 high early strength Portland cement was used for all four specimens. The prototype maximum aggregate size of 20 mm was scaled down to a maximum aggregate size of 10 mm for all model specimens. Although a lower maximum aggregate size would have been desirable due to the 7 mm specified slab clear cover, the smallest maximum size available to the concrete supplier was 10 mm.

The specified air entrainment for the concrete used in Specimens D1 and D2 was 4 to 6 percent. In both of these specimens, the concrete slump was about 100 mm. The specified strength of the concrete supplied by the local supplier was 35 MPa.

Numerous trials for the workability and strength of the model concrete mixes led to the final mix details for Specimens D3 and D4 as follows. Separate individual sieve analyses on each aggregate size batches were made to determine the aggregate proportions as shown in Table 3.1 for a combined aggregate fineness modulus value of 3.7. The grading of the aggregates used in Specimens D3 and D4, based on the results of sieve analysis of the aggregate batch mix using the proportions presented in Table 3.1, is shown in Figure 3.3. The water-cement-aggregates ($W : C : A$) ratio adopted

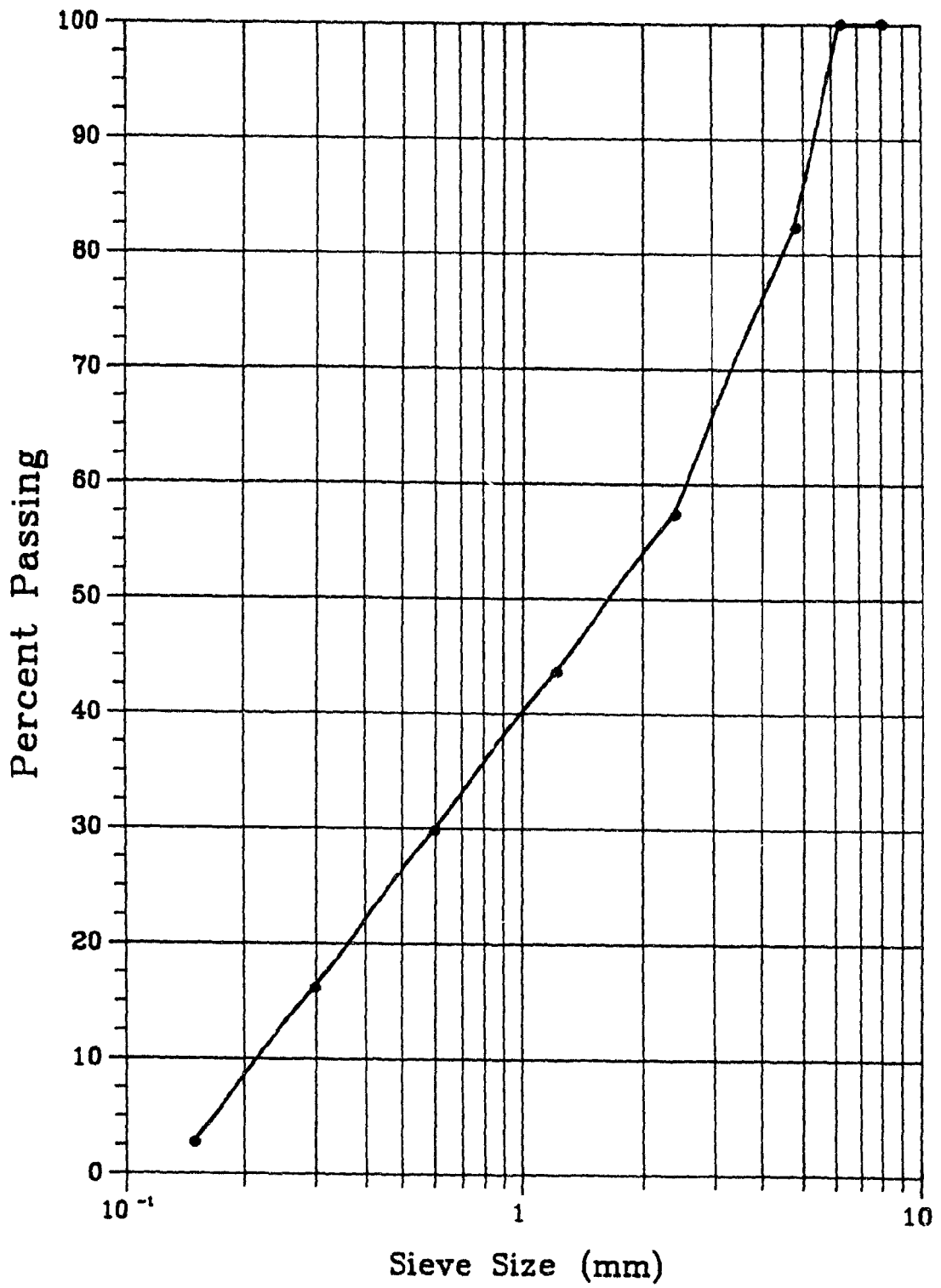


Figure 3.3 Grading of Aggregates Used in Specimens D3 and D4 concrete.

Table 3.1 Proportions of Aggregates Used in Specimens D3 and D4.

Aggregate Size	Proportions (%)
$\frac{1}{4}$ "	40.6
$\frac{1}{8}$ "	8.5
#10	5.9
#16	8.9
#24	12.5
#40	7.2
#50	8.8
#70	7.5

for the model concrete mix was

$$0.45 : 1 : 3.16$$

. The model concrete mix was designed for a nominal compressive strength of 35 MPa.

Twenty concrete cylinders of sizes 150 mm \times 300 mm (6" \times 12") and 100 mm \times 200 mm (4" \times 8") were cast along with each slab. The average compressive strengths and peak compressive strains of the concrete for all specimens together with the typical stress-strain curve for the concrete are shown in Figure 3.4.

3.2.2 Steel

The three sizes of deformed steel wires used, D3, D7 and D8.5, corresponded to the CSA standard G30.14-1972 specification (which is in substantial agreement with the ASTM standard A496, Deformed Steel Wire for Concrete Reinforcement). The specifications of these deformed steel wires are given in Table 3.2.

The D3 and D7 deformed wires, which had yield strengths of 500 MPa and 600 MPa, respectively, before heat treatment, gave yield strengths of 190 MPa and 274 MPa, respectively, after heat treatment, with ultimate strains exceeding $15\epsilon_y$. These heat treated steel wires were used for reinforcement in the slab. The reinforcing steel used in the wall segments comprised of D3 and D8.5 wires that were not heated treated. The yield strength of the D8.5 wires was 500 MPa. Typical stress-strain characteristics of the reinforcing steel are shown in Figures 3.5 to 3.8. Table 3.3 summarizes

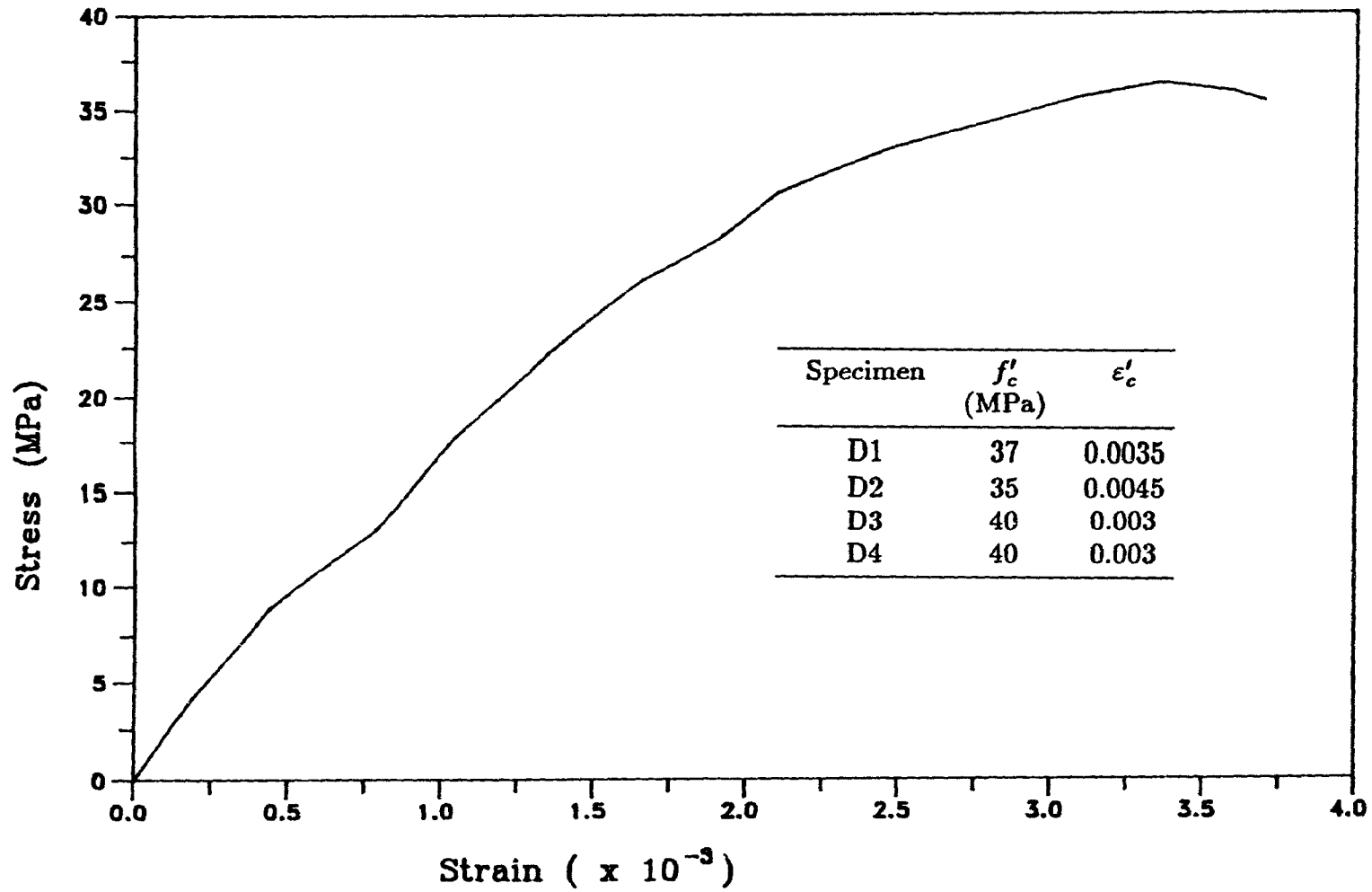


Figure 3.4 Typical Concrete Stress-Strain Curve.

Table 3.2 Reinforcement Specifications.

Bar Designation	Diameter (mm)	Weight (g/m)
D3	4.95	152.3
D7	7.57	354.8
D8.5	8.39	430.6

Table 3.3 Reinforcing Steel Properties.

	Specimen			
	D1	D2	D3	D4
Slab Steel:				
D3 - Yield Stress, MPa	190	190	190	190
- Yield Strain	001	001	001	001
- Ultimate Stress, MPa	310	310	330	330
- Ultimate Strain	.1	.1	.1	.1
D7 - Yield Stress, MPa	274	274	280	280
- Yield Strain	00125	00125	00136	00136
- Ultimate Stress, MPa	380	380	370	370
- Ultimate Strain	0.20	0.20	0.24	0.24
Wall Steel:				
D3 - Yield Stress, MPa	475	475	475	475
- Yield Strain	0025	0025	0025	0025
- Ultimate Stress, MPa	525	525	525	525
- Ultimate Strain	05	05	05	05
D8.5 - Yield Stress, MPa	550	550	550	550
- Yield Strain	0025	0025	0025	0025
- Ultimate Stress, MPa	600	600	600	600
- Ultimate Strain	04	04	04	04

the properties of the steel wires used in each specimen.

3.3 Design of the Model Structure

The basic configuration and reinforcement details of the specimens used in this investigation are shown in Figures 3.9 through 3.14. The main differences between the four test specimens are the stirrup spacing in the central cage and the amount of concentrated transverse reinforcement in the vicinity of the wall toe region. The various reinforcement details are described in the following sections.

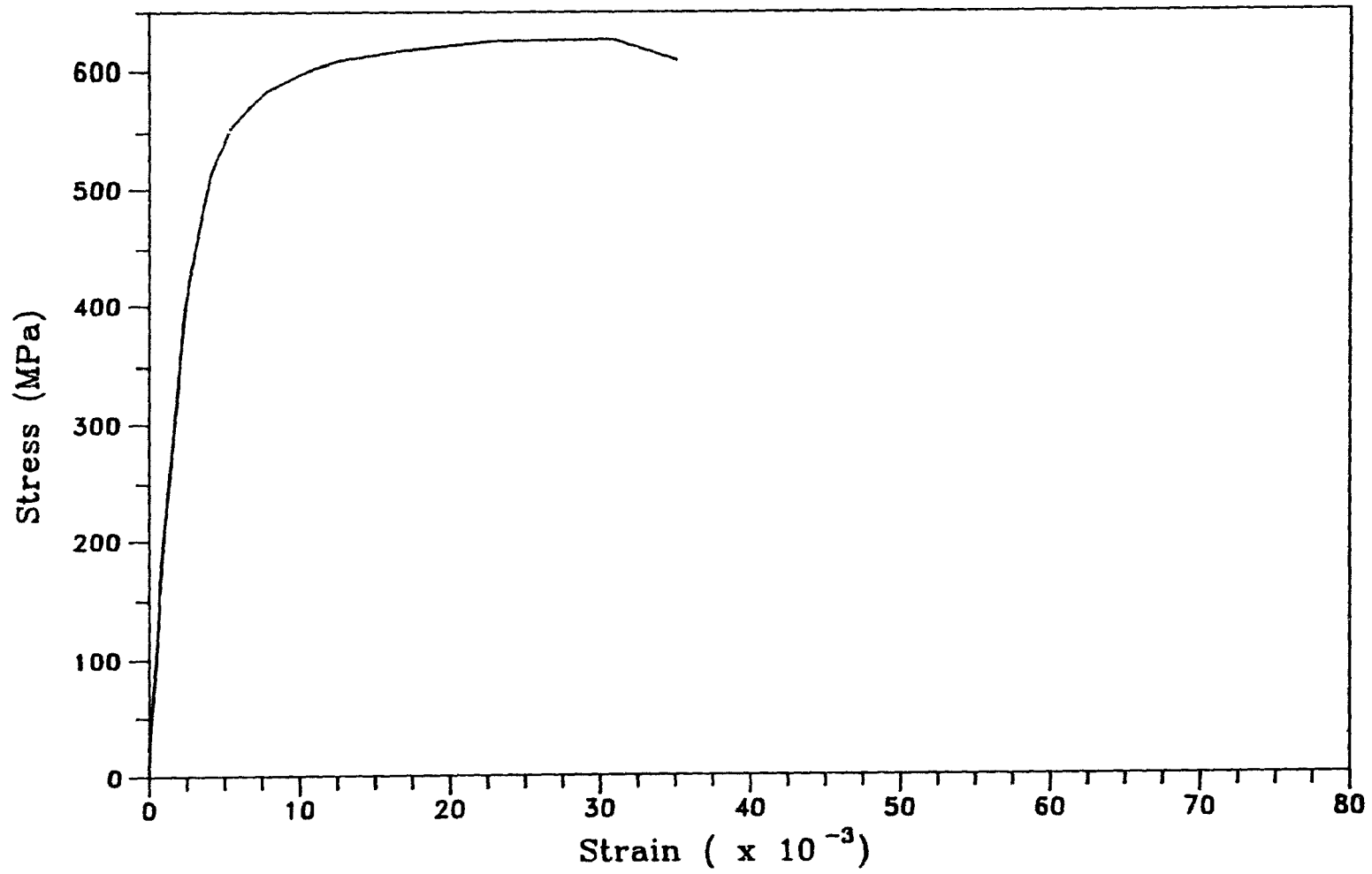


Figure 3.5 Typical Stress-Strain Curve for D8.5 Reinforcing Steel.

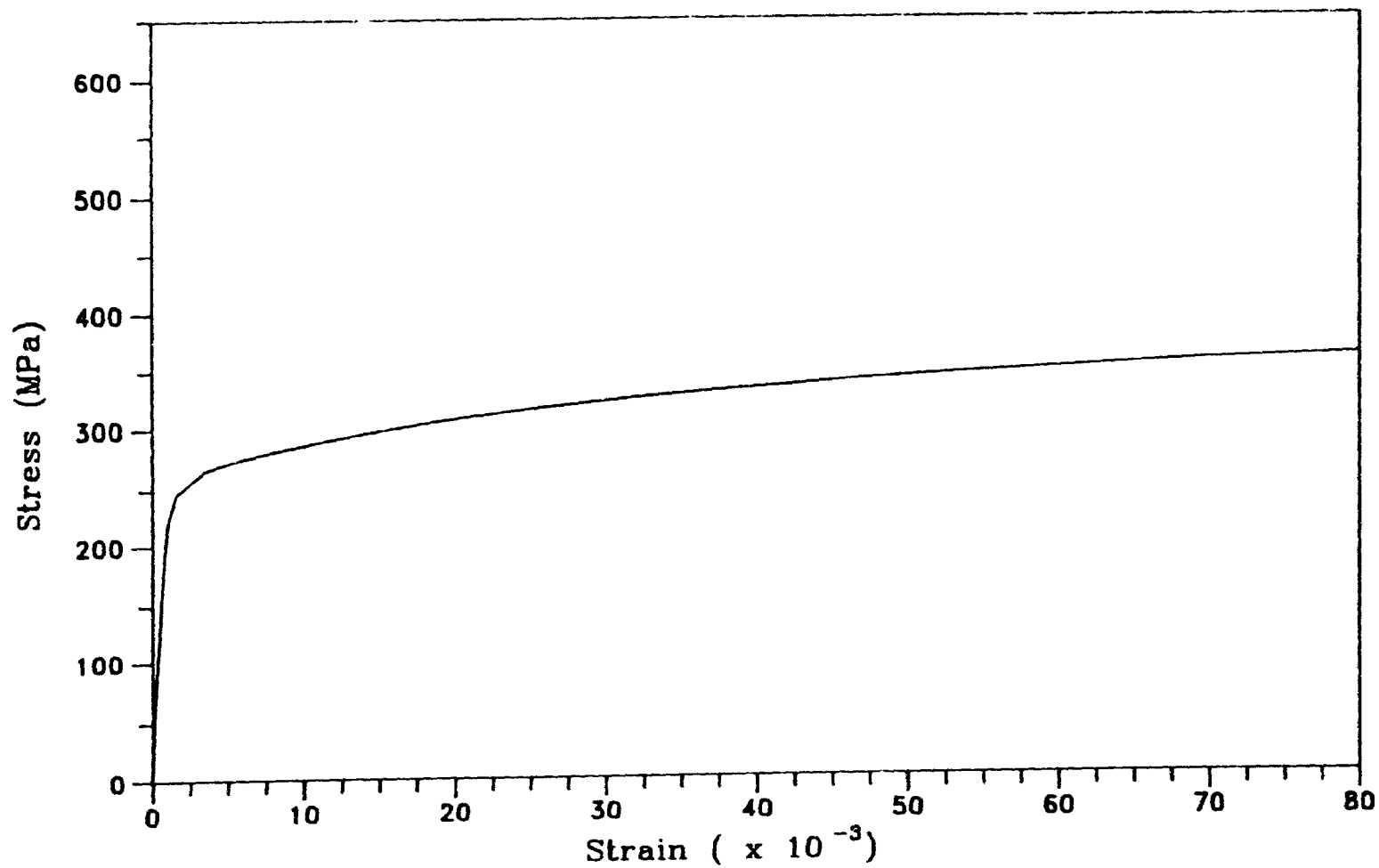


Figure 3.6 Typical Stress-Strain Curve for Heat Treated D7 Reinforcing Steel.

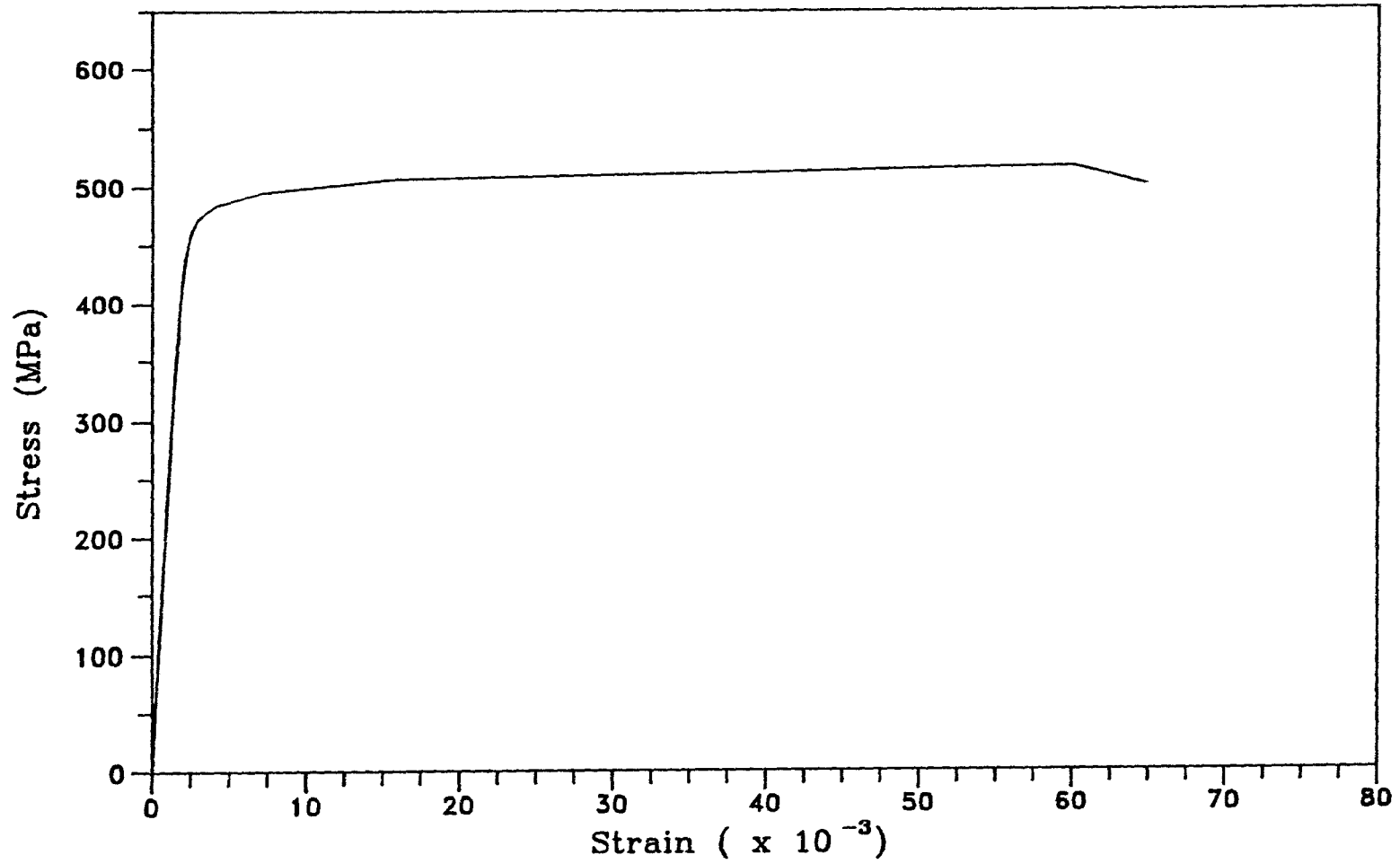


Figure 3.7 Typical Stress-Strain Curve for D3 Reinforcing Steel.

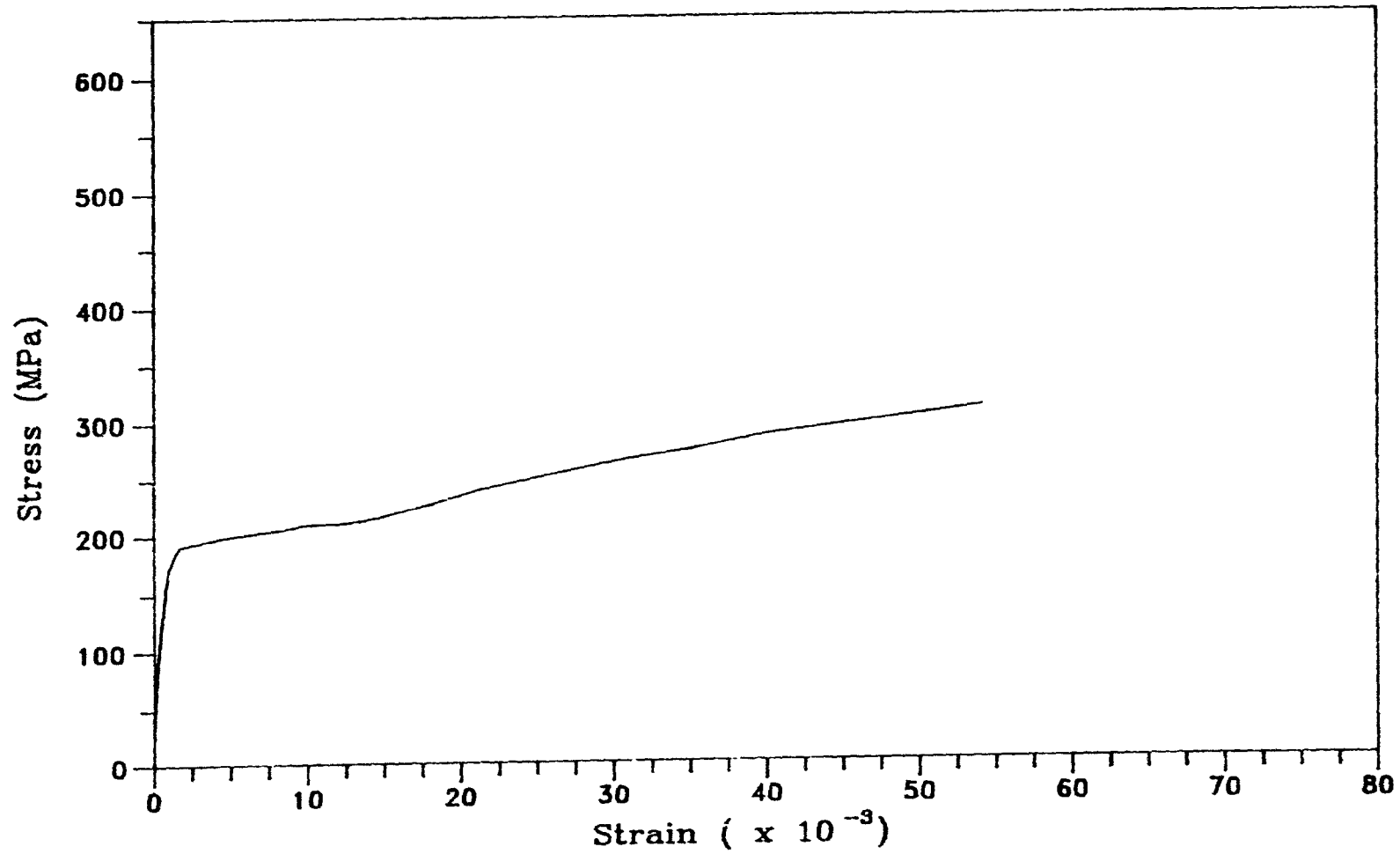


Figure 3.8 Typical Stress-Strain Curve for Heat Treated D3 Reinforcing Steel.

3.3.2 Transverse Slab Reinforcement

The transverse slab reinforcement for Specimens D1 and D2 is shown in Figure 3.10 and 3.13 while the transverse slab reinforcements for Specimens D3 and D4 are shown in Figures 3.11, 3.12 and 3.14.

Transverse reinforcement content of 0.55%, corresponding to the minimum reinforcement content suggested by C.S.A Standard CAN3-A23-M84²⁰, was provided in Specimens D1 and D2 (Figure 3.10). With the exception of the horizontal legs of the stirrups in the central cage of the slabs, no additional transverse reinforcement was provided in the vicinity of the wall toe regions in the above two specimens. The D7 transverse reinforcement, placed 11 mm (clear cover = 7 mm) from the bottom face of the concrete outside the drop panel region, was placed as straight continuous bars across the width of the slab. Hence, within the drop panel, these bars were at a distance of 44 mm from the bottom face of the concrete (Figure 3.13).

In an effort to eliminate punching shear failure, Khan¹⁶ provided concealed beams under the wall toe, which resulted in satisfactory control of the punching shear mechanism. It follows that provision of some sort of special transverse reinforcement near the wall toe region may be adequate to control damage due to punching shear in this region. For practical application, a closely spaced mesh of transverse and longitudinal reinforcement is preferable over the concealed beam in terms of ease of construction. Since closely spaced longitudinal reinforcement (50 mm spacings) was already provided (see Section 3.3.3), it would be economical to simply provide for some concentrated transverse steel across the width of the slab at the wall toe regions. These additional concentrated D7 transverse deformed wires were provided in Specimens D3 and D4. Based on the observations from the tests on Specimens D1 and D2 and that of Malyszko's¹⁵ Specimens S1, S2 and S3, these concentrated transverse reinforcements were spaced over a strip equal to one quarter of the corridor width on either side of the wall toe face. The transverse strips of slab containing the concentrated transverse

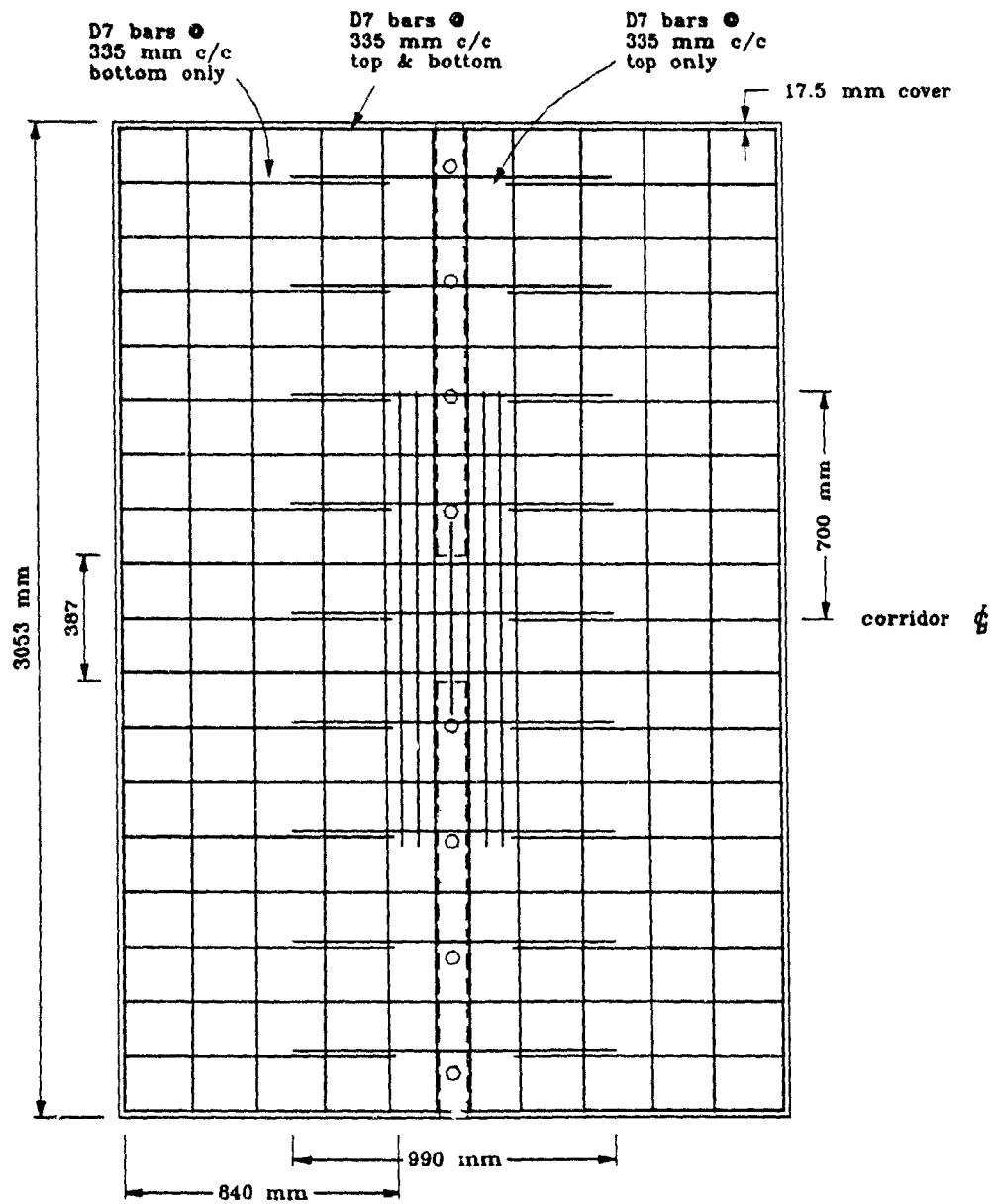


Figure 3.10 Slab Flexural Reinforcement Detail of Specimens D1 and D2.

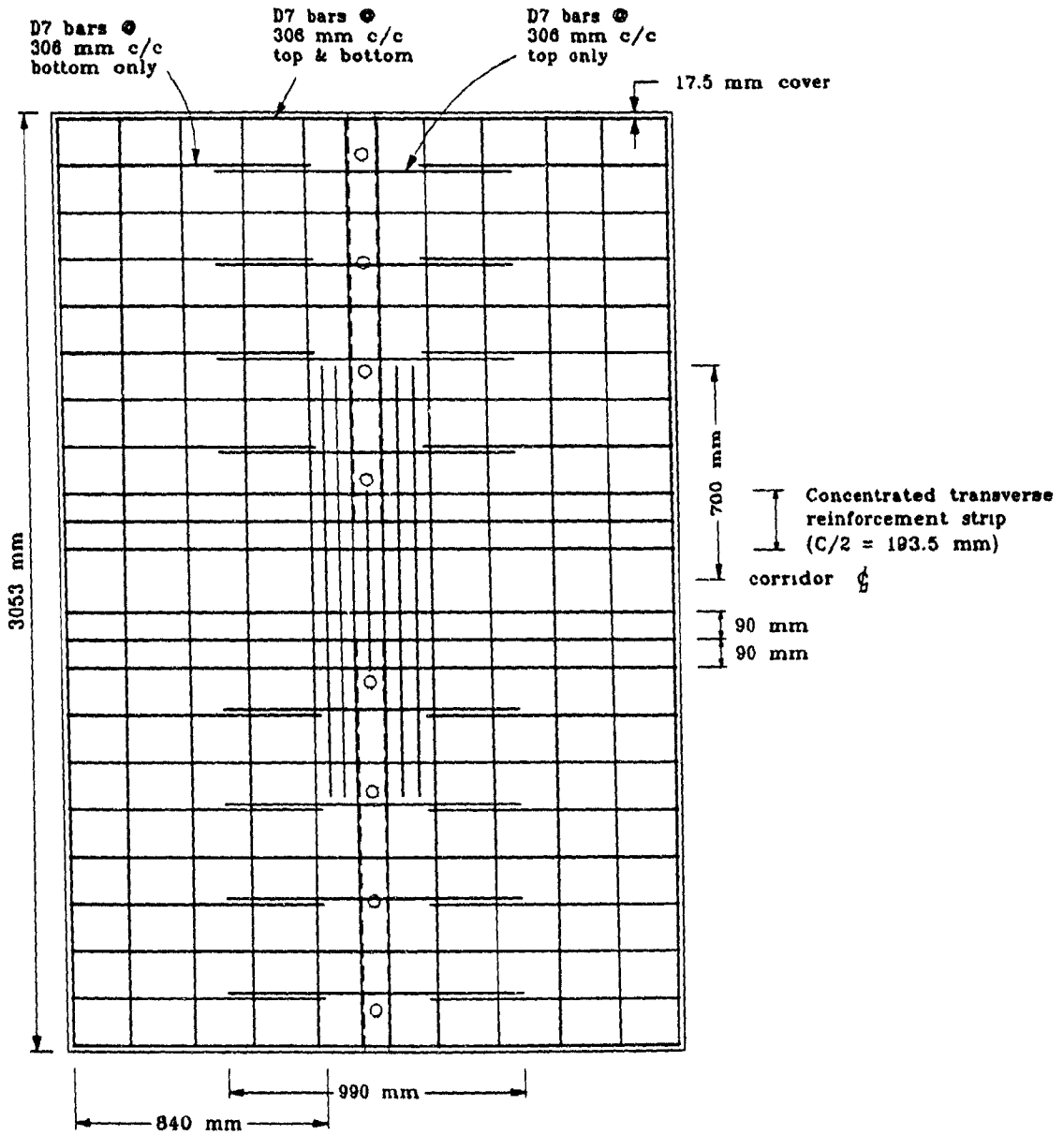


Figure 3.11 Slab Flexural Reinforcement Detail of Specimen D3.

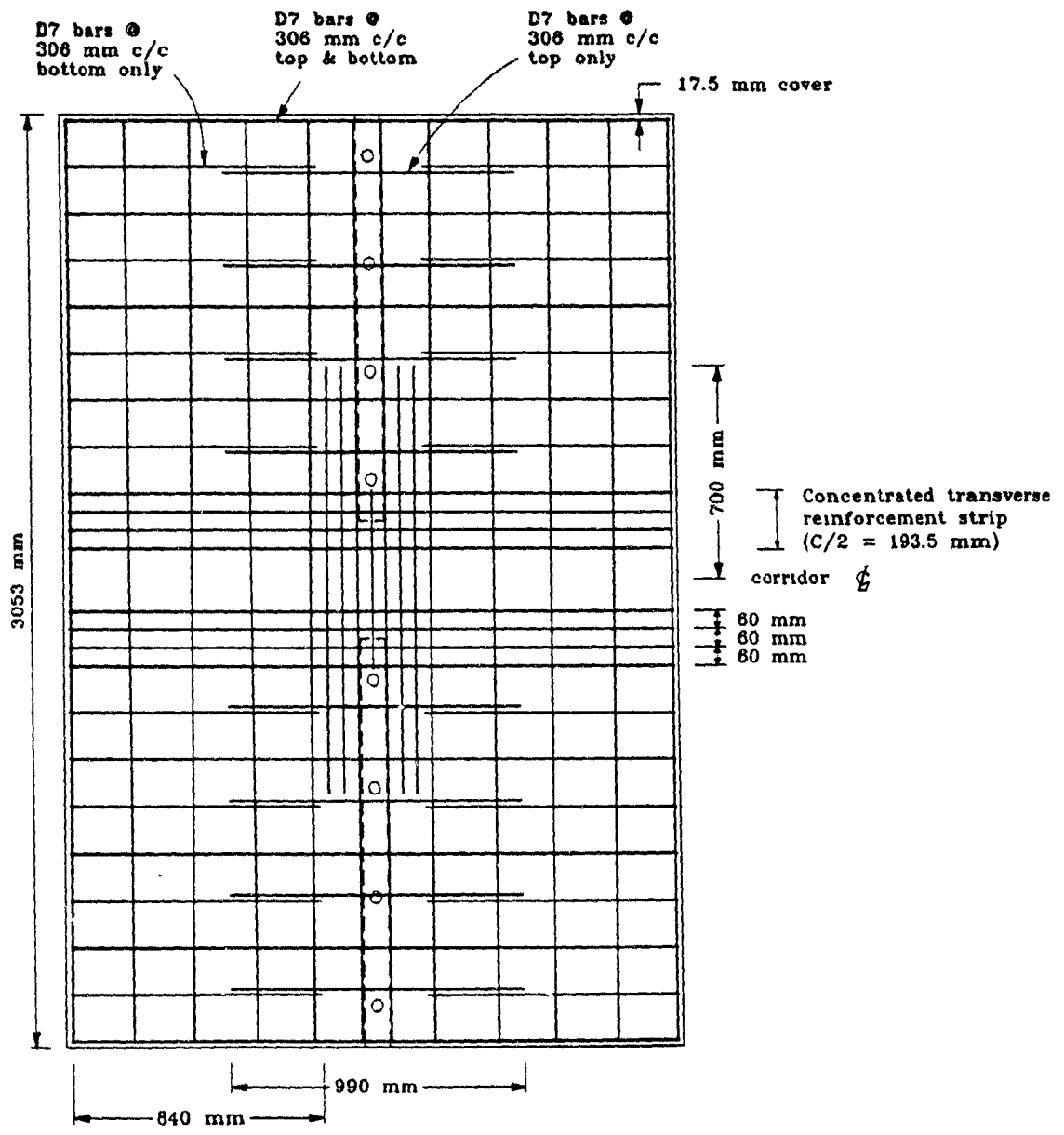


Figure 3.12 Slab Flexural Reinforcement Detail of Specimen D4.

reinforcement in Specimens D3 and D4 were assumed to act as cantilevers extending on either side of each wall toe, and the transverse reinforcement was designed to carry 74% and 96% of the flexural capacity of Malyszko's¹⁵ Specimen S1 central cage, respectively. The capacities of these transverse beams are therefore 35.2% and 45.8% of the central cage flexural strengths of Specimens D3 and D4, respectively. This corresponds to reinforcement contents (excluding the horizontal legs of the stirrups) of 0.79% and 1.05% within the concentrated strip of transverse reinforcement for Specimens D3 and D4, respectively, at the wall toe. These bars extended the entire width of the slab with 45° bends near the edge of the drop panel to accommodate for the change in depth. Outside the strip of the concentrated transverse reinforcement, 0.53% transverse steel was provided.

3.3.3 Longitudinal Slab Reinforcement

The basic longitudinal slab reinforcement outside of the central cage, within the effective width ($b_{eff} = 450$ mm) recommended by Qadeer and Stafford Smith⁷, was designed to carry the gravity load. Within the central cage, the longitudinal steel was designed using the results of SAP IV[†] computer analysis of the 15-storey prototype structure for Zone 3 seismic loads¹⁹, with the coupling element having a width equal to the effective width of the slab as defined by Qadeer and Stafford Smith⁷, a depth of 67 mm (depth of the slab without drop panel), and allowing for 50% reduction in the stiffness due to the cracking of the concrete. The reinforcement content obtained for the coupling element was relocated within the drop panel, resulting in an effective depth of 82 mm and giving a reinforcing content of 1.01%. Outside the central cage, 0.44% longitudinal reinforcement was provided. The overall longitudinal reinforcement content in the slab, taking the entire width of the slab into consideration, was 0.66%. The minimum reinforcement content for flexural sections suggested by the C.S.A. Standard

[†]SAP IV is the mainframe version of the Structural Analysis Program developed at the University of California at Berkeley

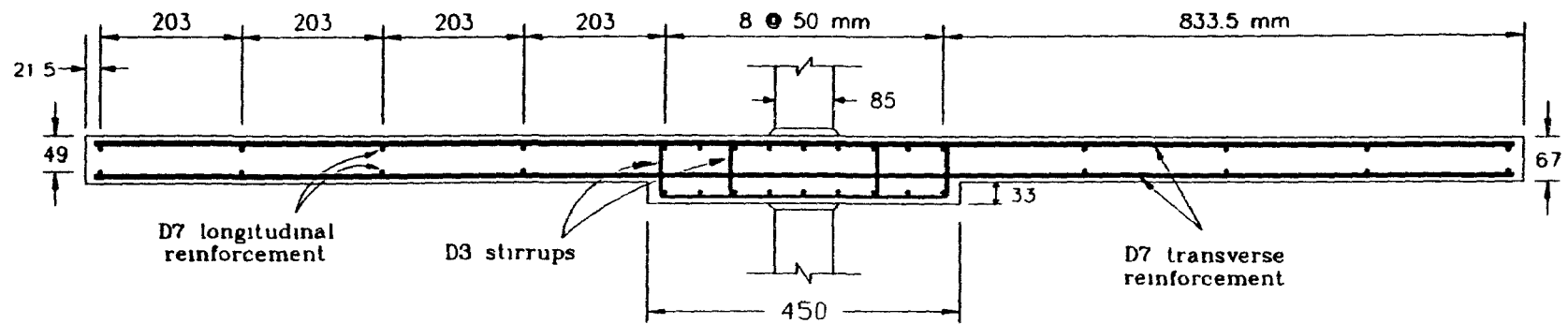


Figure 3.13 Cross-Section of Slab Reinforcement at Wall Toes of Specimens D1 and D2.

55

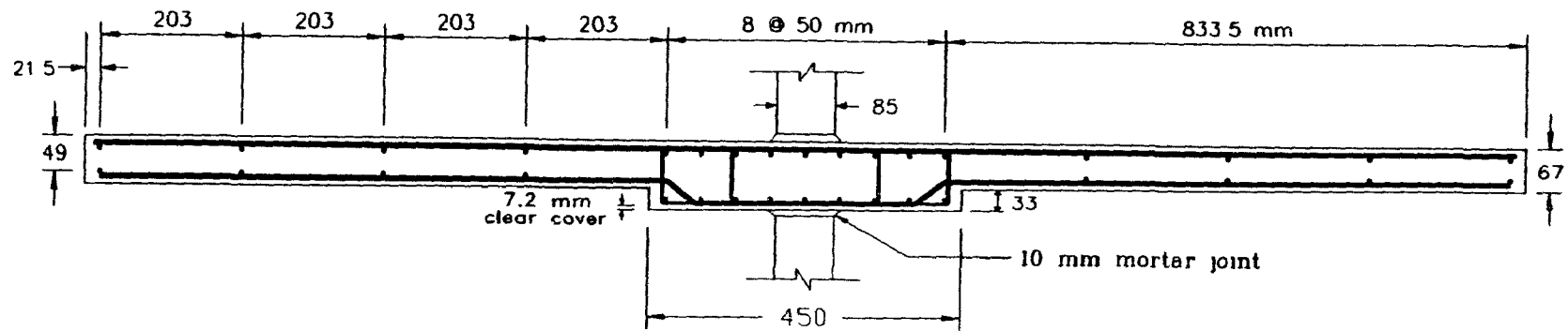


Figure 3.14 Cross-Section of Slab Reinforcement at Wall Toes of Specimens D3 and D4.

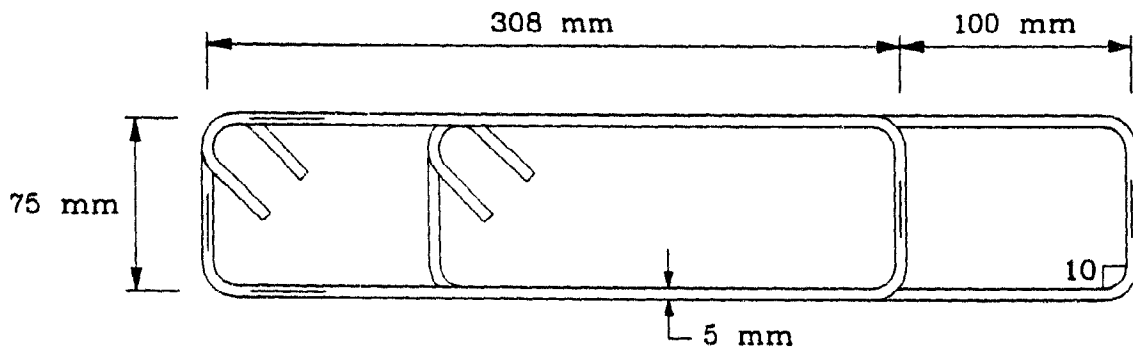


Figure 3.15 Dimensions of the Four-Legged Stirrups.

CAN3-A23.3-M84²⁰ is 0.5% ($\rho_{\min} = \frac{1.4}{f_y}$). The D7 longitudinal seismic reinforcement within the central cage extended 700 mm on either side of the centerline of the corridor (about 1.8 times the corridor width). This arrangement of longitudinal reinforcement was used in all four specimens.

3.3.4 Central Cage Stirrups

The stirrup spacing in Specimen D1 was 23 mm, which was 0.28 of the slab effective depth, d , in the central cage. This spacing of 23 mm was used in Specimen S2 of Malyszko's¹⁵ tests which, showed superior performance over the other two specimens. The choice of this spacing for Specimen D1 served two purposes:

- (1) To allow direct comparison with Malyszko's¹⁵ specimens; and
- (2) To study the effect of smaller stirrup spacings on the coupling slab.

The remaining specimens (Specimens D2, D3 and D4) were constructed with stirrup spacings of 41 mm, which corresponds to $\frac{1}{2}$ of the effective depth in the central cage ($\frac{1}{2}d$). Each set of stirrups comprised of two D3 308 × 75 mm closed stirrups, which formed into a four-legged closed stirrup as shown in Figure 3.15.

3.4 Instrumentation

Because of symmetry of the specimen geometry and loading, only one-half of the specimen was instrumented. Tests by Malyszko's¹⁵ and Khan¹⁶ showed that this method was satisfactory based on the slab deflection profile. This reduced the amount of data acquisition significantly and enabled the load steps to progress at a faster rate, thereby keeping creep effects to a minimum. However, there was damage to a few electronic strain gauges and mechanical demec gauges during the casting and testing processes. The resulting loss of data was predominant for Specimens D3 and D4.

The instrumentation used in this investigation is described in the following sections.

3.4.1 Dial Gauges and LVDT's

Eighteen dial gauges and sixteen linear variable differential transformers (LVDT's) were used to obtain the displacement profiles and the force-displacement relationships and to monitor wall rotations during loading. The locations of the dial gauges and LVDT's are shown in Figure 3.16 and was maintained constant in all four tests. All dial gauges were placed on the underside of the slab, drop panel and the walls. The LVDT's on lines B and D were placed on the top face of the slab while the remaining LVDT's were placed on the underside of the slab. The LVDT's B3, B6, D3 and D6 were used to obtain the relative slab displacement between the wall toes, while the dial gauges C1, C3, C6 and C8 were used to monitor wall rotations. It should be noted that dial gauges C3 and C6 could not be used to obtain the relative displacement of the slab due to wall separations from the slab near the wall toe regions at larger relative displacements. Resetting of some dial gauges was necessary at large displacements due to the limited range of these dial gauges. In general, the range of the dial gauges on the west side of the corridor centerline was 50 mm (2 in) or more. Since reversed cyclic loading was used, the upward and downward travels of these west side dial gauges were reduced to about 25 mm (1 in) and thus resetting at large displacements was expected.

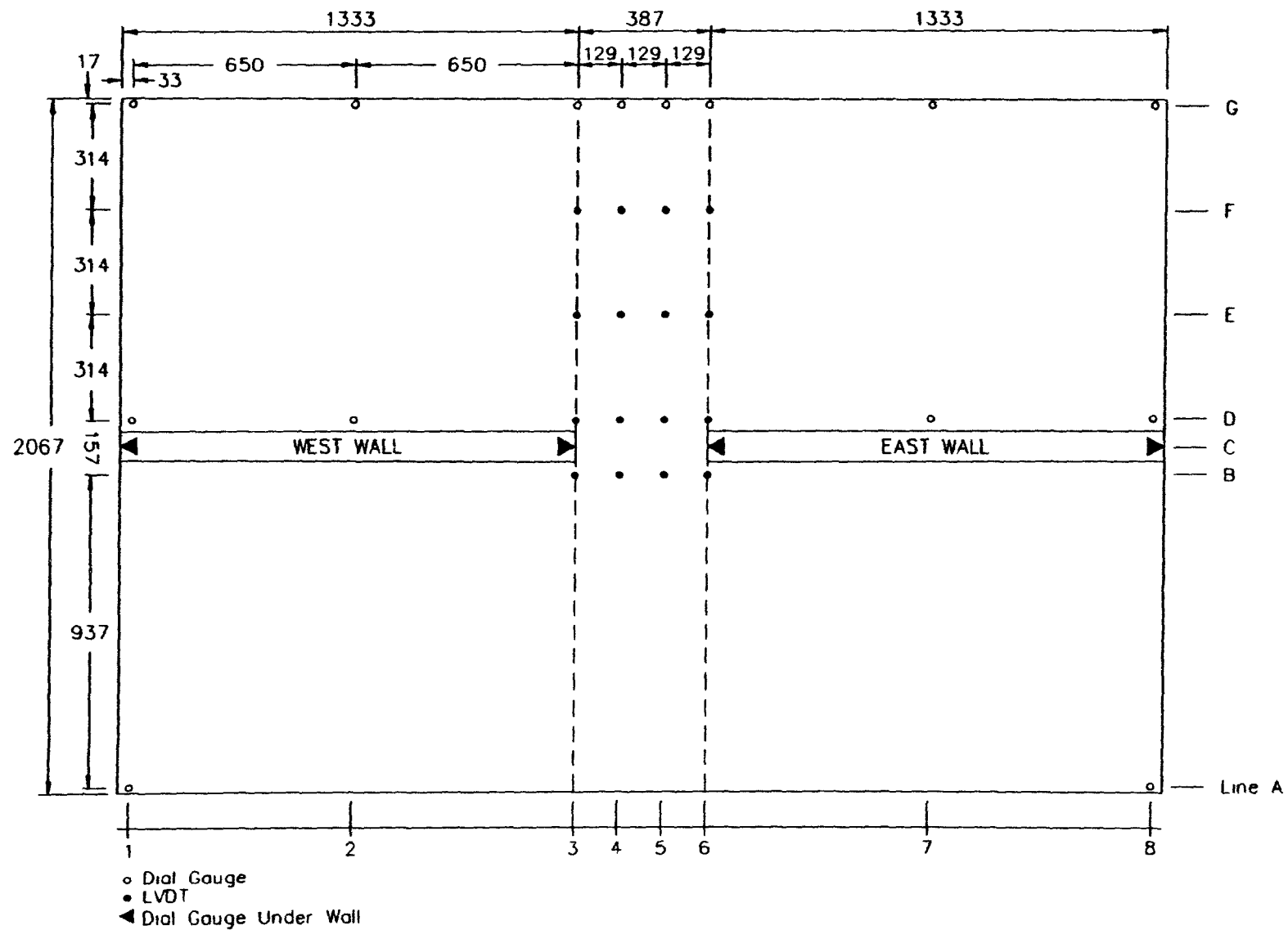


Figure 3.16 Locations of Dial Gauges and LVDT's.

No resetting was necessary for the LVDT's. All dial gauge readings were recorded manually while the LVDT readings were recorded electronically onto a disk via the Optilog data processing unit

3.4.2 Load Cells and Load Jacks

Three load cells were used on three 125 mm (5 in) travel capacity load jacks (shown later in Figure 3.22) for the loading system. Load cells 1 and 2 had load carrying capacity of 445 kN (100,000 lb), and together with load jacks 1 and 2, they were used to provide the primary load on the system. Load cell 3 had a load carrying capacity of 335 kN (75,000 lb), and together with load jack 3, they were used to carry part of the dead load of the system (approximately 5.4 kN). This can be found easily from a consideration of the static equilibrium and was verified during the testing process in all four tests. To allow for the downward displacement of the west wall, load jack 3 was initially set to about half the mark of its travel capacity (approximately 65 mm). All load cell readings were channeled through the Optilog data processing unit and electronically recorded onto the computer disk.

3.4.3 Strain Gauges

Electrical resistance strain gauges (5 mm gauge length) were used on the vertical legs of the stirrups in an effort to determine the participation and effectiveness of the stirrups in resisting shear. These strain gauges were wired from beneath the north side of the slab and connected to the Optilog data acquisition system. The results were electronically recorded onto a computer disk.

Sixteen strain gauges were installed on the stirrup legs of Specimen D1. The locations of these strain gauges are shown in Figure 3.17. Eight strain gauges were located on both the outer and the inner vertical legs of the stirrups.

Eighteen strain gauges were installed onto the stirrup legs of Specimens D2, D3

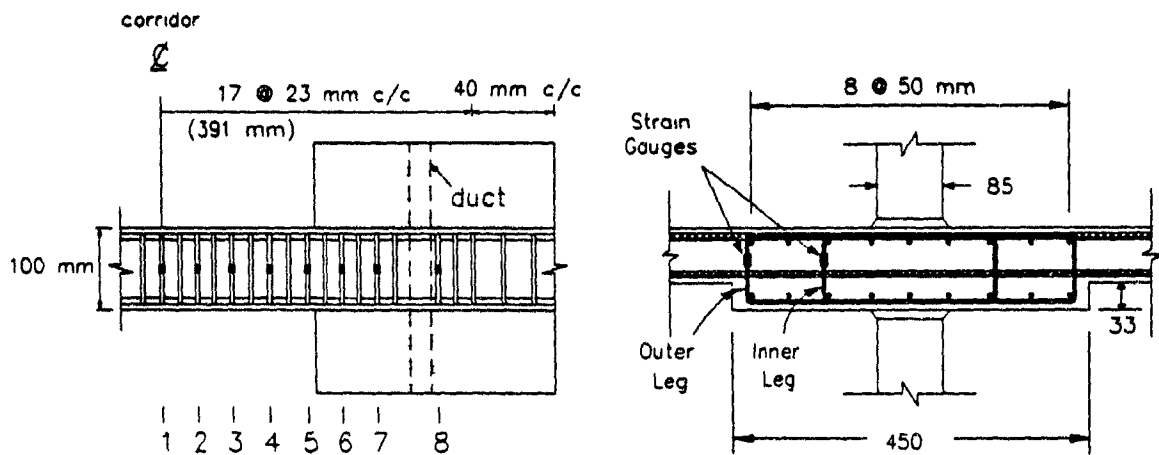


Figure 3.17 Strain Gauge Locations of Specimen D1.

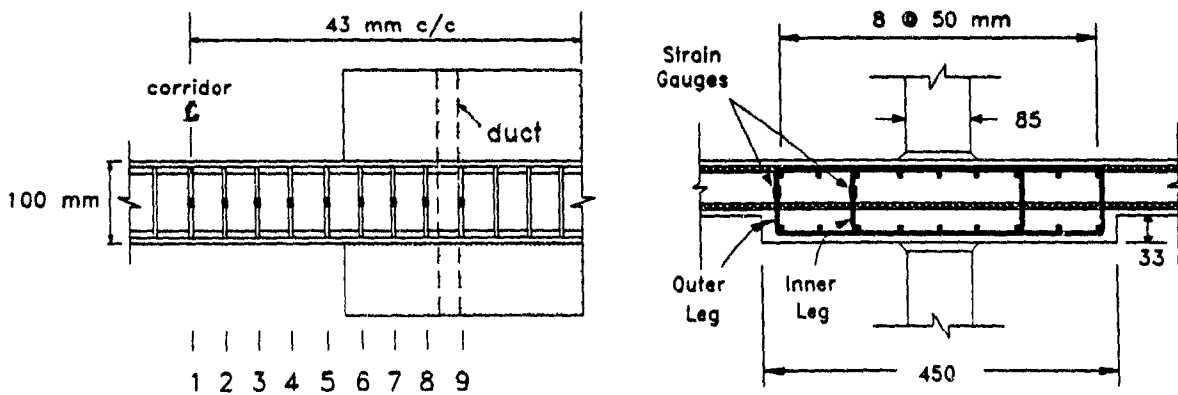


Figure 3.18 Strain Gauge Locations of Specimens D2, D3 and D4.

and D4 as shown in Figure 3.18. Nine strain gauges were located on each of the outer and the inner vertical legs of the stirrups.

3.4.4 Demec Gauges

Due to the unreliability of electrical resistance strain gauges in measuring strains on concrete and top and bottom longitudinal reinforcement at crack locations as well as their post yield behaviour, mechanical strain measuring devices were used. Targets

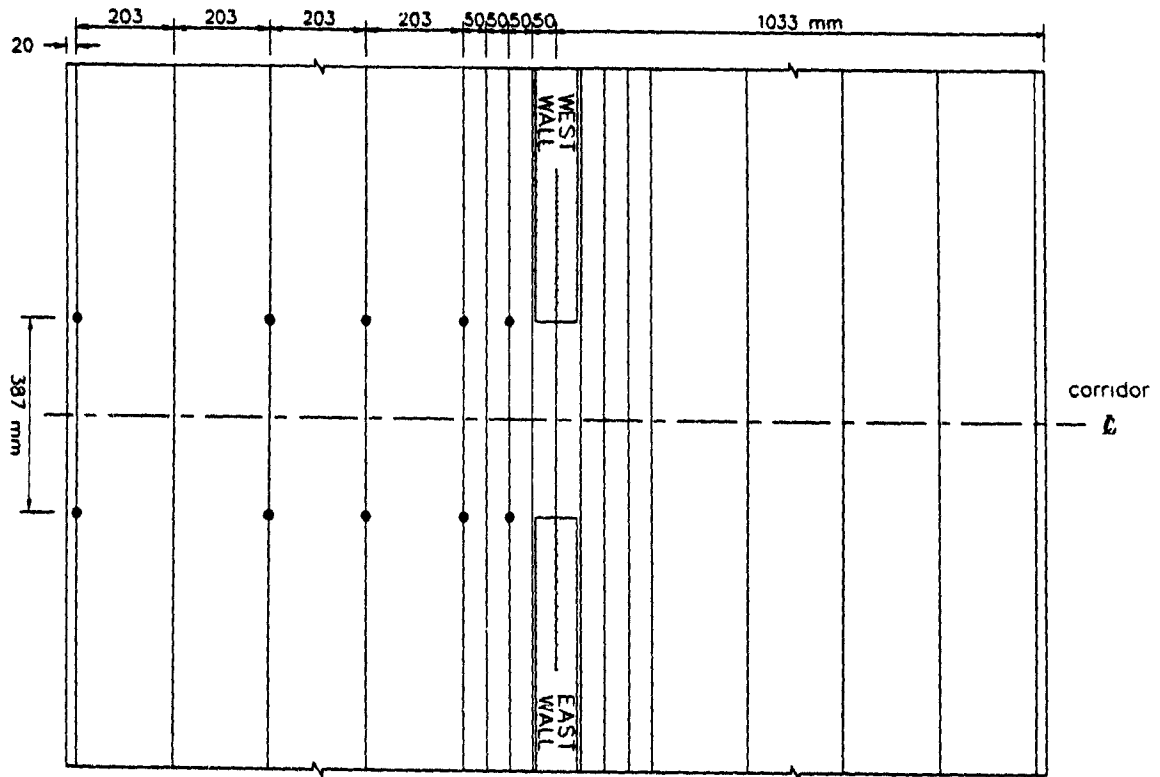


Figure 3.19 Demec Stud Locations on Top and Bottom Longitudinal Slab Reinforcement of Specimens D1 and D2.

made of brass (demec studs) were installed in pairs on the top and the bottom slab surfaces and on the top and the bottom layers of the longitudinal slab reinforcement. Figure 3.19 shows the locations of these demec studs for Specimens D1 and D2. A 100 mm demountable mechanical strain measuring device, having an equivalent strain accuracy of 0.001 mm/mm, was used to measure the change in the distance between these targets. The measured strains, therefore, represent average strains over the target distances.

Strains in the longitudinal direction in both the concrete and the slab reinforcement were not monitored in Specimens D3 and D4. The performance of the concentrated

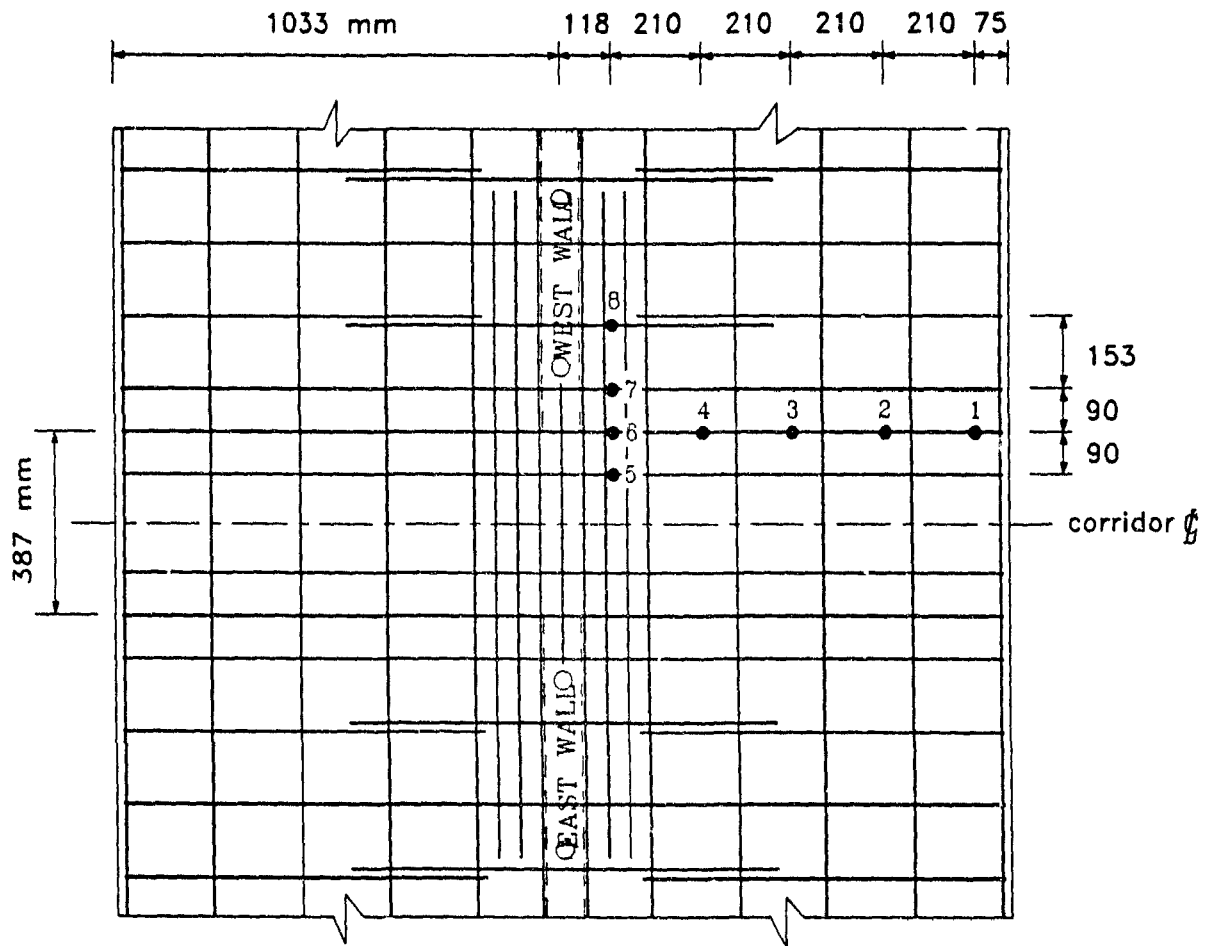


Figure 3.20 Demec Stud Locations on Concentrated Transverse Reinforcement of Specimen D3.

transverse reinforcement in these two specimens was of particular interest. Demec studs were installed on this concentrated transverse reinforcement and on the associated top and bottom concrete surfaces to monitor the strains in the transverse direction at these locations. Figures 3.20 and 3.21 show the locations of these demec studs on Specimens D3 and D4. For the demec studs placed outside the central cage of the slab (demec stud numbers 1 to 4), the 100 mm demountable mechanical strain measuring device was used to obtain the strains in these locations. For the demec studs placed close to the wall face (demec stud numbers 5 and above), a 50 mm demountable mechanical strain measuring device was used to measure the change in the distance between the

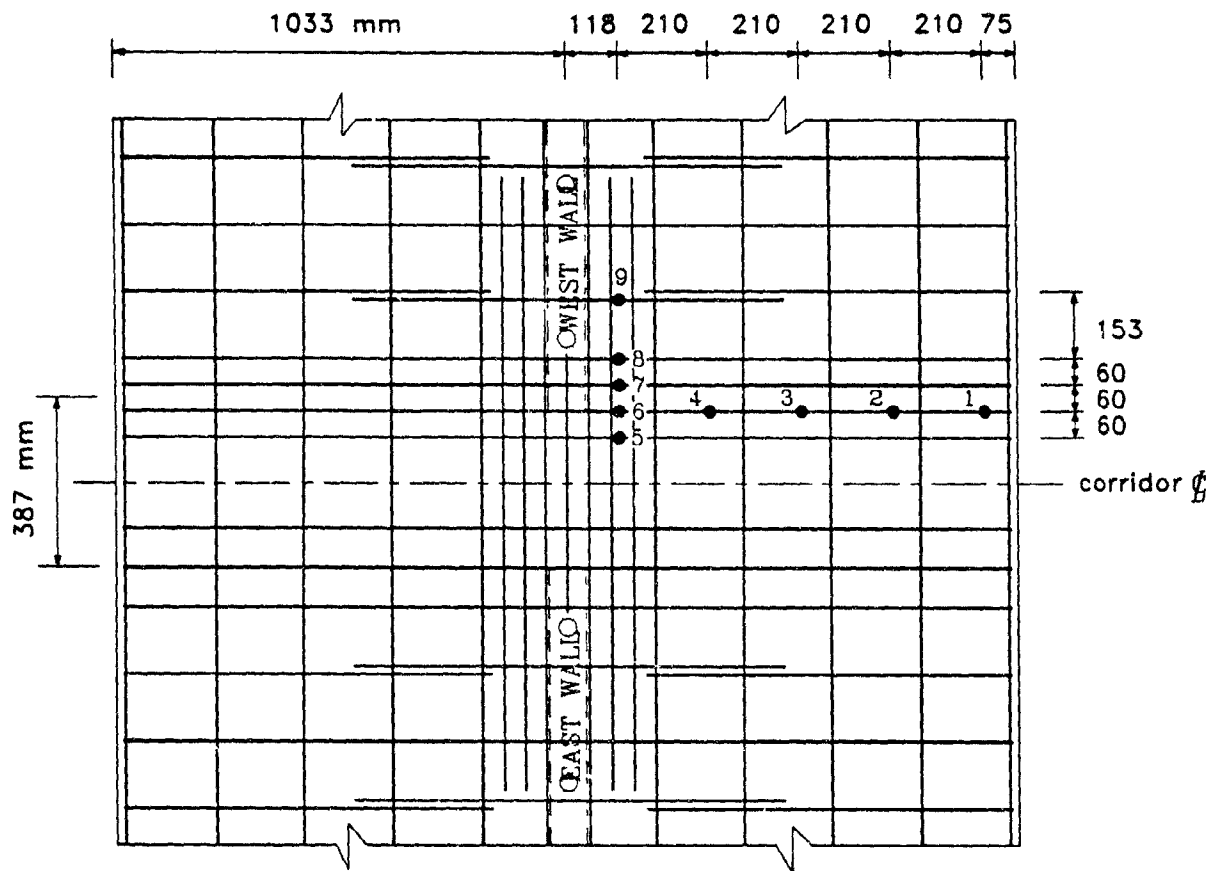


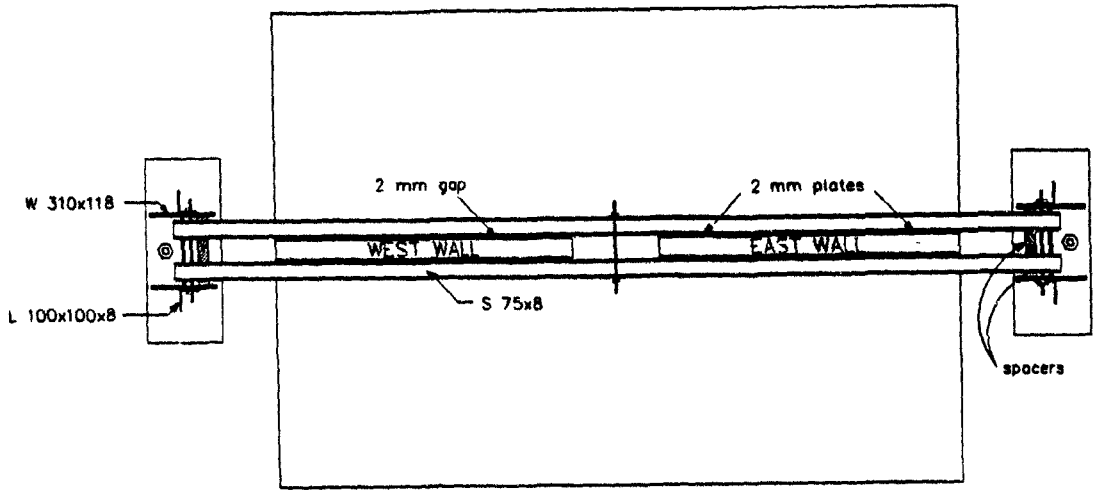
Figure 3.21 Demec Stud Locations on Concentrated Transverse Reinforcement of Specimen D4.

targets.

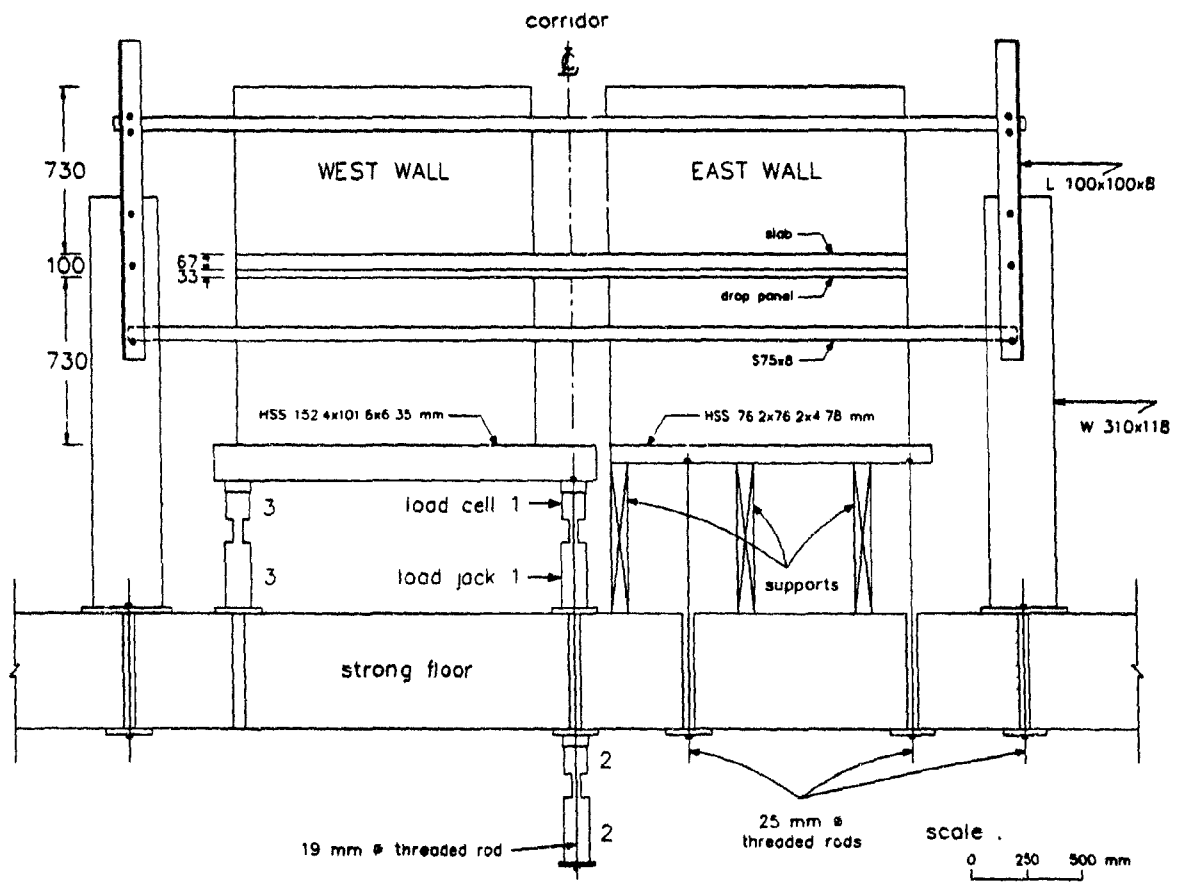
3.5 Loading System

Figure 3.22 shows the elevation and plan view of the loading system used in all four tests. Convenient access to the instrumentation directly underneath the slab and adequate space for the load jacks and load cells were ensured by elevating the entire specimen approximately 500 mm (20 in) above the strong floor.

The west wall was free to move vertically while the east wall was fixed to the strong floor by means of two 25 mm (1 in) diameter threaded rods. Lateral stability



(a) Plan



(b) Elevation

Figure 3.22 Test Set-up and Loading System.

was achieved by clamping two small S75 × 8 mm structural steel beams to the east wall both above and below the slab. A 2 mm gap was provided between these beams and the west wall to permit its unobstructed translation in the vertical direction by means of the three load jacks. These S-shape structural steel beams were designed to carry a concentrated horizontal force at the corridor centreline equivalent to 10% of the anticipated maximum vertical shear force, V , with a maximum restricted transverse horizontal deflection of 5 mm.

Two load jacks, installed along the corridor centreline, were used to apply the shearing force, V , with the load jack 1 immediately below the HSS steel section supporting the west wall and the load jack 2 underneath the strong floor. For the upward translation of the west shear wall, load jack 2 was disengaged and load jack 1 was used to lift the HSS section. The load jack 1 was disengaged for the downward translation and load jack 2 was used to pull the 19 mm ($\frac{3}{4}$ in) threaded rod which passed through the load jack 1 to the HSS section where the rod was bolted. In both directions of loading, load jack 3 was used to balance the shear wall so as not to impose any wall rotation and it carried only a part of the weight of the system (5.4 kN) which was approximately 25% of the total weight of the coupled slab-shear wall system.

The net shear force, V , was used to obtain the force-displacement characteristics in Section 4.3. Although the load jack 3 was expected to carry only the partial self-weight of the system (5.4 kN), observations of load cell 3 revealed that this reading was not constant; the deviation were nevertheless small (approximately ± 0.8 kN). The net positive (upward) shear force in Section 4.3 was obtained by subtracting by 10.7 kN, which was half of the self-weight of the coupled slab-shear wall system, from the sum of the readings for load cells 1 and 3. Conversely, the net negative (downward) shear force was obtained by adding 10.7 kN to the difference in the readings in load cells 2 and 3.

The relative vertical displacements of the west and the east shear wall toes con-

stituted the "relative displacement" (Δ) in Section 4.3. This was obtained by taking the average relative displacements between the LVDT's B3 and B6 and between the LVDT's D3 and D6 (Figure 3.16).

3.6 Testing Procedure

Designing earthquake resistant structures requires the correlation of demand with capacity. In a laboratory investigation, an important consideration is the degree to which the loading program represents the earthquake response conditions. The following subsection reviews the parametric consideration for a valid laboratory loading program. Subsequent subsections describe the loading history and the step-by-step loading sequence.

3.6.1 Loading Program Parameters

A valid correlation of the demand with the capacity of a structure for its earthquake resistance in a laboratory loading program is possible only if the loading program is comparable to, or more severe than, the loading that might reasonably be expected under an earthquake excitation. Estimates of demands can be established through dynamic inelastic analysis of appropriate models

Derecho *et al*²² characterized the load and deformation history of the critical hinging regions in isolated structural walls subjected to strong ground motion and developed a loading program for testing specimens under slowly reversing forces simulating the earthquake loading. They observed that the maximum number of fully reversed cycles that can be reasonably expected for a strong ground motion of 20-second duration is six, with the total number of "small" and "large amplitude" inelastic cycles being ten. In more than 95% of the 170 cases analysed by Derecho *et al.*²², the structures were subjected to less than four fully reversed large amplitude cycles; the corresponding number of inelastic cycles was eight. A "fully reversed" cycle was defined as a complete cycle

in both positive and negative directions with at least one large-amplitude peak and the other peak, on reversal, of at least “moderate amplitude”. Here a “small amplitude” peak is a deformation corresponding to 0.5 or less of the corresponding maximum, while a “large-amplitude” peak is an inelastic half-cycle of deformation having a magnitude between 0.75 and 1.0 of the corresponding maximum amplitude attained and a “moderate amplitude” peak deformation between these ranges. Under dynamic conditions, the shears are more “sensitive” to the higher modes of response, and consequently, change direction much more rapidly than either moment or rotation. Thus, the commonly used test method, as was the case in this investigation, where forces and deformations are applied in-phase, represents a more severe loading condition when compared with a typical dynamic response.

3.6.2 Laboratory Loading History

The loading history used for the tests in this study, and in Malyszko's¹⁵ and Khan's¹⁶ research programs, was similar to that used by Taylor¹⁴. The procedure consists of a series of imposed deformation cycles of slowly reversed loads with progressively increasing amplitudes until failure. This method of loading is commonly used by many researchers involving seismic investigation of large size specimens under slowly reversed loads²³⁻²⁸. Figure 3.23 illustrates the loading program used for this investigation. With the exception of the first four cycles, the load history was followed as closely as possible in all four test specimens. The first four cycles illustrated in Figure 3.23 were used in tests on Specimens D1 and D2, but were changed to displacement controlled cycles to a “displacement ductility” of 1 in the tests on Specimens D3 and D4.

The intermediate “elastic” load cycles were included to observe the effect of each “inelastic” displacement amplitude cycle on the slab coupling stiffness. The 20 kN peak value for these “Cycles to 60% of the Theoretical Ultimate Load” is not equivalent to 60% of the theoretical ultimate load predicted by the yield line theory ($P_{ult} = 86.1$ kN).

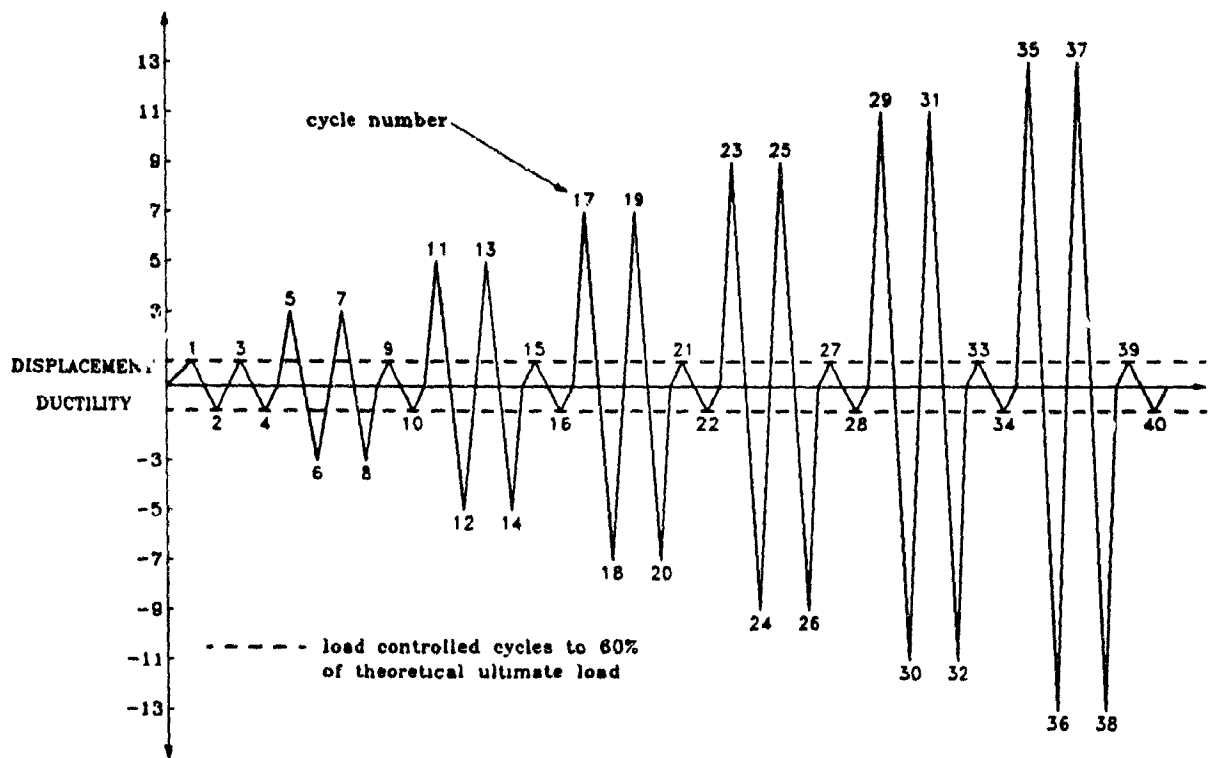


Figure 3.23 Loading History.

The vertical load equivalent to the 24 kN horizontal peak load used by Taylor¹⁴ to "60% Ultimate" was 42.8 kN. Using an elastic scale factor

$$\begin{aligned}
 S.F. &= S_E S_L^2 \\
 &= 1.0 \times 0.6672 \\
 &= 0.444
 \end{aligned}$$

the required load was therefore

$$\begin{aligned}
 P &= 0.444 \times 42.8 \text{ kN} \\
 &= 19.02 \text{ kN}
 \end{aligned}$$

Table 3.4 "Displacement Ductility of 1" During the First Excursion to Inelastic Deformation.

Specimen	Displacement
D1	1.22 mm
D2	1.34 mm
D3	4.00 mm
D4	3.37 mm

For simplicity, this value was rounded off to 20.0 kN.

The value of "displacement ductility of 1" used for all four specimens varied and was based on the observation of the significant change in the slope of the force-displacement plot during the first inelastic cycle during each test. It is, therefore, not equal to the displacement at the onset of yielding, as revealed later by the analysis of the strain data. The values of the "displacement ductility of 1" used during the testing process in all four units are summarized in Table 3.4. It was also revealed, after the complete force-displacement characteristics of all four specimens were obtained that the "displacement ductility of 1" for Specimens D1 and D2, based on the observation of the first significant change of slope of the force-displacement characteristics, should be 3.75 mm and 4.00 mm, respectively.

3.6.3 Loading Sequence

The cycles to "60% theoretical ultimate load" were load-controlled steps with each load step being approximately 4 kN (0.9 Kip), measured by the load cells under the corridor centerline. The load jack 3 was adjusted to nullify any rotation of the west wall. This was achieved by increasing or decreasing the hydraulic pressure of load jack 3 so that the travels of dial gauges C1 and C3 were equal. The readings of the load cells, the LVDT's and the strain gauges were recorded electronically onto the computer disk via the Optilog data acquisition system at each load step. The dial gauges C1, C3, C6 and C8 were recorded manually during each load step. All instruments were recorded at the peak of these cycles when the net shear force, V , equalled 20 kN.

In the unloading portion of these cycles, the load decrement rate was approximately 10 kN/step.

The following test sequence was used for each load step in the inelastic displacement controlled cycle:

- (1) The peak displacement was determined and the load jacks were adjusted to displace the west wall toe in the appropriate direction (see Figure 3.23) by approximately one tenth of the required peak displacement
- (2) The west wall rotation was nullified by adjusting the load jack 3 so as to obtain equal travels on dial gauges C1 and C3 (see Figures 3.16 and 3.22).
- (3) The load cell, LVDT and strain gauge readings were recorded electronically onto the computer disk while dial gauges C1, C3, C6 and C8 were recorded manually. (Steps 4 and 5 were performed at selected load steps and at peak of the inelastic cycle only).
- (4) All dial gauges and demec target readings were recorded manually.
- (5) Crack patterns were marked and photographed.
(Steps 1 to 5 were repeated until the peak displacement was achieved).
- (6) The pressure in load jack 1 (positive inelastic cycles) or load jack 2 (negative inelastic cycles) was reduced by about $\frac{1}{5}$ of the load jack pressure at the peak displacement
- (7) The load cell, LVDT, strain gauge, and dial gauge C1, C3, C6 and C8 readings were recorded as in Step 3. Steps 6 and 7 were repeated until all pressures on the corridor centerline load jacks were released.

3.7 Problems Encountered

The following problems were encountered during the preparation, instrumentation and testing of the specimens:

- (a) Straightening of the D3 bars was required due to warping of the bars following the heat-treatment.
- (b) Several strain gauges on the stirrup legs were damaged and lost after casting of the concrete.
- (c) Losses of several sets of data on the computer disk was encountered for several load steps in all specimens due to minor malfunctioning of the data acquisition system software.
- (d) A major malfunctioning of the Optilog data acquisition system hardware occurred at the peak load step of Cycle 35 during the test on Specimen D1. Only the LVDT readings (which are directly related to the voltage output) could be correctly recorded onto the disk. The load cell readings in the subsequent load steps of the test on Specimen D1, presented in Section 4.3, were recorded manually from the gauge pressure reading of the load jacks (converted from "psi" value). The Optilog system hardware was repaired prior to testing of Specimens D2, D3 and D4.
- (e) Electronic readings of Specimens D3 and D4 were not recorded onto computer disk during testing of these specimens, however, most of these readings were hard-printed onto paper simultaneously at each load step. As a result, some data was lost. This included the LVDT readings on lines E and F (Figure 3.16) and a few strain gauges.
- (f) Problems with resetting of the dial gauges at the extreme slab edges of Specimens D3 and D4 and the loss of data for the LVDT's on lines E and F did not enable definition of the slab deflection profiles for Specimens D3 and D4.

CHAPTER 4

EXPERIMENTAL RESULTS

The responses of the specimens tested in this study are described in this chapter.

4.1 Crack Propagation and Modes of Failure

The cracking patterns of Specimen D1 are illustrated in Figures 4.1 through 4.11. This sequence of crack formation was similar to that observed by Malyszko¹⁵ in his tests and by Taylor¹⁴ in his first test. However, the rate of crack formation was more rapid than that reported by Malyszko¹⁵ in his three tests. Also, due to presence of the drop panel, much less radial and circumferential cracks were observed at the wall toes than in Malyszko's three specimens. The sequence of crack formation for this Specimen D1 test follows.

Primary cracks along the locations where the yield lines formed, referred to as "primary cracks", first appeared near the shear wall toe area and rapidly propagated perpendicular to the centerline of the wall towards the edge of the slab as predicted by the yield line analysis. Figure 4.1 showed that the primary cracks had been fully formed in Cycle 6 at a relative vertical slab displacement Δ of 4.02 mm (a positive value for Δ denotes an upward translation of the west shear wall while a negative value denotes a downward translation of the west shear wall). The location of these cracks was influenced partially by the location of the transverse reinforcement where these

cracks occurred.

Other small cracks promptly followed behind each wall toe, initially starting out at an angle of 45° from the wall face and gradually becoming perpendicular to the wall centerline as they progressed towards the edge of the slab, forming the "secondary cracks". These cracks were denoted as "secondary cracks" because of the smaller rotations compared with those at the primary crack locations. Some cracks, however, appeared directly and perpendicularly from the wall face due to the presence of transverse reinforcement at those locations. Diagonal cracks, forming as the last set of cracks at Cycle 6, appeared near the wall toe and propagated at an angle of approximately 45° from the wall centerline across the slab corridor width and ended at the primary crack on the opposite side of the corridor. Figure 4.2 shows the appearance of the primary cracks, secondary cracks and the diagonal crack at the peak of Cycle 12 (Relative Vertical Displacement of slab at wall toes, $\Delta = 4.91$ mm).

At subsequent larger imposed relative vertical displacements, more secondary cracks formed behind the wall toes in a manner similar to the first secondary crack. The diagonal cracks, which formed in Cycle 6, emanated from the corners of the wall toes as more cracks near the wall toes appeared in Cycle 24, as illustrated in Figure 4.3. Secondary diagonal cracks also appeared at about one corridor width from the wall toes (near the ends of the initial diagonal cracks) at the primary cracks and propagated toward the opposite primary crack near the edge of the slab. Concurrently, cracks parallel to the shear wall centerline and midway between the shear wall centerline and the edge of the slab ($\frac{1}{4}$ bay width) appeared from and behind the primary cracks. Figure 4.3 shows the extent of these cracks at the peak of Cycle 24 ($\Delta = 8.61$ mm). Similar crack patterns were observed on the top of the slab on the south side and on the underside of the slab, as shown in Figures 4.6 and 4.7. Figure 4.8 shows the crack pattern at the onset of crushing at the peak of Cycle 29 ($\Delta = 9.58$ mm) near the wall toe areas. The absence of radial cracks at this stage is noted, and no prominent signs of punching

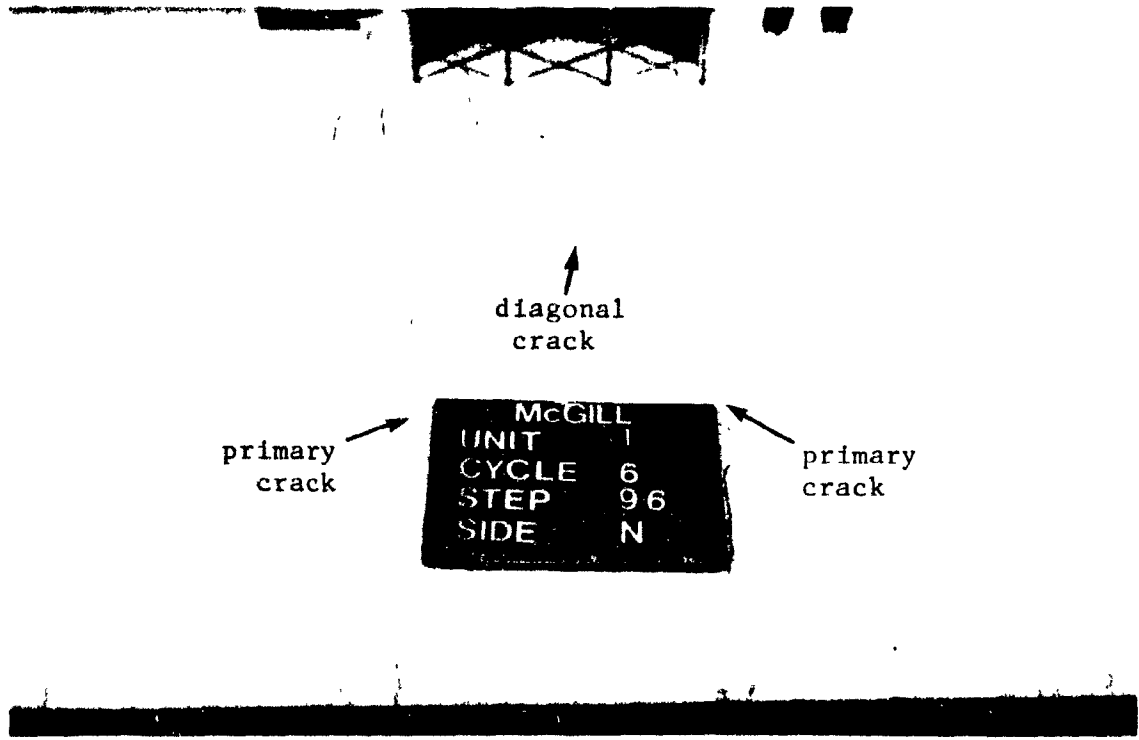


Figure 4.1 Crack Pattern for Specimen D1 at Cycle 6, $\Delta = -4.02$ mm.

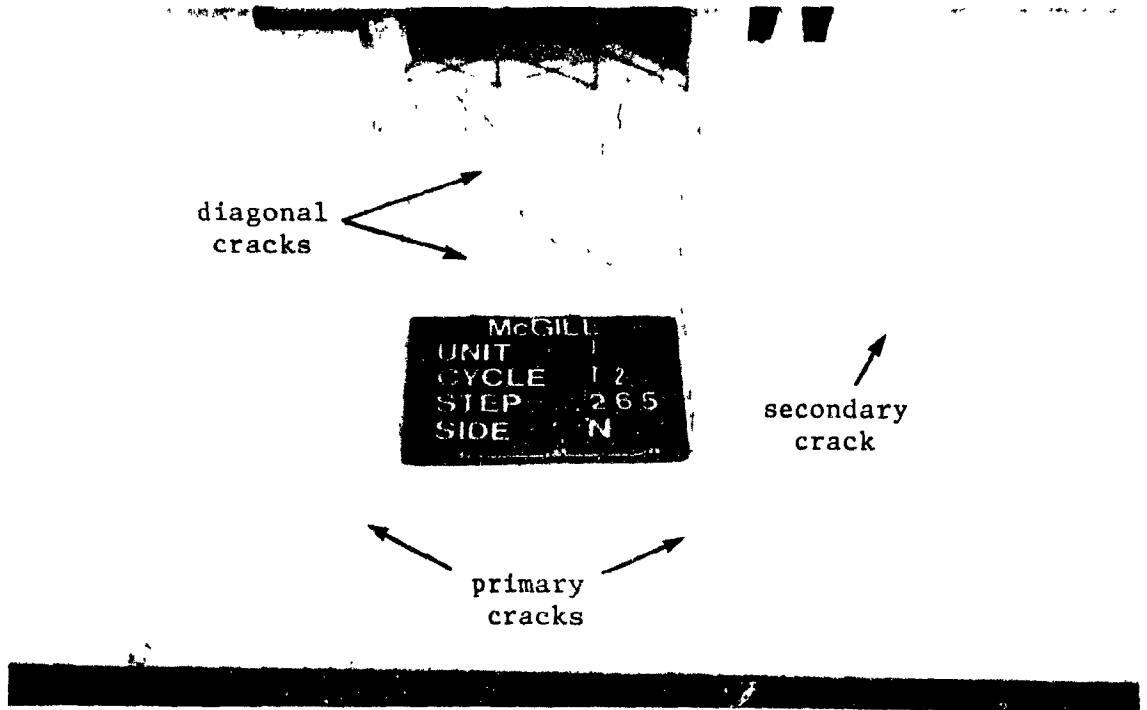


Figure 4.2 Crack Pattern for Specimen D1 at Cycle 12, $\Delta = -4.91$ mm.

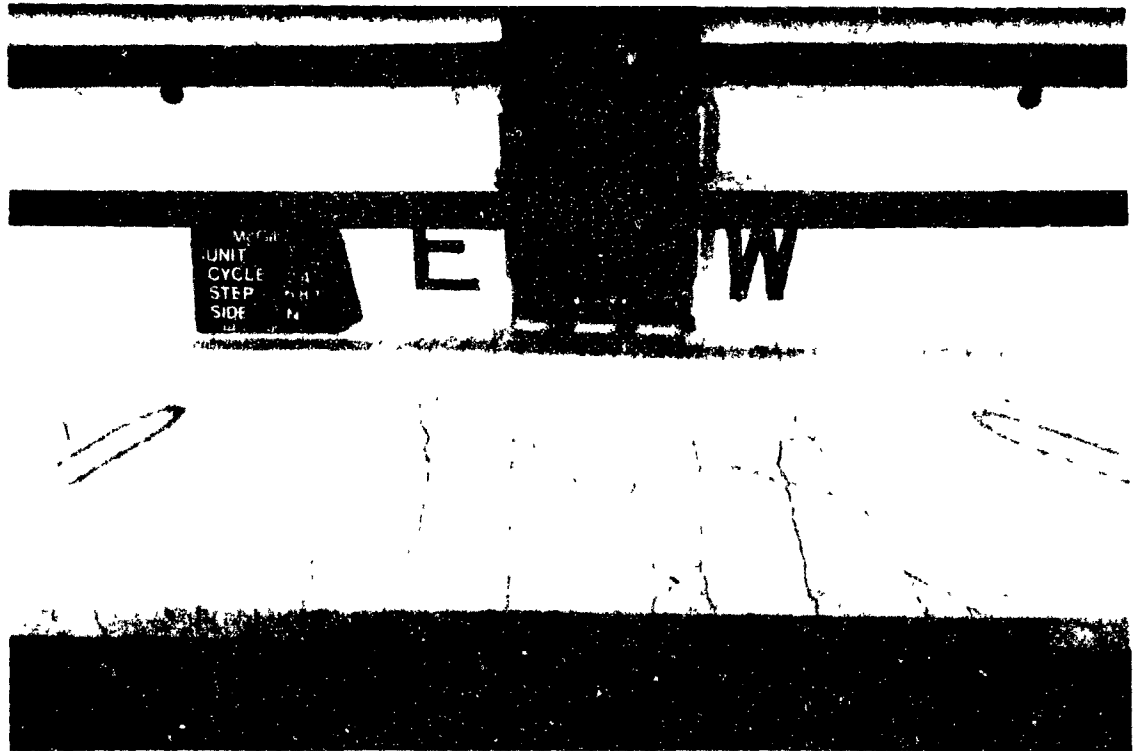


Figure 4.3 Crack Pattern for Specimen D1 at Cycle 24, $\Delta = 8.61$ mm

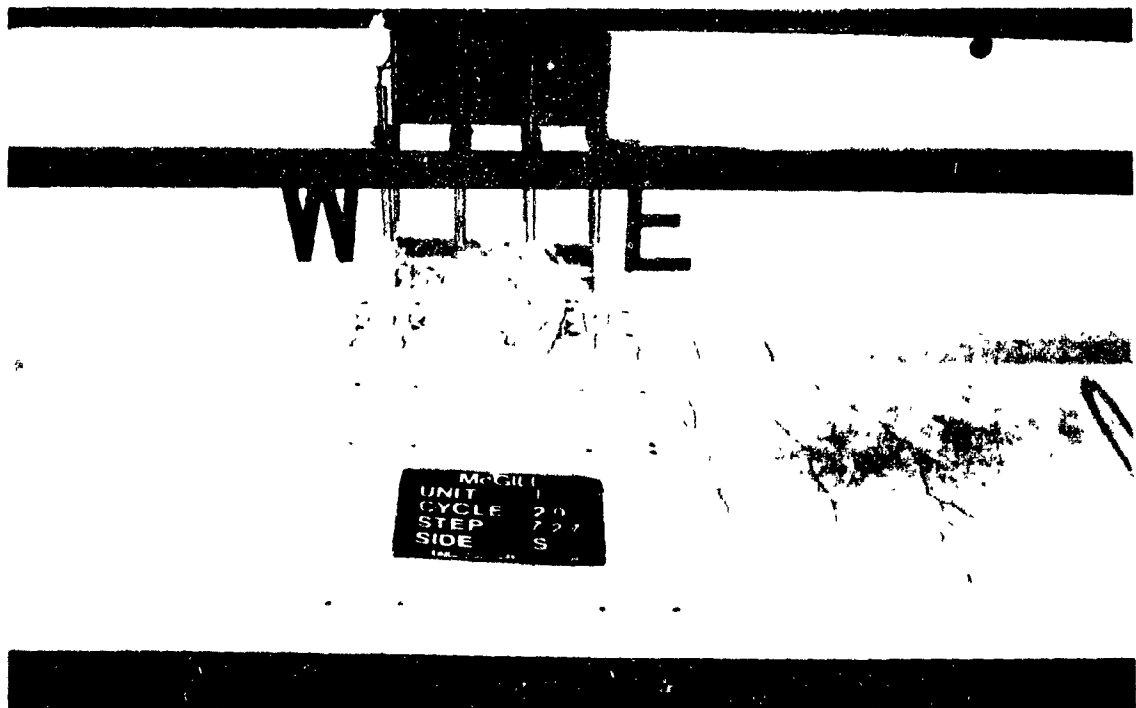


Figure 4.4 Crack Pattern for Specimen D1 at Cycle 29, $\Delta = 9.58$ mm.

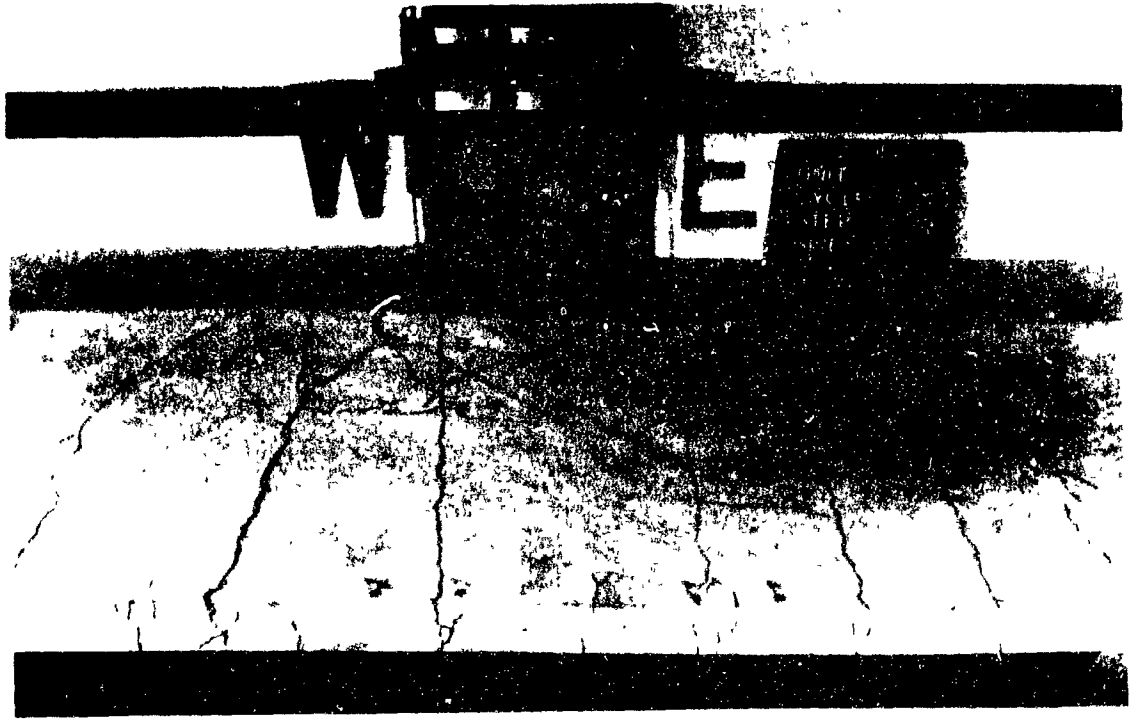


Figure 4.5 Crack Pattern for Specimen D1 at the Onset of Punching Shear Failure.



Figure 4.6 Crack Pattern on the Underside for Specimen D1 at Cycle 24. $\Delta = -8.61$ mm

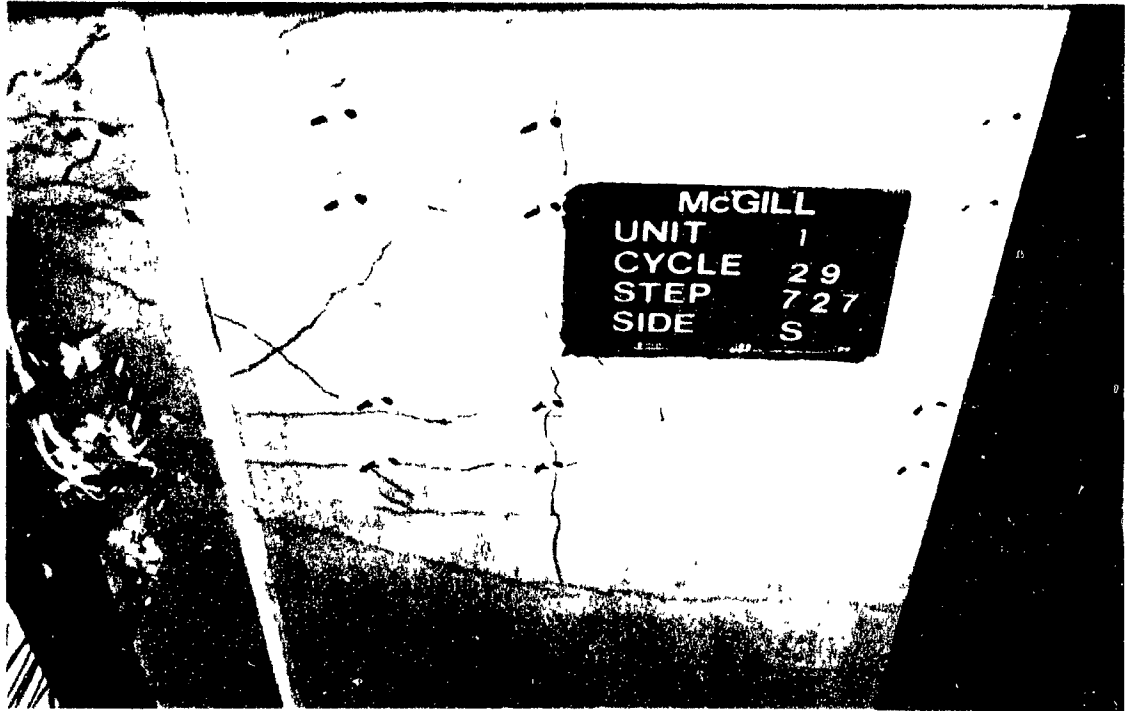


Figure 4.7 Crack Pattern on the Underside for Specimen D1 at Cycle 29, $\Delta = 9.58$ mm

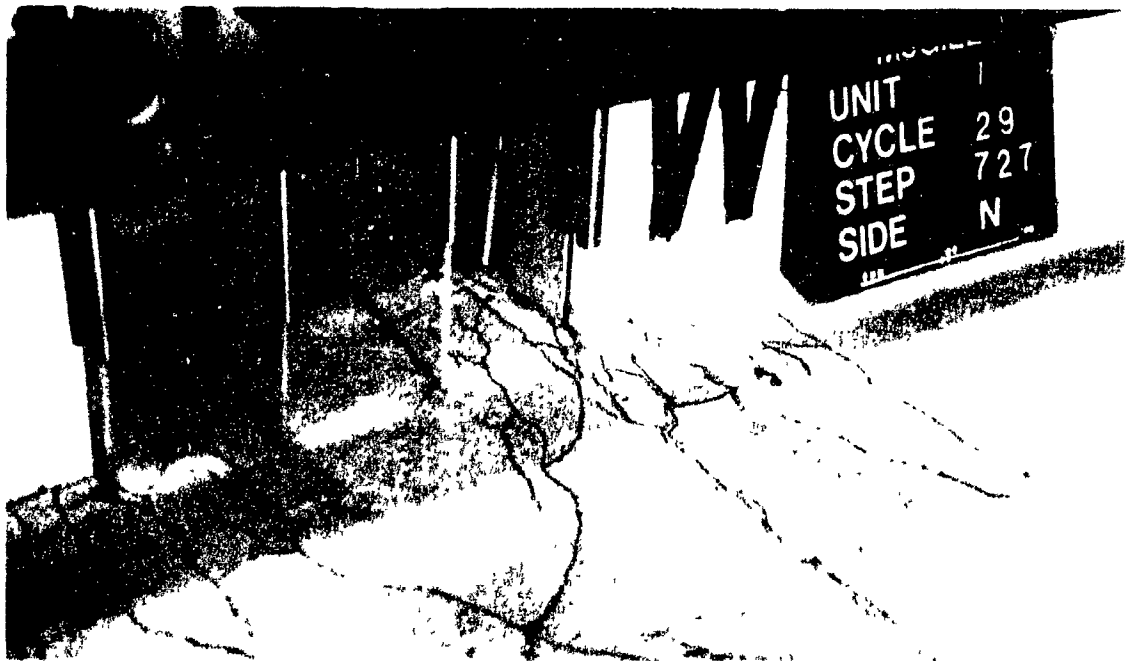


Figure 4.8 Close Up View on the Crack Patterns for Specimen D1 Near the Wall Toes at Cycle 29, $\Delta = 9.58$ mm.

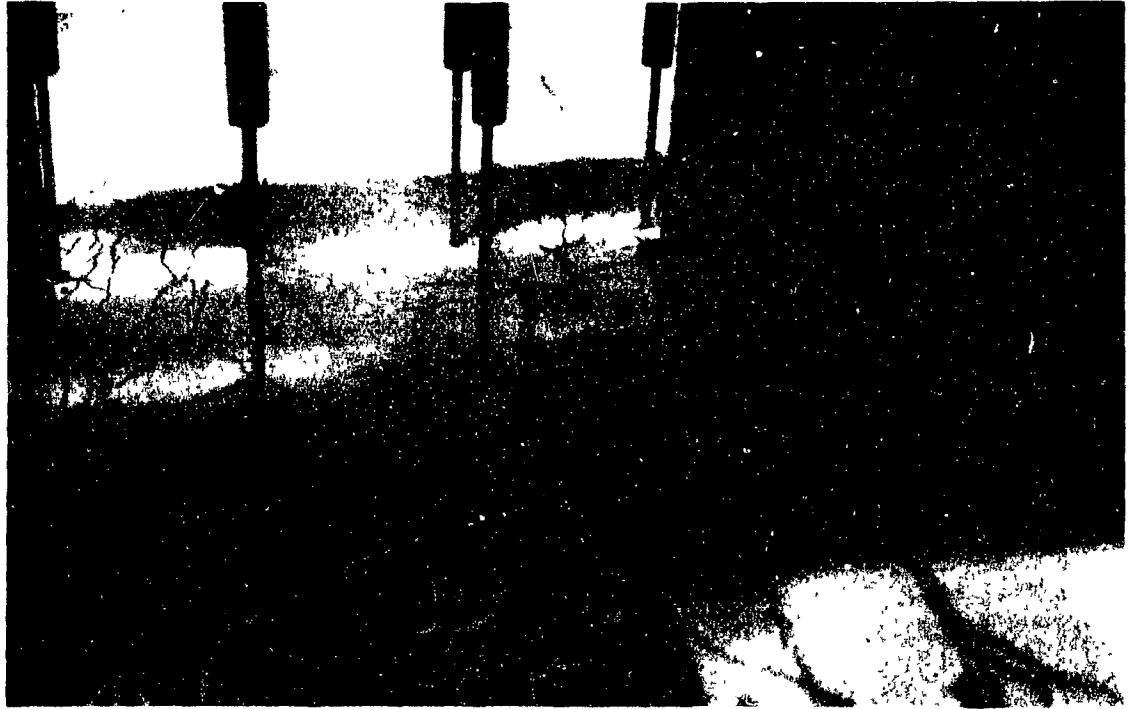


Figure 4.9 Crack Pattern for Specimen D1 Near the Wall Toes at Failure.

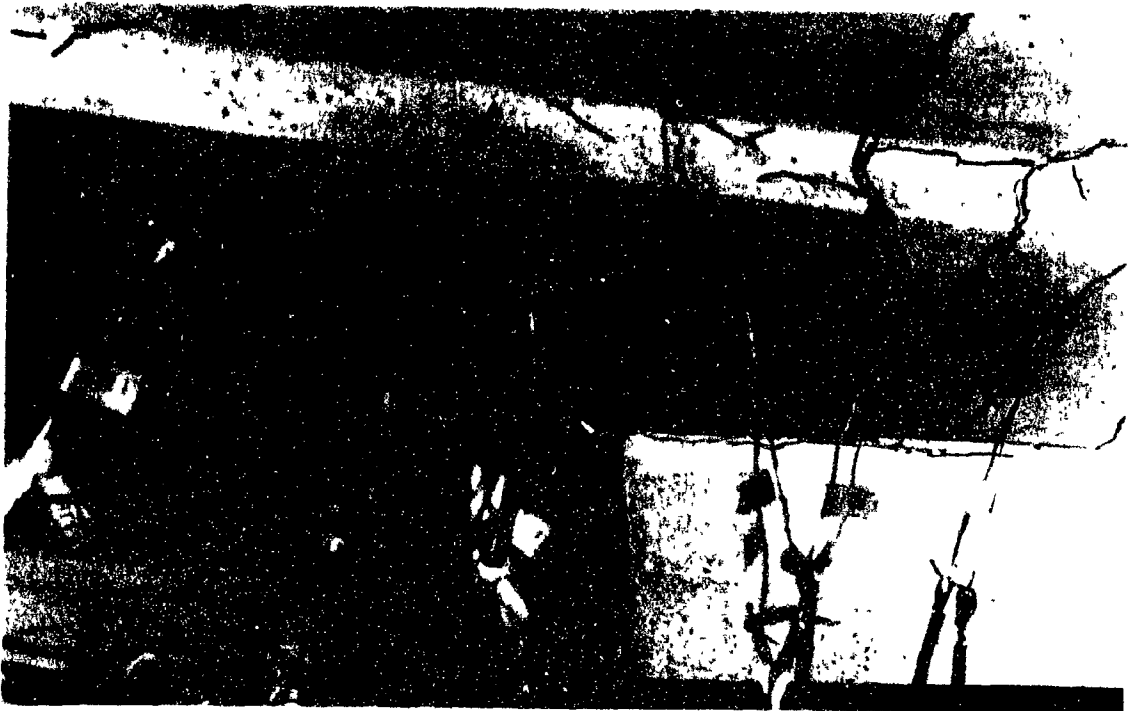


Figure 4.10 Close Up View of the Underside for Specimen D1 Near the Wall Toe Region at Failure (South-East side)

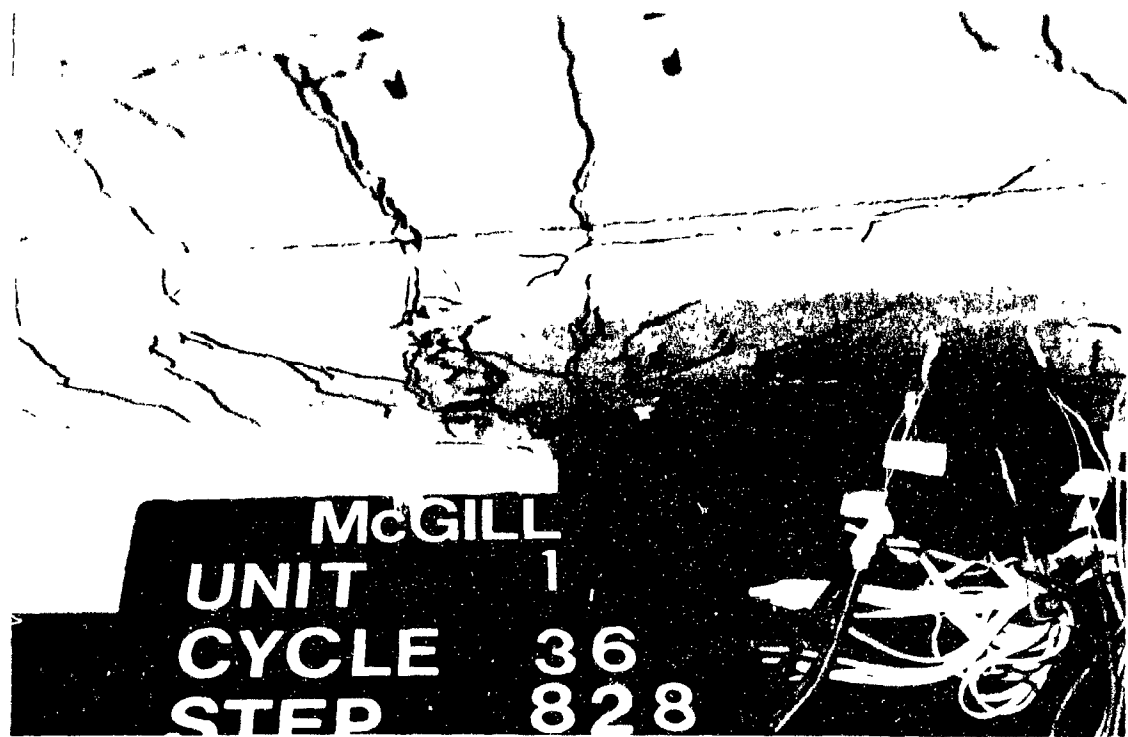


Figure 4.11 Close Up View of the Underside for Specimen D1 Near the Wall Toe Region at Failure (South-West side).

shear can be observed. As indicated in Figure 4.5, punching shear failure occurred in Cycle 35 ($\Delta = 11.19$ mm) with severe distress at the wall toes due to the crushing of the concrete. Closing of the punching shear crack formed in Cycle 35 was observed in Cycle 36. A new punching shear crack was observed near the east wall toe as indicated in Figure 4.9 along with the formation of some radial cracks. Crack patterns on the underside of the slab near the wall toe regions at failure showed higher level of distress, as illustrated in Figure 4.10 and 4.11. More radial cracks and pronounced spalling of concrete at the primary cracks within the drop panel were observed on the underside of the slab in comparison with the crack pattern on top of the slab.

Figures 4.12 through 4.23 shows the sequence of crack formation of Specimen D2. The crack formation on the east side of the corridor centerline were similar to that of Specimen D1 with two notable exceptions. The cracks in Specimen D2 formed at a faster rate than those in Specimen D1, and more cracks were observed near the wall

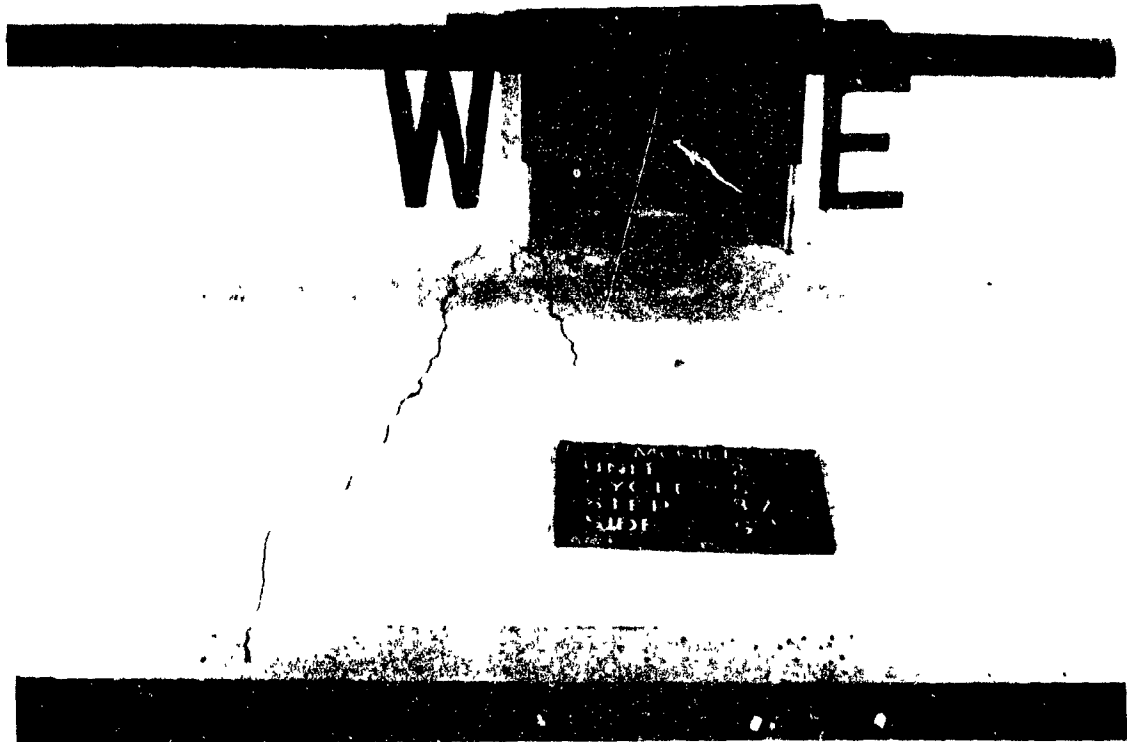


Figure 4.12 Crack Pattern for Specimen D2 at Cycle 5, $\Delta = 1.67$ mm.

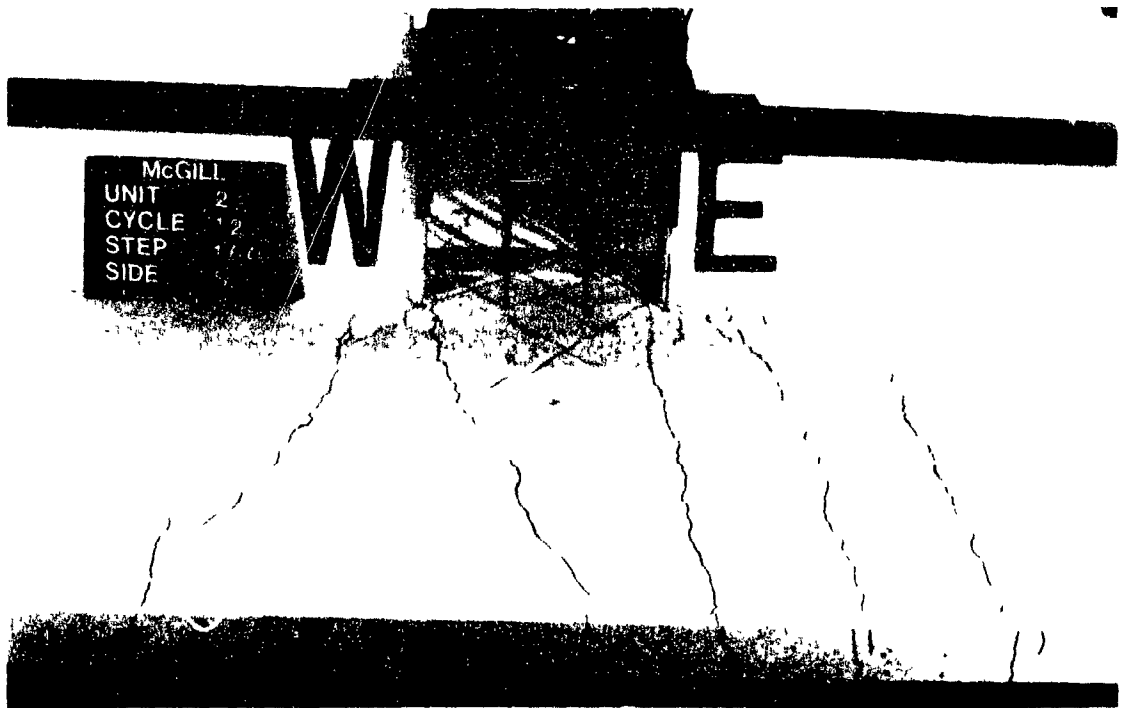


Figure 4.13 Crack Pattern for Specimen D2 at Cycle 12, $\Delta = -5.09$ mm.

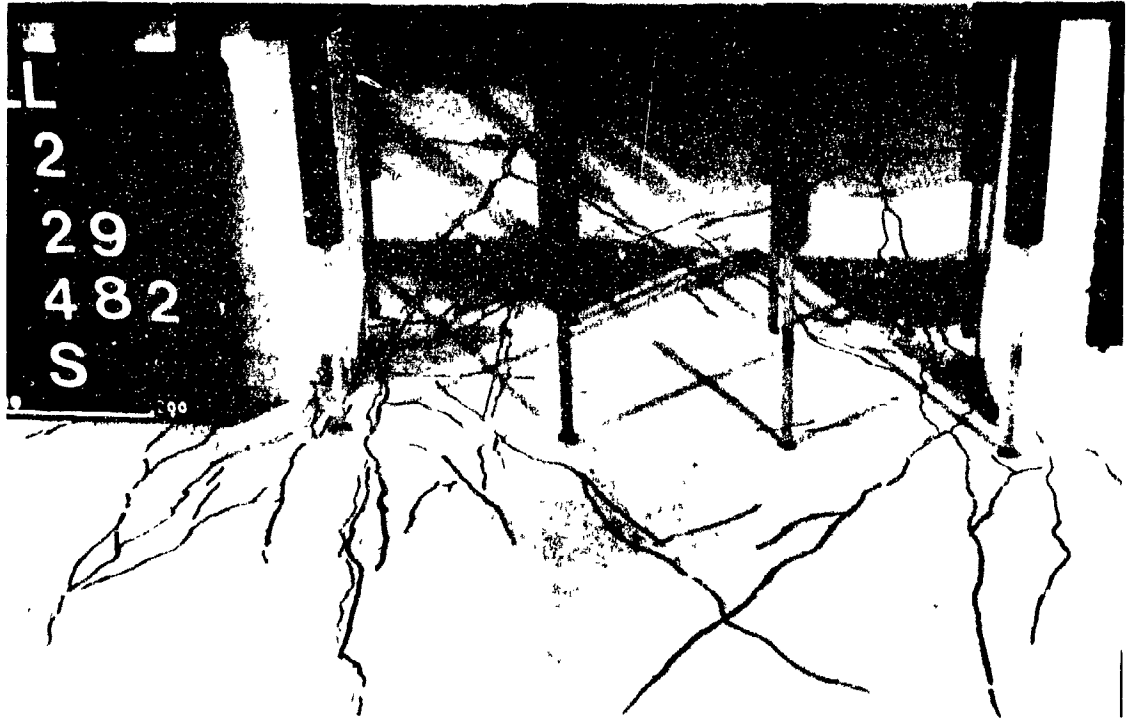


Figure 4.14 Close Up View of Crack Pattern in Specimen D2 Near the Shear Wall Toes at Onset of Punching Shear Failure.

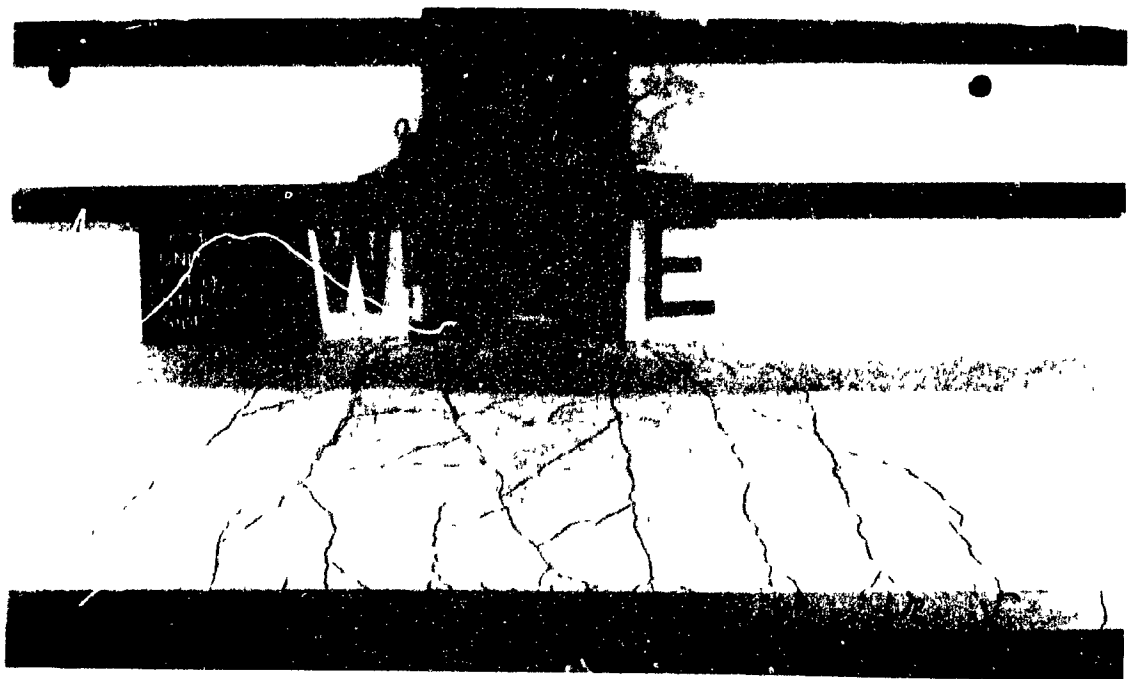


Figure 4.15 Crack Pattern for Specimen D2 at Cycle 31, $\Delta = 14.73$ mm.



Figure 4.16 Close Up View for Specimen D2 Near the Wall Toes at Failure ($\Delta = 18.07$ mm)

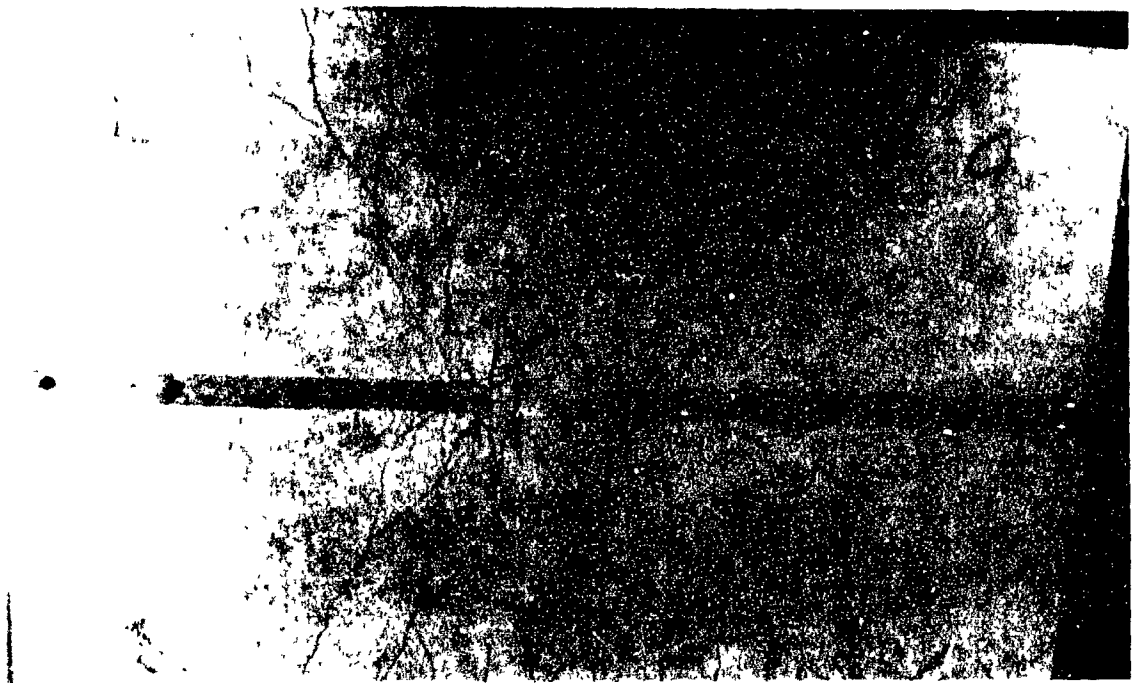


Figure 4.17 Plan View of the Crack Pattern for Specimen D2 at Failure.



Figure 4.18 Close Up Top View for Specimen D2 Near the West Wall Toe After Failure.

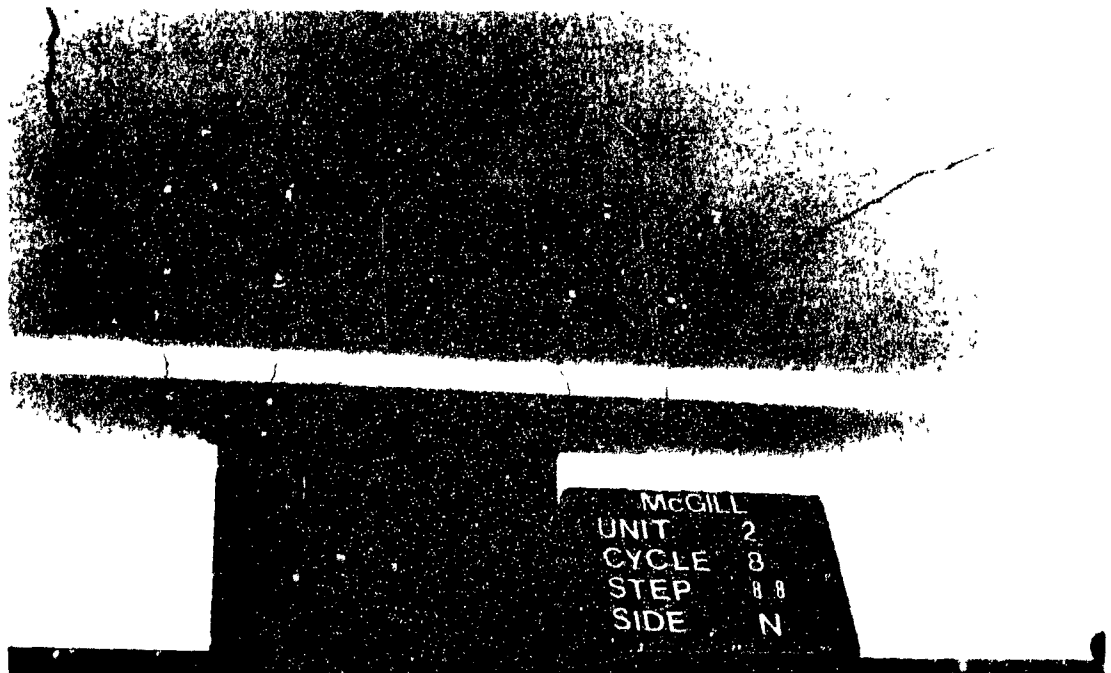


Figure 4.19 Crack Pattern on the Underside for Specimen D2 at Cycle 8. $\Delta = -1.62$ mm.

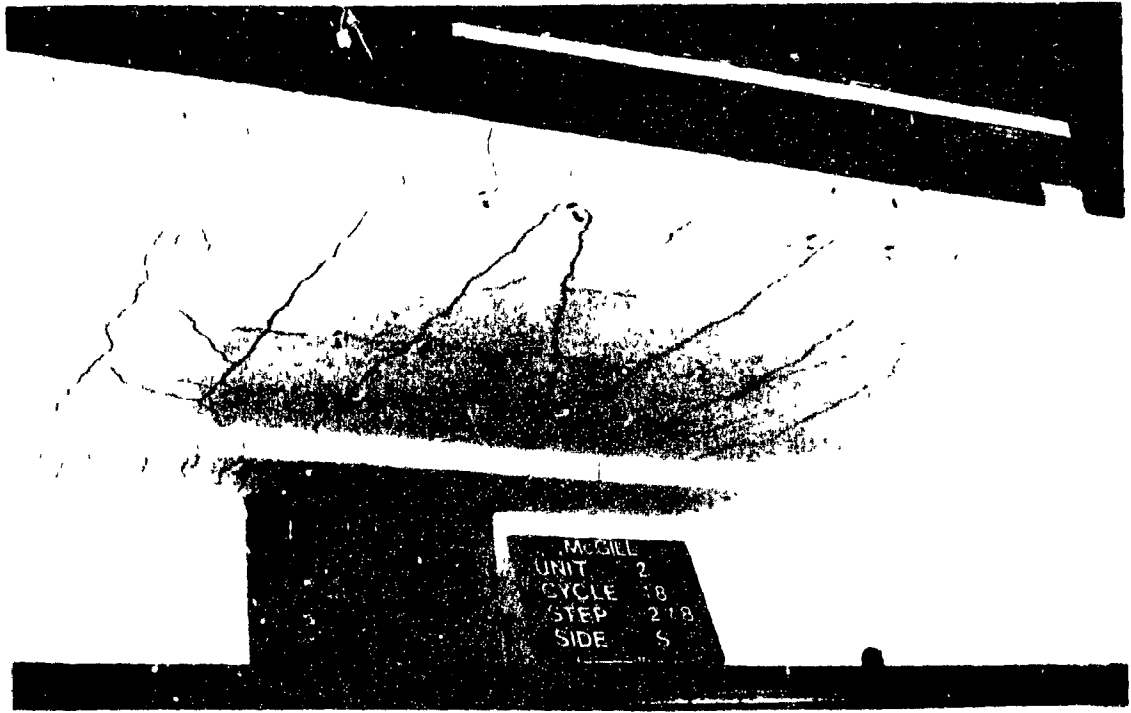


Figure 4.20 Crack Pattern on the Underside for Specimen D2 at Cycle 18. $\Delta = -8.26$ mm



Figure 4.21 Close Up View of Drop Panel for Specimen D2 at Onset of Punching Shear Failure

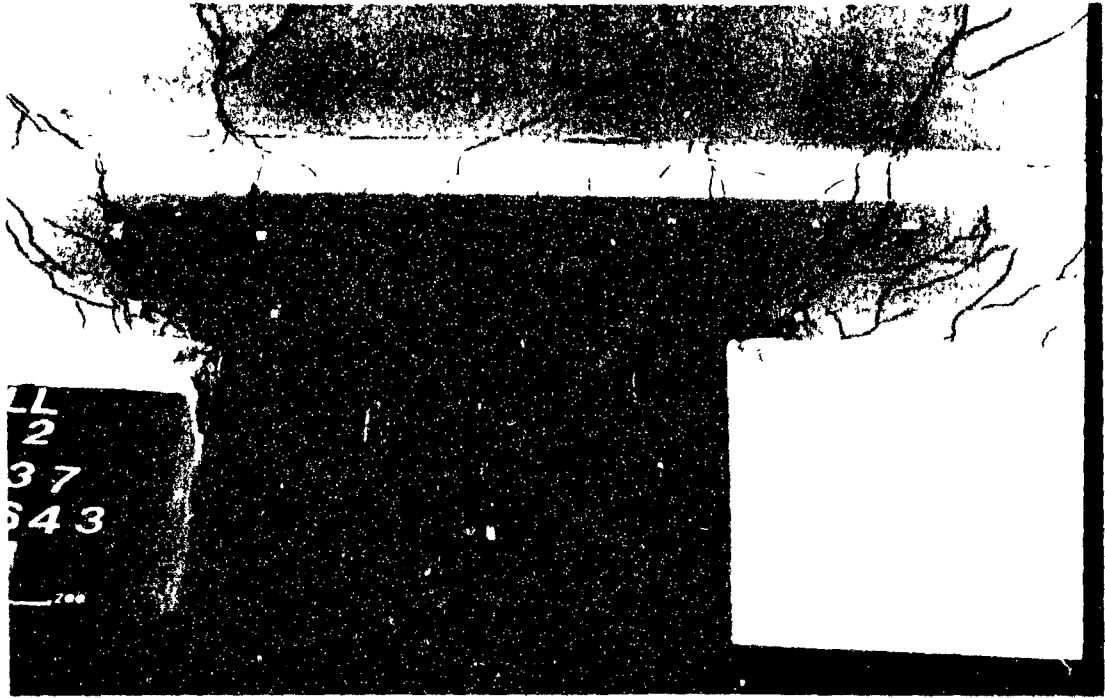


Figure 4.22 Close Up View of Drop Panel for Specimen D2 at Cycle 37, $\Delta = 18.07$ mm



Figure 4.23 Close Up Bottom View for Specimen D2 Near the Wall Toe Regions After Failure

toe regions in Specimen D2.

Like all the other test specimens, the first appearance of crack in Specimen D2 occurred at the face of the wall toe. However, this crack propagated parabolically and extended about one corridor width away from the west wall toe at the peak of Cycle 5 ($\Delta = 1.67$ mm). Meanwhile, a crack about 85 mm behind the west wall toe face appeared at an angle of 45° from the shear wall centerline. This angle increased rapidly to about 80° and extended towards the edge of the slab where it became perpendicular to the shear wall centerline. As in Specimen D1, this crack near the edge of the slab was influenced by the placement of the transverse reinforcement. The crack pattern at Cycle 5 ($\Delta = 1.67$ mm) is shown in Figure 4.12. A more familiar crack pattern on the slab on the east side of the corridor centerline was observed in Cycle 12 ($\Delta = 5.09$ mm) as shown in Figure 4.13. This crack pattern was similar to that observed in Specimen D1. The secondary and diagonal cracks formed at this displacement level. Figure 4.14 shows the appearance of radial cracks at Cycle 28, ($\Delta = 11.54$ mm). Onset of punching shear was observed in Cycle 29 ($\Delta = 14.89$ mm) as illustrated in Figure 4.14. No significant crushing of concrete was observed at this displacement level. Extensive radial cracks near the wall toe areas developed prior to failure of the slab, caused by punching shear and crushing of the concrete near these areas, as illustrated in Figures 4.16 through 4.18 and Figures 4.21 through 4.23. Figures 4.18 and 4.23 show that the punching shear cracks were located at a distance of approximately one effective depth ($d = 82$ mm) from the wall toes. Similar crack pattern was observed on the bottom face of the slab, as illustrated in Figures 4.19 through 4.23.

The crack formation in Specimen D3 was, in general, similar to that of Specimens D1 and D2. As expected, the secondary cracks that developed in Cycle 5 ($\Delta = 12.30$ mm, Figure 4.25) were influenced by the concentrated transverse reinforcement. Figures 4.24 to 4.29 illustrate the sequence of crack formation for Specimen D3. Punching of the slab at the wall toe was preceded by the formation of radial

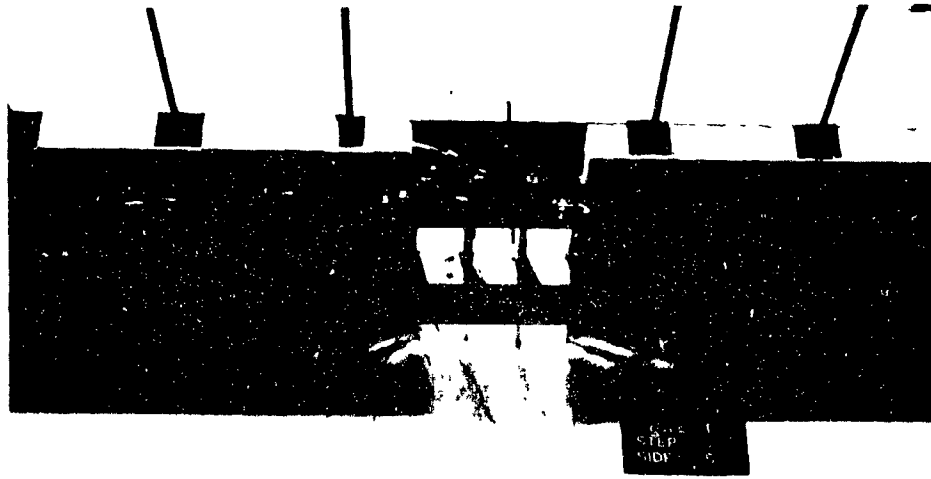


Figure 4.24 Crack Pattern for Specimen D3 at Cycle 1, $\Delta = 3.12$ mm.

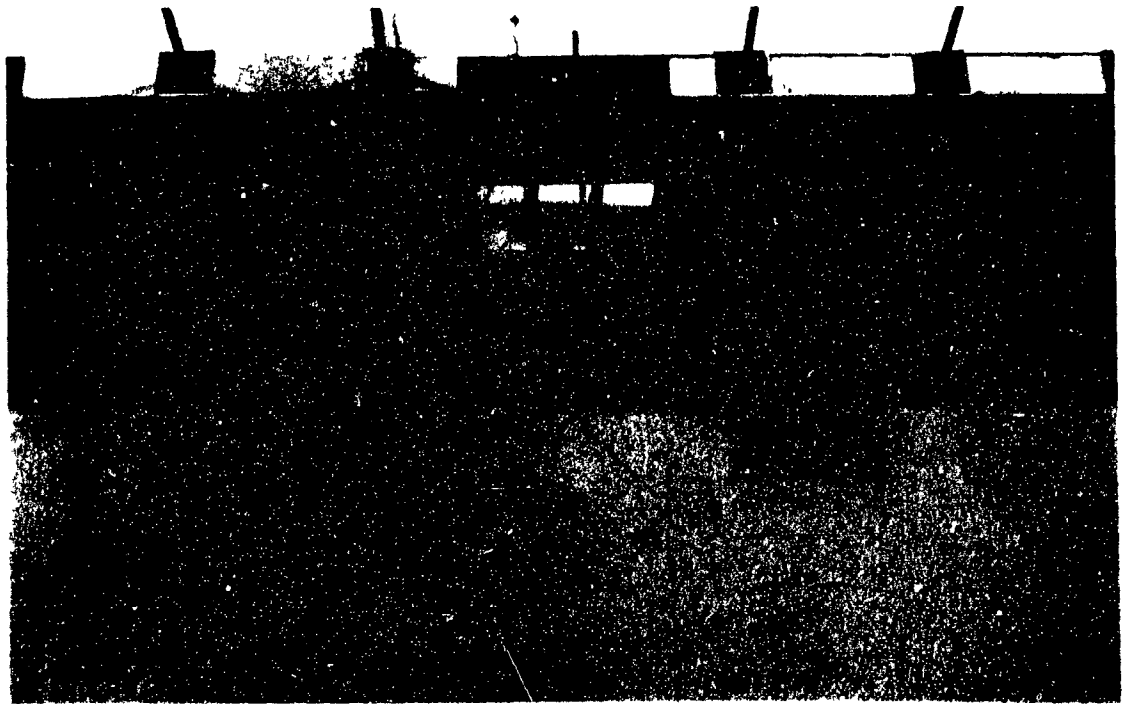


Figure 4.25 Crack Pattern for Specimen D3 at Cycle 5, $\Delta = 12.30$ mm

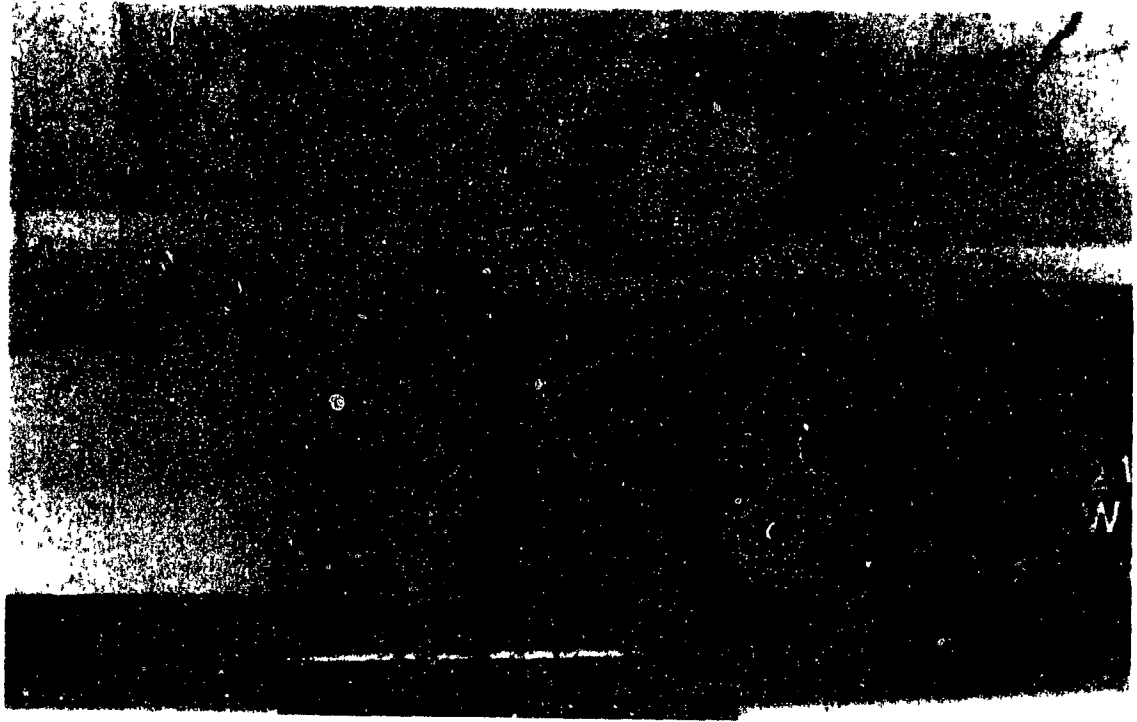


Figure 4.26 Crack Pattern on the Drop Panel for Specimen D3 at Cycle 14, $\Delta = -19.30$ mm

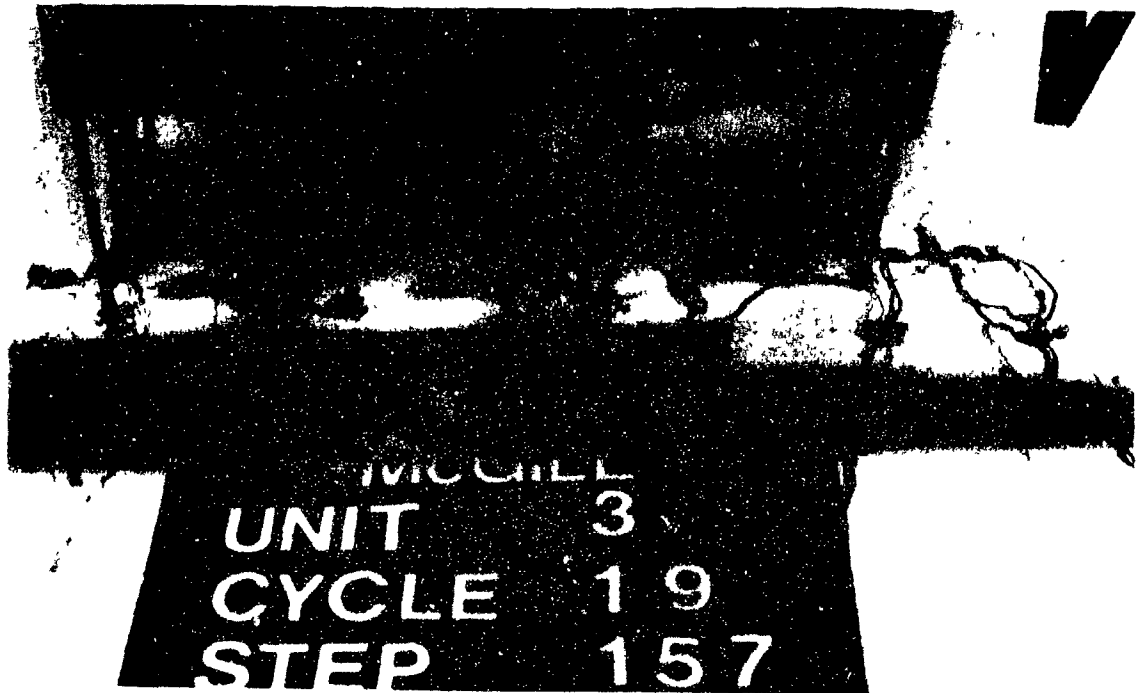


Figure 4.27 Close Up View for Specimen D3 Near the Wall Toes at Onset of Punching Shear Failure ($\Delta = 27.99$ mm)

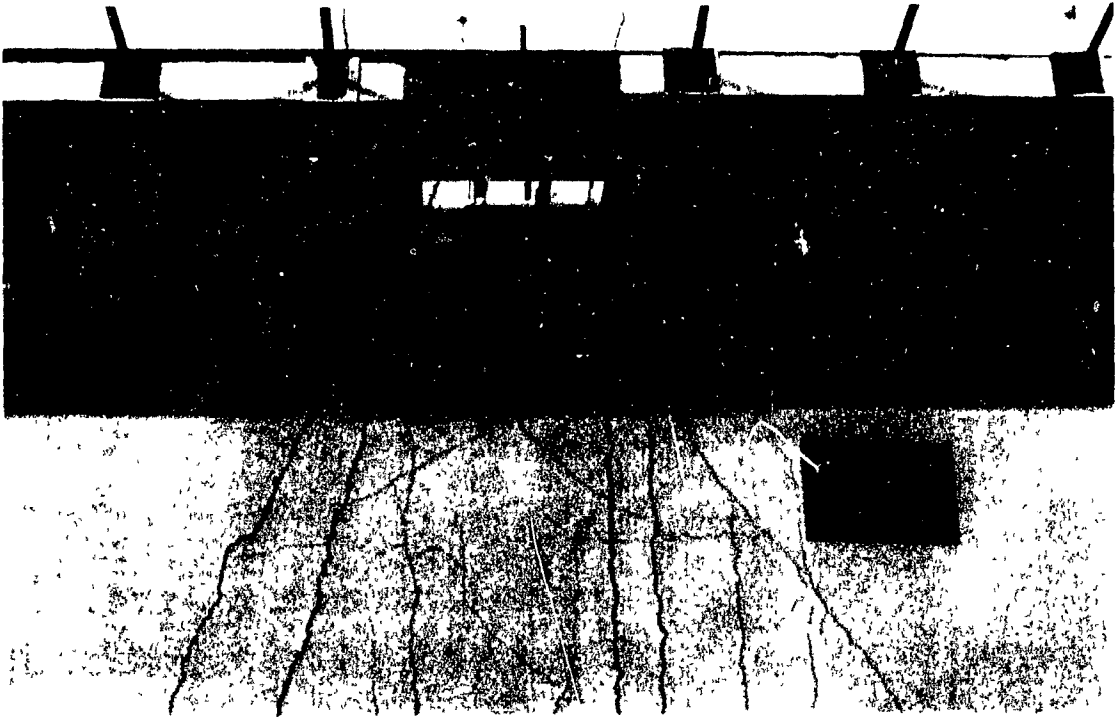


Figure 4.28 Crack Pattern for Specimen D3 at Cycle 20, $\Delta = -26.85$ mm.

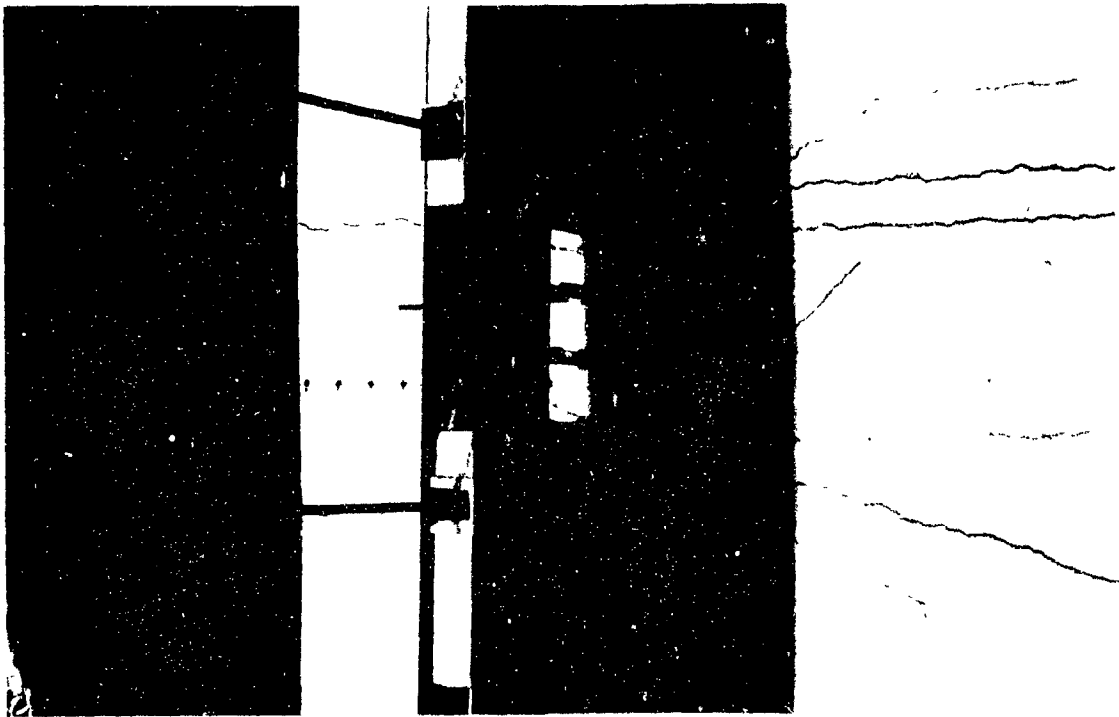


Figure 4.29 Crack Pattern for Specimen D3 at Failure ($\Delta = -34.70$ mm).

cracks as illustrated in Figure 4.27. Spalling of the concrete wall at the wall toe regions was observed, as shown in Figures 4.26 and 4.27, with relatively little crushing of the slab concrete in these areas. Much less cracking was observed in Specimen D3 than in Specimens D1 and D2, particularly on the underside of the drop panel near the wall toe areas.

The sequence of crack formation in Specimen D4 is illustrated in Figures 4.30 to 4.36. In general, these crack patterns were similar to all three specimens described earlier. Signs of punching shear on Specimen D4 slab appear in Cycle 20 on the bottom face of the drop panel at a displacement level of -19.05 mm, much lower than that observed in Specimen D3. However this displacement level is still larger than the displacement at which the onset of punching shear was observed in Specimen D1 or D2. Figure 4.34 shows the crack pattern on the underside of the drop panel of Specimen D4 at the onset of punching shear. Unlike Specimen D3 however, little distress was observed on the top face of the slab near the wall toe areas in Specimen D4. At failure caused by punching and crushing of the slab concrete at the wall toes, extensive crushing of the slab concrete at the wall toes had taken place with similar distress on the wall concrete in the immediate vicinity, as illustrated in Figure 4.36. With the exception of some crushing of the slab concrete near the wall toe, and the distribution of radial cracks emanating from the wall toes, no other severe distress was observed on the top of the slab.

4.2 Force-Displacement Results

The net shear force (V) plotted against the relative vertical wall toe-slab displacement constitute the force-displacement diagrams shown in Figures 4.37 through 4.40.

The displacement corresponding to the general yielding of the slab, as indicated by the first significant change of slope of the force-displacement characteristics, was taken as the yield displacement or the displacement corresponding to the "displacement

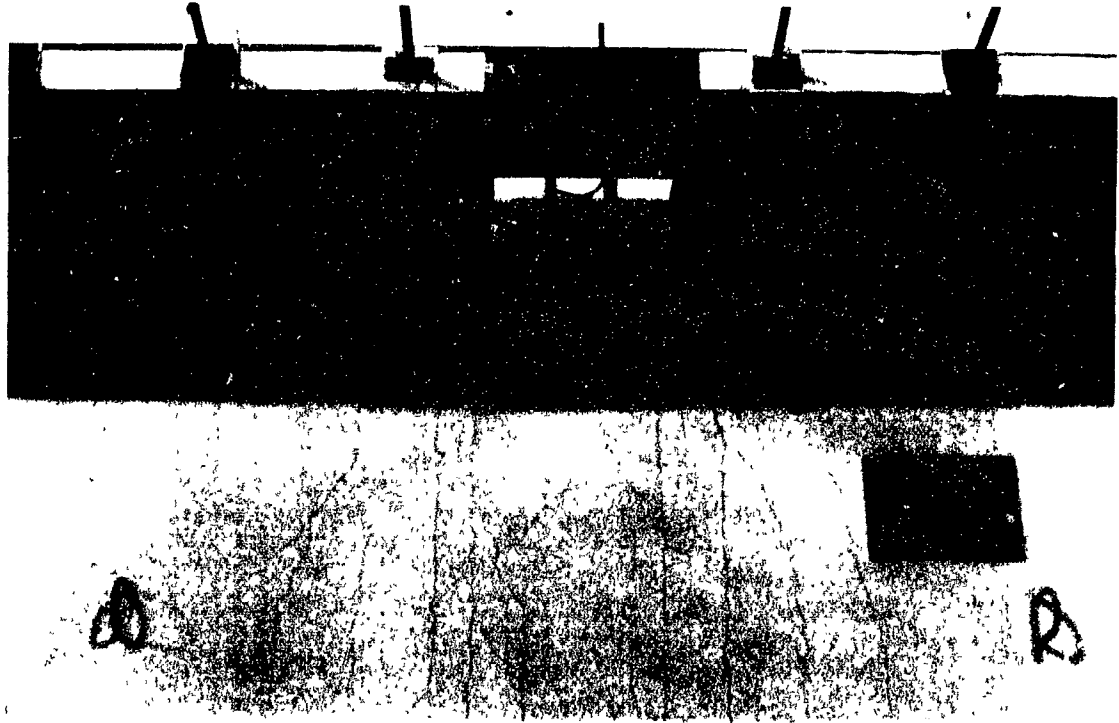


Figure 4.30 Crack Pattern for Specimen D1 at Cycle 8, $\Delta = -7.98$ mm.

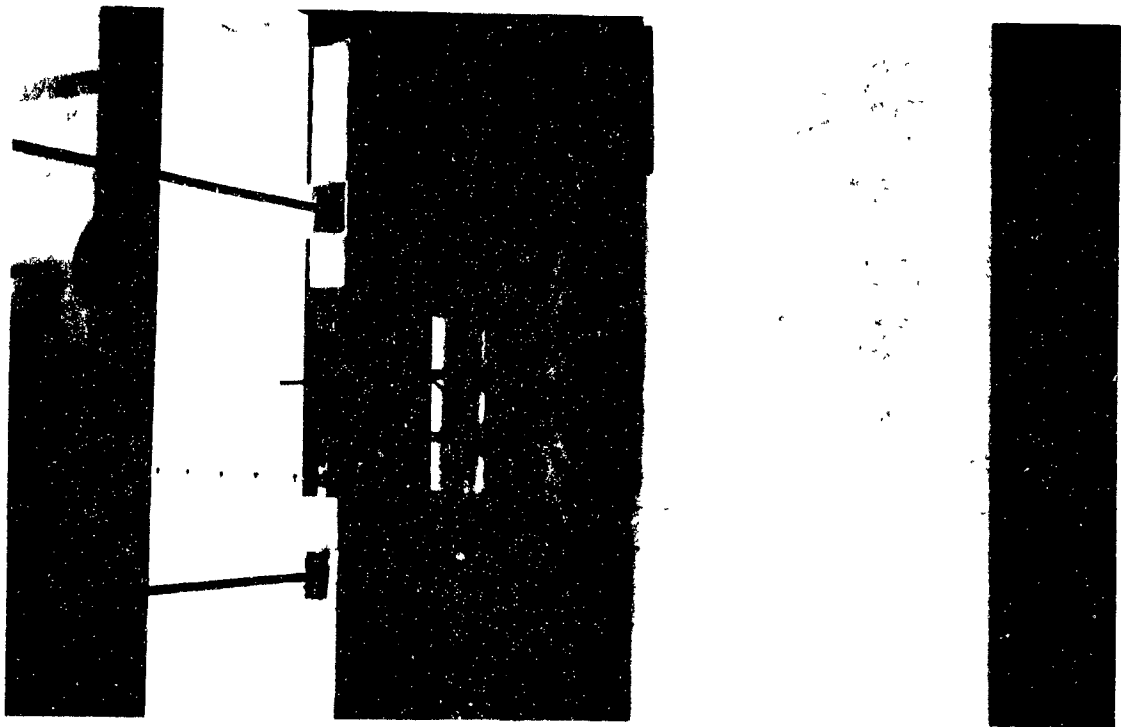


Figure 4.31 Crack Pattern for Specimen D4 at Cycle 13, $\Delta = 13.25$ mm

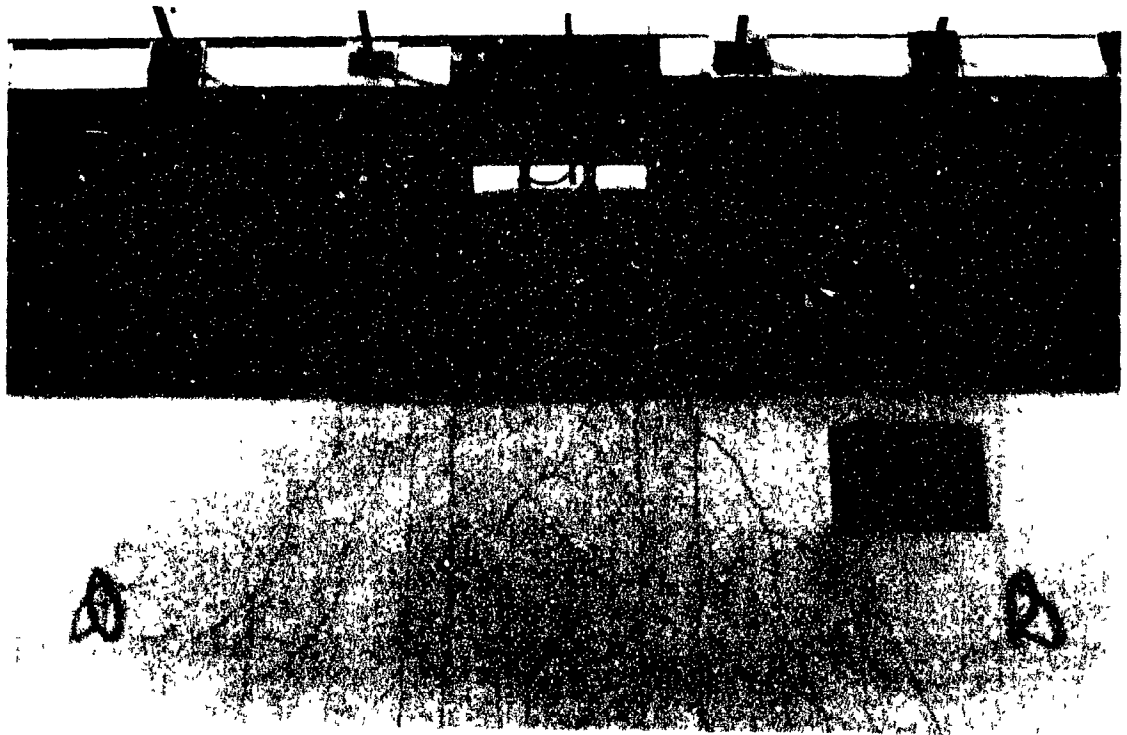


Figure 4.32 Crack Pattern for Specimen D4 at Cycle 20, $\Delta = -19.05$ mm.

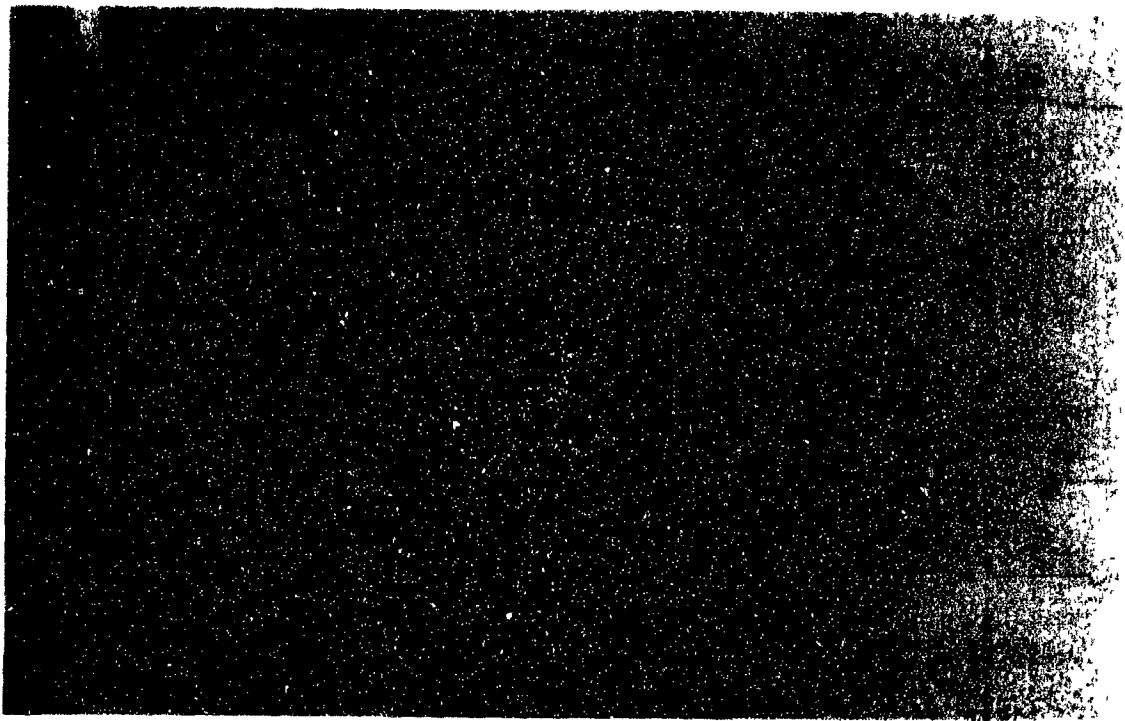


Figure 4.33 Crack Pattern on the Underside for Specimen D4 at Cycle 4, $\Delta = -2.58$ mm

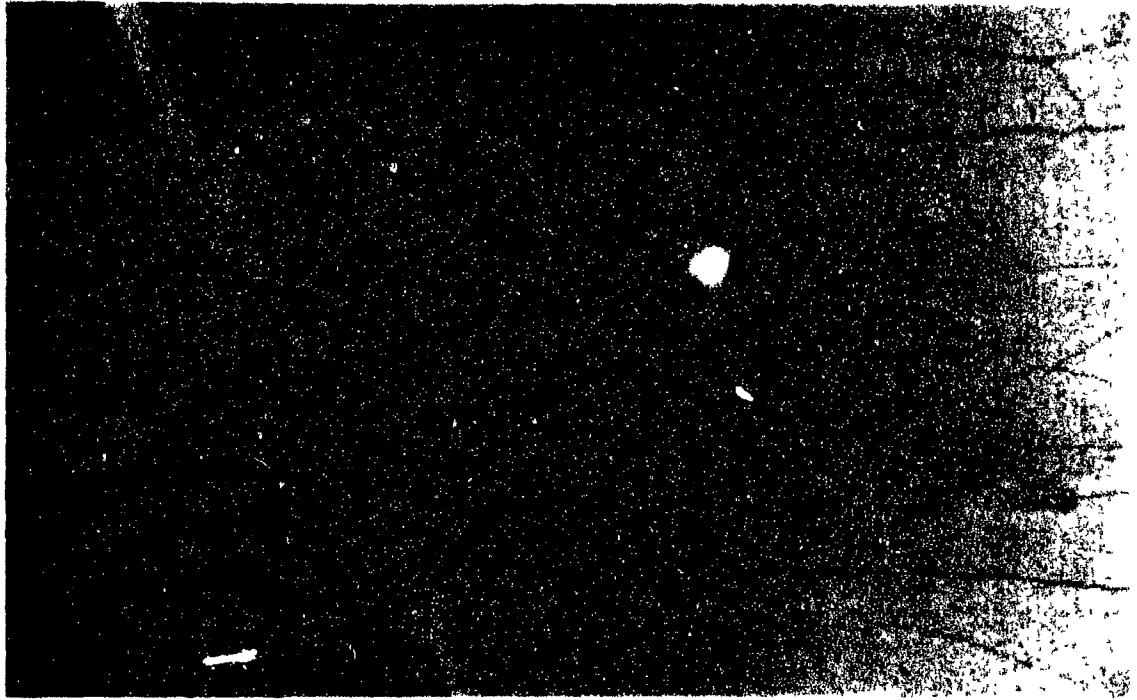


Figure 4.34 Crack Pattern on the Underside for Specimen D1 at Onset of Punching Shear Failure ($\Delta = -19.05$ mm)

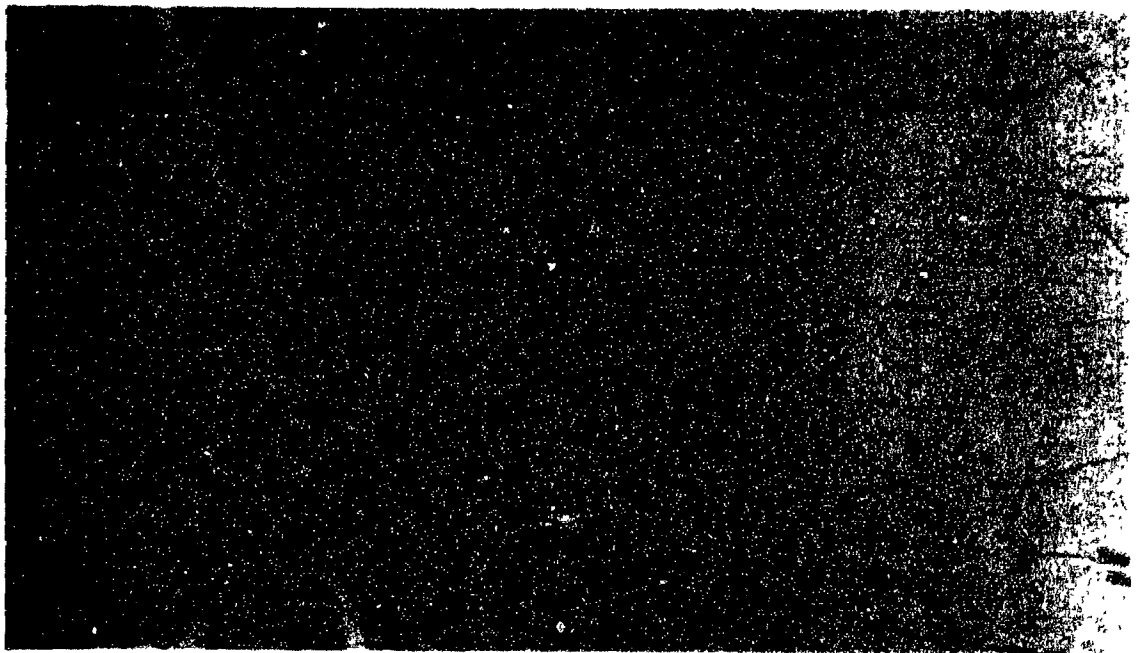


Figure 4.35 Crack Pattern on the Underside for Specimen D1 at Cycle 26, $\Delta = -23.77$ mm

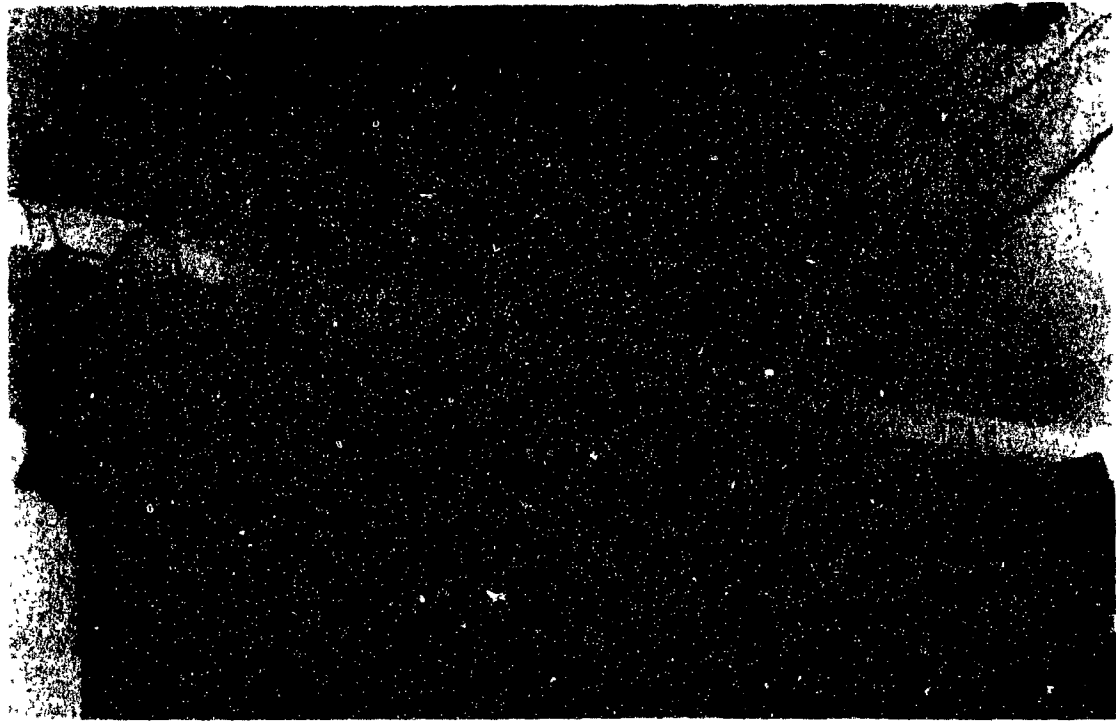


Figure 4.36 Punching and Crushing of Concrete Slab for Specimen D4 at Failure ($\Delta = -28.86$ mm)

ductility ratio" of one. It is noted that this displacement ductility ratio of one is not the displacement at the onset of yielding on which the usual definition of ductility is based. The displacement ductility ratio of one for the four specimens were 3.75 mm, 4.0 mm, 4.0 mm and 3.75 mm, respectively. For the purpose of comparison, the average of these values, $\Delta = 3.88$ mm, was taken as the yield displacement ($\mu = 1$). It was observed from the strain results of Specimens D1 and D2, described in the later sections of this chapter, that at this displacement level ($\mu = 1$), most of the slab's longitudinal reinforcement had yielded.

The ultimate load achieved by the first three specimens, Specimens D1, D2 and D3, were 93.81 kN, 86.50 kN and 90.51 kN, respectively. Specimen D4 exhibited a marked increase in the maximum load achieved (107.18 kN) over the other three specimens. These loads were achieved at displacement levels of -6.25 mm ($\mu = -1.61$), -11.65 mm ($\mu = -3.01$), -11.18 mm ($\mu = -2.89$) and 13.45 mm ($\mu = 3.47$) for Specimens D1, D2, D3

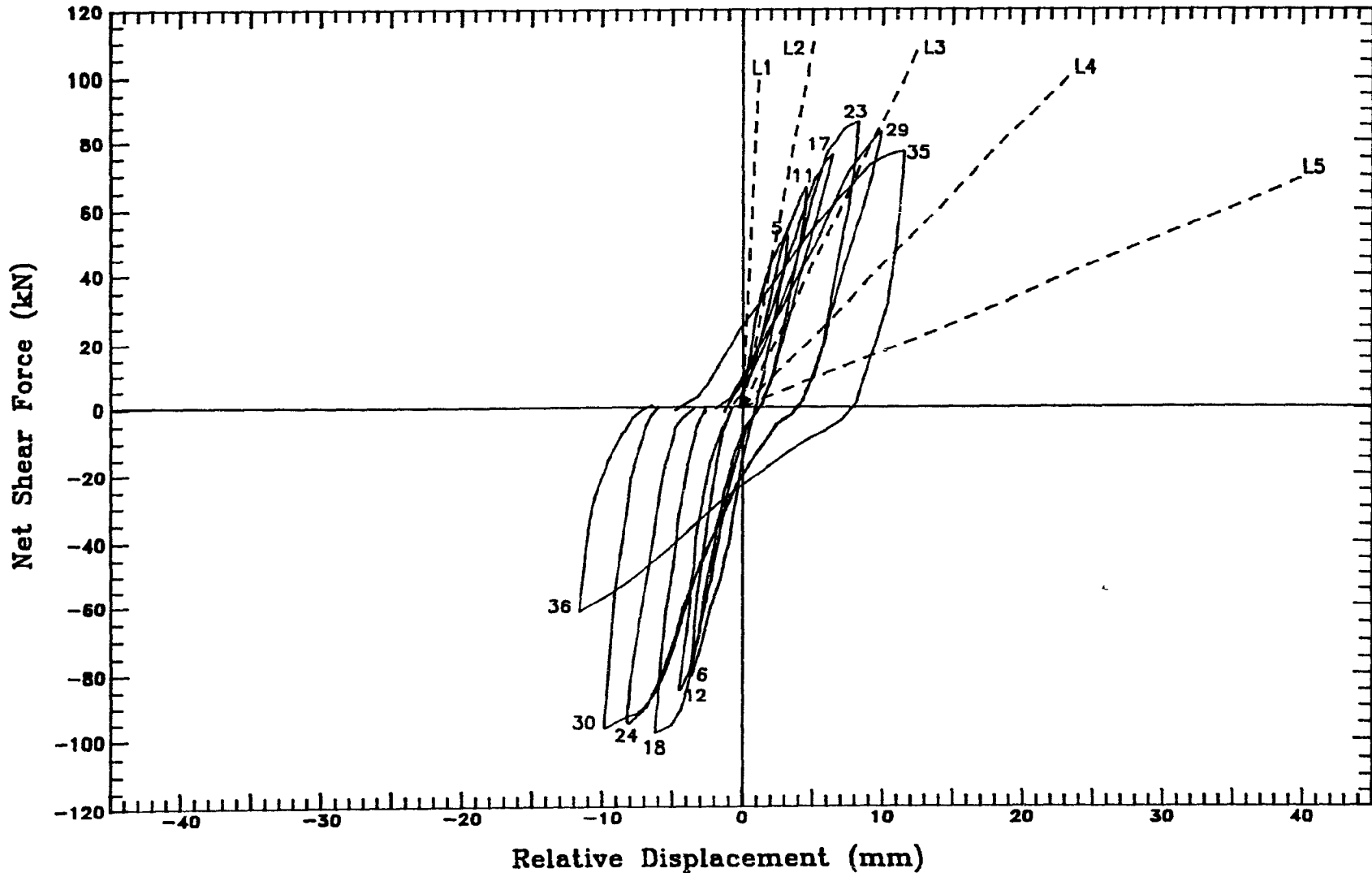


Figure 4.37 Load-Deformation Characteristics for Specimen D1.

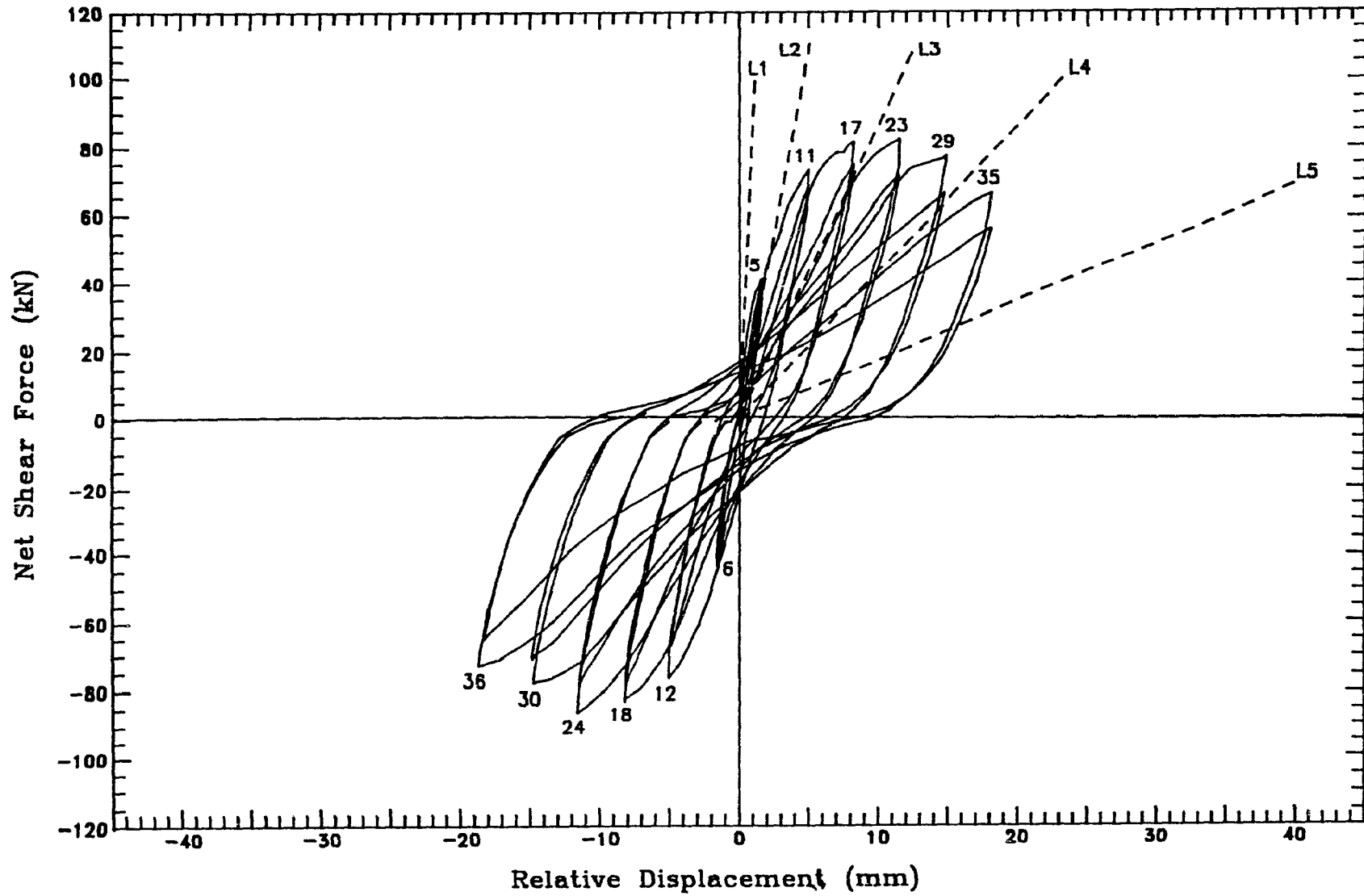


Figure 4.38 Load-Deformation Characteristics for Specimen D2.

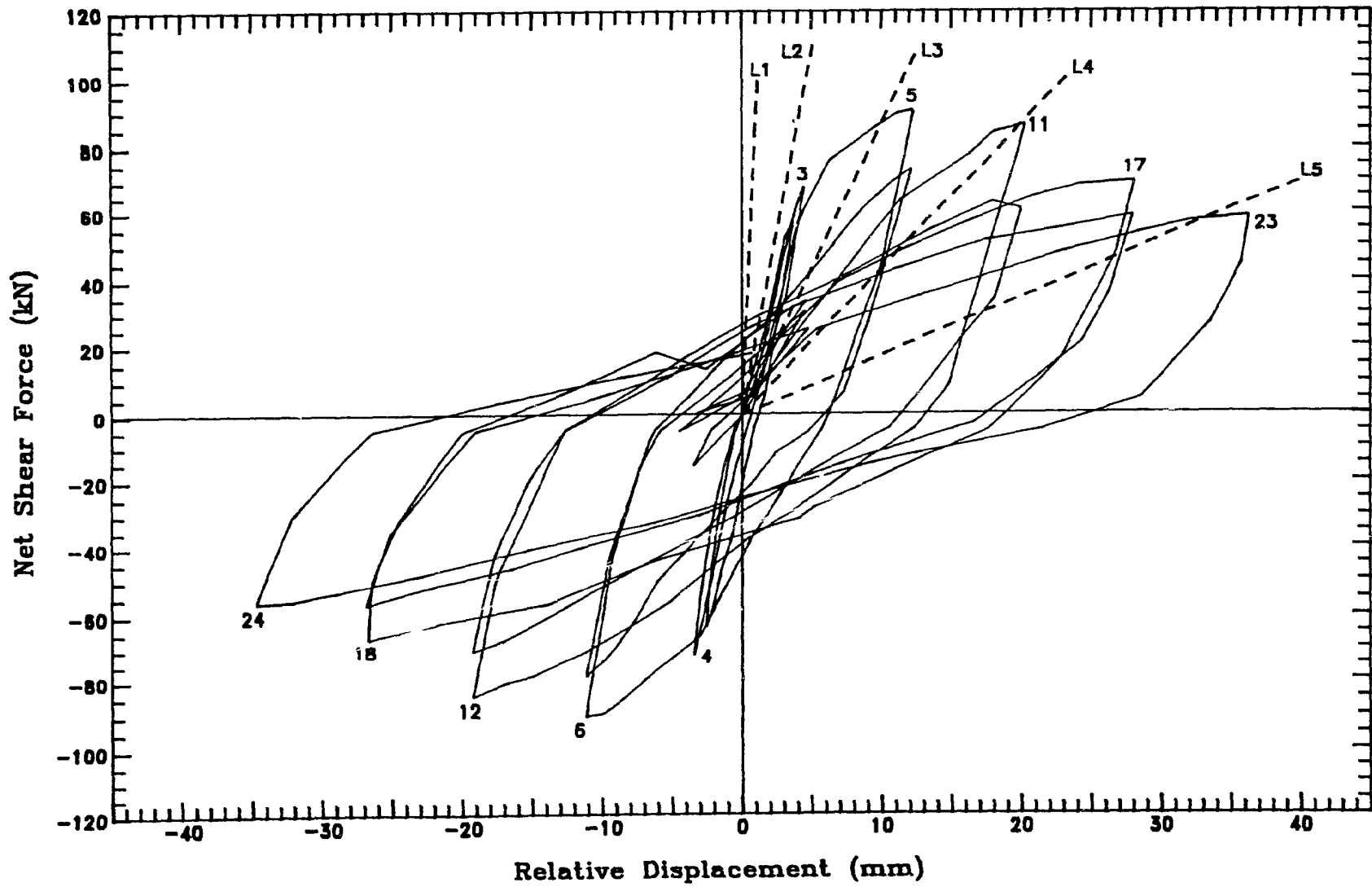


Figure 4.39 Load-Deformation Characteristics for Specimen D3.

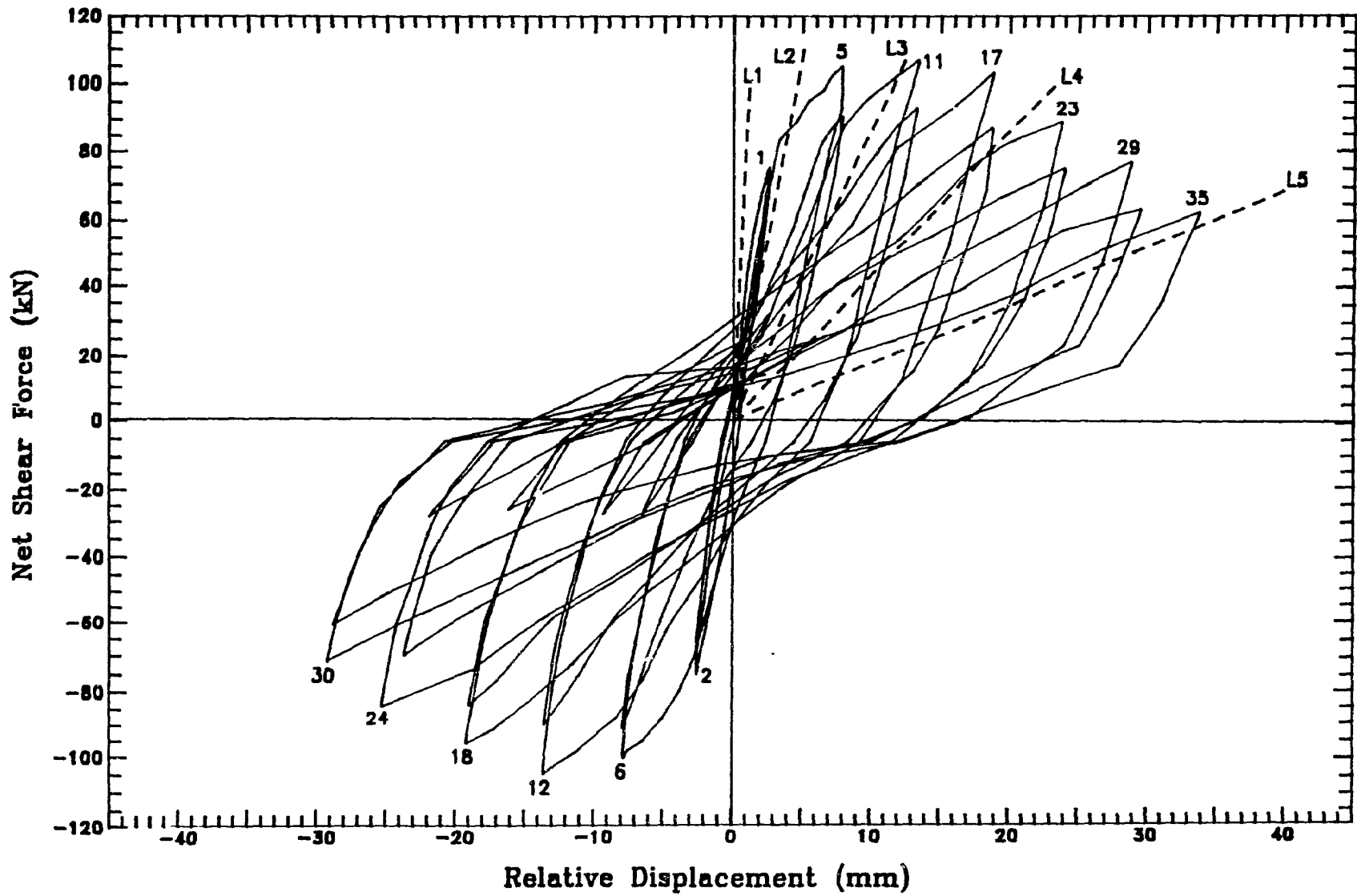


Figure 4.40 Load-Deformation Characteristics for Specimen D4.

and D4, respectively.

All four specimens displayed similar shapes of hysteresis loops, as shown in Figures 4.37 to 4.40. Although the shapes of the "loops" are generally the same, they differ in their characteristics related to the energy absorption capacity, the pinching effect and the ultimate ductility.

The energy absorption capacity of a structural system is measured by the area enclosed by the load-deformation curves. For a coupling member, the ability to provide high energy absorption capacity helps to improve the response of the overall system by dissipating the energy in the coupling member. For low ductility ratios ($\mu \leq 2.1$) or a relative displacement level of about 8 mm, the energy absorption capacity of Specimens D1, D2 and D3 were about the same. At higher displacement levels, a rapid drop of strength was observed in Specimen D1 which also depletes its energy absorption capacity significantly. The overall energy absorption capacity of Specimen D2 was better than that of Specimen D1 but Specimen D3 showed an improved energy absorption characteristic compared with Specimens D1 and D2. Specimen D4 displayed a much better energy absorption characteristic at every ductility level over all of the other specimens.

Pinching effects were observed in all specimens although they were less obvious in Specimen D3. The loads attained in the second cycles to the same peak inelastic displacement levels were lower than the initial cycles to these displacement levels. These inelastic shear distortions are typical of reinforced concrete coupling members.

The ultimate upward displacement imposed on Specimen D1 was 11.54 mm. The test was terminated at this displacement level due to the malfunctioning of the Optilog data acquisition system, although adequate load carrying capacity of this specimen would have been attainable for higher displacement levels. The ultimate displacement levels of Specimens D2, D3 and D4 were 18.15 mm, 36.3 mm and 33.81 mm, respectively.

Five lines, L1, L2, L3, L4 and L5, were included in the force-displacement char-

acterics for all four specimens. The slopes of these lines represent the slab stiffnesses assuming 20%, 5%, 2%, 1% and 0.4% of the entire slab width participate in carrying the applied load, respectively.

4.3 Slab Deflection Profile

The longitudinal and transverse deflection profiles of Specimens D1 and D2 are shown in Figures 4.41 through 4.44. These displacement profiles were obtained from the dial gauge and LVDT instrumentation shown in Figure 3.14. The deflection profiles of Specimens D3 and D4 were not available due to problems mentioned in Section 3.7.

Since relative vertical displacements were imposed on the walls, the longitudinal slab displacement profile of the slab at the slab-wall connection should be relatively horizontal in the absence of local slab deformations at these locations. The longitudinal slab displacement profiles of the slab near the slab-wall interface of Specimen D1 are shown by lines D in Figure 4.41, which showed that deviation from the horizontal position of the slab at the west wall toe occurred in all displacement cycles, indicating the presence of local shear deformation at this location. In general, sharp discontinuities were observed along the wall toe faces for Specimens D1 and D2 indicating the approximate locations of the largest rotations and strains where the transverse primary yield lines formed. The longitudinal displacement profiles near the walls (lines D) were flatter behind the wall toes and steeper along the corridor when compared to the longitudinal displacement profiles near the edge of the slab (lines G), which showed a more gradual change of slope from one end of the slab to the other. Smaller yet significant slab rotations, at approximately 850 mm from the corridor centreline, indicate the extent of the region from the wall toe faces where secondary yield lines formed along with the accompanying rotations.

The LVDT's and dial gauges located along the lines across the width the slab at the wall toes, Lines 3 and 6 in Figure 3.16, were used to obtain the transverse

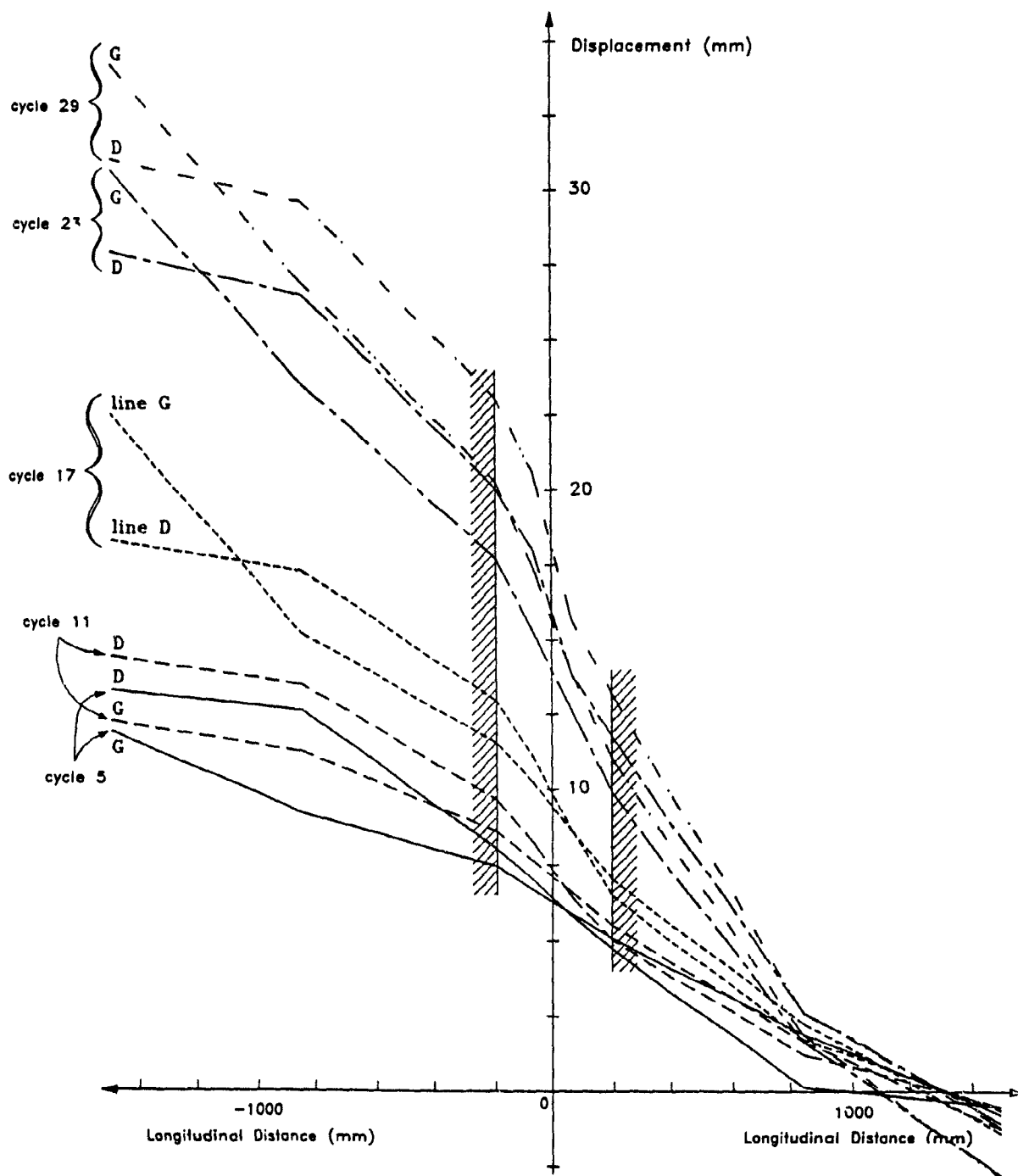


Figure 4.41 Longitudinal Slab Displacement Profiles for Specimen D1.

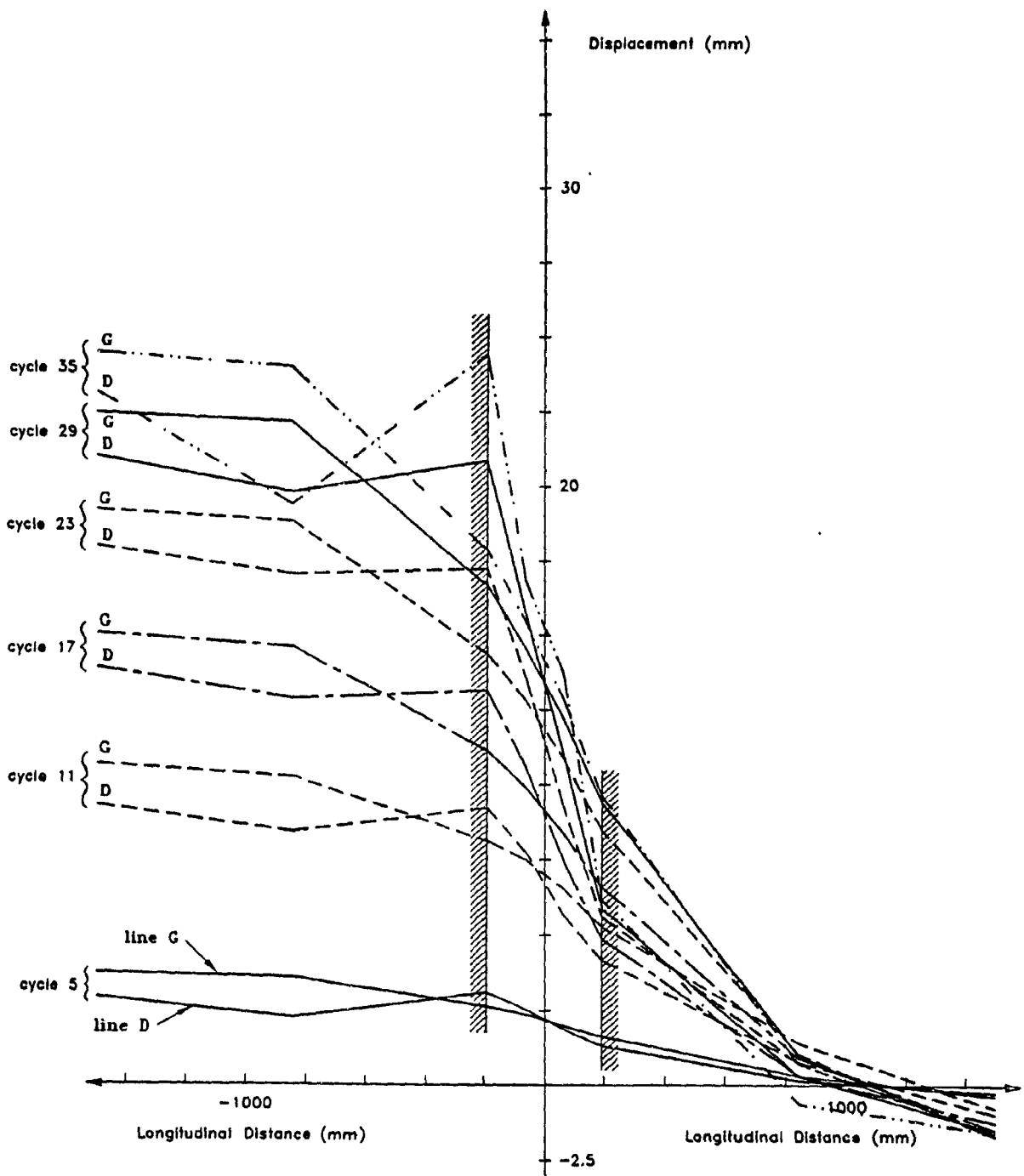


Figure 4.42 Longitudinal Slab Displacement Profiles for Specimen D2.

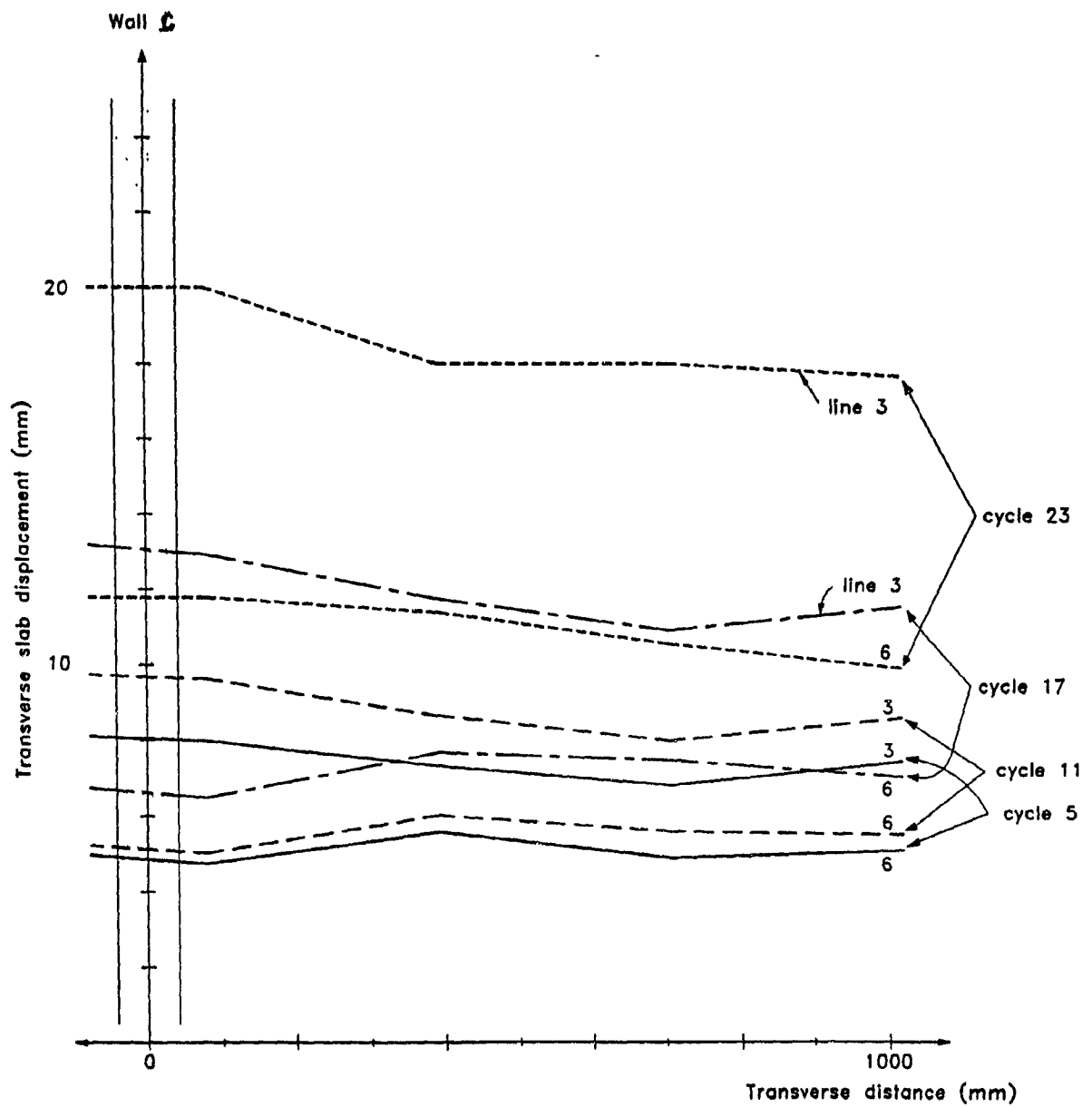


Figure 4.43 Transverse Slab Displacement Profiles for Specimen D1.

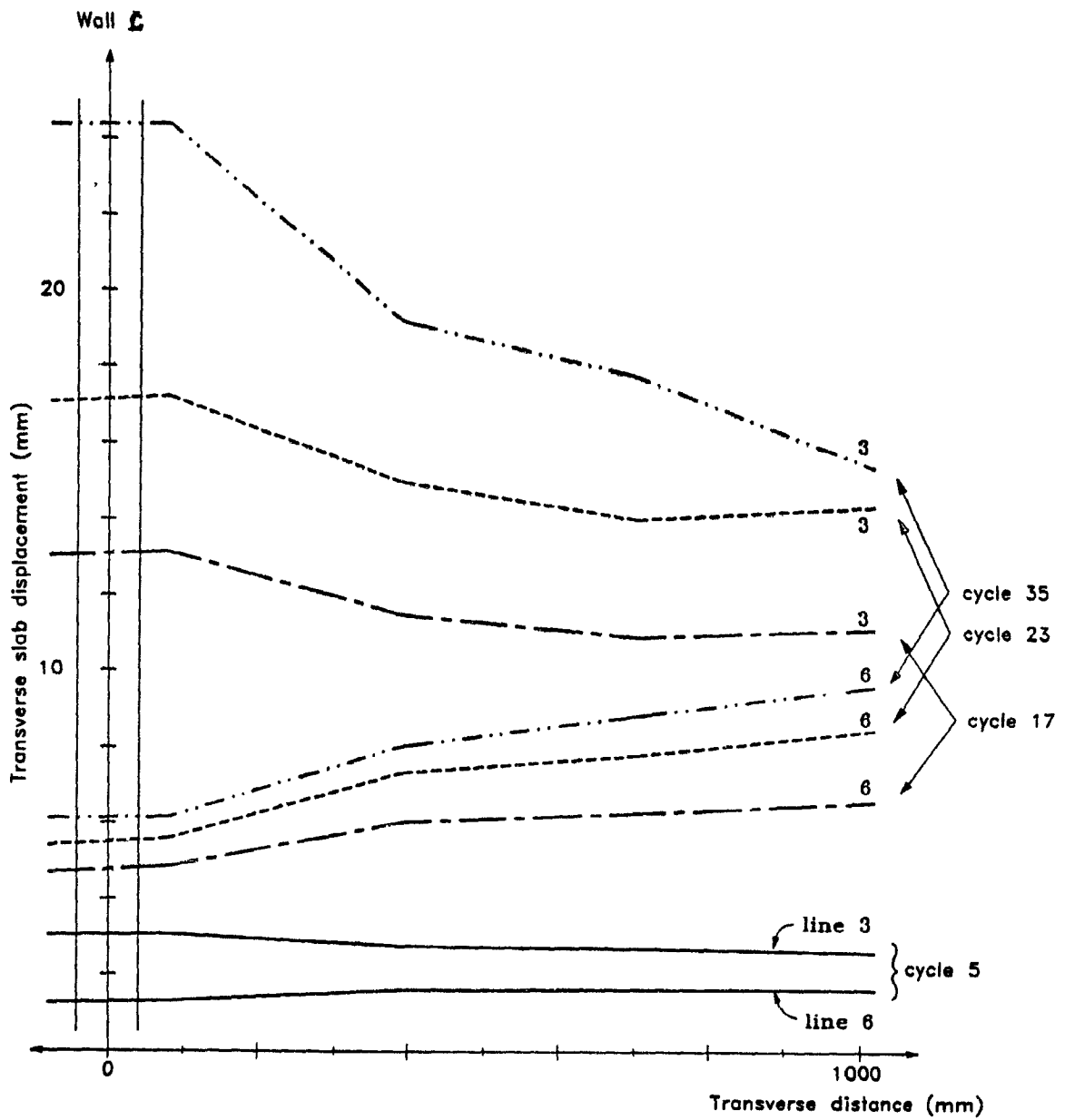


Figure 4.44 Transverse Slab Displacement Profiles for Specimen D2.

displacement profiles for Specimens D1 and D2 shown in Figures 4.43 and 4.44. These displacement profiles were similar to that observed by Malyszko¹⁵ in his tests. The greatest transverse slab rotations occurred close to the shear wall centerline. As higher displacements were imposed, these rotations near the wall increase and the transverse displacement profiles flatten out at a distance of approximately 350 mm from the shear wall centerline.

4.4 Longitudinal Seismic Reinforcement and Concrete Strains

The longitudinal seismic reinforcement and concrete strains plotted in Figures 4.45 and 4.46 were obtained from the demec gauge instrumentation described in Section 3.4.4. Therefore, these strains are average strains over the gauge distance of approximately 100 mm. However, on the tension face of the concrete slab, the opening of cracks between the demec studs also contributed to the change of distance between the demec studs. Hence, the strains on the tension face of concrete are concrete strains including the widths of these cracks. Although the imposed reversed cyclic loadings resulted in the cracking of the concrete slab on the top and the bottom faces as described in Section 4.2, the closing of the cracks in the concrete under compression prevented any additional tensile strains due to the cracks in the concrete. At higher peak displacement levels, spalling of the concrete and widening of the cracks passing directly through the demec studs caused these studs to detach from the concrete, making the reading of the strain measurements at these gauges almost impossible. No longitudinal strains were measured in Specimens D3 and D4.

In both Specimens D1 and D2, the steel and concrete strains near the shear wall centerline were higher than at the slab edges. Most of the top longitudinal reinforcement in Specimens D1 and D2 yielded at relative displacement levels of 2.85 mm and 5.01 mm, respectively, corresponding to displacement ductility ratios of 0.74 and 1.29. As shown in Figure 4.46, at a displacement ductility ratio of about 3, it was observed that the

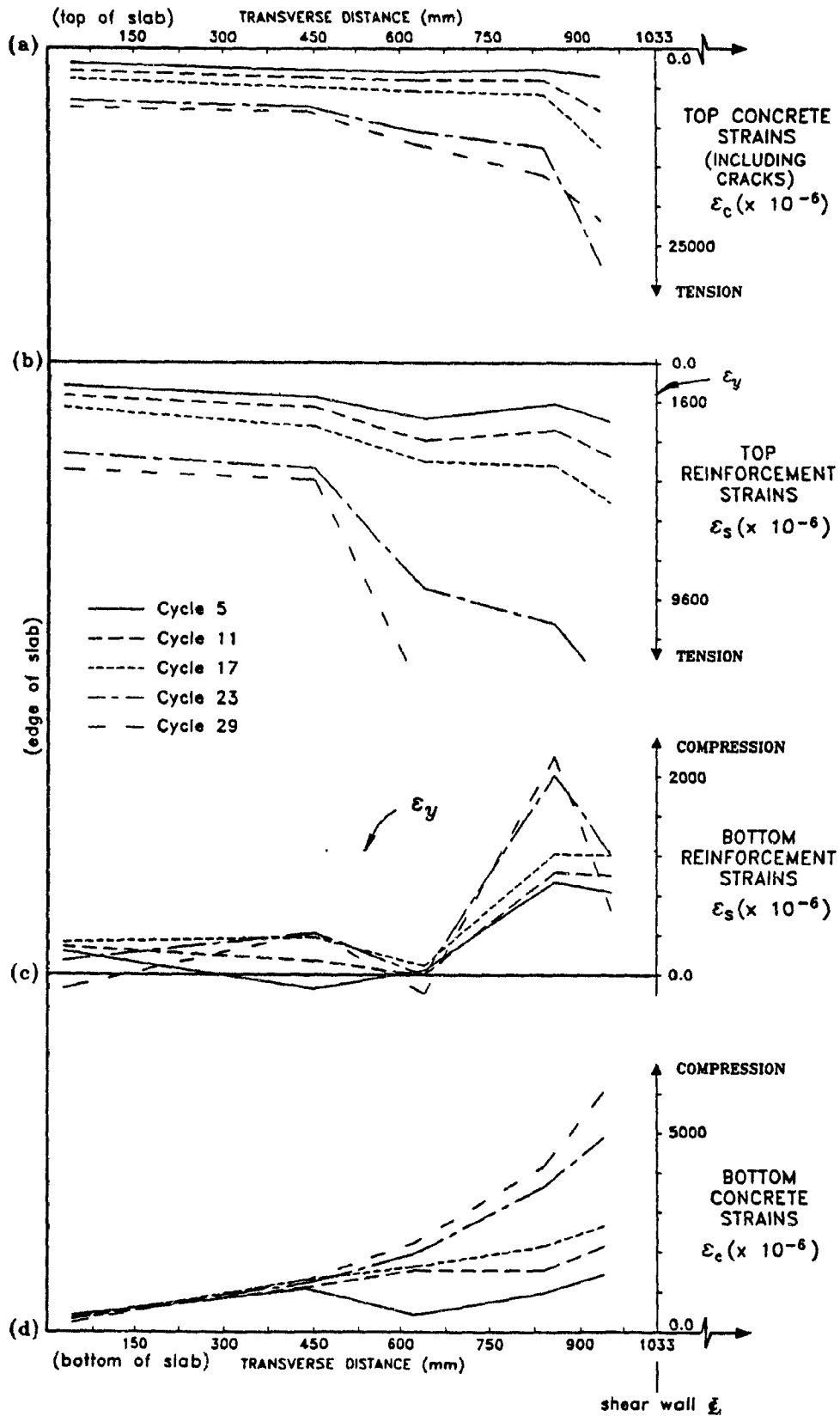


Figure 4.45 Longitudinal Strains for Specimen D1.

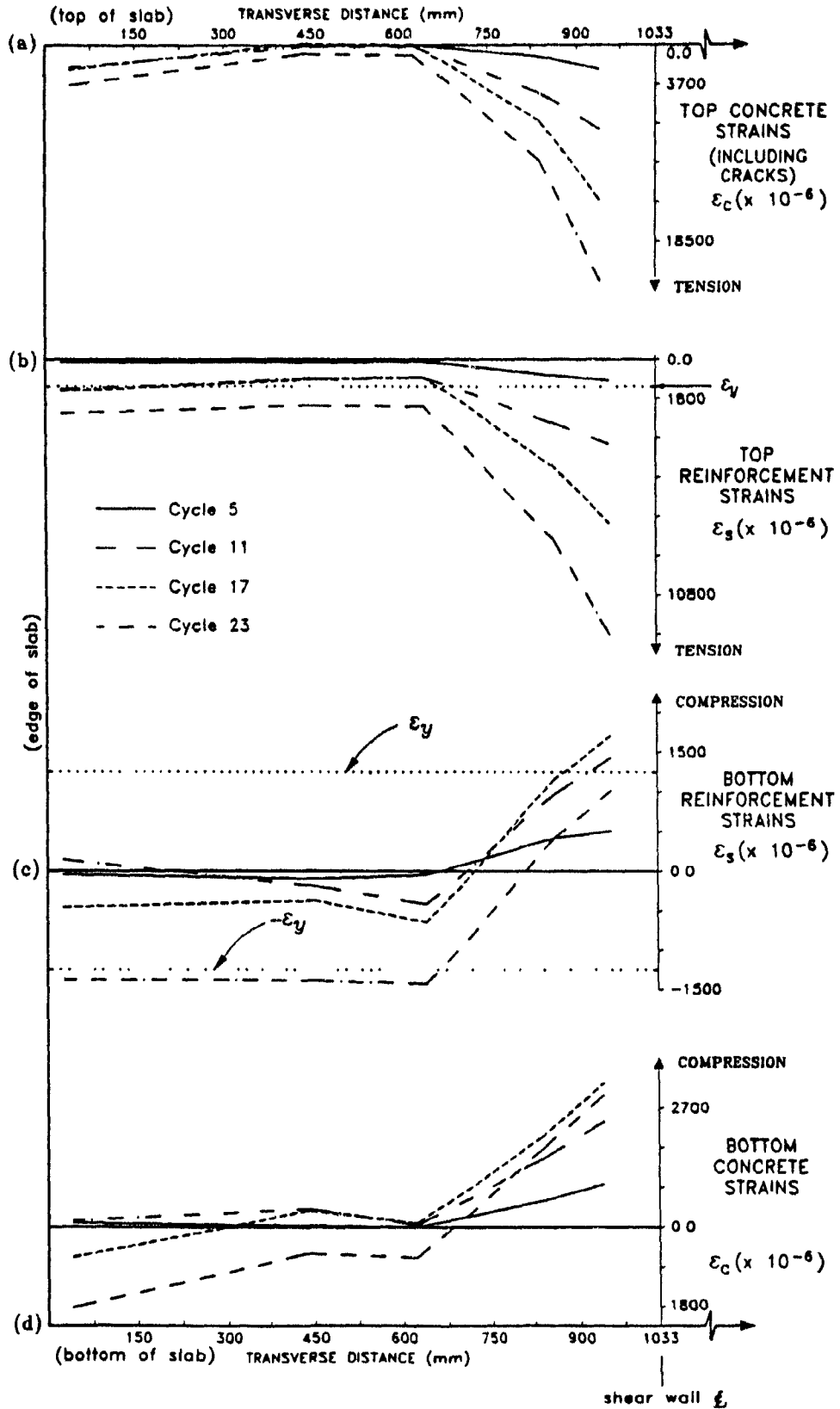


Figure 4.46 Longitudinal Strains for Specimen D2.

entire slab longitudinal seismic reinforcement had yielded or had almost reached yield, indicating the full participation of the slab in carrying the load.

4.5 Concrete and Steel Strains – Transverse Direction

The strains in the transverse reinforcement of Specimens D3 and D4 along a line underneath the wall toe and the strains in the concrete in this area in the transverse direction were obtained using the demec gauge instrumentation described in Section 3.4.4. The transverse strain variations were measured in two directions — transverse direction across the half slab width and longitudinal direction near the wall face. No transverse strain measurements were obtained for Specimens D1 and D2.

The transverse strain results for Specimen D3 are shown in Figures 4.47 through 4.50. The strains for the top transverse reinforcement near the wall toe could not be obtained after the first cycle because the demec studs at this location had separated from the reinforcement. Results of the strain variation in the transverse direction (Figure 4.47) show that the bottom transverse reinforcement across the wall toe had a strain value of about one to two times the yield strain within the drop panel region. Outside the drop panel region, these strains in the bottom transverse reinforcement were negligible. The strain variation in the transverse direction of the top concentrated transverse reinforcement (Figure 4.47) shows a strain reversal during Cycle 1, varying from a compressive strain value of over twice the yield strain near the wall face to a tensile strain of about 0.75 times the yield strain midway between the wall face and the edge of the slab. At higher displacement cycles ($\mu \geq 3$), the strains in the top concentrated transverse reinforcement, midway between the wall face and the edge of the slab, showed significant tensile yielding of the reinforcement, which tapered off to negligible values further away from the wall face. Also, the variation of the concrete strains in the transverse direction shown in Figure 4.48 indicates high tensile strains at the bottom face of the concrete within the drop panel region at higher displacement cycles.

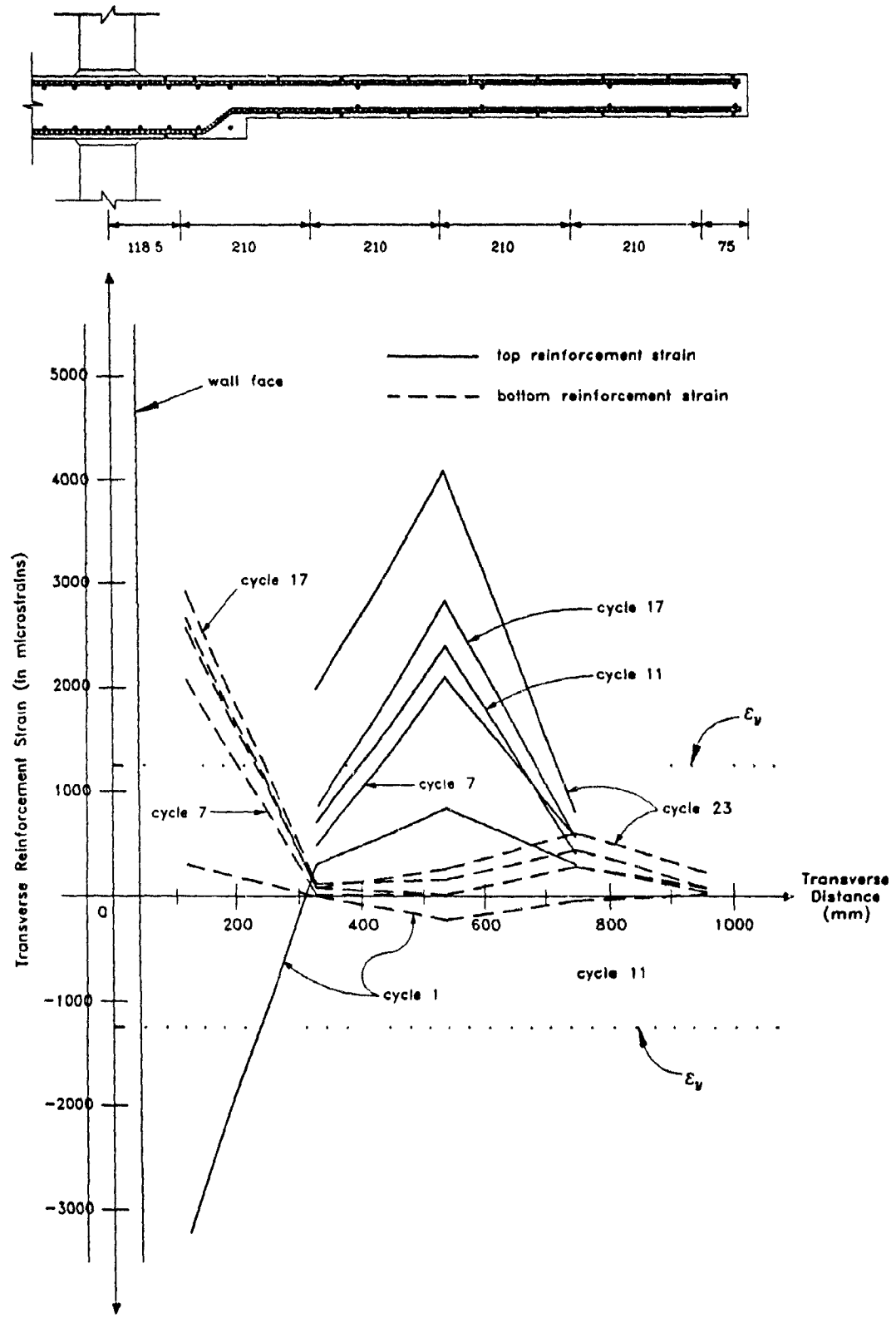


Figure 4.47 Transverse Variation of the Concentrated Transverse Reinforcement Strain of Specimen D3.

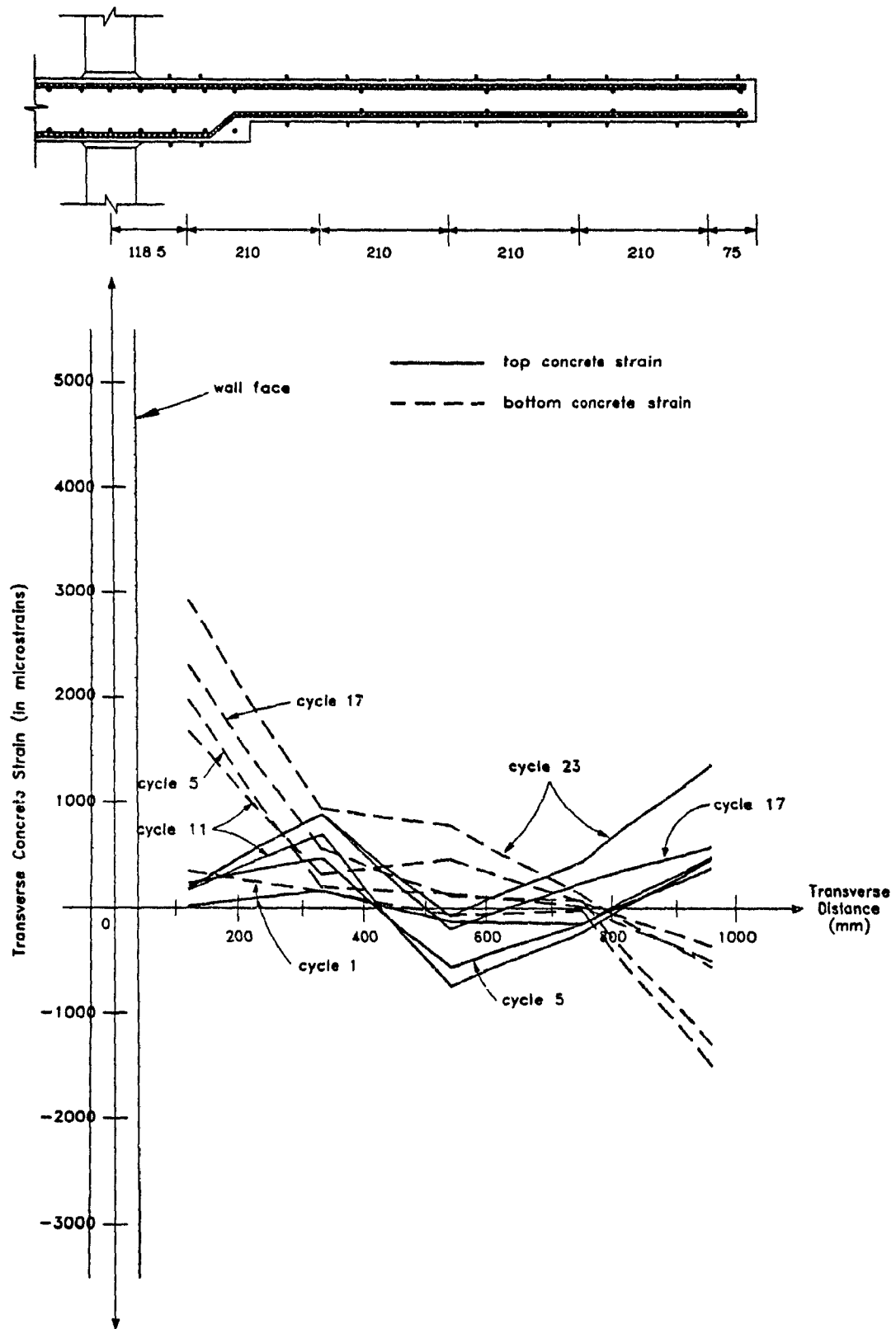


Figure 4.48 Transverse Variation of the Concrete Strain of Specimen D3 in the Transverse Direction.

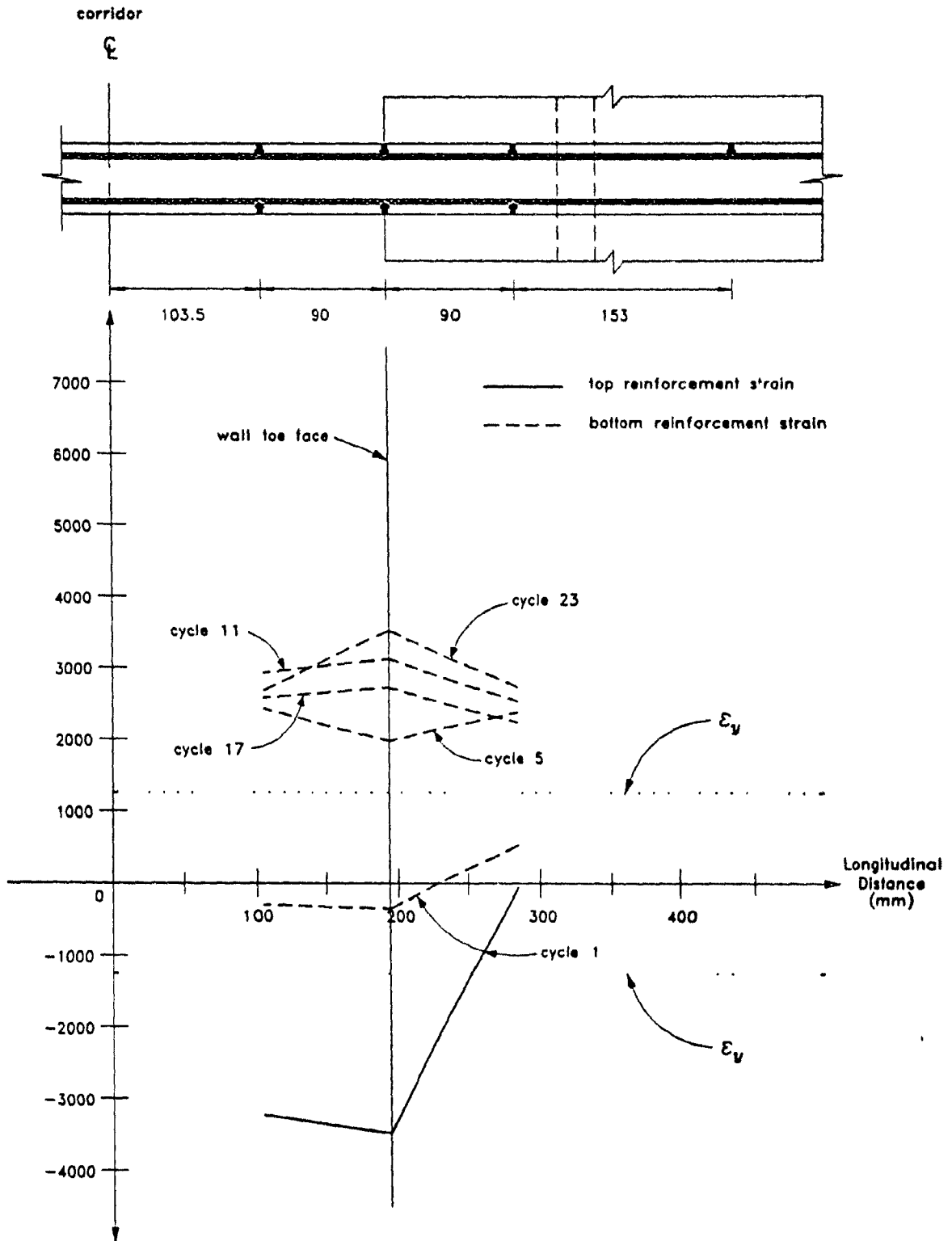


Figure 4.49 Longitudinal Variation of the Concentrated Transverse Reinforcement Strain of Specimen D3.

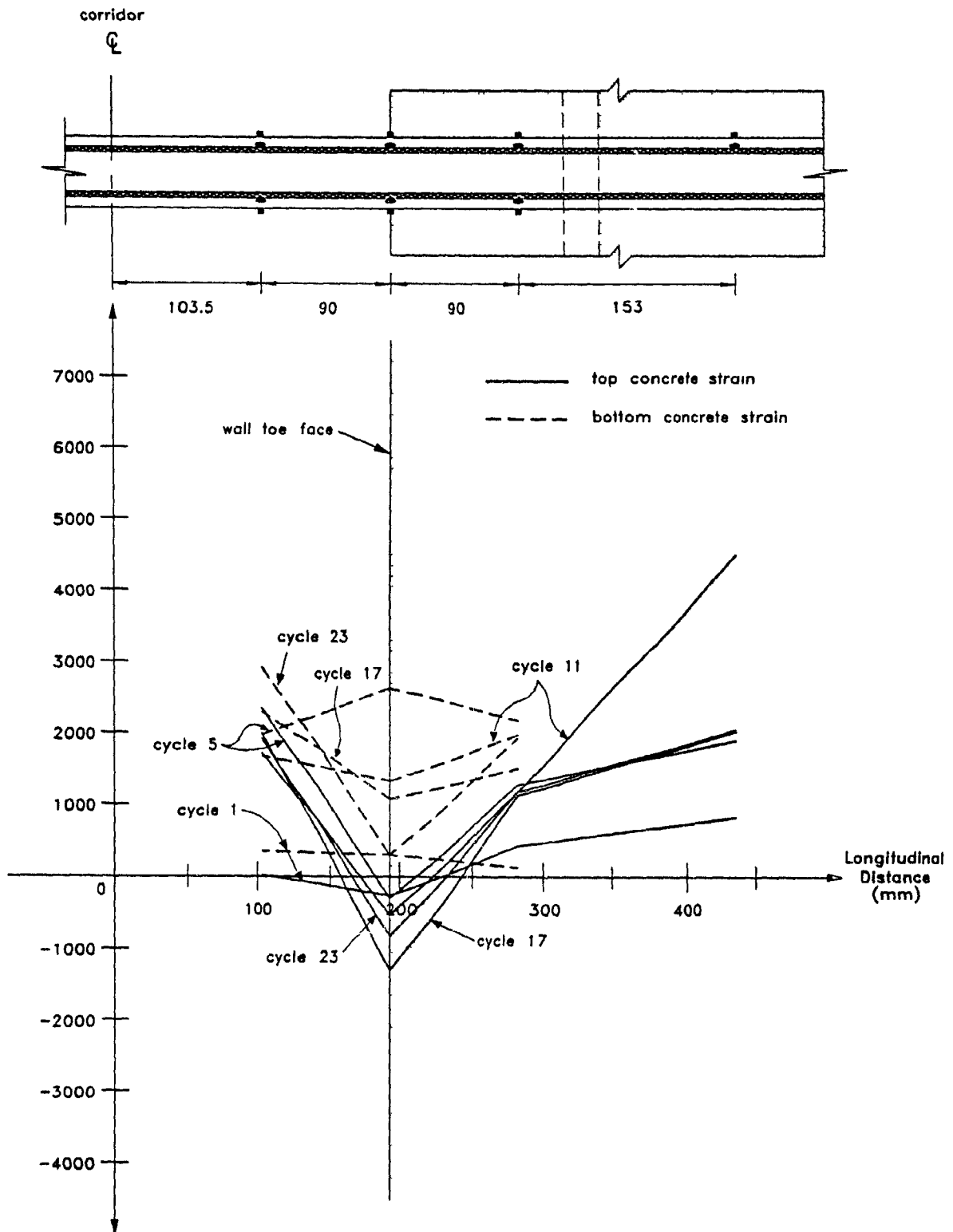


Figure 4.50 Longitudinal Variation of the Concrete Strain of Specimen D3 in the Transverse Direction.

($\mu \geq 3$). In the longitudinal direction, the strains in the bottom concentrated transverse reinforcement (Figure 4.49) show that all of the bottom concentrated transverse reinforcement had yielded at higher displacement ($\mu \geq 3$) cycles with an average value of about 2800 microstrains (or about $2.24\epsilon_y$). The bottom concentrated transverse reinforcement strain results also show that within the band of concentrated transverse reinforcement, the strains were quite evenly distributed. Plots of the top concentrated transverse reinforcement strains are not presented because of the insufficiency of the data due to the demec studs separating from the reinforcement after Cycle 1.

The strain variations in the transverse direction of the concrete and transverse reinforcement strains for Specimen D4 are shown in Figures 4.51 through 4.54. The concentrated transverse reinforcement strain variation of Specimen D4 in the transverse direction (Figure 4.51) was similar to that of Specimen D3 (Figure 4.47) with one notable exception. The strains in the bottom concentrated transverse reinforcement for Specimen D4, at a distance of 540 mm from the shear wall centerline, were approximately equal to the yield strain of the reinforcement while that of Specimen D3 was negligible. However, the results of the strains in the transverse concentrated reinforcement in Specimens D3 and D4 show that these reinforcements contributed significantly to the distribution of forces up to 750 mm from the shear wall centerline. Although the concrete transverse strain variation in the transverse direction in Specimen D4 (Figure 4.52) was similar to that of Specimen D3 (Figure 4.48), much lower transverse concrete strain values were observed within the drop panel region in Specimen D4 than in Specimen D3. However, it should be noted that the variation of the transverse strain in Specimen D4 in the transverse direction was measured along a line which was at a distance of approximately 30 mm in front of the wall toe face (Figure 3.21), instead of along a line directly underneath the shear wall toe as was the case in Specimen D3 (Figure 3.20). In the longitudinal direction, the concentrated transverse reinforcement strain variation of Specimen D4 (Figure 4.53) near the wall face showed that much of

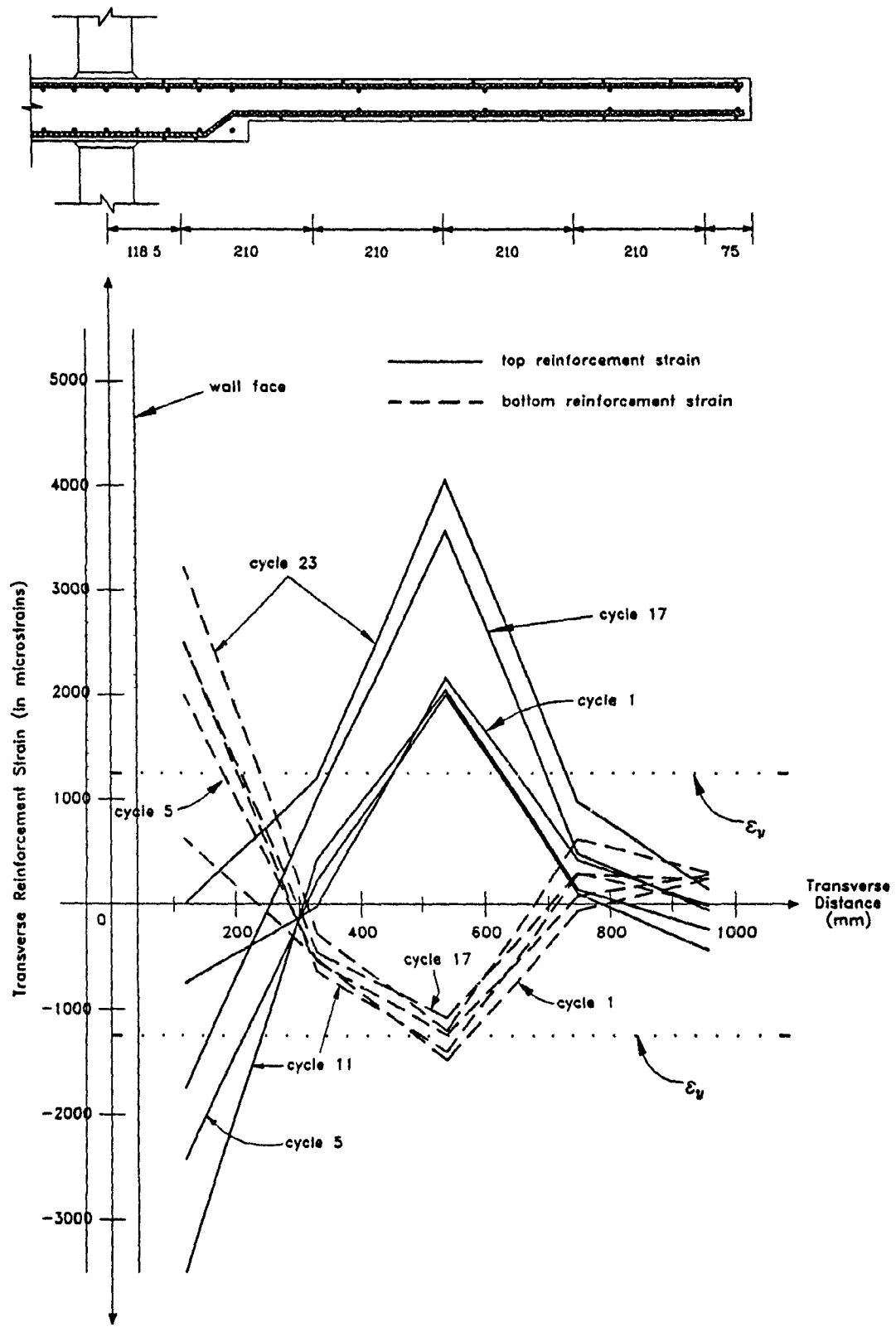


Figure 4.51 Transverse Variation of the Concentrated Transverse Reinforcement Strain for Specimen D4.

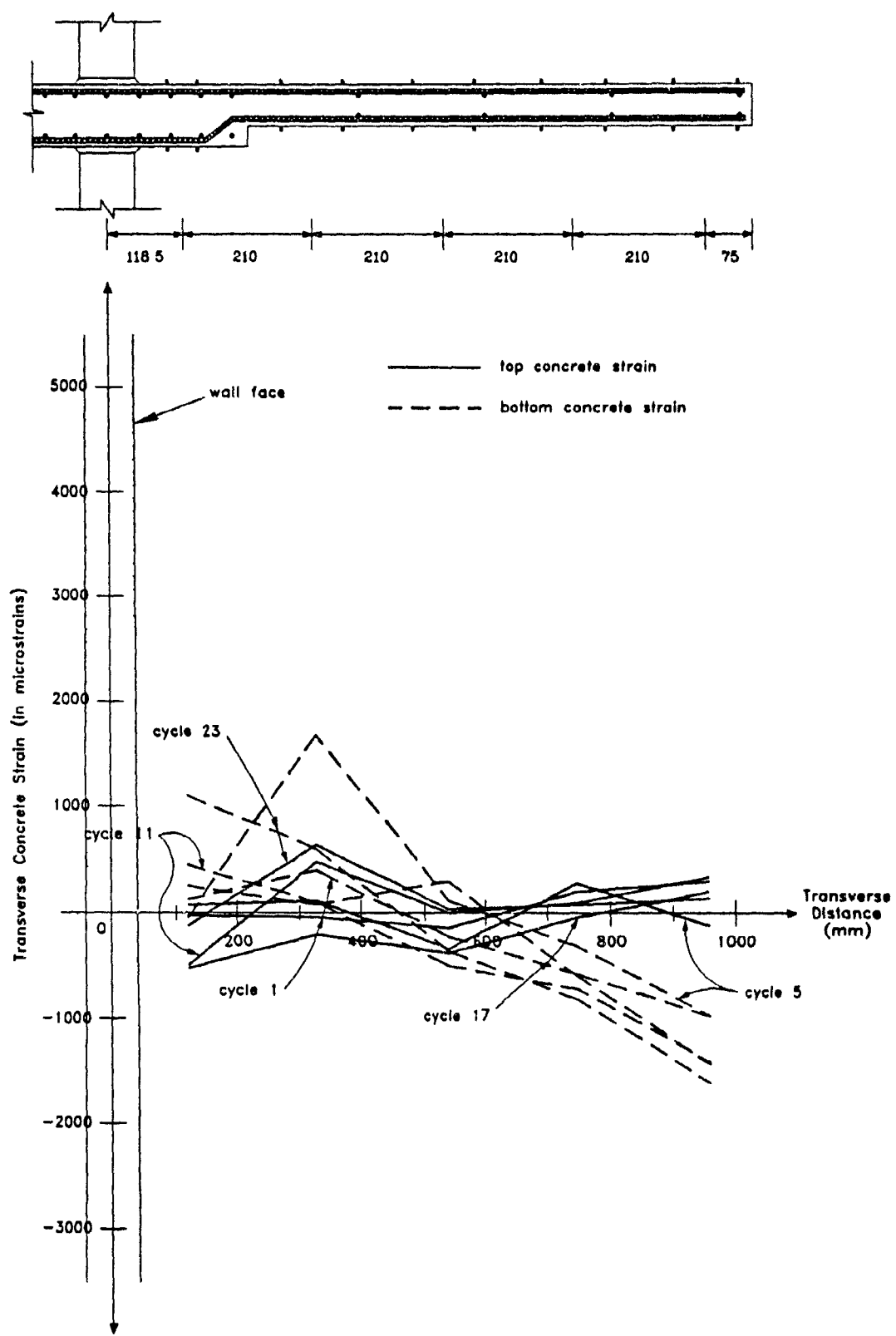


Figure 4.52 Transverse Variation of the Concrete Strain for Specimen D4 in the Transverse Direction.

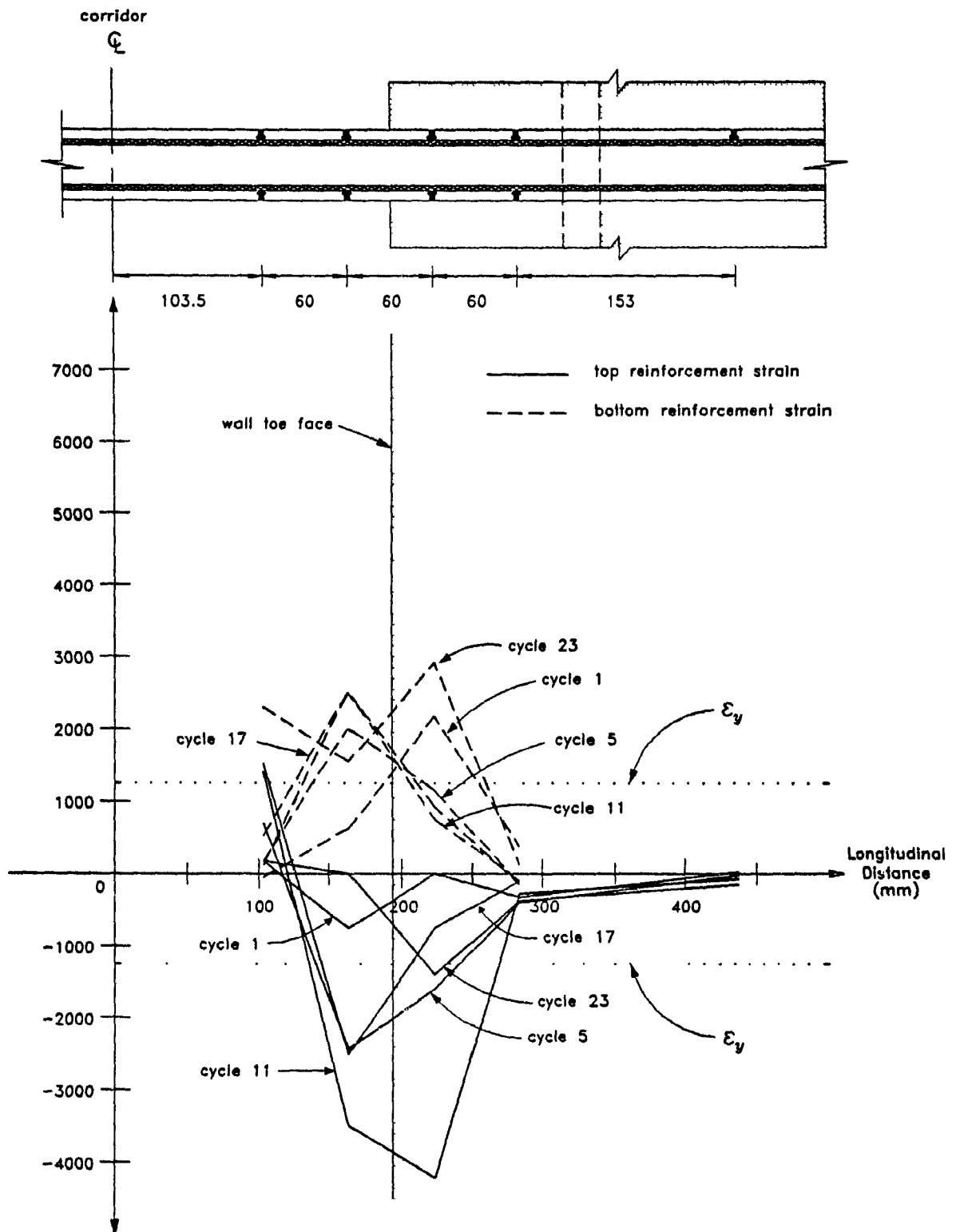


Figure 4.53 Longitudinal Variation of the Concentrated Transverse Reinforcement Strain for Specimen D4.

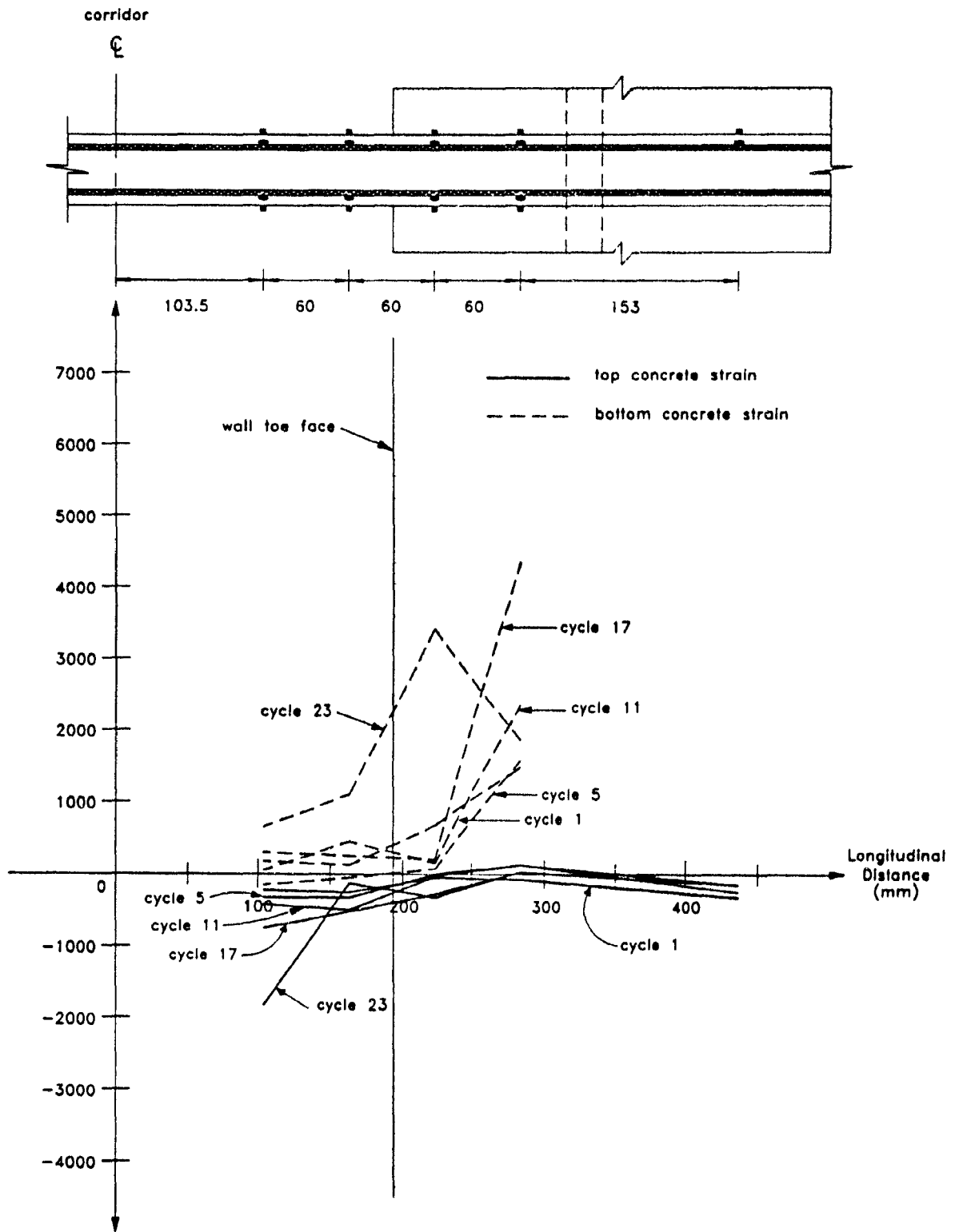


Figure 4.54 Longitudinal Variation of the Concrete Strain for Specimen D4 in the Transverse Direction.

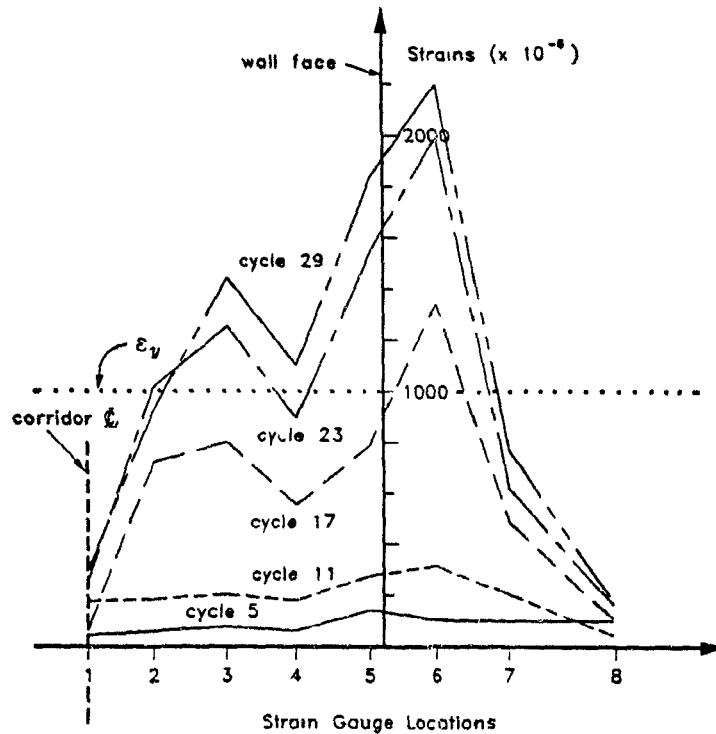


Figure 4.55 Strains in Inner Vertical Stirrup Legs for Specimen D1.

the distribution of forces occurred within the four transverse bars closest to the wall toe. The longitudinal variation of the concrete strains in the transverse direction in Specimen D4 (Figure 4.54) is negligible, except at a distance of about 90 mm behind the wall toe where significantly high tensile strains were observed on the bottom face of the concrete.

4.6 Strains in Vertical Stirrup Legs

Electrical resistance strain gauges placed on the inner and outer vertical stirrup legs of all four specimens provided limited but useful data. The locations of these strain gauges were described in Section 3.4.3. The results of the strains in these vertical stirrup legs are presented in Figures 4.55 through 4.61. The strains in the outer vertical stirrup legs of Specimen D1 were not available due to the damage during casting to most of the strain gauges locations at these outer vertical legs.

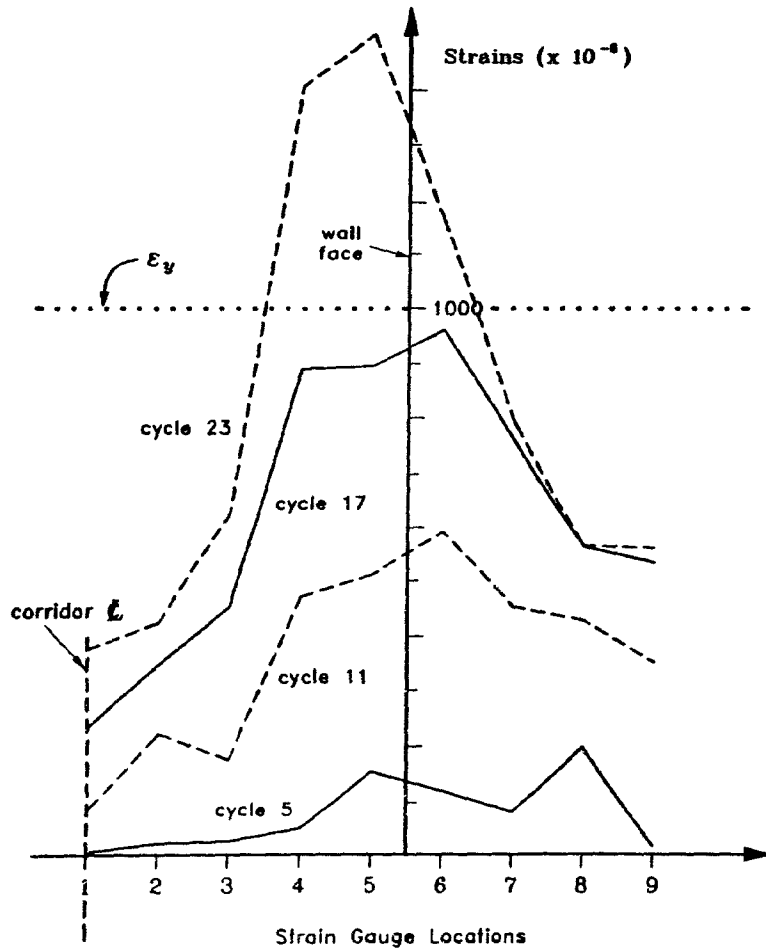


Figure 4.56 Strains in Inner Vertical Stirrup Legs of Specimen D2.

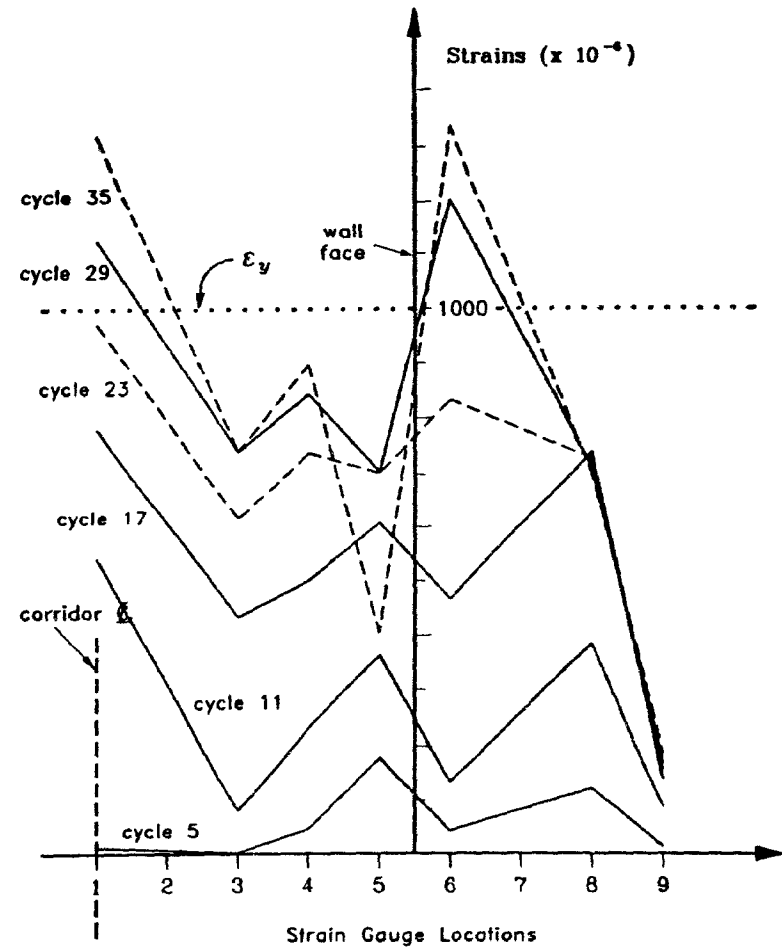


Figure 4.57 Strains in Outer Vertical Stirrup Legs of Specimen D2.

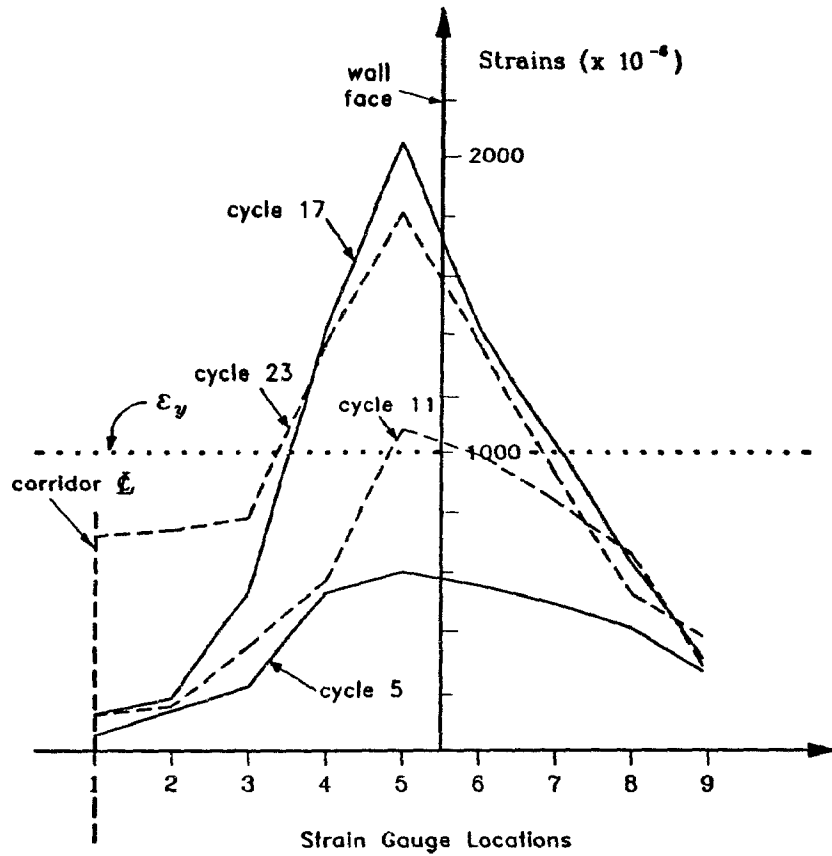


Figure 4.58 Strains in Inner Vertical Stirrup Legs of Specimen D3.

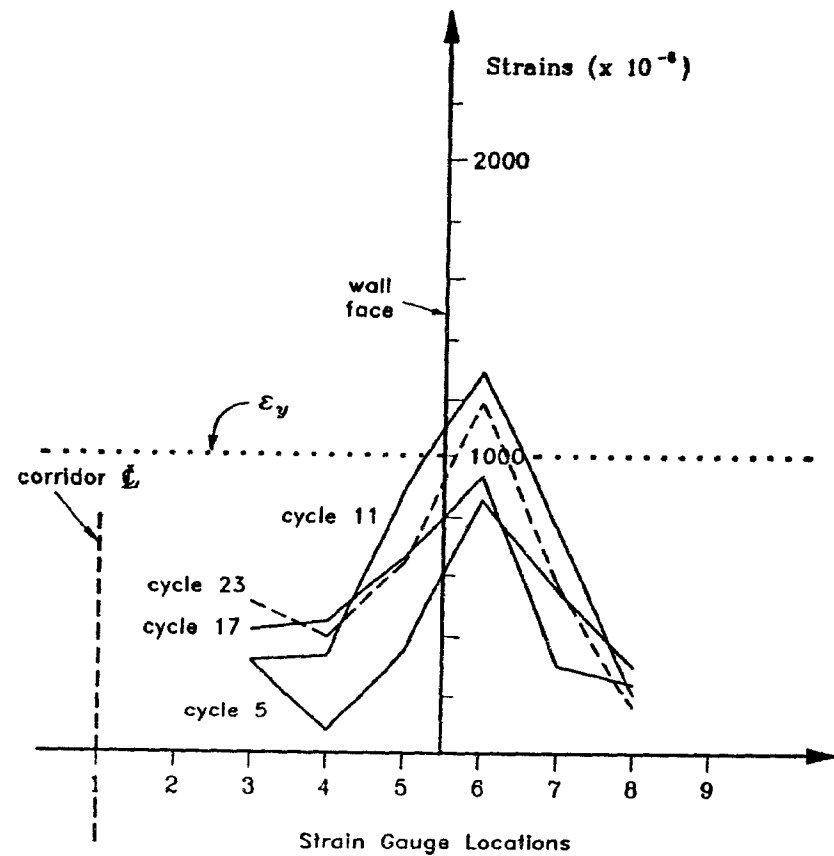


Figure 4.59 Strains in Outer Vertical Stirrup Legs of Specimen D3.

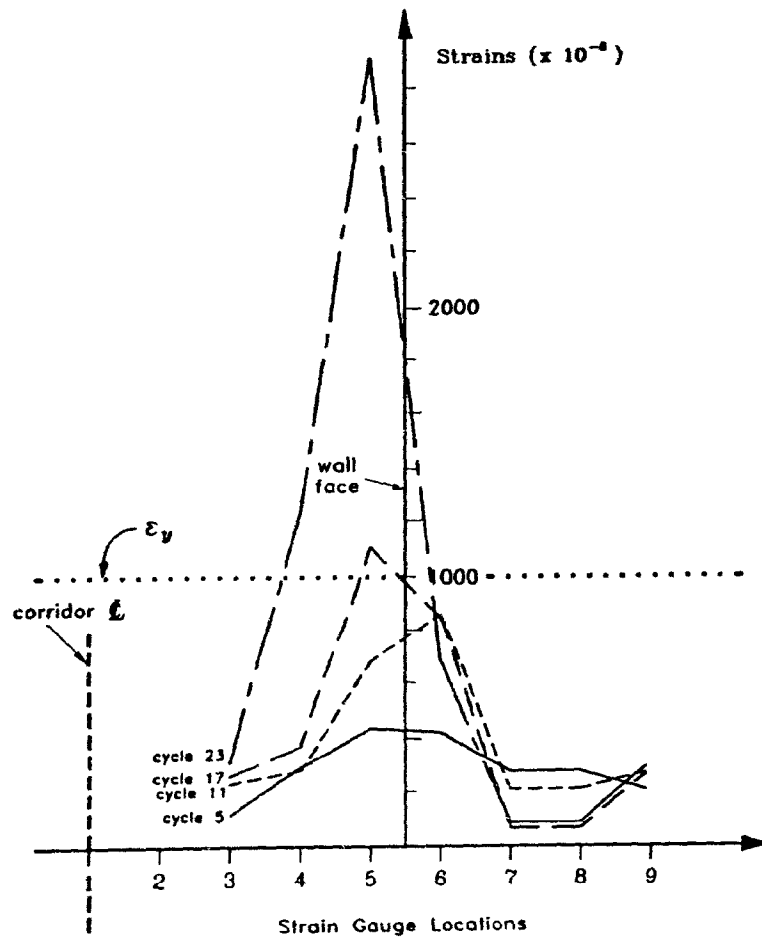


Figure 4.60 Strains in Inner Vertical Stirrup Legs of Specimen D4.

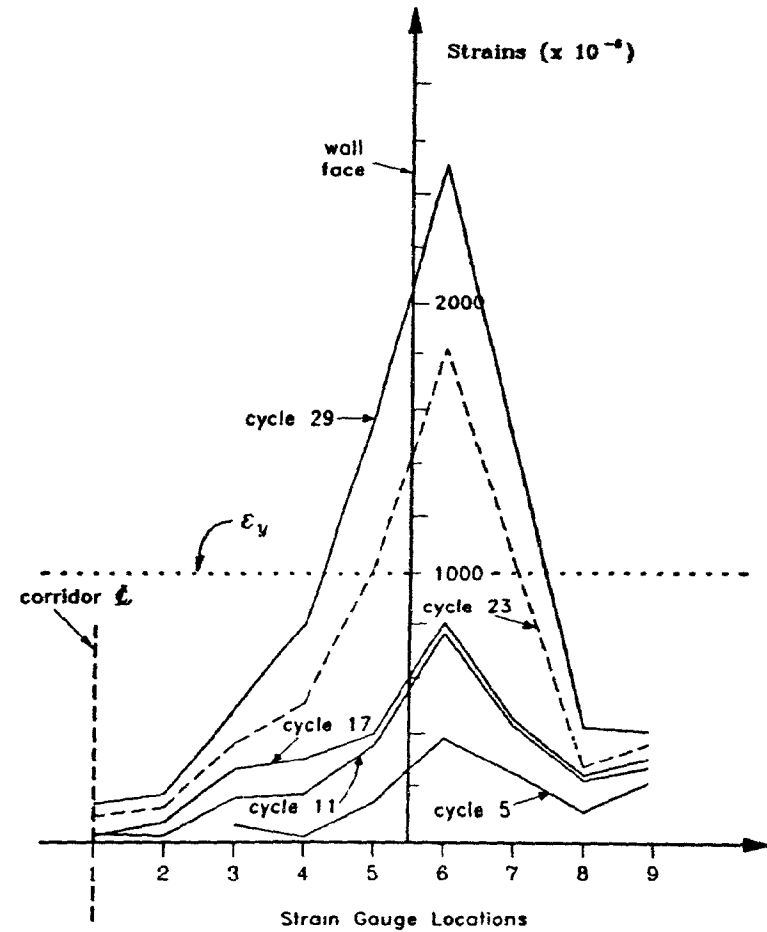


Figure 4.61 Strains in Outer Vertical Stirrup Legs of Specimen D4.

The results of the strains in the vertical stirrup legs for all four specimens clearly show that the bulk of the stirrup participation in carrying the applied shear force occurred within one-fourth of the corridor width on either side of the wall toe. The results also show that at a displacement level of 6.1 mm ($\mu = 1.6$), the stirrup leg of Specimen D1 close to the wall toe was just about yielding (Figure 4.55), while that of the other specimens had not yielded (Figures 4.56—4.61). The strains in the outer vertical stirrup legs of Specimens D2, D3 and D4 were generally lower than those in the inner legs.

The strains in the vertical stirrup legs of Specimens D2, D3 and D4 reached the yield strain at displacement levels of 8.2 mm ($\mu = 2.1$), 20.3 mm ($\mu = 5.2$), and 18.8 mm ($\mu = 4.9$), respectively (Figures 4.56, 4.58 and 4.60). It can be noted that the provision of a band of concentrated transverse reinforcement had caused the shear force to be distributed transversely across the width of the slab, and hence, delayed the “shear damage” to the concrete in the wall toe regions. Hence, a delayed participation of the stirrups was expected for Specimens D3 and D4. The strains in the vertical stirrup legs of Specimens D3 and D4 also showed that fewer stirrups participated in carrying the applied shear force than in Specimens D1 and D2.

Generally, a significant number of inner and outer vertical stirrup legs of all specimens yielded after some significant shear deformation had occurred in the slab. Therefore, it must be emphasized that the primary function of these stirrups was not in carrying the shear force but as clamping devices for the confinement of the concrete to permit increased shear friction to be developed due to the aggregate interlock.

CHAPTER 5

DISCUSSION OF RESULTS

5.1 Crack Propagation

Similar trends were observed for the crack patterns in all four specimens presented in Section 4.1, and hence, these can be generalized for all coupled slab-shear wall structures as follows. Similar observations were obtained from tests performed by Taylor¹⁴, Malyszko¹⁵ and Khan¹⁶.

As predicted by the yield line analysis, primary cracks form first (see Figure 5.1a), starting from the face of the wall toes and extending perpendicular to the centerline of the wall towards the edge of the slab. This is followed by secondary cracks forming at a distance approximately equal to the wall thickness, t , from the face of the wall toe and gradually extending to the edge of the slab, with an initial angle of about 45° from the shear wall centerline which increases rapidly to 90° (Figure 5.1b). Other secondary cracks form immediately afterwards with the emergence of diagonal cracks at an angle of 45° from the corners of the wall toes, extending to the primary crack line (for bay widths $>$ corridor width). However, the full formation of the primary diagonal cracks (Figure 5.1c) occurs only after the yielding of the longitudinal seismic reinforcement. At higher ductilities ($\mu \geq 3$), more secondary cracks and secondary diagonal cracks (Figure 5.1d) form, but more importantly, radial cracks begin to emanate from the face of the wall toes. These radial cracks are the result of highly localized shear at the wall toes

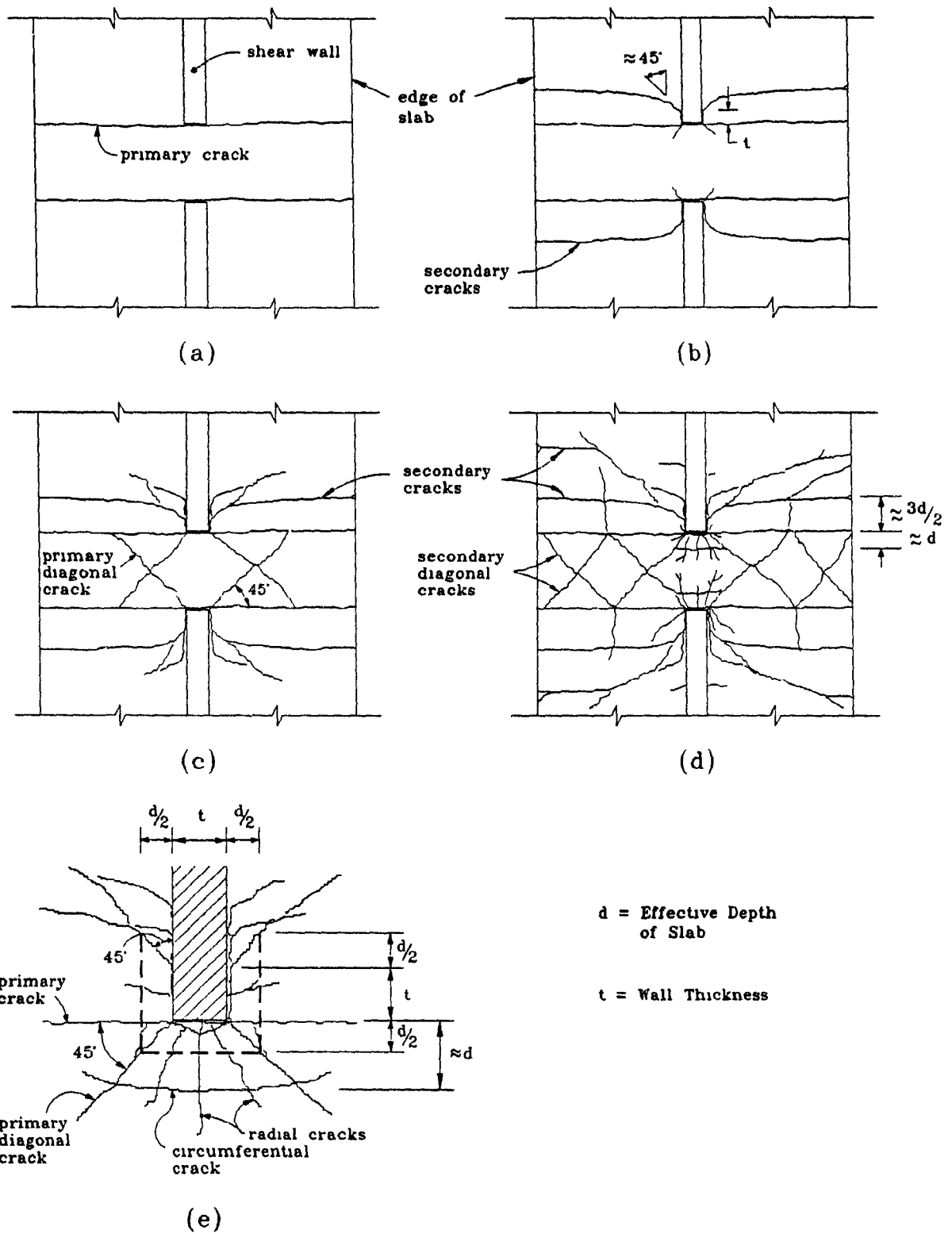


Figure 5.1 Schematic Diagrams of Crack Propagation.

Table 5.1 Experimental Ultimate Strength Results and Predictions.

Specimen	Experimental Ultimate Load (kN)	Theoretical Ultimate Strength [†] (Y.L. Theory) (kN)	Theoretical Ultimate Strength [‡] (P.S.S.) (kN)
D1	93.81	84.8	82.5
D2	86.50	86.14	80.2
D3	90.51	87.05	85.7
D4	107.18	87.05	85.7

[†] Based on Yield Line Analysis

[‡] Based on Punching Shear Strength

$$V_u = d(t + d)\sqrt{f'_c} \text{ (Mpa)}$$

or $V_u = 12d(t + d)\sqrt{f'_c} \text{ (Psi)}$

and are, therefore, signs of punching shear. Punching shear failure, which could not be avoided in all four tests, is often preceded by circumferential cracks forming at a distance of approximately d , the effective depth of the slab, from the face of the wall toe. (Figure 5.1e).

5.2 Ultimate Strength

The crack patterns observed at failure showed that a critical section can be taken midway between the circumferential crack and the wall face up to the primary diagonal crack line, as shown by the dotted line in Figure 5.1e. The critical punching shear area based on the critical section is $3d(t + d)$, where d is the effective depth of the slab and t is the wall thickness. Thus, the punching shear stress based on this critical section is

$$v_n = \frac{V}{3d(t + d)} \quad (5-1)$$

Assuming that the ultimate shear stress of concrete is $0.33\sqrt{f'_c}$ (MPa) (or $4\sqrt{f'_c}$ psi), the theoretical punching shear strengths of all four specimens were computed. The computed values are tabulated in Table 5.1.

The crack formation also conforms with the prediction of the yield line theory. Based on this theory and assuming the participation of the seismic longitudinal rein-

forcement across the entire width of the slab, the theoretical ultimate shear strengths of the slab were computed. These values are also shown in Table 5.1.

In comparison with the experimental results as shown in Table 5.1, it is shown that the ultimate shear strength of the coupling slab can be predicted with reasonable accuracy by either the yield line theory or the empirical Equation (5-1). It can also be noted that these predictions are slightly on the conservative side.

The results also revealed that an increase in ultimate load was achieved with an increase in the transverse reinforcement in the slab underneath the wall toe regions. Specimens D3 and D4, both with stirrups spaced at $0.5d$, displayed ultimate strengths of 86.8 kN and 103.1 kN, respectively. Specimen D3, with a concentrated transverse reinforcement ratio of 1.3% underneath the wall toe, showed only 2.6% strength increase over that of Specimen D2. However, increasing this transverse reinforcement ratio to 1.6%, as provided in Specimen D4, led to a strength increase of 21.9% over that of Specimen D2, showing an improved load distribution near the wall toe and, therefore, a significant increase in the ultimate strength. Although Specimen D1 had stirrups at $0.28d$ spacing compared with a $0.50d$ spacing for Specimen D2, the increase in strength was insignificant (1.9%). Provision of stirrups around some of the longitudinal reinforcement did not improve the ultimate strength significantly.

5.3 Degradation of Strength and Stiffness

The basic load-deformation characteristics for all four specimens displayed similar features, with Specimens D3 and D4 showing much less pinching and greater dissipation of energy than those in Specimens D1 and D2 (see Figures 4.37 to 4.40). The area within the hysteresis loops and, hence, the energy absorption capacities of Specimens D3 and D4 were also comparatively larger than Specimens D1 and D2. Specimens D1 and D2 exhibited gradual increase in strength at displacement ductility ratios of 2.04 and 2.98, respectively, although flexural tension cracks appeared in front of the wall toes during

the first cycle. Specimens D3 and D4 exhibited flexural cracking during the first load cycle, and showed a much higher rate of strength increase, attaining their maximum strengths at ductility ratios of 3.17 and 2.04, respectively.

Tables 5.2 to 5.5 show the load-deformation relationships and the corresponding ductility ratios. In all four specimens, the strengths at higher displacements ($\mu \geq 2$) were above 60% of the ultimate load.

Table 5.6 to 5.9 show the stiffness degradation of all four specimens. The initial stiffness of all four specimens averaged at 26.6 kN/mm. At relative vertical displacement of about 11 mm ($\mu = 2.8$), the stiffnesses of Specimens D1 and D2 were about 15% of their initial stiffnesses while Specimens D3 and D4 showed stiffnesses of 23% and 19% of their initial stiffness values. The addition of concentrated transverse reinforcement near the wall toe regions increased the participation of the slab further away from the wall during the early cycles, resulting in a lower stiffness degradation. However, during the later cycles, when much of the damage has occurred, the participation of the outer slab became negligible. As the participation of the outer slab becomes insignificant, the rate of damage and, hence, the strength and stiffness degradations of Specimens D3 and D4 became rapid. At failure due to punching shear near the wall toes, the displacement levels of Specimens D3 and D4 were over 30 mm while that of Specimen D2 was under 20 mm. Although punching shear damage of Specimen D1 was not as pronounced as the other specimens at the end of the test which was terminated prematurely, it can be deduced from the force-displacement characteristics for Specimen D1 (Figure 4.37) that the higher displacement levels would not be achievable with adequate strength. This is reflected by a more severe strength degradation of Specimen D1 at its largest displacement level of 11 mm, a 13% strength reduction off its ultimate load, compared with the other specimens at the same displacement level where Specimen D2 had a 5% strength reduction while Specimens D3 and D4 were just about to reach their ultimate loads. The larger displacement level and, hence, improved ductility was achieved by

Table 5.2 Relative Load-Deformation Relationships for Specimen D1.

Relative Displacement (mm)	Ductility Ratio	Load (kN)	$\frac{\text{Load}}{\text{Ultimate Load}} \times 100\%$
1.22	0.31	29.63	31.6
2.85	0.74	57.77	61.6
4.20	1.08	70.91	75.6
6.09	1.57	80.24	85.5
7.91	2.04	90.62	96.6
9.58	2.47	87.71	93.5
11.19	2.89	81.32	86.7

Table 5.3 Relative Load-Deformation Relationships for Specimen D2.

Relative Displacement (mm)	Ductility Ratio	Load (kN)	$\frac{\text{Load}}{\text{Ultimate Load}} \times 100\%$
1.34	0.35	37.5	43.4
1.67	0.43	40.81	47.2
5.01	1.29	73.06	84.5
8.22	2.12	81.51	94.2
11.54	2.98	82.35	95.2
14.89	3.84	77.33	89.4
18.15	4.68	66.53	76.9

Table 5.4 Relative Load-Deformation Relationships for Specimen D3.

Relative Displacement (mm)	Ductility Ratio	Load (kN)	$\frac{\text{Load}}{\text{Ultimate Load}} \times 100\%$
4.00	1.03	52.1	57.6
4.45	1.15	67.64	74.7
12.30	3.17	90.19	99.7
20.28	5.23	86.07	95.1
28.13	7.26	69.61	76.9
36.30	9.37	58.53	64.7

Table 5.5 Relative Load-Deformation Relationships for Specimen D4.

Relative Displacement (mm)	Ductility Ratio	Load (kN)	$\frac{\text{Load}}{\text{Ultimate Load}} \times 100\%$
3.37	0.87	55.5	51.8
7.90	2.04	105.33	98.3
13.45	3.47	107.18	100
18.81	4.85	103.88	96.9
23.81	6.14	89.05	83.1
28.83	7.44	76.95	71.8
33.81	8.73	62.72	58.5

Table 5.6 Stiffness Variation for Specimen D1.

Relative Displacement (mm)	Ductility Ratio	Stiffness (kN/mm)	% of Initial Stiffness
0	0	27.6	100
2.85	0.74	14.0	50.7
4.20	1.08	10.4	37.7
6.09	1.57	8.7	31.5
7.91	2.04	7.9	28.6
9.58	2.47	5.7	20.7
11.19	2.89	4.3	15.6

Table 5.7 Stiffness Variation for Specimen D2.

Relative Displacement (mm)	Ductility Ratio	Stiffness (kN/mm)	% of Initial Stiffness
0	0	26.1	100
1.67	0.43	24.6	94.3
5.01	1.29	10.2	39.1
8.22	2.12	6.1	23.4
11.54	2.98	4.5	17.2
14.89	3.84	2.4	9.2
18.15	4.68	1.7	6.6

Table 5.8 Stiffness Variation for Specimen D3.

Relative Displacement (mm)	Ductility Ratio	Stiffness (kN/mm)	% of Initial Stiffness
0	0	25.0	100
12.30	3.17	5.8	23.2
20.28	5.23	4.3	17.2
28.13	7.26	2.4	9.6
36.3	9.37	1.0	3.9

Table 5.9 Stiffness Variation for Specimen D4.

Relative Displacement (mm)	Ductility Ratio	Stiffness (kN/mm)	% of Initial Stiffness
0	0	27.5	100
7.90	2.04	5.5	20.0
13.45	3.47	5.1	18.5
18.81	4.85	2.4	8.7
23.81	6.14	1.4	5.1
28.83	7.44	1.3	4.7

Specimens D3 and D4 compared with that of Specimens D1 and D2 due to the pronounced participation of the concentrated transverse reinforcement. Figure 5.2 shows a typical shape of the deformed coupling slab at failure of Specimen D2, indicating the severe disturbances in the vicinity of the wall toe regions. The 35×50 gridded surface plot shown in Figure 5.2 was generated from the 14 dial gauge and 16 LVDT readings shown in Figure 3.16, using the PLOTCALL[†] computer program and assuming surface symmetry about the centerline of the shear walls.

5.4 Steel Strains

Most of the top longitudinal reinforcement in Specimens D1 and D2 yielded at deformations corresponding to ductility levels of $\mu = 1.0$ and $\mu = 1.3$, respectively, while the bottom reinforcement yielded at ductility ratios near 2 in both specimens.

[†]PLOTCALL is a commercial computer software by Golden Software for producing topographical contours and surface plots.

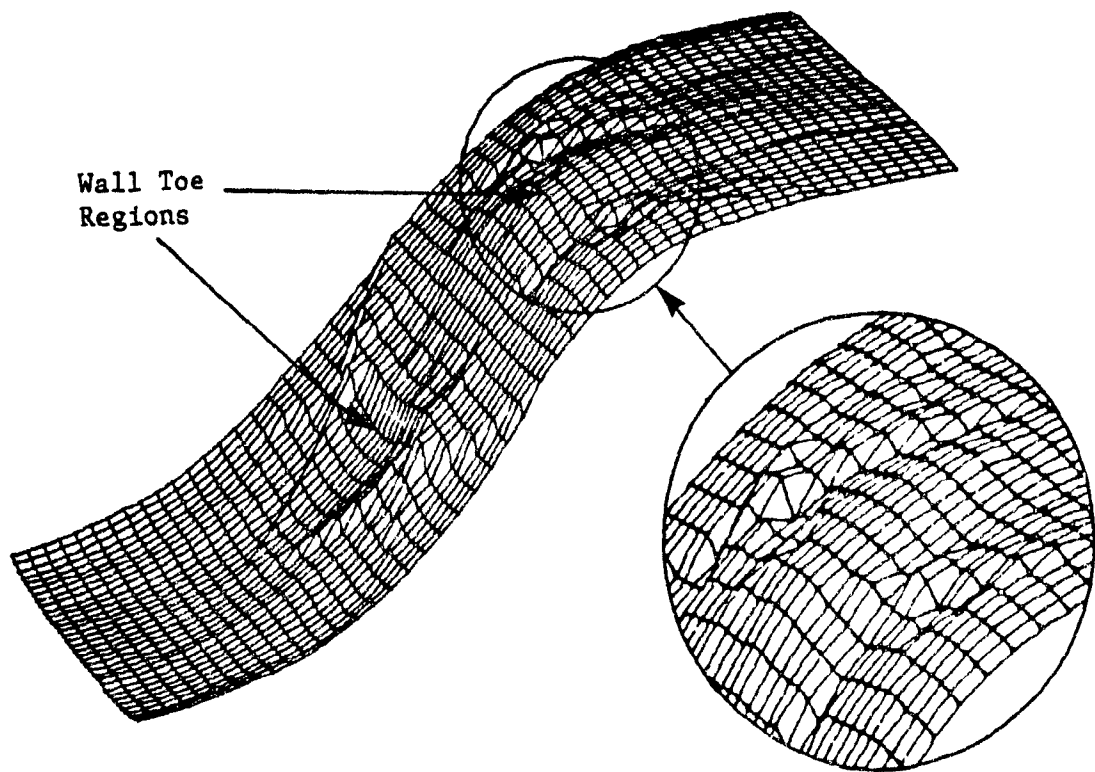


Figure 5.2 Deformed Shape of Coupling Slab at Failure (Specimen D2).

This yielding was more prominent within a width of 375 mm from the shear wall with the strains in this strip being considerably larger (about twice) than the strain in the bars outside this region. An examination of the strains in the longitudinal reinforcement near the shear wall, along with the curvatures caused by the longitudinal displacements, showed that the transfer of load to the wall occurred over a length of about 750 mm from the corridor centerline. Hence, it is recommended that for structural integrity, the longitudinal seismic reinforcement be continued up to a distance equal to two corridor widths from the corridor centerline.

Strains in the concentrated transverse reinforcement showed that significant yielding of these transverse reinforcement occurred up to 750 mm (about 36% of the entire slab width) from the shear wall centerline. The strain variation in the transverse direc-

tion shown in Figures 4.47 and 4.51 clearly indicated that a stress reversal was present along this band of concentrated transverse reinforcement. Significant localized deformation shown in Figure 5.2, within the region whereby the stress reversal in Specimens D3 and D4 occurred, also indicated that stress reversal was present in Specimen D2 despite the absence of concentrated transverse reinforcement.

Strains in the vertical stirrup legs show that the stirrups yielded only after the yield lines had been fully developed. The strains in the inner legs of the stirrups were generally higher than those in the outer legs. Also, the inner and the outer legs of some stirrups in the vicinity of the wall toe and the corridor centerline exhibited yielding after significant shear deformations in the slab had occurred. Therefore, the contribution of these stirrups to resist vertical shear must be ignored. This conclusion was also reached by Malyszko¹⁵ in his tests. However, as observed experimentally, these stirrups should be provided to control damage and to confine the concrete at higher levels of displacements.

5.5 Effective Slab Width

One way of evaluating the cracked slab coupling stiffness is to express it in terms of an effective slab width. The relationship between the stiffness and the effective width can be determined by considering a fixed-ended beam subjected to a relative vertical displacement at each end as shown in Figure 5.3.

The couple required to obtain this relative vertical displacement is

$$V = \frac{12EI}{c^3} \Delta \quad (5-2)$$

where c = length of the beam

E = modulus of elasticity

Δ = relative vertical displacement

I = moment of inertia for a rectangular section

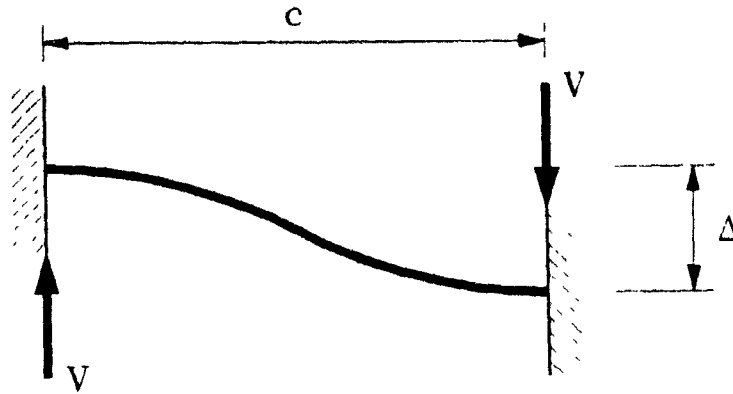


Figure 5.3 Fixed-Ended Beam Subjected to Relative Vertical Displacement, Δ .

$$= \frac{b_{eff} h^3}{12}$$

b_{eff} = effective slab width
 h = thickness of the beam

Thus, for the coupled-slab shear wall, the effective width can be expressed as:

$$b_{eff} = \frac{c^3}{Eh^3} \times \frac{V}{\Delta} \quad (5-3)$$

For the dimensions used in this study, Equation (5-3) results in

$$b_{eff} = 0.002318 \times \frac{V}{\Delta} \quad (5-4)$$

The experimental tangent stiffness values for the slab obtained at selected load cycles are listed in Tables 5.6 to 5.9. The corresponding effective slab widths, calculated using Equation (5-4), are listed in Tables 5.10 to 5.13. Also presented are the slab widths, taken as a percentage of the stirrup cage width (400 mm) which corresponds closely to the corridor width (387 mm).

In order to relate these effective widths and the corresponding slab stiffnesses with the load-deflection response of the test specimens, lines L1 through L5, with varying slopes representing different slab stiffnesses, were introduced in Figures 4.37 to

Table 5.10 Effective Slab Width for Specimen D1.

Relative Displacement (mm)	Ductility Ratio	b_{eff} (mm)	% of Cage Width Stiffness
0.91	0.23	64.3	16.1
1.22	0.31	56.3	14.1
2.85	0.74	47.0	11.7
4.20	1.08	39.1	9.8
6.09	1.57	30.5	7.6
7.91	2.04	26.6	6.6
9.58	2.47	21.2	5.3
11.19	2.89	16.8	4.2

Table 5.11 Effective Slab Width for Specimen D2.

Relative Displacement (mm)	Ductility Ratio	b_{eff} (mm)	% of Cage Width Stiffness
1.34	0.35	64.9	16.2
1.67	0.43	56.6	14.2
5.01	1.29	33.8	8.5
8.22	2.12	23.0	5.7
11.54	2.98	16.5	4.1
14.89	3.84	12.0	3.0
18.15	4.68	8.5	2.1

Table 5.12 Effective Slab Width for Specimen D3.

Relative Displacement (mm)	Ductility Ratio	b_{eff} (mm)	% of Cage Width Stiffness
1.617	0.42	63.07	15.8
4.00	1.03	30.19	7.5
4.45	1.15	35.23	8.8
12.30	3.17	17.00	4.2
20.28	5.23	9.84	2.5
28.13	7.26	5.74	1.4
36.30	9.37	3.74	0.9

Table 5.13 Effective Slab Width for Specimen D4.

Relative Displacement (mm)	Ductility Ratio	b_{eff} (mm)	% of Cage Width Stiffness
2.64	0.68	65.75	16.4
3.37	0.87	38.17	9.5
7.90	2.01	30.91	7.7
13.45	3.47	18.47	4.6
18.81	4.85	12.80	3.2
23.81	6.14	8.67	2.2
28.83	7.44	6.19	1.5
33.81	8.73	4.30	1.1

Table 5.14 Stiffness Values of Lines L1 to L5 Used in Figures 4.37 through 4.40.

Line	b_{eff} (mm)	% of Cage Width	% of Full Slab Width	Stiffness (kN/mm)
L1	400	100	20	86.30
L2	100	25	5	21.57
L3	40	10	2	8.63
L4	20	5	1	4.31
L5	8	2	0.4	1.73

4.40. These slab stiffnesses were calculated using Equation (5-3), with the moment of inertia replaced by the cracked moment of inertia taken to be 50% of the homogeneous uncracked moment of inertia of the slab having an effective width of b_{eff} :

$$\begin{aligned}
 K &= \frac{V}{\Delta} = \frac{12E_c I_{cr}}{c^3} \\
 &= \frac{12E_c}{c^3} \left(0.5 \times \frac{b_{eff} h^3}{12} \right) \\
 &= 0.5E_c \left(\frac{h}{c} \right)^3 b_{eff} \quad (5-5)
 \end{aligned}$$

Table 5.14 summarizes the stiffness values, which are slopes of the lines L1 to L5 based on Equation (5-5), and the associated effective widths.

CHAPTER 6

SUMMARY AND COMPARISON WITH PREVIOUS WORK

6.1 Comparison with Previous Work by Malyszko¹⁵ and Khan¹⁶

6.1.1 Introduction

Figure 6.1 depicts the three phase experimental program which is comprised of the work by Malyszko¹⁵, Khan¹⁶ and the findings of this investigation. Phase 1 tests, performed and reported by Malyszko¹⁵, comprised of the shear walls coupled by flat slabs with various stirrup spacings, and are denoted as the S-series. Phase 2 tests were carried out by Khan¹⁶. Although he tested three specimens, only two specimens are discussed here because Khan's¹⁶ first test was merely an extension of Malyszko's¹⁵ work. Khan¹⁶ used a narrow rectangular reinforced concrete beam with dimensions of 100 × 83 mm across the corridor opening above the slab. Also included in his specimens were concealed transverse beams under the wall toe regions. These two specimens were denoted as the B-series. The primary difference between the B specimens was the flexural reinforcement content within the concealed transverse beam, with Specimen B2 having a larger reinforcement content than Specimen B1. Finally, the tests on slabs with drop panel investigated in this investigation constituted the Phase 3 tests. A brief summary of the experimental results for all three phase specimens is shown in Table

Table 6.1 Summary of Experimental Results of Phases 1, 2 and 3 Specimens.

	Specimen No.								
	S1	S2	S3	B1	B2	D1	D2	D3	D4
Central Longitudinal Cage (or Beam) Reinforcement									
-Longitudinal Steel Top, Bottom, %	1 84	1 84	1 84	1 94	1 94	1 01	1 01	1 01	1 01
-Yield Strength, MPa	214	214	205	270	270	274	274	280	280
-Stirrup Spacing, mm	—	46	23	60	60	23	41	41	41
-Yield Strength, MPa	—	234	243	250	250	190	190	190	190
Transverse Reinforcement or Reinforcement in Concealed Beam									
-Main Reinforcement	—	—	—	3 D7 T 3 D7 B	4 D7 T 4 D7 B	0.95	0.53	1.32	1.58
-Yield Strength, MPa	204.8	214.3	213.6	270	270	274	274	280	280
-Stirrup Spacing, mm	—	—	—	33	33	—	—	—	—
-Yield Strength, MPa	—	—	—	250	250	—	—	—	—
Beam Stem or Drop Panel Geometry, mm	—	—	—	100×83	100×83	450×33	450×33	450×33	450×33
Concrete Strength, MPa	37	37	36.4	39	39	37	35	40	40
Specimen Strength, kN									
At $\mu = 3$	42.8	43.6	43.4	84.0	92.2	57.4	66.1	89.4	106.1
At $\mu = 5$	41.5	37.1	38.3	75.0	74.4	74.3	77.5	85.8	105.1
Experimental Ultimate Strength, kN (Corrected to $f'_c = 35$ MPa)	42.8	43.6	43.4	84.0	92.2	86.2	84.6	86.8	103.1
Theoretical Ultimate Strength, (Yield Line Theory), kN	46.8	46.8	46.8	70.5	70.5	84.8	86.1	87.1	87.1
Theoretical Punching Shear Strength, kN	39.2	39.5	39.5	N.A.	N.A.	89.5	80.2	85.7	85.7
Initial Stiffness, kN/mm	12.55	12.70	12.14	16.0	16.8	27.6	26.1	25.0	27.5
Stiffness ($\mu = 3$), kN/mm	4.91	2.57	3.25	6.0	6.8	13.7	14.6	6.2	5.6
Mode of Failure	F.Y.L. P.S.	F.Y.L. P.S.	F.Y.L. P.S.	F.Y.L. S.S.	F.Y.L. S.S.	F.Y.L. P.S.	F.Y.L. P.S.	F.Y.L. P.S.	F.Y.L. P.S.

- N.A. — Not Applicable
 F.Y.L. — Flexure, Yield Lines
 P.S. — Punching Shear
 S.S. — Sliding Shear at Slab-Beam Interface
 T. — Top
 B. — Bottom

6.1.

6.1.2 Strength and Stiffness Degradation

Specimen S1 forms the basis of comparison for all specimen results since it represents the structural layout mostly used in practice at present. The results in Table 6.1

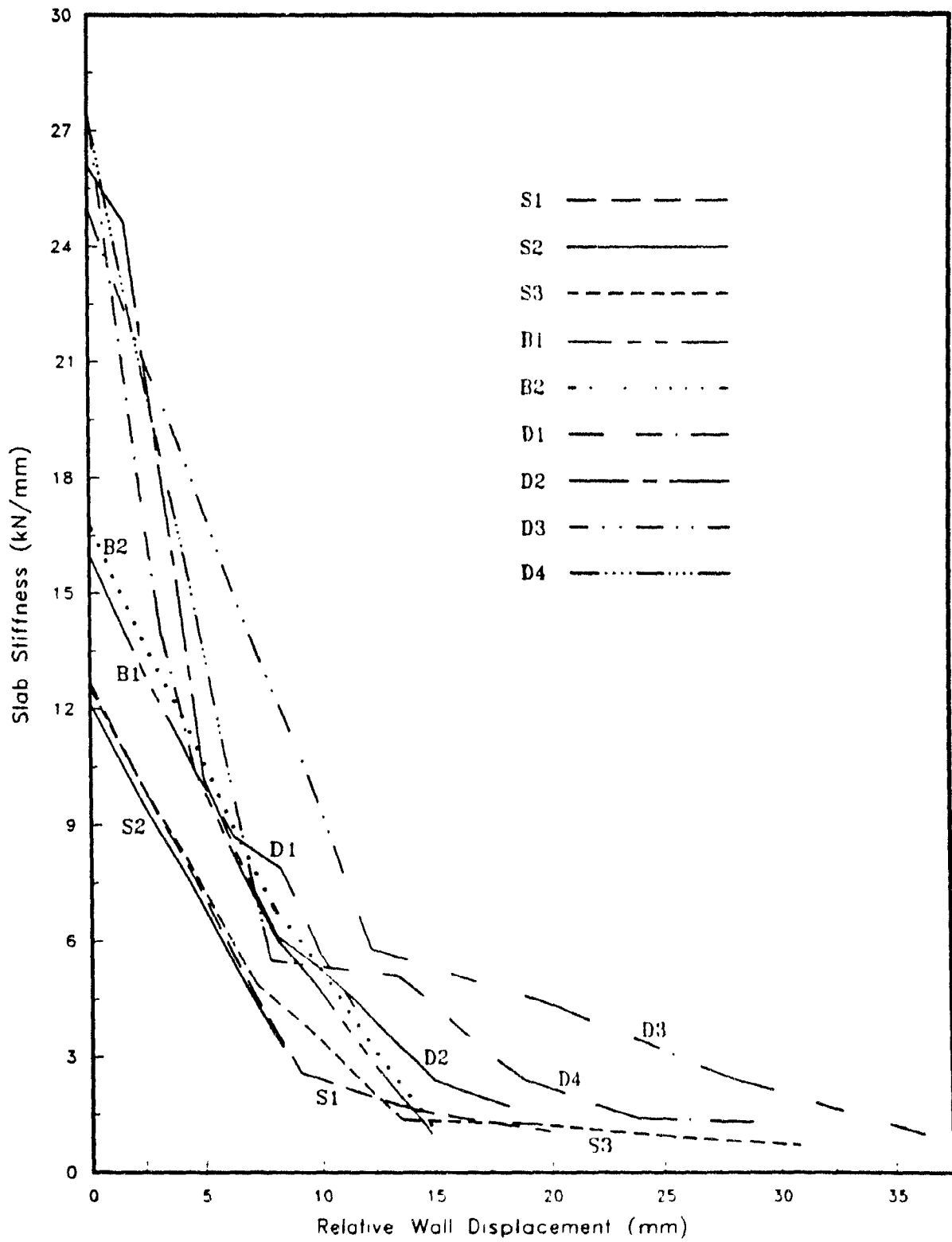


Figure 6.2 Variation of Coupled Slab-Shear Wall System Stiffness with Relative Wall Displacement.

show that the strengths and stiffnesses of the slabs with drop panel were, in general, a little more than twice those of the specimens without drop panel. The stiffnesses of the slabs with drop panel were also 56% higher than those of specimens with beams while the strengths of the Phase 2 and Phase 3 specimens were generally of the same magnitude. Figure 6.2 shows the stiffness variation with relative wall displacements for all 9 specimens. It is obvious from this figure that the slabs with drop panel (Specimens D1, D2, D3 and D4) have higher stiffnesses than Phase 1 and Phase 2 specimens, with stiffness values of more than 10% of their initial stiffnesses at a moderate relative wall displacement of about 12 mm ($\mu \geq 3$). However, the slopes of the graph in Figure 6.2 also indicate that the slabs with drop panel, showing steeper slopes, have a higher rate of stiffness degradation. As observed by Taylor¹⁴, the stiffness of the various specimens decreased significantly as cycles of increasing displacements were imposed. At ductility ratios near 3, the observed average stiffnesses of the specimens without drop panel was about 0.35 of the uncracked stiffness while those of the specimens with drop panels was about 0.25 of the uncracked stiffness. The stiffnesses of Specimens B1 and B2 decreased drastically during the inelastic cycles because of the horizontal sliding shear damage in the shallow beams during the reversed displacement cycles. The ultimate deformations observed in Phase 2 specimens were about half those observed in the specimens with drop panels in Phase 3. For light earthquakes, the stiffness variation response of coupled slab-shear wall systems with drop panels was more favorable than those using narrow beams across corridor openings. For heavy earthquakes, the use of narrow beams across corridor openings should be avoided because of severe distress at the beam-slab intersection that caused sliding shear failures in the Phase 2 specimens. Slabs with or without drop panels, however, provide approximately 10% of the initial stiffness values during heavy earthquakes ($\mu \geq 6$). Because of the ease of construction over the narrow beam system, the use of drop panel is recommended where high initial stiffness is required.

The variations of strength with relative wall displacements for all nine specimens were also plotted and are shown in Figure 6.3. Provision of a shallow beam or a drop panel in Phase 2 and Phase 3 specimens increased the ultimate shear strength by a factor of 2 over that of Specimen S1, except for Specimen D4 where an increase of 140% in strength over that of Specimen S1 was observed. All slabs with drop panel exhibited average strengths of 55%–60% of their ultimate strengths at higher displacement levels ($\mu \geq 7$) and displayed a much smaller rate of strength deterioration at intermediate displacement levels ($3 \leq \mu \leq 6$) as compared with specimens with shallow beam (Phase 2 specimens), which exhibited an average strength of only 20% at higher displacements ($\mu \geq 7$).

6.1.3 Ultimate Strengths

The punching shear strengths of Specimens S1, S2, and S3 were calculated using Equation (5-1) (see Table 6.1), and the results showed that these theoretical punching shear strengths agreed reasonably well with experimental ultimate strengths observed by Malyszko¹⁵. Equation (5-1) is identical to the expression proposed by Schwaighofer and Collins¹ based on their test on one coupled slab-shear wall system subjected to monotonically increasing loads until failure. The presence of the concentrated transverse reinforcement near the wall toe regions resulted in an improved load distribution near the wall toe region, basically due to the load transfer by transverse flexure and dowel action, in addition to increased shear friction at the cracks. It can be noted from Table 6.1 that the punching shear strength prediction for Specimen D4 using Equation (5-1) is quite conservative. It is recommended that transverse reinforcement be provided in all slab-shear wall systems in the vicinity of the shear wall toe. While more research is needed in this area to develop quantitative relationships, it is recommended that this concentrated transverse reinforcement ratio should not be less than 1.05% (this does not include the stirrups provided), which is the ratio of the steel

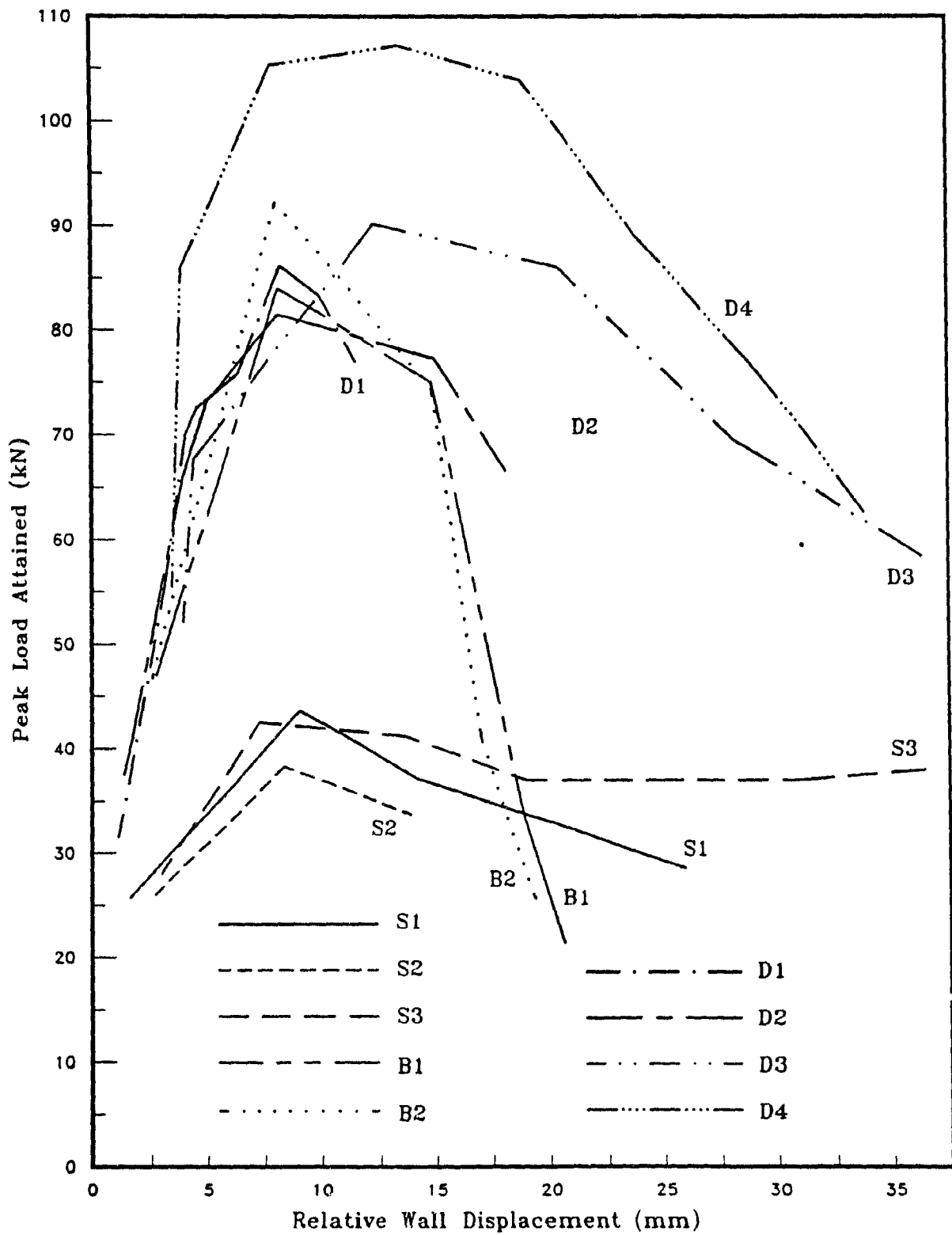


Figure 6.3 Variation of Coupled Slab-Shear Wall System Strength with Relative Wall Displacement.

reinforcement used in Specimen D4.

6.2 Effective Slab Width

An important parameter related to the design of slabs as coupling members is the concept of effective width, b_{eff} . The implementation of an effective width of the slab allows the engineer not only to design the appropriate slab reinforcement, but also to enable the engineer to grasp the extent of the slab participation in the distribution of the load.

Qadeer and Stafford Smith⁷ presented non-dimensional graphs (see Figure 1.3) from the results of their finite difference analysis on coupled slab-shear wall systems for evaluating the stiffness and the effective width of the coupling slabs. Based on their recommendations, the parameters required for the determination of the effective slab width of the model structures in this investigation would be

$$Y = 2067 \text{ mm}$$

$$C = 0.0$$

$$L = 387 \text{ mm}$$

$$X = 3053 \text{ mm}$$

Thus, the appropriate non-dimensional parameters would be

$$\frac{C}{X} = 0$$

$$\frac{Y}{X} = 0.68$$

$$\frac{L}{X} = 0.13$$

Using Figure 1.3a, the ratio of the effective width of the slab to the width of the bay, $\frac{Y_e}{Y}$, is 0.14. Hence, the corresponding effective width of the slab according to Qadeer

and Stafford Smith⁷ is

$$\begin{aligned} Y_e &= 0.14 \times 2067 \text{ mm} \\ &= 289 \text{ mm} \end{aligned}$$

which is 72% of the stirrup cage width or 75% of the corridor width.

Schwaighofer and Collins¹ observed from Szalwinski's¹³ experimental and analytical work on a coupled slab-shear wall system loaded monotonically until failure that the theoretical stiffness calculated using an "effective width" of the slab equal to half of the corridor width (c) and the gross concrete section agreed well with the initial slope of the load-deformation curve. To calculate the stiffness of the cracked coupled system, they suggested that the gross second moment of area of the slab section (effective width = $\frac{1}{2}c$), I_g , be replaced by the second moment of area of the cracked cross-sectional area, I_{cr} .

$$b_{eff} = \frac{12}{d^3} I_{cr} \quad (6-1)$$

To account for the severe cracking at the wall toe region at later test stages, they suggested increasing the span from c to $(c + t)$ where t is the thickness of the wall. Replacing c in Equation (5-2) with $(c + t)$ and I with I_{cr} , the stiffness of the coupling slab can be expressed as

$$\frac{V}{\Delta} = \frac{12EI_{cr}}{(c + t)^3} \quad (6-2)$$

Hence, using Equation (5-3) and replacing the thickness of the coupling member, h , by the effective depth of the slab, d , the resulting effective slab width of the slab is

$$\begin{aligned} b_{eff} &= \frac{c^3}{Ed^3} \times \frac{V}{\Delta} \\ &= \left(\frac{c}{c + t} \right)^3 \frac{12}{d^3} I_{cr} \end{aligned} \quad (6-3)$$

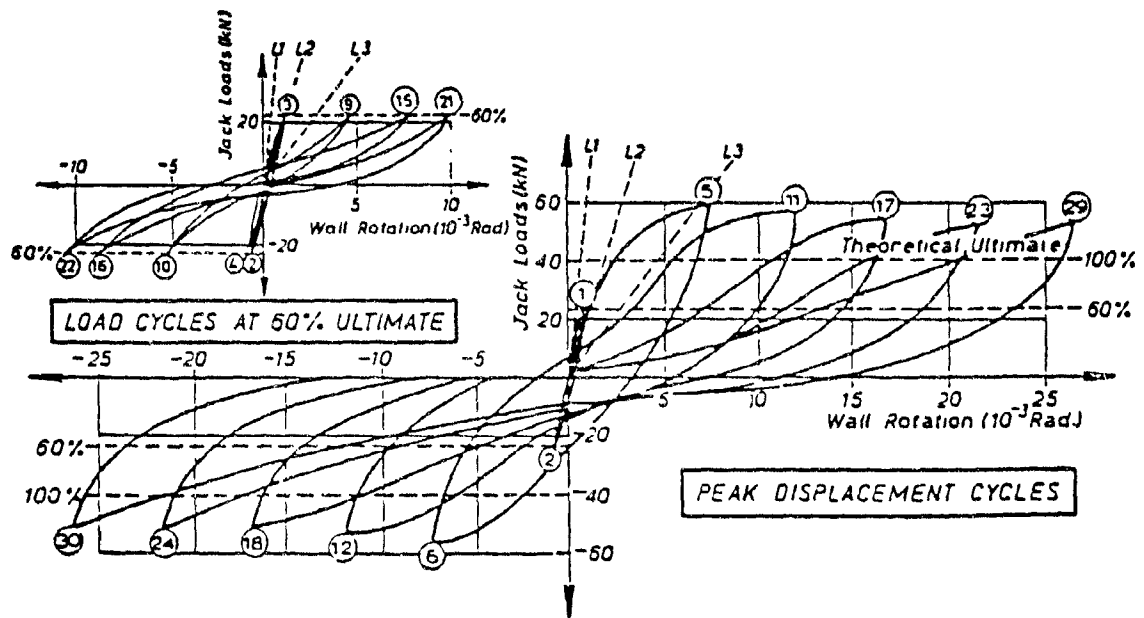


Figure 6.4 Taylor's Unit 2 Force-Displacement Characteristics (ref 14).

Paulay and Taylor¹³ presented load-deformation characteristics of their test specimens which included three lines (Lines L1, L2 and L3) in their graphs - two representing the stiffness of an uncracked coupling slab with widths equal to $0.5c$ and $0.2c$, and the third stiffness based on the second moment of the steel area alone, I_{st} , within the stirrup cage, neglecting the concrete (Figure 6.4). The effective width based on I_{st} can be expressed as

$$b_{eff} = \frac{12}{d^3} I_{st} \quad (6-4)$$

Szalwinski¹³ reported from his experimental study and elastic finite element analysis effective widths of $0.68c$ and $1.58c$, respectively. Taylor⁴ compared his test results with those of Szalwinski's¹³ and suggested that the initial coupling slab stiffness be calculated based on an uncracked section (gross) with a width equal to 20% of the stirrup cage width.

Table 6.2 Equivalent Effective Widths of Model Structure Suggested by Various Investigators.

Investigators	Effective Width (mm)
Barnard and Schwaighofer ⁶	2065
Tso and Mahmoud ²⁸	413
Black <i>et al</i> ¹¹	366
Wong and Coull ²⁹	342
Qadeer and Stafford Smith ⁷	289
Schwaighofer and Collins ¹ - $b_{eff} = 0.5c$	193
Szalwinski ¹³ - $b_{eff} = 1.58c$	611
Szalwinski ¹³ - $b_{eff} = 0.68c$	263
Paulay and Taylor ³ - $b_{eff} = 0.5c$	193
Paulay and Taylor ³ - $b_{eff} = 0.2c$	80
Taylor ¹⁴ - $b_{eff} = 0.2c$	80

Using the charts and suggestions of the following investigators, the values of the effective coupling slab widths participating in the lateral stiffness of the system used in this investigation were calculated and are shown in Table 6.2.

The equivalent values of the effective coupling slab widths participating in the lateral stiffness of the system based on the second moment of area of the cracked cross-sectional area (I_{cr}) as suggested by Schwaighofer and Collins¹ and based on the second moment of the steel area alone (I_{st}) as suggested by Paulay and Taylor³ were also computed, using the dimensions of Phase 1 and Phase 3 model dimensions. The values of the second moment of area of the cracked concrete section, based on a slab width of $0.5 \times$ the corridor width for Phase 1 and Phase 3 specimens, are $I_{cr} = 1.482 \times 10^6 \text{ mm}^4$ and $I_{cr} = 5.217 \times 10^6 \text{ mm}^4$, respectively. The values of the second moment of area of the seismic longitudinal reinforcement within the stirrup cage for Phase 1 and Phase 3 specimens are $I_{st} = 1.56 \times 10^6 \text{ mm}^4$ and $I_{st} = 7.299 \times 10^6 \text{ mm}^4$, respectively. The values of the effective widths thus computed are tabulated in Table 6.3.

The calculated values of b_{eff} for Phase 1 specimens, reported by Malyszko¹⁵, and for Phase 3 specimens, tested in this investigation, are shown in Table 6.4.

It can be concluded that all of the elastic analysis methods overestimate the stiff-

Table 6.3 Effective Widths of Phase 1 and Phase 3 Specimens Based on I_{cr} and I_{st} .

	Equivalent Effective Width (mm)	
	Phase 1 Specimens	Phase 3 Specimens
Schwaighofer and Collins¹:		
(i) $b_{eff} = \frac{12}{d^3} I_{cr}$	151	113.6
(ii) $b_{eff} = \left(\frac{c}{c+t}\right)^3 \frac{12}{d^3} I_{cr}$	83.2	62.6
Paulay and Taylor¹³:		
$b_{eff} = \frac{12}{d^3} I_{st}$	159	159

Table 6.4 Calculated Effective Widths of Phase 1 and Phase 3 Specimens Based on Experimental Results.

Phase	Specimen	Effective Width
1	S1	$b_{eff} = 96.0 \text{ mm} = 0.25c$
	S2	$b_{eff} = 97.2 \text{ mm} = 0.25c$
	S3	$b_{eff} = 92.9 \text{ mm} = 0.24c$
3	D1	$b_{eff} = 64.3 \text{ mm} = 0.16c$
	D2	$b_{eff} = 64.9 \text{ mm} = 0.16c$
	D3	$b_{eff} = 63.07 \text{ mm} = 0.16c$
	D4	$b_{eff} = 65.75 \text{ mm} = 0.16c$

ness of the coupled slab-shear wall system. The calculated stiffnesses, using a coupling slab width equal to $0.5 \times$ the corridor width, also overestimate the initial stiffness of the coupled slab-shear wall system without drop panels by a factor of about 2 and the initial stiffness of the coupled slab-shear wall system with drop panels by a factor of about 3. Despite the use of I_{cr} in place of I_g and a slab width of $0.5c$ for calculating the I_{cr} , the initial stiffness as proposed by Schwaighofer and Collins¹ also overestimates the initial stiffness of the coupled slab-shear wall system without drop panels by a factor of 1.6 and the initial stiffness of the coupled slab-shear wall system with drop panels by a factor of 1.75. When the more stringent evaluation of stiffness by Schwaighofer and Collins¹, where the span was increased from c to $(c + t)$, is employed, the calculated equivalent effective coupling slab width is slightly conservative in comparison with the observed initial stiffness of the coupled slab-shear wall system without drop panels and

is in good agreement with the observed initial stiffness of the coupled slab-shear wall system with drop panels. Taylor's¹⁴ suggestion of using an effective slab width equal to 0.2 of the stirrup cage width yields a value of 80 mm, which is slightly conservative for the coupled slab-shear wall system without drop panels. Paulay and Taylor's³ recommendation for evaluating the initial stiffness based on the second moment of the steel area alone within the stirrup cage yields an equivalent effective width of 159 mm for the coupled slab-shear wall system with and without drop panels.

Although the provision of a drop panel increases the strength and stiffness considerably (by more than a factor of 2), the relative value of the effective slab width decreases. More experimental and analytical research is needed in this area. However, it is suggested that, for the evaluation of the lateral stiffness of the coupled slab-shear wall system, Equation (6-3) be used to calculate the effective width of the coupling slab and that the values computed should not exceed $\frac{1}{4}c$ for coupling slabs without drop panels and $\frac{5}{32}c$ for coupling slabs with drop panels (drop panel depth = $\frac{1}{2}$ slab thickness).

As observed by Taylor¹⁴, Szalwinski¹³ and Malyszko¹⁵, all of the specimens in the present investigation exhibited considerable deterioration of stiffness as increasing levels of displacements were imposed on the system. The stiffness near the ultimate load was less than 13% of the initial stiffness for Specimens D2, D3 and D4. Specimen D1 had a stiffness of 26% of the initial stiffness at the end of the test because the test was stopped prematurely due to the malfunctioning of the Optilog data acquisition system.

Based on the findings of this investigation and those of Malyszko¹⁵, Paulay and Taylor³ and Szalwinski¹³, it is suggested that the following values be used to evaluate the stiffness of coupled slab-shear wall systems reinforced with closed stirrups in the slab subjected to lateral loads caused by earthquakes.

Stiffness of a slab-shear wall system subjected to light earthquakes:

— without drop panel - (0.35 of the initial stiffness)

— with drop panel - (0.25 of the initial stiffness)

Stiffness of a slab-shear wall system subjected to moderate and heavy earthquakes:

— with and without drop panel (0.1 of the initial stiffness)

6.3 Summary

The experimental results of this investigation and that of Malyszko¹⁵ and Khan¹⁶ can now be summarized in the following sections.

6.3.1 Ultimate Strengths

The ultimate strength of the specimens can be predicted reasonably accurately using the yield line theory. Cycling the load at a given displacement caused progressive strength deterioration because of accumulated damage as a result of the repeated and reversed shear displacements.

Provision of shallow beams in Phase 2 specimens increased the ultimate strength by a factor of about 2. Provision of drop panels also resulted in a strength increase by a factor of more than 2 in all of the specimens tested in this investigation. Specimens D1 and D2 had no concentrated transverse reinforcement. The Specimen D4, with 1.58% concentrated transverse reinforcement ratio (this includes the horizontal legs of the stirrups), showed a 140% increase in strength over Malyszko's¹⁵ Specimen S1 which did not have a drop panel or stirrups.

The test specimens in this investigation exhibited strengths of 55%–60% of their ultimate strengths at higher displacements levels ($\mu \geq 7$) and displayed a much smaller rate of strength deterioration at intermediate displacement levels ($3 \leq \mu \leq 6$) as compared with Khan's¹⁶ specimens with shallow beams, which exhibited an average strength of only 20% of their ultimate strengths at higher displacements levels ($\mu \geq 7$). Therefore, it is recommended that concentrated transverse reinforcement be provided in all slab-shear wall systems in the vicinity of the shear wall toe, as shown in Figure

6.5. While more research is needed in this area to develop quantitative relationships, it is recommended that this concentrated reinforcement ratio should not be less than 0.79% (this does not include the stirrups provided). This will help with an improved distribution of loads due to transverse flexure, increased dowel action and augmented shear friction at the cracks due to the additional damping action.

6.3.2 Crack Propagation

Fewer and wider cracks were observed for the slab with no stirrups than in the slabs with stirrups. The cracks propagated and widened after some additional load cycles. These cracks were more distributed and much smaller in width as increased amount of transverse reinforcement near the wall toes was used.

The crack patterns observed were similar in all cases and can be assumed to occur in stages, as shown in Figure 5.1

6.3.3 Stirrup Performance

Provision of stirrups around some of the longitudinal reinforcement did not improve the ultimate strength significantly. However, it did help with the control of the rate of damage near the wall toe region and the punching shear failure that occurred after formation of the yield lines. Provision of stirrups caused a significant delay in this damage and the subsequent punching shear failures. It was shown by Malyszko¹⁵ that stirrups spaced at spacings of d (the slab effective depth) in Specimen S2 were not as effective as the stirrups spaced at spacings of $\frac{1}{2}d$ in Specimen S3. The horizontal legs were effective in distributing the load due to flexural and dowel actions and augmentation of the shear friction phenomenon due to their clamping action. The vertical legs of the stirrups were not as effective in resisting the vertical shear transferred to the shear wall resulting from the moments along the yield lines. Thus, the main function of the stirrups was in the basic control of the cracking damage and in the delay of the

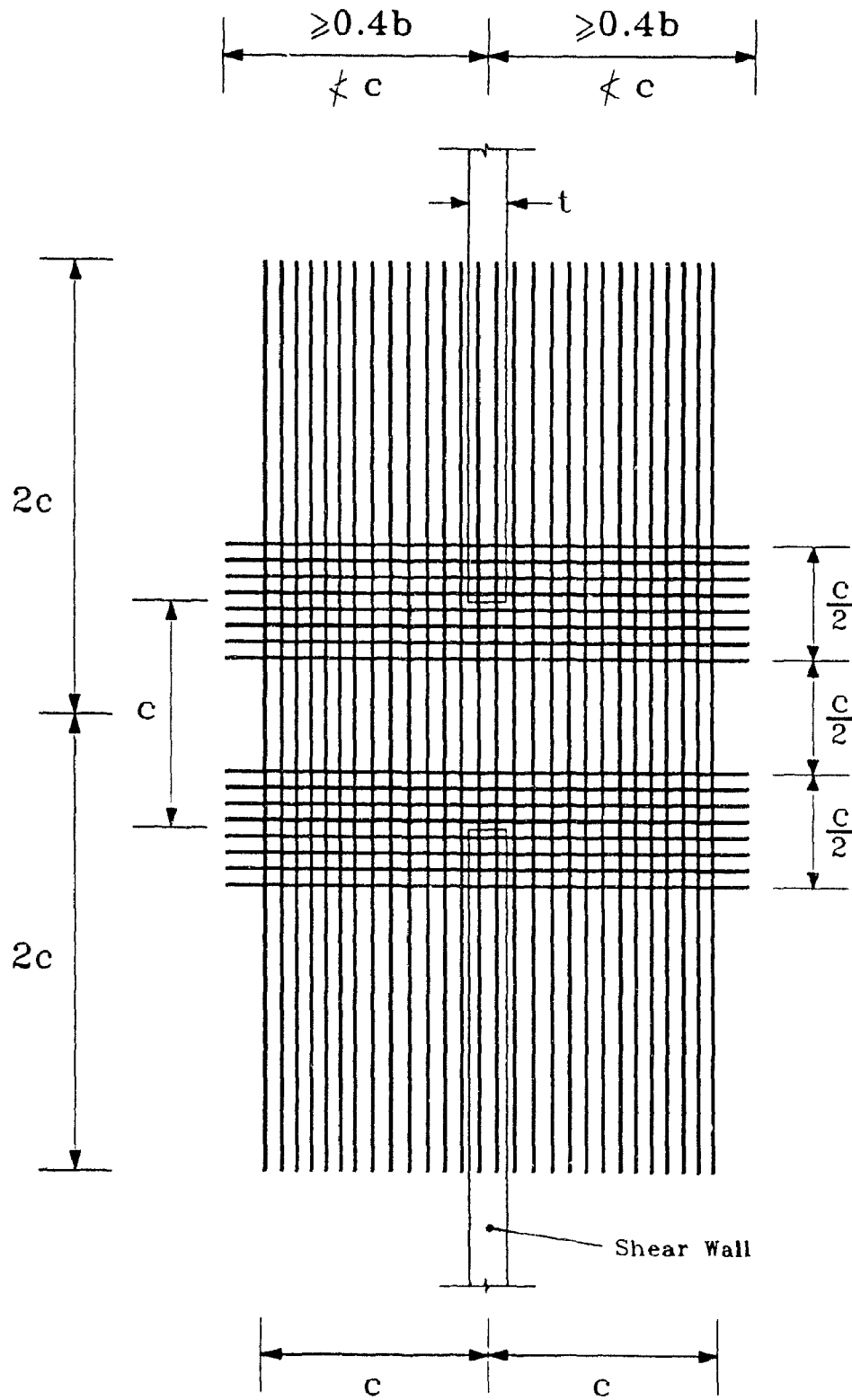


Figure 6.5 Longitudinal and Transverse Reinforcement Detail.

punching shear failure. Therefore, it is recommended that four-legged closed stirrups with total width equal to the corridor width be used at a spacing of $\frac{1}{2}d$ along the entire corridor width and up to a distance of two corridor widths from the corridor centerline.

6.3.4 Stiffness

The observed stiffness of the various specimens tested in this investigation and by Malyszko¹⁵, Khan¹⁶ and Taylor¹⁴ decreased significantly as cycles of increasing displacements were imposed. The initial stiffnesses of the specimens with drop panels were a little more than twice those of Phase 1 specimens without drop panels, with an average value of 266 kN/mm but the relative value of the effective slab width decreased by a factor of 0.68. The provision of concentrated transverse reinforcement decreases the rate of stiffness degradation. At a displacement level of 11 mm ($\mu = 2.84$), the stiffnesses of Specimens D1 and D2, which had transverse reinforcement ratios of 0.95% and 0.55%, respectively, (contributed by the horizontal legs of the stirrups) were about 15% of their initial stiffnesses while the stiffnesses of Specimens D3 and D4, which had transverse reinforcement ratios of 1.32% and 1.58% (including the horizontal legs of the stirrups), respectively, were about 23% and 19% of their initial stiffness values, respectively. At ductility ratios of about 3, the observed average stiffnesses of Malyszko's¹⁵ specimens without drop panels was about 0.35 of the uncracked stiffness, while that of the specimens tested in this investigation with drop panels was about 0.25 of the uncracked stiffness

6.3.5 Longitudinal Strains

All of the longitudinal reinforcement in the slabs yielded at higher levels of relative displacements ($\mu \geq 2$). However, the strain in the longitudinal reinforcement near the wall were much higher than the corresponding strains near the free slab edge. This relationship also prevailed at lower displacements, showing a concentration of higher

strains and, therefore, a more effective load transfer over a width equal to $0.9 \times$ the corridor width, on each side of the shear wall centerline.

6.3.6 Displacement Profiles

The deflection profiles in the longitudinal direction show that the curvatures developed in the slab decreased gradually down to very small values at a distance of about two corridor lengths from the corridor centerline, beyond which these curvatures and the associated load transfer were minimal at all loading stages.

Based on these displacement profiles and the longitudinal strains, it is recommended that the special longitudinal seismic reinforcement be provided over a rectangular area, two corridor lengths by four corridor lengths centered about the centerlines of the shear walls and the corridor (see Figure 6.5).

6.3.7 Punching Shear Strength

The nominal punching shear stress, $v_n = \frac{V}{3d(t+d)}$ (Equation (5-1)), based on observation of the crack pattern in all Phase 1, Phase 2 and Phase 3 specimens tested under reversed, cyclic loads, is exactly the same as the expression proposed by Schwaighofer and Collins¹, which was based on their test on one coupled slab-shear wall system subjected to monotonically increasing loads until failure.

The punching shear strength prediction using Equation (5-1) agreed with the experimental data from Malyszko's¹⁵ specimens and Specimens D1, D2 and D3 of this investigation, assuming $v_n = 0.33\sqrt{f'_c}$ MPa. All of the calculated punching shear strengths, using Equation (5-1), were slightly on the conservative side.

The presence of concentrated transverse reinforcement near the wall toe regions resulted in an improved load distribution, basically due to the load transfer by transverse flexure and dowel action, in addition to increased shear friction at the cracks. It can be noted from Table 6.1 that Equation (5-1) results in fairly conservative punching

shear strength prediction for Specimen D4, which had a transverse reinforcement ratio of 1.58%. However, Specimen D3, which had a transverse reinforcement ratio of 1.32%, did not show as much deviation (5.5%) in punching shear strength from that predicted by Equation (5-1) as did Specimen D4 (20.3%). More experimental and analytical research is needed in this area.

CHAPTER 7

RECOMMENDATIONS AND CONCLUSIONS

7.1 Design Recommendations

The following tentative design recommendations can be formulated from the findings of this and other previous investigations on coupled slab-shear wall systems at McGill University :

1. Provision of closed stirrups, preferably 4-legged (overall width equal to the corridor width) at a spacing of $\frac{1}{2}d$ to contain part of the longitudinal seismic reinforcement.
2. Provision of additional longitudinal seismic reinforcement in a plan area, two corridor lengths by four corridor lengths (Figure 6.5), calculated according to the needs.
3. Provision of concentrated transverse reinforcement ratio of at least 0.8% near the wall toe regions (see Figure 6.5) for improved load transfer through transverse flexure, increased dowel action, and augmented shear friction at the cracks due to the clamping action of the stirrups. These concentrated transverse reinforcement should extend at least 40% of the bay width on either side of the shear wall centerline and should also extend no less than the width of the corridor opening on either side of the shear wall centerline.
4. For buildings in areas which can be subjected to moderate or heavy earthquakes, it is recommended that a drop panel, projecting $\frac{1}{3}h$ to $\frac{1}{2}h$ below the slab, where

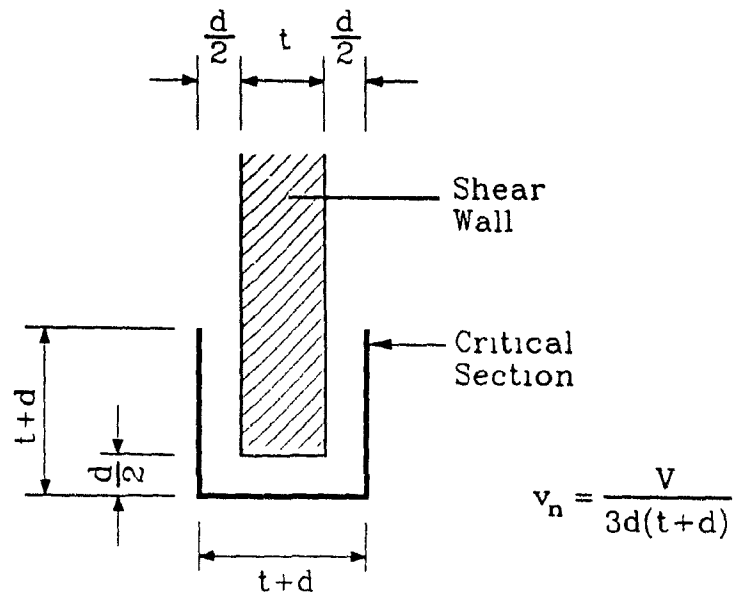


Figure 7.1 Critical Section for Punching Shear Around the Wall Toe.

h = overall slab thickness, be used with reinforcement details as in (1) above.

5. Shallow beams should not be used until adequate ductility and damage control provisions can be provided with confidence. The shallow beams in Khan's specimens displayed considerable damage in the beam stem and much less cracking damage in the slab. Also, the rate of deterioration of strength and stiffness with increasing deformations was quite drastic. More research is needed in this area.
6. The slab punching shear strength at the wall toe region can be estimated conservatively using Equation (5-1). The critical section of the slab at the wall toes due to punching shear can be taken as the perimeter around the wall toes at a distance of $\frac{1}{2}d$ from the wall faces and extending a distance of $(t + \frac{1}{2}d)$ behind the wall toe (Figure 7.1).
7. All of the available elastic analysis methods overestimate the stiffness of the coupled slab-shear wall systems. Based on the findings of this and other investigations, it is suggested that to calculate the initial lateral stiffness of the coupled slab-shear wall systems subjected to lateral loads, Equation (6-3) should be used to compute an

effective slab width but that the value computed should not exceed $\frac{1}{4}c$ for coupling slabs without drop panels and $\frac{5}{32}c$ for coupling slabs with drop panels. The stiffness of coupled slab-shear wall systems subjected to light or heavy earthquakes can be estimated using the following values:

- (a) Stiffness of a coupled slab-shear wall system subjected to light earthquakes (ductility ratio $\mu \leq 3$)
 - without drop panels - (0.35 of the initial stiffness)
 - with drop panels - (0.25 of the initial stiffness)
- (b) Stiffness of a coupled slab-shear wall system subjected to heavy earthquakes (ductility ratio $\mu \geq 6$)
 - with or without panels - (0.1 of the initial stiffness)

The latter value can be so small that the slab coupling effect can be ignored for heavy earthquakes. For moderate earthquakes, the stiffness of the coupled slab-shear wall system may be interpolated between the above two limits.

7.2 Conclusions

The response of slab coupling with drop panels in coupled slab-shear wall structures was investigated in this experimental investigation. The tests were performed on four $\frac{1}{3}$ -scale reinforced concrete models of coupled slab-shear wall assemblies. Various stirrup arrangements and concentrated transverse reinforcement layouts were utilized and the test specimens were subjected to progressively increasing displacement cycles under reversed cyclic loading conditions. The results of this investigation are compared with those of Malyszko¹⁵, Khan¹⁶ and Taylor¹⁴ and the following conclusions are drawn:

- The provision of drop panels increases the strength and initial stiffness of the coupling slab system by factor of about two.
- Improved damage control and prevention of rapid deterioration of strength and stiffness can be achieved from the provision of a drop panel than from the provision

of a shallow beam.

- The ultimate flexural strength of the coupling slab can be predicted with reasonable accuracy by the yield line method of analysis.
- Punching shear failure of the slab can not be entirely eliminated with the provision of the drop panel but can be delayed when stirrups and concentrated band of transverse reinforcement under the shear wall toes are included.
- The punching shear strength of the slab near the wall toe regions can be conservatively predicted using Equation (5-1) :

$$v_n = \frac{V}{3d(t+d)}$$

- The stirrups provided within the drop panel region of the slab act not as much in resisting the applied shear force but rather as a clamping mechanism for the concrete under the wall toe regions which underwent severe shearing deformations.
- The transverse reinforcement aided in delaying the punching shear failure, in distributing the forces to the slab further away from the shear wall centerline and in providing dowel action near the wall toe region where punching shear deformation was prominent.
- All four specimens exhibited rapid strength and stiffness degradation at high displacement levels (displacement ductility ratio, $\mu \geq 3$).
- All of the available elastic analysis methods overestimate the initial stiffness of the coupled slab-shear wall systems. However, a more stringent evaluation of the initial stiffness, using the second moment of cracked cross-sectional area of concrete and a span equivalent to the sum of the corridor width and the wall thickness, show good agreement with the observed initial stiffness of all four specimens tested. Typically, the effective width of the slab is about 16% of the corridor opening for coupling

slabs with drop panels and is about 25% of the corridor opening for coupling slabs without any drop panel.

7.3 Recommendations for Future Research

There are many questions arising from this investigation, which merit further consideration in future research in this area.

The strength and stiffness degradation characteristics investigated thus far had been mainly qualitative. More research is necessary to establish quantitatively as to how these characteristics can be accurately assessed. So far, the initial stiffness and the stiffness at failure can be conservatively predicted. However, in an analysis, the degradation of the stiffness within these two limits is an integral part of producing the correct response of a structure. Research in this area could be in the form of developing finite element computer models using the results of this and other investigations.

The damage of the slab near the wall toe regions due to punching shear has yet to be eliminated without the use of a shallow beam. Although improvement in damage control was indicated with the provision of concentrated transverse reinforcement near the affected regions in the slab, the mechanism of punching shear of the slab by the walls at the wall toe regions needs to be closely examined. Although some empirical equations were established in this and other investigations, these equations can not generally be used for various slab coupling systems with special provisions. Research in this area would involve experimental investigation as well as analytical work concentrating on this fundamental punching shear phenomenon alone. This will require the isolation of the wall and slab regions near the wall toes for the study. The effects of dowel action, aggregate interlock, clamping action of the reinforcement, shear friction, and the extent of punching action would be the basic parameters involved in the study.

Although a depth of $\frac{1}{2}h$ was used in this investigation for the drop panel, the response of the slab with various drop panel depths may be studied. Similarly the choice

of the width of the drop panel could also be examined. Generally, the dimensions of these drop panels are largely governed by the size of the stirrup cage. The recommendations for the size of the stirrup cage presented was mainly to ensure a similar response to that observed in this investigation. However, with more experimental and analytical research involving varying drop panel and stirrup cage geometry, quantitative relationships can be established for the dimensions of the drop panels and stirrup cages for each specific coupling slab-shear wall system.

Derecho *et al.*²² had pointed out that in developing a design procedure for earthquake-resistant structures, the information on demand as well as capacity must be obtained. In an experimental investigation, the degree to which the laboratory loading represents the conditions imposed by an earthquake is an important consideration in correlating demand with capacity. In this investigation slow progressively increasing displacement ductility levels were employed for the testing of the specimens. During an actual earthquake where rapid reversal of loads can occur within a period of about 30 seconds, various combinations of ductility levels are possible throughout the period of the earthquake. For each of these loading history, the response of the structure can be very different. Therefore, appropriate load history models must be developed in a laboratory testing of structures under slowly reversing loads to simulate earthquake loading. A valid correlation of the energy demand of the structure with its energy-absorption capacity is possible only if the loading program is comparable to, or more severe than, the loading that might reasonably be expected under earthquake excitation. An adequate characterization of demands would include parameters such as the maximum amplitude of deformation, the number of large-amplitude cycles relative to small amplitude cycles, and the associated maximum forces.

Plain rectangular shear walls were used in this investigation. Various other wall configuration with short projections at the inner wall edge, such as the T- and L-shaped walls, could be used to study the effects of these short projections on the behaviour

of the coupling slab. Figure 7.2 shows the several combinations of the shear wall configuration that can be used in a laboratory investigation on the coupling slab.

Other research in the slab coupling of shear walls can involve the repair of the damaged slab after an earthquake, the evaluation of reserve strength and stiffness of the system during an earthquake, use of high-strength concrete for specific regions of the slab where severe damage occurs and development of appropriate computer models for the coupling slab using a non-linear finite element analysis.

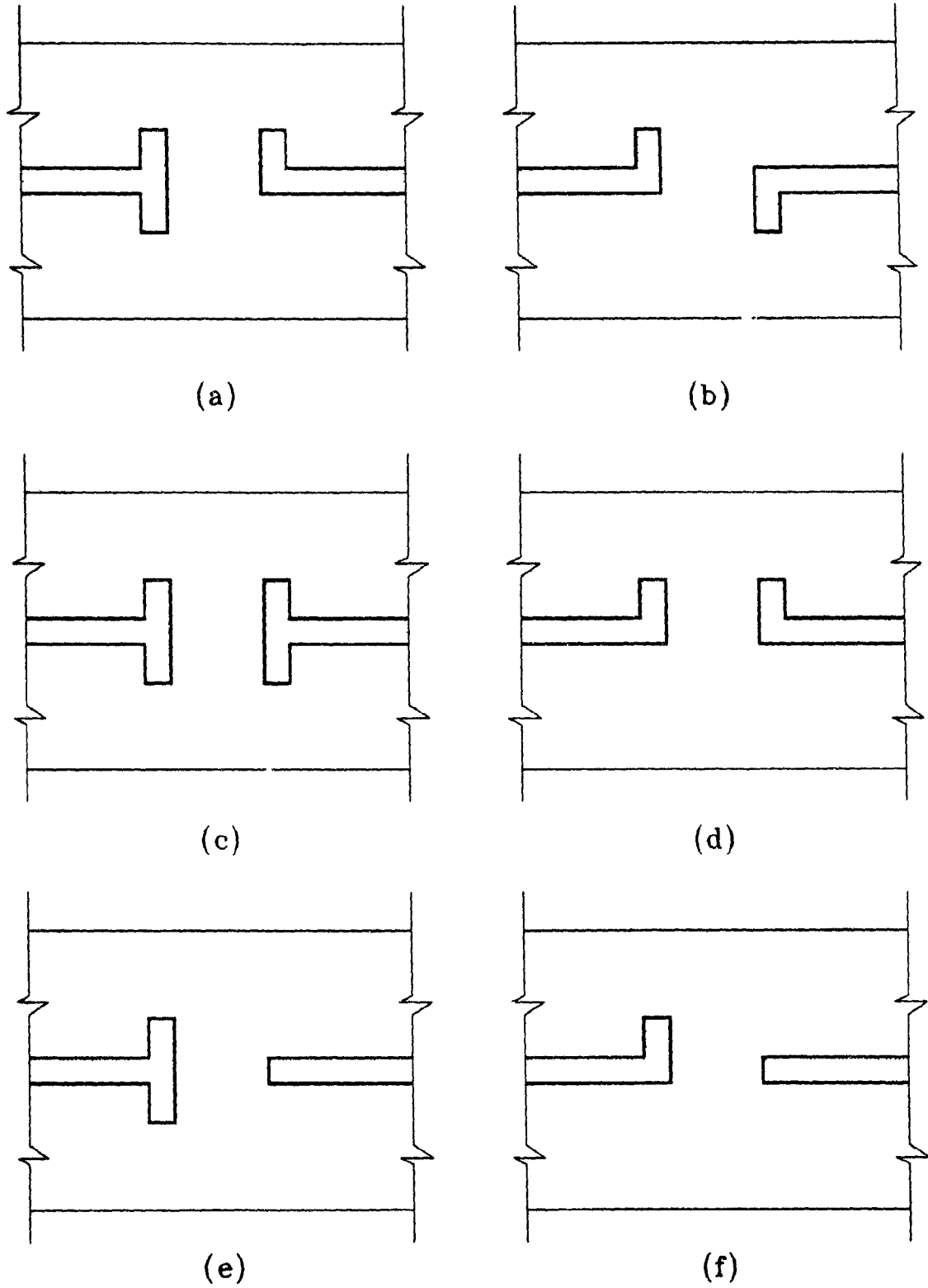


Figure 7.2 Possible Wall Configurations for Future Studies.

REFERENCES

1. Schwaighofer, J. and Collins, M P, "Experimental Study of the Behaviour of Reinforced Concrete Coupling Slabs". *ACI Journal*, Vol 74, No 3, March 1977, pp. 123-127.
2. Park, Robert and Paulay, Thomas, "Shear Walls of Multistory Buildings", *Reinforced Concrete Structures*, John Wiley and Sons, New York, 1975, pp 610-662.
3. Paulay, Thomas and Taylor, Roy G., "Slab Coupling of Earthquake Resisting Shearwalls", *ACI Journal*, Vol. 78, No 2, March-April 1981, pp 130-140
4. Paulay, Thomas, "The Design of Reinforced Concrete Ductile Shear Walls for Earthquake Resistance" *Research Report No. 81-1*, Dept of Civil Engineering, University of Canterbury, Christchurch, February 1981. 119 pp
5. Hawkins, Neil M., "Seismic Response Constraints for Slab Systems", *Proceedings of a Workshop On Earthquake-Resistant Reinforced Concrete Building Construction*, University of California, Berkeley, Vol 3, July 11-15, 1977, pp 1253-1275
6. Barnard, P and Schwaighofer, J "The Interaction of Shear Walls Connected solely through Slabs", *Proceeding of the Symposium on Tall Buildings*, University of Southampton, Pergamon Press, Oxford, April 1966, pp. 157-173
7. Qadeer, A and Stafford Smith, B., "The Bending Stiffness of Slabs Connecting Shear Walls", *ACI Journal*, Vol. 66, June 1969, pp 464-473.
8. Chang, Yin-Chow, "Slabs in Shear Wall Buildings", M.A.Sc. Thesis, University of Toronto, September 1969. 108 pp.
9. Mirza, S. and Jaeger, L G., "A Study of the Behaviour of Coupled Shear Wall Structures", *Proceedings of the First Canadian Conference on Earthquake Engineering*, Canadian National Committee for Earthquake Engineering of the National Research Council, Vancouver, Canada, May 1971, pp. 252-268
10. Coull, A. and El-Hag, A.A. "Effective Coupling of Shear Walls by Floor Slabs", *ACI Journals*, Vol. 72, No 8, August 1975, pp. 429-431.
11. Black, D., Pulmano, V.A and Kabaila, A.P., "Stiffness of Flat Plates in Cross-Wall Structures", *UNICV Report No. R-133*, University of New South Wales, Kensington, Australia, 1974.
12. Schwaighofer, J. and Collins, M.P. "Experimental Study of the Behaviour of Reinforced Concrete Coupling Slabs", *ACI Journal*, Vol. 74, No 3, March 1977, pp. 123-127.
13. Szalwinski, C.M., "Inter-Connecting Slabs in Shear Wall Structures", M.Sc. Thesis, Department of Civil Engineering, University of Toronto, Oct. 1976 144 pp.
14. Taylor, Roy G., "The Nonlinear Seismic Response of Tall Shear Wall Structures", *Research Report No. 77/12*, Department of Civil Engineering, University of Canterbury, Christchurch, 1977, 234 pp.

15. Malyszko, Thomas E., "The Nonlinear Response of Reinforced Concrete Coupling Slabs in Earthquake-Resisting Shearwall Structures", M.Eng. Thesis, Department of Civil Engineering and Applied Mechanics, McGill University, Montreal, August 1986, 130 pp
16. Khan, Mohammad Jalil, "The Nonlinear Response of Reinforced Concrete Coupling Members in Earthquake-Resisting Shearwall Structures", M.Eng Thesis, McGill University, Montreal, (Thesis being finalized).
17. Sabnis, M G., Harris, H.G., White, N.R. and Mirza, M.S., *Structural Modelling and Experimental Technique*. Prentice-Hall, Edgewood, Cliffs, New Jersey, 1983, 585 pp.
18. Mirza, M.S , "Reliability of Structural Models", *Proceedings of the Joint Institution of Structural Engineers/Building Research Establishment Seminar on Reinforced and Prestressed Microconcrete Models*, Garston, England, May 1978
19. National Research Council of Canada. *National Building Code of Canada, 1980*, The Associate Committee on the National Building Code, NRCC, No. 17303, Ottawa, Canada.
20. Canadian Standards Association, *Design of Concrete Structures for Buildings*, CSA Standard CAN3-A23.3-M77, Rexdale, 1984, 281 pp.
21. Mirza, M.S and Lim, Albert K.W. "Behaviour and Design of Coupled Slab-Shear Wall Systems", *Proceedings of the 1989 CSCE/CPCA Structural Concrete Conference*, Canadian Society for Civil Engineering and Canadian Portland Cement Association, Montreal, Canada, March 20-21, 1989, pp 209-244.
22. Derecho, A T., Iqbal, M., Fintel, M. and Corley, W.G., "Loading History for use in Quasi-Static Simulated Earthquake Loading Tests", *ACI Publication SP-63*, 1980, pp. 329-356.
23. Oesterle, R.G., Fiorato, A.E., Johal, L.S., Carpenter, J.E., Russell, H.G. and Corley, W.G., "Earthquake-Resistant Structural Walls-Tests of Isolated Walls", *Report to the National Science Foundation, RANN*, Portland Cement Association, November, 1976, 315 pp.
24. Bertero, V.V., Popov, E.P. and Wang, T., "Hysteretic Behaviour of Reinforced Concrete Flexural Members with Special Web Reinforcement", *Report No. EERC 74-9*, University of California, Berkeley, August 1974.
25. Park, R. and Paulay, T., "Behaviour of Reinforced Concrete External Beam-Column Joints under Cyclic Loading", *Proceedings of the Fifth World Conference on Earthquake Engineering*, Paper No. 88, Rome, 1973.
26. Uzumeri, S.M. and Seckin, M., "Behaviour of Reinforced Concrete Beam-Column Joints Subjected to Slow Load Reversals", *Publication No. 74-05*, Dept. of Civil Engineering, University of Toronto, March 1974, 84 pp.
27. Wight, J.K. and Sozen, M.A., "Shear Strength Decay in Reinforced Concrete Columns Subjected to Large Deflection Reversals", *Report No. SRS403*, Dept. of Civil Engineering, University of Illinois, Urbana, August 1973, 290 pp.

28. Tso, W.K. and Mahmoud, A.A., "Effective Width of Coupling Slabs in Shear Wall Buildings", *ASCE Journal of the Structural Division*, Vol. 103, No. ST3, March 1977, pp. 573-586.
29. Wong, Y.C. and Coull, A., "Interaction Between Floor Slabs and Shear Walls in Tall Buildings", *ACI Publication SP-63*, 1980, pp. 543-573.
30. Wong, Y.C. "Interaction Between Floor Slabs and Shear Walls in Tall Buildings", Ph.D. Thesis, Dept. of Civil Engineering, University of Strathclyde, Glasgow, Scotland, 1979.
31. Petersson, H., "Bending Stiffness of Slabs in Shear Wall Structures", Draft Report, Division of Structural Design, Chalmers University of Technology, Gothenberg, Sweder 1972.